The Location and Effect of Aluminium in Zeolites

Rachel E. Fletcher

A thesis submitted to

University College London

in partial fulfilment of the degree of

Doctor of Philosophy

Supervised by Professor Ben Slater

September 2018

Department of Chemistry

20 Gordon Street

London

WC1H 0AJ

United Kingdom

Declaration

I Rachel E. Fletcher, declare that the work included in this thesis is my own. Where information has been derived from other sources, I confirm this has been indicated in the work.

Rachel E. Fletcher

Abstract

A systematic DFT study has been carried out to investigate the thermodynamic driving force of Al distribution in zeolites and the effect of Al position on catalytic reactions. Much of this study is concerned with small-pore zeolite SSZ-13, which exhibits a CHA-type framework, although Al distribution is also examined in a range of other zeolite framework-types, including RHO, LTA, ABW, AEI and MOR. Al distribution across framework T-sites was examined in zeolite frameworks at different Si/Al ratios, where Al is compensated by different counter-cation species, including alkali metal cations and protons. The most thermodynamically favourable Al distribution in protonated zeolites was found to be that which violates Löwenstein's rule of Al avoidance. On the contrary, alkali metal-containing frameworks favour Löwenstein Al arrangements, demonstrating the influence of cation identity on Al distribution in zeolites. On investigation of the effect of the organic template on these distributions, it was found that whilst the template has some Al directing ability, in the presence of Na^+ and H^+ counter-cations the influence of the SDA on Al arrangement is greatly reduced. The diminished influence of the SDA over Al distribution compared to the Na^+ and H^+ counter-cations is primarily due to sterics and the decreased charge/size ratio of the SDA. Furthermore, introducing water to sodium-containing frameworks screens the charge of the cation, causing Dempsey ordered Al distributions, driven by Al-Al repulsions, to become more thermally accessible in SSZ-13. To examine the distribution of Al throughout the zeolite crystal, SSZ-13 slab structures with (001) and (011) terminating faces were examined. Surface enrichment of Al was found to be favourable in H-SSZ-13 slab structures, whilst well distributed Al was favoured in Na-SSZ-13 structures. Finally, the effect of Al on Mo speciation during methane dehydroaromatisation was examined in Mo/MFI catalysts. The evolution of the catalytically active Mo species was investigated in both silicalite and ZSM-5, these simulations were informed by experiment. Improved binding between the MFI framework and the Mo species was observed in ZSM-5, indicating that the presence of Al is necessary to prevent catalyst deactivation by migration of the active species to the surface of the zeolite.

Impact Statement

The petrochemical industry is one of the world's biggest industries, and is set to be worth $783 billion dollars by 2022. Zeolites are the workhorse catalysts of the petrochemical industry and have been involved in a range of petrochemical processing technologies for several decades, including cracking, isomerisation and alkylation. The global production of gasoline, olefins and other chemical derivatives depends on the catalytic efficacy of zeolites. At a time of increased concern for the environment due to dwindling traditional fuel sources, rising global temperatures and increasing pollution, there has been a mass movement towards the development of alternative approaches to traditional petrochemical processing technologies, which are less harsh on the environment and altogether more sustainable. Zeolite catalysts are at the forefront of this development and are involved in a range of processes including the conversion of natural gas to higher value chemicals, biofuel production and in the curtailment of noxious emissions from vehicle exhausts. Whilst the use of zeolites as catalysts is well-established, many of the mechanisms by which zeolite materials catalyse reactions, and the mechanisms by which the catalyst consequently deactivates, remain poorly understood. This is primarily due to ambiguity surrounding the nature and location of the catalytic active sites within these materials. It is well known that aluminium, the element which introduces a negative charge to the zeolite framework, and its associated counter-cations typically act as the active sites for many important catalytic reactions. In this thesis, computational approaches are used to provide insight into the specific location of aluminium within a range of zeolite framework types in different cationic forms, with much attention given to understanding the forces that determine the distribution of aluminium throughout real zeolite samples. This data is currently being used to develop a transferable machine learning model for the rapid and accurate prediction of aluminium and cation location in zeolites. In the latter part of this thesis simulation is used to aid the understanding of catalyst deactivation during methane dehydroaromatisation (MDA) in which methane is converted directly to benzene. This process circumvents the production of synthesis gas, which is a costly and energy intensive process, however MDA is currently not commercialised due to the rapid deactivation of the zeolite catalyst, hence improving the lifetime of this catalyst is extremely beneficial. The research contained within this thesis has been communicated to the wider scientific community through conference presentations and a research publication.

Publications Related to This Work

Fletcher, R.E., Ling, S., Slater, B. Violations of Löwenstein's rule in zeolites *Chemical Science* **8,** 7483–7491 (2017) DOI: 10.1039/C7SC02531A

Acknowledgements

Thank you to UCL, EPSRC, the MCC and ARCHER HPC for the funding and computer time without which this project would not have been possible.

Thank you to my supervisor, Professor Ben Slater, for his guidance and support over the past three years, the work contained within this thesis would not have been possible without his invaluable feedback.

Thank you to my secondary supervisor and experimental collaborator Professor Andrew Beale, and his group at UCL, particularly Dr Inés Lezcano-González and Miren Agote Aran who provided the experimental Mo/MFI data in Chapter 6. And to Dr Jack Evans at TU Dresden who provided the machine learning data included in Chapter 7.

Thank you to the original members of room 349 in the Kathleen Lonsdale Building for always laughing at all my terrible jokes and eating all my (hopefully less terrible) cakes.

Thank you to Mr Gwyn Williams for making chemistry my favourite subject.

Thank you to the University of Bath and everyone I met there for making me a 'Master of Chemistry' and giving me the best university experience I could have asked for. A special thanks to Craig Franklin, I will forever be grateful that lab partners were assigned alphabetically. And to Dr Mary Mahon, who is amazing, and probably doesn't even know how integral she was to me finishing my degree.

Thank you to the University of South Australia for the amazing opportunity to work there as an intern and for allowing me to discover that I'm not really suited to biochemistry after all, and to Dr Asel Sartbaeva and Dr Stephen Wells for introducing me to zeolites and computational chemistry.

Of course, the biggest thank you to my parents, who told me I could be anything that I wanted to be. Thank you for absolutely everything, I quite literally wouldn't be here without you. Thank you to my grandmothers, for putting the "E" in R.E. Fletcher. And to my grandfathers, to whom I promised I would do this one day. Thank you all for being so unconditionally proud of me. A special thank you to my "little" brother, who *I* am

unconditionally proud of, you are not only a brilliant brother but a brilliant friend.

Finally, thank you to Matt Franceschi for being the one-man practice audience for every single one of my talks, for never letting me give up (even when I *really* wanted to), and for constantly reminding me of what I'm capable of. I couldn't have done this without you.

This thesis is dedicated to my late and very good friend Chris Taylor, who brought chocolate and laughs to the library when we were both finishing our undergraduate lab reports at the last minute. Thank you for being my friend.

Contents

List of Figures

List of Tables

“I pronounce it ‘aluminium’

because there’s an ‘i’ next to the ‘u’ and ‘m’.”

- **Biffy Clyro**

Chapter 1: Introduction

1.1 Overview

This thesis is concerned with the use of computer simulation to provide insight into the structures of microporous aluminosilicates. In this chapter the basic science of porous aluminosilicates, specifically zeolites, is introduced. Next, some of the key challenges in this field are highlighted and explored, particularly challenges in precisely identifying the distribution of aluminium within zeolite frameworks and the impact this has had on understanding zeolite catalyst activity and performance.

1.2 Zeolites

1.2.1 A brief history

In mineralogy, zeolites form a specific family of aluminosilicate minerals that have been known since the 18th Century.[1] However, following St Claire Deville's alleged synthesis of Levynite in 1862[2] and the extraordinary developments made towards the synthesis of novel zeolite structures by Barrer and Milton in the mid-20th Century, now over 80% of known zeolite types are synthetic.[3,4]

The word 'zeolite' comes from the Greek ζέω (*zeo*) meaning 'to boil' and λιθοσ (*lithos*) meaning 'stone'. The term was first coined in 1756 by Swedish mineralogist A.F. Cronstedt, following his discovery of the first identified zeolite mineral, stilbite, from which he observed steam on heating.[1,5]

In nature, zeolites occur in geothermal and hydrothermal settings, desert soils, and sediments, including deep-sea sediments. At present, there are 55 naturally occurring, purely aluminosilicate zeolites, displaying 35 different framework structures. Of these natural zeolites, laumontite, heulandite-clinoptilolite and analcime are the most common, it terms of volume and frequency of occurrence.[3,4,6] Many of these natural zeolites have striking colours and crystal shapes, which has caused some of the more attractive stones, for example scolecite and natrolite, to be used as gemstones in jewellery and ornaments.

Zeolites possess a range functional properties, which arise as a consequence of their unique chemistries and structures. Such properties have been exploited in a range of industries since the 1960s requiring zeolites to be developed and synthesised on

industrial scales, at present it is estimated that between 2·7 and 3·2 billion metric tons of zeolite are synthesised industrially each year.[7] The use of zeolites is most prominent in the petrochemical industry, where they are used as catalysts for a range of processes, including refining crude oil and converting natural gas to higher value chemicals.

Figure 1.1 *A selection of common natural zeolite crystals. From left to right: (Top) chabazite and analcime, (bottom) natrolite and gmelinite.*

1.2.2 Classification

Zeolites are microporous crystalline aluminosilicates. They are characterized by open-framework three-dimensional structures containing cavity spaces accessible through a network of microporous channels. Zeolites are hence classed as molecular-sieves; a family of porous solids whose cavities span a diameter of 0·3 to 2·0 nm.[8] Whilst pore dimensions vary between different zeolite types, pore diameters exceeding 8 Å are rarely observed, and the few zeolites that exist with such sizeable cavities are appropriately referred to as *'extra-large pore zeolites'*. Typical zeolites, with void-spaces on a smaller scale, have a greater commercial history and are most popular in industry, these zeolites are classed as *'small'*, *'medium'* or *'large pore'*.

Zeolites can be represented empirically by the following formula:

$$\left| M_x\ (H_2O)_y \right| \left[Al_x\text{-}Si_{(t-x)}O_{2t} \right] \qquad (1.1)$$

where *t* denotes the total number of tetrahedral species, or T-atoms, present within the framework. Typically, 'T-atom' refers to Si or Al, however in some cases the term 'zeolite' is extended to include non-alumina framework species, for example gallosilicates and silicoaluminophosphates, which contain Ga and P T-atoms, respectively. *x* is the number of framework aluminium atoms, which, uncoincidentally, is equal to the number of extra-framework monovalent cations, *M*. Substituting tetravalent silica for trivalent alumina introduces a negative charge to the framework necessitating the presence of these counter-cations, hence Al and *M* are present in equal amounts. *y* is the total number of water molecules associated with the pores of the as-synthesised zeolite. The presence of this water is responsible for the emission of steam from zeolites on heating. Zeolite composition can hence be considered generally as a 'T-atom' - oxygen framework structure containing extra-framework counter-cations and a sorbed phase.[9]

1.2.3 Framework and structure

The zeolite framework can be defined as the infinitely extending, three-dimensional, inorganic framework structure, which demarcates the zeolite void-space, *i.e.* pores and channels.[10] At present, there are 228 different zeolite framework topologies, as defined by the structure commission of the International Zeolite Association.[4] Each of these frameworks structures is assigned a three-letter type-code. Typically, these codes are either an abbreviation of the name of a natural mineral which displays the given framework type, for example *chabazite* is simply shortened to CHA, or in the case of purely synthetic structures, the initials of the material's discoverers, for example ABW, which was first synthesised and observed by Barrer and White in the early 1950s.[11]

The unique structure of each framework topology arises from the specific arrangement of tetrahedral units (TO_4) of alumina (T = Al) and silica (T = Si) in space. These tetrahedral units are commonly referred to as the primary building units (PBUs) of the zeolite framework, they are the first of three discrete levels of zeolite framework structure. The PBUs are the basis of the zeolite framework and are common to all framework types. They are rigid structures, with near-perfect tetrahedral geometry (θ(O-T-O)= ~109·5˚). Each of these PBUs come together *via* bonding oxygen at the apices of each tetrahedra to form the second level of zeolite structure, complex polyhedral shapes referred to as the secondary building units (SBUs). SBUs usually

contain less than 20 T-atoms, and like frameworks, the most common SBUs are given names and corresponding codes. The simplest SBUs take the form of planar ring structures, typically composed of 3 - 8 PBUs, for example 6-rings (6R) and 8-rings (8R). However, due to the complex nature of the zeolite framework, it is often convenient to talk in terms of larger, three-dimensional polyhedra, for example double-rings and cages. Figure 1.2 shows some of the most common zeolite SBUs, the double 6-ring denoted by the abbreviation D6R, and the β- and α-cages. Cages are typically described by their polyhedral faces, for example the β-cage, which is comprised of six 4-rings and eight 6-rings is described by the notation [$4^6 6^8$].

Considering zeolite frameworks as sequentially increasing levels of structure is useful for many reasons. Particularly in understanding and rationalising the zeolite crystallisation process during synthesis. It is generally thought that zeolite crystallisation from a solution occurs in two major parts, first nucleation from a solution, forming discrete aluminosilicate clusters, and then crystal growth, which involves the assimilation of aluminosilicate material resulting in the final zeolite framework structure.[12] It is widely agreed that although the TO_4 unit is considered to be the most basic structure present in aluminosilicate zeolites, certain SBU structures, particularly 4-rings and double 4-rings, play a prominent role in the nucleation process. This has been extensively researched using both experimental and theoretical approaches [13,14] (the processes of nucleation and crystallisation are discussed in greater detail in section 1.1.4). SBU structures also give an indication of the dimensions of the pore space, and the accessibility of small molecules, for example water and other extra-framework species, to channels and cages.

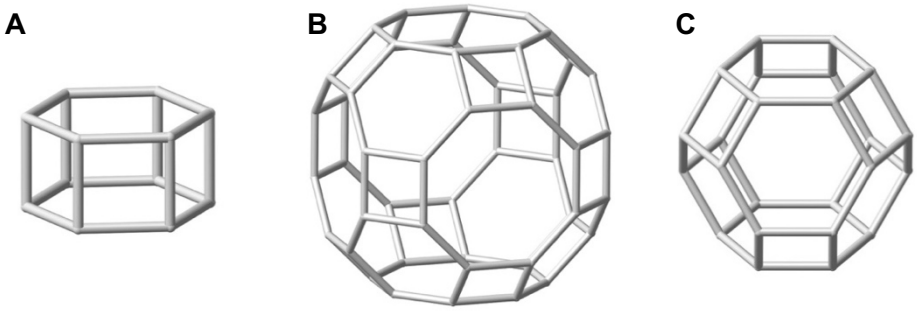

Figure 1.2 *A selection of common SBUs in their all-silica forms,* ***a)*** *double 6-ring (D6R),* ***b)*** α-cage (or LTA cage), ***c)*** β-cages (or SOD cage).

1.2.3.1 Frameworks studied in this thesis

1.2.3.1.1 CHA

The CHA-type, or *chabazite*, framework (Figure 1.3a) has been observed in a range of zeolites, including the natural mineral chabazite, from which it takes its name. Discovered in the late 18th Century, natural chabazite is typically found in the cavities of volcanic rocks, such as basalt, and presents itself as attractive colourless or pink cube-like crystals.[15] Synthetic zeolite SSZ-13 and silicoaluminophosphates SAPO-34 and SAPO-44 also display a CHA-type framework .[3]

CHA belongs to the ABC-6 family of zeolite frameworks, all of which are fundamentally composed of 6-ring (6R) or double 6-ring (D6R) SBUs arranged in a hexagonal array forming a single layer. In order to form the framework structure multiple 6-ring layers are stacked in the sequence ABC, interconnected by tilted 4-rings. Variation in the stacking sequence yields different ABC-6 zeolite frameworks, for CHA, the 6-ring stacking-sequence is AABBCC, whereas, in the SOD framework for example, the sequence is simply ABC.[10]

This sequence of stacked layers gives rise to the characteristic *'cha'* cavity. An 18-face cage, comprised of twelve small 4-ring faces, and six larger 8-ring faces, described by the notation [$8^6 4^{12}$]. Access to the cavity is limited by the largest aperture, the 8-ring, which has an approximate diameter of 3·8 Å. CHA zeolites are hence considered 'small pore'.[3] The CHA framework is a mid-range density framework type, with a framework density of 15·1 T/1000 Å^3, which adopts the $R\bar{3}m$ space group, with a hexagonal unit cell of idealized cell dimensions: $\boldsymbol{a}$ = 13·7 Å, $\boldsymbol{c}$ = 14·8 Å.[3] Each unit cell contains a total of 36 crystallographically indistinct tetrahedral atoms, or T-sites, connected by 72 bridging oxygen atoms, arranged in two D6R units, connected by a tilted 4-ring (Figure 3a). The framework may also be described using a smaller rhombohedral cell, however, this cell contains a total of 12 crystallographic distinct T-sites, and therefore, although smaller this cell is more complex. Vertex symbol notation is a useful way to simply describe the composition of a zeolite framework, as it gives clear indication of the largest and smallest apertures within the structure. The notation is made up of six numbers per T-site corresponding to the six angles of the tetrahedron, the hexagonal CHA unit cell is described by the vertex symbol 4·4·4·8·6·8,[3] Figure 1.3b demonstrates how this vertex symbol is attained. The unit cell may also be described by the face symbol [$4^6 \cdot 6^2$] + [$4^{12} \cdot 6^2 \cdot 8^6$].[3]

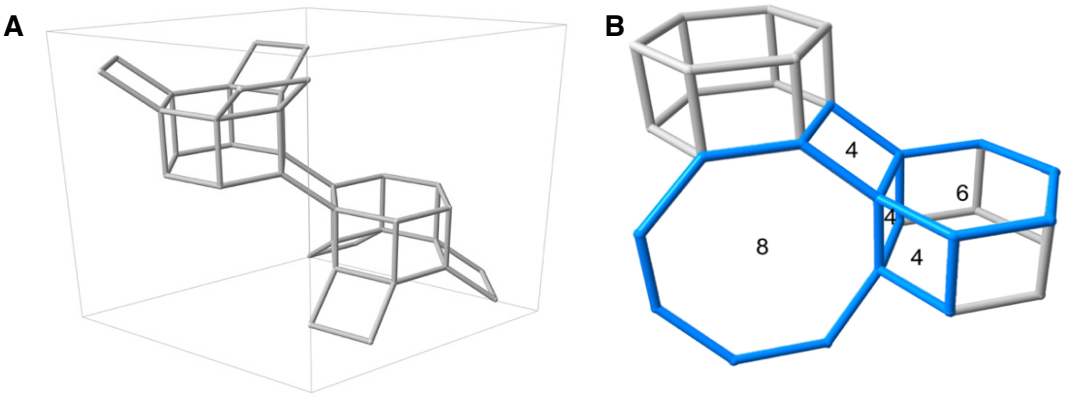

Figure 1.3 a) *Silicon backbone of the CHA framework, viewed along [$\bar{1}$ 1 0]* ***b)*** *The origin of the CHA vertex symbol,* 4·4·4·8·6·8, the 8-ring window is one of the six 8-ring faces of the *'cha' cavity*.

1.1.3.1.2 LTA

The LTA or Linde Type A framework, Figure 1.4a, is constructed from β-cages, 24 T-atom cages, connected through double 4-rings. This arrangement of SBUs gives rise to larger α-cages, 48 T-atom cavities which, like the *'cha'* cavity in the CHA framework, are accessible through an 8-ring pore system.[3,10] It is notable that the smaller β-cages, comprised of six 6-ring faces and six 4-ring faces are considered inaccessible as the apertures are too small for molecules larger than water to diffuse through.[10] The vertex symbol for LTA is 4·6·4·6·4·8.[3]

The LTA framework adopts the *Pm$\bar{3}$m* space group, with an ideal cubic unit cell of ***a*** = 11·9 Å. Each unit cell contains a single α-cage, with β-cages positioned at each of the eight corners of the cube. Like CHA, each of the 24 T-sites in this unit cell are crystallographically indistinct. LTA has a low density of 14·2 T/1000 Å^3, this is due to the large amount of void space, in the α and β cage system.[3]

1.2.3.1.3 RHO

The RHO framework, Figure 1.4b, is remarkably similar to the LTA framework and has a comparable density of 14·1 T/1000 Å^3, due to similarities between the frameworks' SBUs. RHO is also constructed from α-cages, however these cages are linked by interconnecting double 8-rings without the presence of the smaller β-cages. Hence, RHO, like both CHA and LTA, possesses an 8-ring channel system, however, unlike LTA, all channels are considered accessible to molecules larger than water.

The RHO framework possesses a cubic unit cell, with an idealized cell parameter of ***a*** = 14·9 Å, which crystallizes in the *Im$\bar{3}$m* space group.[3] Like LTA, each cubic unit cell contains a single α-cage, however, a further eight α-cages, rather than β-cages, sit at each of the corners of the cell in RHO. The framework is described by the vertex symbol 4·4·4·6·8·8.[3]

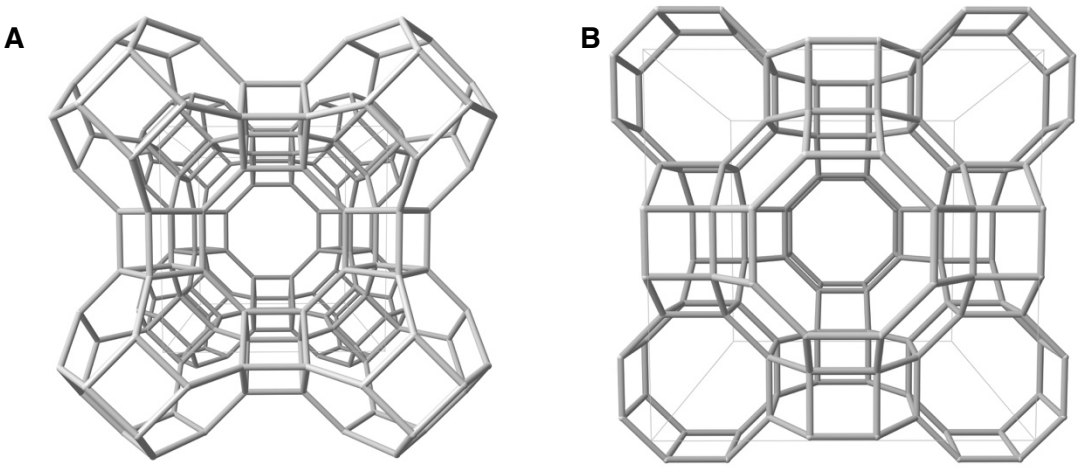

Figure 1.4 *Silicon backbone of the* ***a)*** *LTA framework and* ***b)*** *RHO framework*

1.2.3.1.4 ABW

The ABW framework, Figure 1.5a, was first observed in a synthetic lithium-containing zeolite, Li-A(BW) synthesised by Barrer and White in 1951.[11] This extremely dense zeolite framework has a framework density of 17·6 T/1000 Å^3 due to very little void space present between the compact atypical *abw* SBUs (Figure 1.5b). The *abw* SBUs are characterized by a strained 8-ring connected to a small 4-ring by two 6-ring structures, an 8-ring and another 4-ring. These SBUs are arranged in what is referred to as a double zigzag chain, four infinitely extending chain motifs are present per orthorhombic unit cell. The ABW unit cell is considerably smaller than the cells of most zeolite frameworks, and crystallises in the *Imma* space group with idealized cell parameters of ***a*** = 9·9 Å, ***b*** = 5·3 Å, ***c*** = 8·8 Å. The vertex symbol for the ABW framework is 4·6·4·6·6·8$_2$.[3]

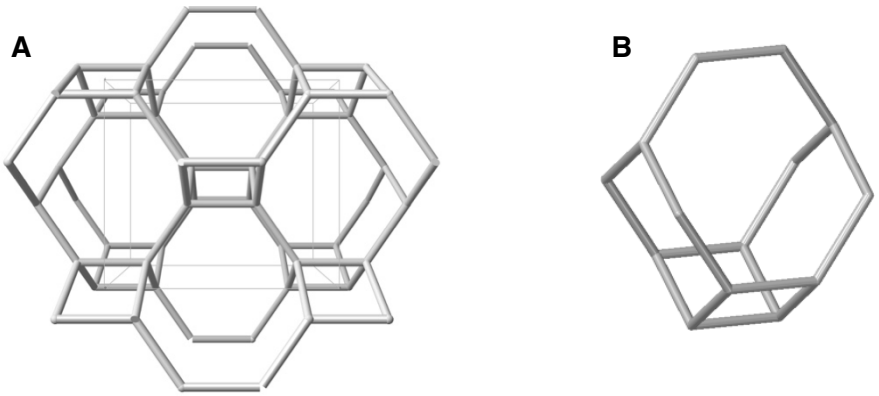

Figure 1.5 a) *Silicon backbone of the ABW framework* ***b)*** *the abw SBU*

1.2.3.1.5 MOR

The MOR framework (Figure 1.6a) takes its name from the naturally occurring zeolite mineral mordenite, in which it is exhibited.[16,17] Of the 55 naturally occurring zeolite types, mordenite is one of the most abundant and tends to be highly siliceous with a typical Si/Al ratio of 5. MOR is also one of the most commercially important zeolites, and for this reason has also been made synthetically with Si/Al ratios ranging from 4 to 22.[10,18]

The MOR framework is constructed from chains of linked 5-membered rings forming alternating 8- and 12-ring channel systems in one direction, each with approximate maximum apertures of 7 Å and 5·7 Å, respectively. The MOR framework possesses an orthorhombic unit cell, which crystallises in the *Cmcm* space group with idealised cell parameters ***a*** = 18·3 Å, ***b*** = 20·5 Å, ***c*** = 7·5 Å. Unlike the previously discussed frameworks, each MOR unit cell contains four crystallographically distinct T-sites. The vertex symbols of which are T_1 $5{\cdot}5{\cdot}5{\cdot}5_2{\cdot}8{\cdot}12$, T_2 $5{\cdot}5{\cdot}5{\cdot}5_2{\cdot}5{\cdot}8$, T_3 $4{\cdot}5_2{\cdot}5{\cdot}8_2{\cdot}5{\cdot}8_2$, T_4 $4{\cdot}5_2{\cdot}5{\cdot}8{\cdot}5{\cdot}8$. MOR is a high density zeolite with a framework density comparable to that of ABW, typically 17·2 T/1000 $Å^3$.[3]

1.2.3.1.6 AEI

Like MOR, the AEI framework also possesses an orthorhombic unit cell, which crystallises in the *Cmcm* space group. The AEI unit cell (Figure 1.6b), however, is less dense than the MOR framework, with idealised cell parameters of ***a*** = 13·7 Å, ***b*** = 12·6 Å, ***c*** = 18·5 Å, and a framework density of 14·8 T/1000 $Å^3$, comparable to that of LTA. The AEI framework also has multiple crystallographically distinct T-sites, in this

case there are three, each with the same vertex symbol T_1 4·4·4·8·6, T_2 4·4·4·8·6, T_3 4·4·4·8·6.[3]

Like CHA, AEI is comprised solely of D6R SBUs connected by tilted 4-rings, forming large cavities accessible through an 8-ring pore system. However, unlike CHA, AEI does not belong to the ABC-6 family of zeolite frameworks. This is due to the fact that each layer of D6R units, arranged in a hexagonal array, is related to the next by a rotation of 180˚ along the normal plane, where in CHA, or any other ABC-6 zeolite, each layer is related by pure translation along the normal plane.[3,19] Since the AEI and CHA frameworks are so closely related the frameworks are known to exists as intergrowths.[20,21]

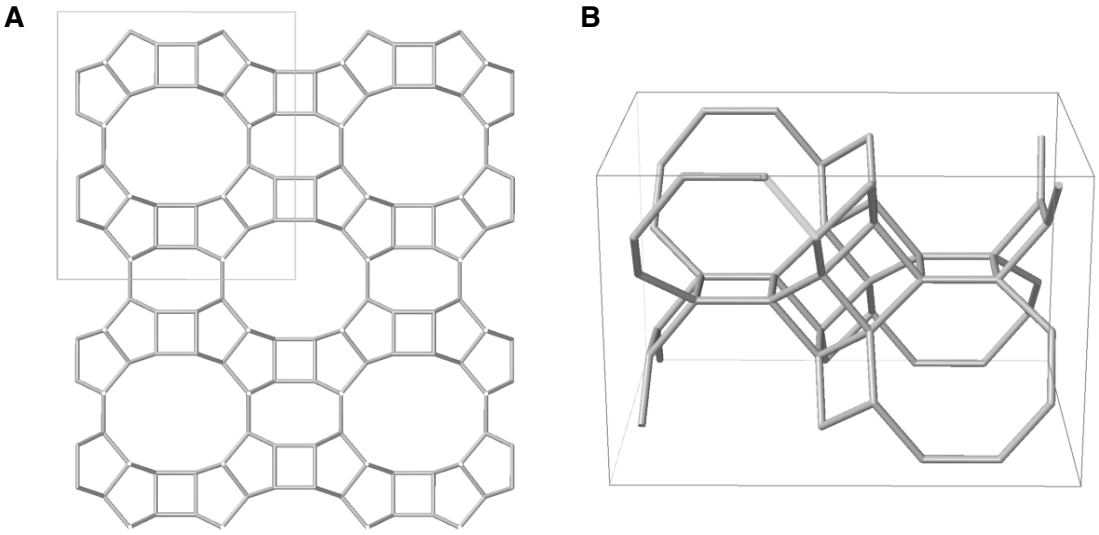

Figure 1.6 a) *Two-dimensional silicon backbone of the MOR framework, showing a single unit cell,* ***b)*** *Silicon backbone of the AEI framework*

1.2.3.1.7 MFI

The MFI framework (Figure 1.7a) is built from 5-1 SBUs, pentagonal structures with a single branch or bond protruding from one vertex of the pentagon. Due to the abstract nature of these SBUs, MFI is generally referred to as as being constructed from pentasil units (Figure 1.7b), where a single pentasil unit is formed of eight interconnecting pentagons, or of T-12 units, which are made up of two 5-1 SBUs related by a 180˚ rotation. These T-12 units form what are known as pentasil chains, which further connect in one plane to form a pentasil layer. It is this layer that acts as

the MFI *periodic building unit*, and the MFI framework is obtained when each of these successive pentasil layers is related by inversion. [3,10,19,22,23]

MFI has an orthorhombic framework structure, containing cavities connected by a series of straight and sinusoidal 10-ring channel systems, with maximum apertures of approximately 5·6 Å. The channels lie orthogonal to one another, the straight channels running along the ***b*** parameter and the sinusoidal channels along ***a,*** points at which the channels meet are referred to as intersections. MFI-type zeolites are typically highly siliceous, and examples of such zeolites have been synthesised with Si/Al ratios of 10 to infinity. [3,10,19,22,23]

MFI crystallises in the *Pnma* space group, with idealised cell parameters of ***a*** = 20·1 Å, ***b*** = 19·7 Å, ***c*** = 13·1 Å. Due to the compact nature of the pentasil units, MFI is the densest framework discussed in this work, with an idealised framework density of 17·9 T/1000 Å^3. The MFI framework also has the highest number of crystallographically distinct T-sites of any other framework structure in this work, with each 288 atom unit cell containing 12 geometrically distinguishable T-sites. It is notable that when synthesised at lower temperatures, typically less than 340 K, a monoclinic form of the framework is engendered, this polymorph contains 24 distinct T-sites.[3,10,19,22,23] The vertex symbols of all MFI's T-sites have been omitted for conciseness, but all are listed in Appendix A of the IZA's Atlas of Zeolite Framework Types.[3]

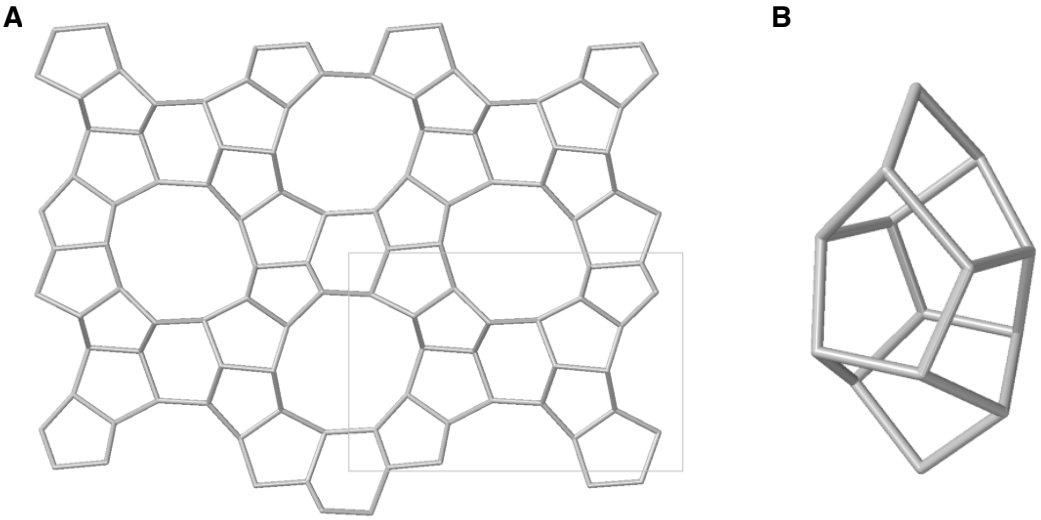

Figure 1.7 a) *Two-dimensional silicon backbone of the MFI framework, showing a single unit cell,* ***b)*** *Pentasil unit, made up of eight 5-rings.*

1.2.4 Synthesis, crystallisation and growth

The most successful method for generating good quality zeolite crystals is hydrothermal synthesis - the process of making crystalline structures in aqueous solution at temperatures exceeding 373 K. During hydrothermal synthesis, framework precursor materials, sources of silica and alumina, are mixed together with a cation source in a high pH medium, forming an aluminosilicate gel. This gel is then heated in an autoclave for a matter of hours, days or weeks, depending on the identity of the desired zeolite.[24]

A basic medium is achieved through the addition of aqueous alkaline salts, typically metal hydroxides, to the initial synthesis mixture, and is required to increase the solubility of the alumina and silica precursors during gel formation.[25] Such hydroxide salts, along with various fluoride salts, are referred to as 'mineralizing agents' due to their ability to increase the activity and mobility of the precursor materials in solution.

During hydrothermal synthesis, several reactions and species are formed in a series of stages. Firstly, the induction period, defined as the time elapsed between the start of the reaction and the point at which crystals are formed, this period can be broken down into three distinct parts; the relaxation time, where particles in the gel are completely amorphous; nucleation, where molecules in the reactant phase arrange themselves to form stable clusters, or seeds; and growth of the crystals to a visible size, where the amorphous gel begins to develop areas of local order. The induction period is then followed by rapid crystal growth to form the final crystalline zeolite structure.[24–26] Detailed explanations of the discrete stages of zeolite formation, and the underlying thermodynamics of each of the stages are included in references 24–27.

There is considerable debate concerning the identity of the dissolved precursor particles present within the initial aluminosilicate gel at high pH, since following the reactions that form these species, and the subsequent reactions that they are involved in, are difficult to study experimentally. However, it is generally accepted that alumina adopts the form of tetrahedral alumina $Al(OH)_4^-$, whereas silica is thought to exist as a range of oligomeric species.[13,24,28–30] It is proposed that these silica oligomers are formed through the dimerization and subsequent polymerization of tetrahedral silica monomers, which proceed *via* a series of condensation reactions. These molecular species go on to form larger aluminosilicate oligomers, often termed the 'pre-

nucleating' species, which continue to grow to form nuclei with proceeding reaction time.[24,25,31–35]

The solubilized precursor and pre-nucleating species are not entirely dissimilar to the T-O-T linked alumina and silica tetrahedra observed in the final zeolite framework. Similarities in composition between the starting materials and final structure causes the overall change in Gibbs free energy for zeolite synthesis to be very small.[24,33,36–38] Zeolite synthesis is hence considered to be a kinetically controlled phenomenon. In fact, zeolites are metastable, and during synthesis the tendency of the system to form transient, intermediate-state materials with high resemblance to the starting materials with very little loss of free energy can cause the formation of a series of 'kinetic products', which can lead to the generation of a mixture of co-framework products, present in the form of intergrowths, rather than one pure 'target framework'. These co-frameworks products are termed 'competing phases' and will be present in lesser or greater amounts depending on the conditions, and hence the kinetics of the synthesis.[24,39] Furthermore, prolonged synthesis or synthesis at higher temperatures can result in further transformations into more stable, denser zeolite materials, and eventually non-porous solids, this is due to the reduced free-energy barrier to nucleation on the formation of non-porous nuclei over porous nuclei.[39]

One of the most prominent problems in zeolite science has been the inability to confirm the identity of the pre-nucleating and nucleating species present during zeolite formation, and hence derive an accurate formation mechanism. Although there is a wealth of literature on this topic, it seems that for a given zeolite, the number and type oligomeric species observed strongly depends on the choice of analysis technique and interpretation of the data (see review articles in references 24, 33, 40 and 41).

Advances in computational methods have made it possible to calculate the structures, energetics, and reactions of discrete aluminosilicate clusters during the pre-nucleation and nucleation stages of zeolite formation. A large amount of theoretical work was done in this area in the mid-1990s to early 2000s (see reference 42), however, this work was primarily concerned with the formation of silica clusters. Arguably, the most exhaustive computational studies on the subject of pre-nucleating aluminosilicate species are two works by Yang *et al.*[13,43] It is well known that the nucleation and growth of zeolite crystals is strongly affected by the hydrothermal conditions in which they are formed, and hence the identity of the pre-nucleating species will be strongly influenced

by thermal effects, and of course the presence of the solvent, usually water. Yang *et al.* examined the importance of solvent effects during zeolite formation, evaluating the stability of potential aluminosilicate clusters in solution[13] and then using these clusters as initial structures in modelling the nucleation of zeolite A.[43]

In the former study, the authors investigated the thermodynamic stability of a range of aluminosilicate clusters, ranging from 1T to 4T, in the gas phase through DFT. To simulate the solvation of the aluminosilicate clusters, the authors re-optimised these clusters using the COSMO approach,[44] in which the effect of solvation is simply treated as a dielectric continuum. They found that the stability of the clusters could not be attributed to a single factor, but instead to a collection of factors, including the distribution of aluminium, the position of the extra-framework cations, both inter- and intramolecular hydrogen bonding and, of course, the solvent. In the latter study on LTA, the authors found that in the presence of the solvent, asymmetric clusters were thermodynamically favoured, where they were disfavoured in the gas phase. Furthermore, hydrogen bonding between the clusters and available water molecules further stabilised the clusters in solution, compared to in the gas phase.[13] Once again the COSMO approach was employed to model the stabilities of the two proposed competing condensation reactions occurring during zeolite nucleation, chain polymerisation and cyclisation. They found cyclisation reactions to be the most favourable in the nucleation of zeolite A, noting that cyclisation reactions become relatively more favourable with increasing temperature. Using the relative energies of the successive condensation reactions the authors determined the mechanism of nucleation in zeolite A to be as follows: dimer → tetramer → 4ring → 4–4ring → tri4ring → openD4R → D4R (Figure 1.8).[43]

Following nucleation, crystallization is observed. It is notable that the final crystallisation phase proceeds at a far more rapid rate than the prior nucleation phase, hence nucleation is the rate determining process occurring during hydrothermal synthesis. However, crystal growth in zeolites proceeds at a considerably slower rate than that of more dense systems.[27]

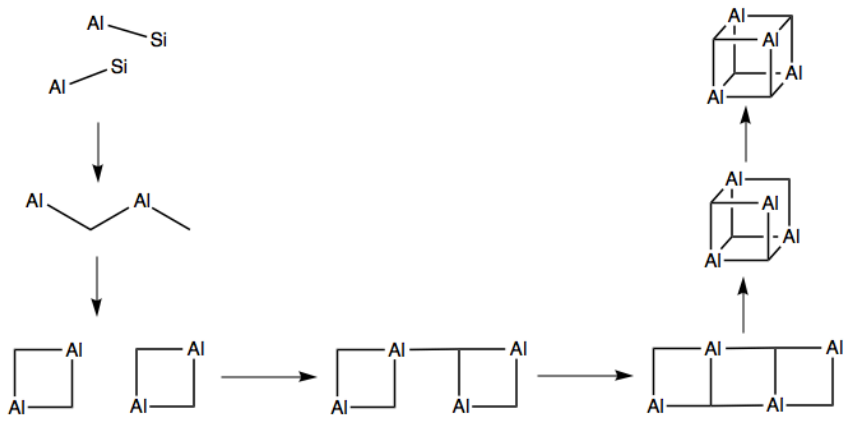

Figure 1.8 *Proposed mechanism for the formation of a D4R during the nucleation stage of LTA synthesis. Figure adapted from Yang et al.*[43]

Crystal growth can be described as a series of processes involving the assimilation of material from solution (transport processes), followed by the incorporation of atoms or molecules into a crystal's surface (surface processes), causing an increase in dimension. It is understood that crystal growth is limited by the slowest of these processes, and hence growth is often referred to as either transport or surface controlled.[27]

There is much ambiguity surrounding the specific pathways by which a zeolite crystal may grow during synthesis, and in recent years, a great effort has been dedicated to forming a fundamental understanding of these mechanisms. A range of surface-sensitive microscopy approaches, such as AFM and TEM, along with more conventional analytical techniques, such as NMR and mass spectroscopy, have been used to monitor zeolite crystal growth in real time, and in some cases, these techniques have been combined with computational methods.[45–48]

There are generally two schools of thought relating to the zeolite crystallisation process: classical crystallisation, which has been the hypothesis described throughout this section, involving pre-nucleation, nucleation and crystallisation; and non-classical crystallisation, which involves the aggregation and attachment of nanoparticles that range in complexity.[47] A recent *in situ* AFM study on the growth of the (100) surface of LTA by Kumar *et al.*,[46] revealed that multiple modes of growth, both classical molecule-by-molecule growth and non-classical growth, occur during the crystallisation of LTA

and that these growth mechanisms depend on the conditions of synthesis. This work supports earlier findings by Lupulescu *et al.*, which demonstrated that growth mechanisms in silicate-1 (MFI) proceed by the addition of both silica molecules and precursors, an amalgamation of classical and non-classical pathways.[45]

1.2.4.1 Templates

Since zeolites are thermodynamically metastable phases zeolite synthesis often requires the presence of an organic structure directing agent (SDA). The main responsibility of the organic SDA is to prevent the synthesis of thermodynamically stable dense or amorphous phases (competing phases), which are otherwise favoured. In essence, this is achieved by using an SDA to template the characteristic cavity spaces of a desired aluminosilicate framework, which forms around the SDA during nucleation.[36,49] The final structure of the zeolite framework hence reflects the shape of the organic SDA, and it has been shown that there is a correlation between the van der Waals shape of the SDA and the architecture of the zeolite pore.[33,50,51] In 1961 Barrer and Denny reported the first instance of zeolite synthesis in the presence of organic SDA, using tetramethylammonium (TMA) to direct the formation of SOD.[52] Since then a range of SDAs have been used to synthesise the 228 zeolite framework types, with typical SDAs including alcohols, ethers, amines and quaternary ammonium salts.

Whilst the importance of the presence of an organic SDA has been recognised for many years, there is still a great deal of ambiguity concerning the mechanisms by which SDAs direct the synthesis of a given zeolite framework. It is generally agreed that during hydrothermal synthesis of a zeolite, the initial aluminosilicate gel condenses to give the zeolite framework, which encapsulates the templating molecule.[36,42,49] It has also been established that a successful SDA must effectively fill the pore space of the desired zeolite framework, and through combined Monte Carlo and molecular dynamics (MD) calculations, Lewis *et al.* showed that the degree of 'good fit' between the SDA and the host framework could be quantified by van der Waals interactions, whereby efficacious SDAs show maximum interaction with the aluminosilicate framework.[50,51] Although it has also been shown that an organic SDA's charge, hydrophobicity, rigidity and rotational dynamics may also play a significant role.[50,53,54] However, the fact that several templating molecules may be used to synthesise a single zeolite framework, and reciprocally, several different framework types may be

synthesised from a single template, indicates that templating effects in zeolites are not as specific as might be anticipated.[55]

Although it is certainly possible to target the synthesis of given framework through an adroit choice of SDA, developing a successful *a priori* approach for the precise generation of SDA molecules for specific target frameworks has been a topic of intense interest within the zeolite community for decades. In 1996 Lewis *et al.*[35] developed ZEBEDEE a computational method for the *de novo* design of templating molecules, in which, the SDA is 'grown' within the void space of the target framework. The template is constructed from an initial 'seed' molecule and a library of molecular fragments through a series of random actions. Successful additions are controlled by a van der Waals overlap function, and the final structure of the template is geometry optimised within the fixed host framework *via* an external minimizing program.[35] This method has been successful in generating new template structures for known zeolite frameworks.[56]

In many cases the template molecule alone cannot direct the synthesis of a given framework, and successful synthesis of a target structure can only be achieved when in the presence of both a template and a metal cation. For example, whilst the TMA cation is a notoriously efficient SDA for the synthesis of a range of zeolites, the presence of Na^+ is also required for the synthesis of zeolites A to N. It is thought that the Na^+ cation is required to template the formation of the double ring SBUs, for example D4R and D6R, present within these frameworks, whilst the larger TMA cation templates the larger framework cavities.[57] This idea of cation-mediated assembly was first recognised by Flanigen in 1973, who noted that certain cations stabilise certain structural subunits during zeolite synthesis.[58] It is noteworthy that in the same year Meise *et al.* also reported that whilst the presence of small Na^+ cations aids the synthesis of LTA and decreases the crystalisation time, the presence of larger cations impedes crystallisation.[59] Whereas Burkett *et al.* showed that the addition of larger cations, alongside Na^+, actually helped rather than hindered the crystallisation of certain frameworks, such as OFF and CHA.[60]

The complex role of inorganic cations in zeolite synthesis has become a topic of increasing interest over the years, as new zeolite templates, zeolites and synthesis methods have been realised. One interesting intricacy is the ability of organic templates and metal cations to form supramolecular complexes during synthesis. An example is the use of 18-crown-6 and Na^+ in the synthesis of the EMC-2 zeolite (EMT), in which

the crown ether distorts to facilitate coordination between its six oxygens and the Na^+ cation, which lies above the plane of the ring. Whilst it is common to refer to the organic molecule as the template in this synthesis, the real template is in fact the resultant crown ether-cation complex.[60–62]

It should also be mentioned that whilst the use of an organic SDA during zeolite synthesis often ensures the successful generation of a particular target framework, it is generally preferable to avoid the use of an organic template altogether. This is for two main reasons: firstly, organic templates, particularly larger, more complex templates are expensive; secondly, post-synthesis, templates have to be removed from the framework *via* calcination. Whilst these considerations pose few problems for small lab-based syntheses, they are a serious concern for large-scale industrial syntheses due to economic and environmental considerations. In recent years there has hence been a move toward template-free synthesis. Some early template-free syntheses rely on cation-mediated assembly, in which large framework cavity spaces are 'templated' by introducing larger cations to the initial synthesis mixture, or alternatively increasing the number of 'usual' synthesis cations.[63,64] Alternative template-free approaches include well-established techniques such as seeding and interzeolite transformations, and more exotic approaches, for example those that include the use of polymer hydrogels.[65–67] However, such syntheses are rarely as reliable as 'traditional' approaches involving organic SDAs. Zeolites synthesised *via* template-free approaches are often formed as a mixture of products due to problems in stabilising the target framework relative to more dense competing phases, it can also be difficult to control the Si/Al ratio of the resulting zeolite.

1.2.5 Industrial and commercial applications of zeolites

The functional properties of zeolite materials have been widely exploited in industry for over half a century. Their microporous networks allow them to work as efficient molecular sieves in synthetic organic procedures, where they are able to selectively isolate desired products from reactions governed by unfavourable equilibria. The presence of extra-framework cationic species causes zeolite materials to be useful ion exchangers. Different framework topologies have been shown to have different affinities for specific cations, this property has been exploited in water softening technologies, where 'hard' cationic species, for example Ca^{2+}, are exchanged for softer Na^+ cations. Zeolite A (LTA) has been shown to be one of the most efficient water

softening zeolites, and has been used as such since the 1970s.[68,69] Similar cation-release behaviours in zeolites have also been exploited for agricultural uses, namely as a means to supply micronutrients to plants, both Rho (RHO) and Li-A(BW) (ABW) have been included in this technology.[70] Zeolites have also been employed as sorbents, both for laboratory use, most notably as mercury sorbents,[71] and for military use, where they are incorporated into wound dressings to absorb excess blood, promoting haemostasis and ultimately expediting the wound healing process.[72] The latter use has recently been extended to exploit the gas storage and release properties of zeolites, along with sorbent effects. NO loaded Zn^{2+} exchanged LTA-type zeolites have recently been developed as prospective biocompatible medical devices which have been shown to reduce infection of known bacteria strains. This is due to the bactericidal effects of NO which is measuredly released from the LTA-framework.[73–75]

1.2.5.1 Catalysis

Arguably, the most significant application of zeolite materials is their use as heterogeneous catalysts. Zeolites have two unique properties that make them especially adept catalytic materials; their exchangeable cations, which act as catalytically active site (discussed in detail in subsequent sections) and their microporous networks of channels and cavities, which have one or more discrete sizes per zeolite framework type. The latter property allows zeolites to act as extremely selective size-excluding catalysts, as only reactants whose dimensions are lower than a critical size can enter the zeolite pores and react with internal catalytic sites. Furthermore, pore dimensions also restrict the formation of certain transition states, and only molecules with dimensions small enough to exit the pore network appear in the final product.[76]

Heterogeneous zeolite catalysts have been most prominently used in the petrochemical industry, as catalysts for petroleum refining and petrochemical processing. The next few sections will discuss the use of zeolites in petrochemistry, and other notable zeolite catalysed industrial processes in detail.

1.2.5.1.1 Petroleum refining

The principle task of a modern petroleum refinery is to adapt a largely unstable supply of feedstock (crude oil) to fluctuating product demand, typical main products include transportation fuels, lubricants, alkanes, bitumen. This task is made more difficult by the increasing tendency of crude oils to have heavier molecular weights, lower H/C

ratios due to the presence of aromatics and to be loaded with impurities such as metals, sulfur and nitrogen; alongside more and more stringent regulations which require refineries to produce products with increased H/C fractions and reduced pollutants whilst working at optimal efficiency.[77]

A typical modern refinery is an assemblage of processes, which can be categorised into two main types, physical separations and chemical transformations. The majority of the chemical processes are catalytic, and the three main refinery processes in which zeolite catalysts are involved are fluid catalytic cracking (FCC), hydrocracking (HDC) and C_{4-6} alkane hydro-isomerization.[77,78] The following paragraphs provide a brief overview of these three processes, detailed descriptions of these processes can be found in references 77–79.

FCC is one of the most important processes used in oil refineries. It is the process that converts heavy gas oil (HGO) into gasoline. HGO is the fraction of crude oil with the highest boiling point (> 340˚C) and molecular weight (> 200). The catalyst of choice for this reaction is zeolite Y (FAU), which acts as a mono-functional catalyst, as the reaction is endothermic FCC is usually carried out at high temperatures and low to moderate pressures. One drawback of using zeolite Y as a catalyst for FCC is the catalyst cokes very quickly (< 1 second) and hence needs to be regenerated frequently.[77] When the process was first introduced in the 1940s amorphous catalysts were used, however, the introduction of a zeolite Y catalyst in the 1960s increased the octane content of the gasoline produced because of the ability of the zeolite to selectively produce molecules less prone to further cracking and condensation. Since then ZSM-5 (MFI) additives and other engineering innovations have further improved the octane yield and the quality of gasoline produced from FCC.[77,79]

Whilst FCC produces gasoline from HGO fractions, HDC produces middle distillates, for example diesel and kerosene by a hydrogen addition process. The reactions take place at high temperatures and hydrogen pressures, and as in FCC, zeolite Y plays a crucial role in catalysing the process. However, in HDC the zeolite works alongside amorphous silica, or a mixture of amorphous oxides, these catalysts are bi-functional, and contain both acidic cracking and hydrogenation functions. [77,79]

The aim of C_{4-6} alkane hydro-isomerization is to transform the light naphtha fraction of petroleum crude oil to increase the octane rating. Mordenite (MOR) is the typically

zeolite catalyst for this reaction, however catalysts based on zeolite omega (MAZ) have been demonstrated to have superior catalytic abilities to mordenite, although they are not generally used in scaled-up industrial processes.[77,79]

1.2.5.1.2 Methane upgrading

Following their successful use as catalysts in petroleum refining, zeolites were later incorporated into atypical petrochemical processes, and in the 1980s large-pore zeolite ZSM-5 (MFI) was at the crux of the first major synfuel development since the Fischer-Tropsch process, Mobil's methanol-to-hydrocarbon (MTH) process; a lucrative method for the conversion of coal to high-octane gasoline.[80–82]

At a time of dwindling traditional fuel sources, and increased concern for the environment, methane, which has the highest H/C ratio of all hydrocarbons and hence low CO_2 emissions on combustion, has come to be seen as a 'cleaner' alternative to coal-derived fuels until a more permanent solution to the fuel crisis is discovered. This fact, coupled with the emergence of modern fracking in the 1990s, and the 'shale oil boom', which was driven by increasing oil prices in the mid 2000s, has caused a striking increase in natural gas production over the last few decades. However, the transportation of natural gas is difficult and costly due to methane's high chemical and thermal stability, and it is estimated that 30 – 60% of methane gas reserves are not utilized for this reason. In fact, natural gas is often allowed to escape from, or deliberately flared at remote drilling sites where methane cannot be readily transported. The development of direct processes for the conversion of natural gas into more transportable, high-value products poses a potential solution to the global methane waste problem.[83–85]

One increasingly popular subsidiary of the MTH process is methanol-to-olefin (MTO) conversion. MTO, which provides a non-petroleum route to industrially important light olefins, namely ethylene and propylene, is described by the following reaction:[86]

$$\textit{Synthesis Gas} \rightarrow \textit{Methanol} \underset{+H_2O}{\overset{-H_2O}{\rightleftarrows}} \textit{DME + Methanol + Water} \xrightarrow{-H_2O} \textit{Ethylene + Propylene} \quad (1.2)$$

Unlike MTH, which proceeds over large-pore zeolite ZSM-5 (MFI), MTO is catalysed by small-pore zeolite SSZ-13, a CHA-type zeolite developed by Chevron in 1985,[87,88] and its silicoaluminophosphate counterpart SAPO-34. It is generally accepted that zeolite catalysed MTO proceeds *via* a 'hydrocarbon pool', a collection of organic

compounds, typically large olefinic or cyclic compounds formed by reactions between DME and methanol, confined within the pores of SSZ-13. Whilst the hydrocarbon pool is augmented throughout the MTO process, light olefins, ethylene and propylene are created and eliminated in a closed cycle, due to the ability of these small organic compounds to diffuse through the 8-ring pore systems of SSZ-13 and SAPO-34.[80,89] It is the small-pore architecture and moderate catalytic strength of the CHA-type zeolites that allows for the efficient conversion of MTO. Large-pore ZSM-5, has a higher catalytic strength and promotes secondary olefin reactions, for example the trimerization of propylene. Whilst suitable for MTH, where the goal is longer chain hydrocarbon production, for MTO these reactions must be supressed to suspend the process at light olefin synthesis.[90,91]

Due to the diverse nature of zeolite topology, other zeolite catalysts can be used to catalyse and facilitate a range natural gas to organic molecule conversion processes. For example, zeolite Rho has been shown to be an effective catalyst for the conversion of methanol and ammonia to dimethylamine, a small organic compound with widespread use as a chemical intermediate.[92]

In recent years, the direct conversion of methane to benzene – an industrially important chemical precursor – *via* methane dehydroaromatization has attracted a considerable amount of attention. The process of MDA involves the conversion of methane into benzene with the formation of only a single side-product, hydrogen gas ($CH_4 \rightarrow C_6H_6 + 9H_2$). At present, the most effective catalyst for this conversion is Mo/H-ZSM-5, which affords benzene selectivities of up to 80% and conversions of 10-12% at 700˚C in oxygen-free conditions.[93,94] However, the mechanism of MDA over Mo/H-ZSM-5 remains poorly understood, and although the majority of studies indicate a bi-functional mechanism, there is alternative evidence that the conversion proceeds *via* a mono-functional mechanism.[93–98] Figure 1.9 illustrates how the two mechanisms are proposed to proceed.

Despite the integral nature of the Mo carbide/ oxycarbide species to both proposed mechanisms, little is known about the exact identity of this species, or where it is located within the MFI framework. Furthermore, little is known about the nature of the active Mo species from which it originates, although it is generally accepted to originate from either $[MoO_2]^{2+}$ monomers or $[Mo_2O_5]^{2+}$ dimers.[99–103] In addition, the deactivation mechanism, which is caused by the formation of carbonaceous deposits (coking), also

remains poorly understood despite the fact this process is currently the major limitation to the commercialisation of MDA.[93,104]

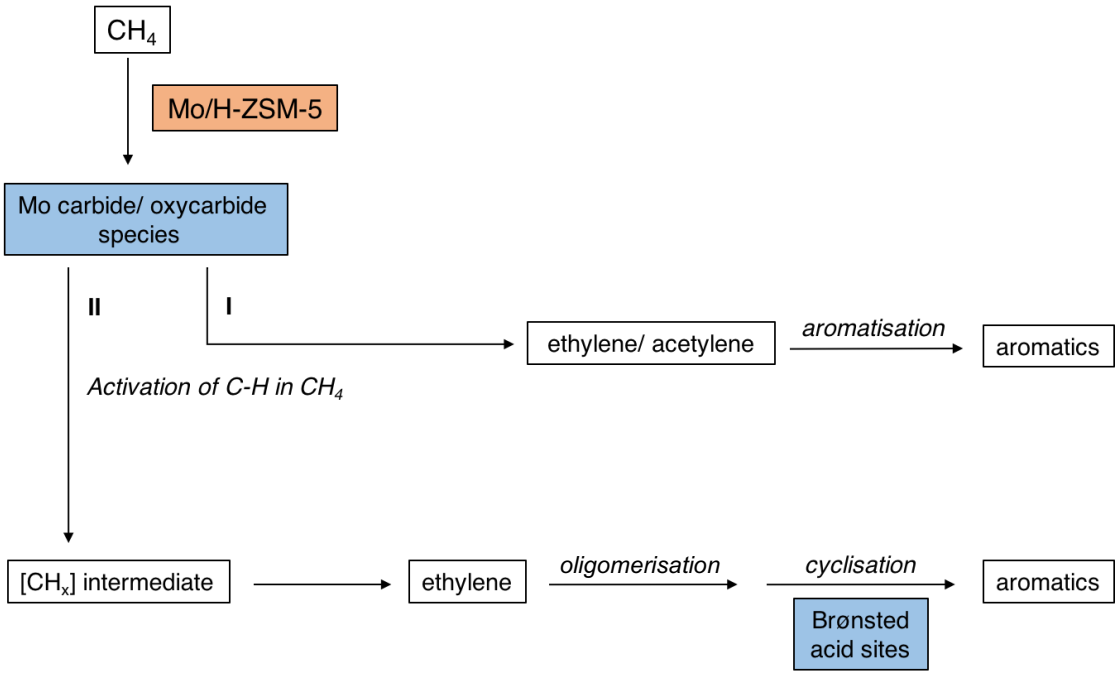

Figure 1.9 *Proposed mechanisms for the conversion of methane to benzene via MDA over Mo/H-ZSM-5.* ***I)*** *The mono-functional mechanisms where aromatization into benzene occurs exclusively over Mo carbide.* ***II)*** *The bi-functional mechanism, involving both Mo carbide or oxycarbide sites and Brønsted acid sites.*

1.2.5.1.3 Pollution control

Recently, CHA zeolite SSZ-13 has been commercialised as a diesel vehicle exhaust catalyst for the selective catalytic reduction (SCR) of nitrogen oxides (NO_x), a family of gases which have shown to be harmful to both humans and the environment, contributing to eutrophication of aquatic ecosystems, the generation of tropospheric ozone and acid rain, and linked to the onset of dementia in humans.[105–107] NO_x emissions are predominantly attributed to the highly oxidizing, or lean-burn conditions experienced in diesel-fuelled vehicle exhausts. At present, there are two leading methods for NO_x emission control, NO_x storage-reduction (NSR) and SCR.

The latter involves a metal-exchanged zeolite catalyst and an external reductant, typically NH_3 from urea, which are used in tandem to reduce NO_x under highly oxidising conditions. Initial research into zeolite catalysed SCR began in the early 1990s,

following a 1986 paper by Iwamato *et al.*, outlining the ability of Cu-ZSM-5 (MFI) to decompose NO into N_2 and O_2.[108] Although this reaction proved too slow to be used practically, it paved the way for further investigation into the use of metal-exchanged zeolite catalysts for NO_x reduction.[106,109] Due to problems with hydrothermal stability, many zeolite catalysts were found to be unsuitable for use in such high temperature conditions.[105,106,109,110] A hydrothermally robust catalyst with sufficient low temperature activity was required, and a simultaneous discovery by researchers from Johnson Matthey and BASF found the most suitable catalysts to be the copper forms of small pore CHA-type zeolite materials, SSZ-13 and SAPO-34.[111–113]

LTA-type zeolites may also be used for gas emission control. A 2010 study, by Asedegbega-Nieto *et al.,* explored the use of transition metal-exchanged zeolite A (LTA) as alternative catalysts for methane combustion.[114] Large quantities of methane are emitted into the atmosphere every day, much of which can be attributed to mine ventilation air, coke ovens, livestock management and wastewater treatment plants. Due to increasing concern for the environment, the abatement of these wasteful greenhouse gas emissions is of vital importance. A number of studies have been carried out concerning the use of catalysts to combust this methane and recover the energy generated in doing so.[114,115] Typically, the first-choice materials for such processes are supported noble metals, or transition metal oxide catalysts. Asedegbega-Nieto *et al.* demonstrated the improved catalytic activity of Fe-LTA (Si/Al = 1) for catalytic methane combustion, compared to its parent bulk oxide.[114]

The gas-capture properties of zeolite materials have also been explored for use in hydrogen energy systems, currently an intensely studied scientific area, due to the fuel crisis and previously discussed challenges concerning toxic emissions. For a long time, zeolite A and Rho, along with petrochemically popular zeolites ZSM-5 and zeolite Y were at the forefront of this research, each having proven to be effective for hydrogen separation, purification and production, along with hydrogen storage. However, due to their higher surface areas and gas storage capacities, MOF materials are now widely viewed as more efficient alternatives. [116]

1.2.5.2 Brønsted and Lewis acidity

The extensive use of zeolite catalysts in industry is attributed to the many factors. Firstly, the zeolite architecture, which allows zeolites to act as size excluding catalysts improving selectivity compared to non-porous catalytic materials. Furthermore, the synthesis materials required to generate zeolites, primarily alumina and silica sources

are not only readily available, but cheap, safe and easy to work with. Zeolites also possess good thermal stability, and are not prone to degradation at high temperatures and reasonable pressures, they are therefore suitable for scaled up industrial processes. Finally, and most importantly, zeolites possess a large number of catalytic active sites distributed throughout the aluminosilicate framework.

The nature of these active sites has been a topic of great controversy within the zeolite community, although now it is generally agreed that zeolite catalysts contain both Brønsted and Lewis acidic active sites. The presence of these sites is attributed to the negative charge engendered when tetravalent silica is substituted for trivalent alumina, which necessitates the association of positively charged cation species to maintain charge neutrality.

In nature, and during hydrothermal synthesis this cation takes the form of a monovalent alkali metal ion, typically Na^+ or K^+. As mentioned in section 1.1.4, these cations have been shown to have important roles during synthesis. However, post-synthesis, cationic species can act as Lewis acidic sites, as can extra-framework electron deficient alumina that may be present within the zeolite pores. Metal exchanged zeolite catalysts are generally thought to facilitate reactions through Lewis acidity introduced by the presence of the metal cation.

Many catalytic processes, including FCC, HDC and MTO, require Brønsted acidic catalysts. Brønsted acid sites may be generated in zeolite frameworks through post-synthesis ion exchange, where the synthesis cation is replaced with a proton. Whilst large alkali metal cations require a considerable amount of space to avoid steric clashes, and hence tend to sit within the most sizeable zeolite cavities, coordinated electrostatically to nearby framework oxygen atoms, protons are significantly smaller and may covalently bond to one of the four oxygen atoms at the vertices of the alumina tetrahedra. Therefore, for each aluminium atom present within a proton-exchanged zeolite, there are four potential Brønsted acidic active sites.

Post-synthesis zeolite cation exchange to afford protonated frameworks is a reasonable facile process. Typically, the as-synthesised, alkali metal cation-containing zeolite, for example Na-SSZ-13 (CHA) will be treated with ammonium nitrate. The sodium cations are exchanged for ammonium cations, yielding the ammonium form of the zeolite, NH_4-SSZ-13. The protonated form of the zeolite, H-SSZ-13, is attained by decomposition of the ammonium cations at temperatures exceeding 700 K.[117]

SCR of NO_x requires a copper exchanged form of SSZ-13, and transition metal exchanged zeolites are common catalysts in industry due to the highly variable oxidation states of transition metals. Further functionalization of zeolite materials with transition metal cations can be achieved *via* two main methods. Firstly, aqueous ion exchange, whereby the transition metal ion, for example Cu^{2+} is introduced to the framework in solution and exchanged for a proton yielding the Cu-exchanged zeolite. One major drawback of this method is it must be continually repeated to obtain high metal ion concentrations, furthermore, for some small-pore zeolites narrow channel apertures can impede the exchange process. The major alternative to aqueous ion exchange is solid state exchange, which proceeds in the absence of a solution, and instead a dry powder mixture of the desired transition metal, in the form of an oxide or a salt, and the zeolite in either its protonated or ammonium form is heated to high temperatures. On heating the metal diffuses through the channels of the zeolite, however can lead to partial destruction of the zeolite framework.[118,119]

1.2.6 Aluminium distribution

Both Brønsted and Lewis acidic active sites are determined by extra-framework cation location, and are therefore their positions are inherently linked to aluminium location. Hence, understanding the distribution and position of framework aluminium within zeolite structures is imperative to untangling the mechanisms by which zeolite catalyse reactions, and furthermore, to the development and design of new, more efficient catalytic materials.

Over the years a considerable amount of research has emerged concerning framework aluminium distribution in zeolites, however a straightforward conclusion is yet to be reached. Despite major advances in experimental techniques,[120] at present it is not possible to determine the absolute position of framework aluminium exactly.

Whilst X-ray absorption spectroscopic techniques (XAS), predominantly EXAFS and XANES studies, have proved to be useful tools in characterizing and monitoring the catalytic activity of some large pore zeolites, and have also been successful in determining the oxidation states of copper exchanged CHA-type zeolites,[113,121] the techniques provide limited insight to the exact locations of silicon and aluminium within the framework.[121–123] Other techniques, including solid state NMR, powder X-ray diffraction (PXRD) and powder neutron diffraction (PND), have been more successful

in addressing the problem. However, each of these methods possess limitations which may impact the reliability of any conclusions drawn from data obtained by these methods. Firstly, diffraction techniques are limited by their inability to distinguish silicon and aluminium atoms due to their comparable X-ray scattering powers, except in rare cases where there is strict ordering, such as in Goosecreekite.[124] Furthermore, in typical synthetic zeolite samples the concentration of Al is often far lower than that of Si. Solid-state NMR investigations face problems arising from the quadrupolar nature of ^{27}Al, which can cause signal broadening and peak distortions.

However, modifying the samples to include large characterisable extra-framework species allows aluminium position to be inferred indirectly, anticipating that the most proximate cation – oxygen interactions will involve those oxygen atoms bound to framework aluminium. An early example of using cations with substantial X-ray scattering power is by Calligaris and co-workers, who in 1982 attempted to reveal the positions of calcium and strontium cations present within the pores of natural chabazite using X-ray diffraction.[125] As mentioned in previous sections, the copper exchanged CHA-type zeolite Cu-SSZ-13 has many industrially important applications, and information concerning the location of the catalytically important Cu^{2+} ions is significant to further catalyst understanding and development. Fickel *et al.* reported the first detailed investigation of the identity and distribution of copper in Cu-SSZ-13 using Reitveld refinement.[126] Their work revealed that at low loadings, copper exists only as isolated Cu^{2+} and resides at the centre of the faces of the D6R, what is commonly referred to as the SII site, with a coordination number of three.[126] Further work at higher copper loadings revealed that Cu^{2+} ions are not confined to the D6R and are also present at the 8-ring windows of the large *cha* cage, SIII sites, in order to minimize unfavourable electrostatic interactions.[112,127] These findings were confirmed in a recent work by Andersen *et al.,* which demonstrated, using a combination of PXRD and the Rietveld/maximum entropy method (MEM) approach, that Cu^{2+} cations reside in both the SII and SIII sites of the CHA framework (Si/Al ratio = 15·5).[128] Figure 1.10 illustrates the known cation positions within the CHA framework. Similar strategies involving the use of large cationic species to circumvent analytical limitations have also been employed for a variety of other zeolites, for example caesium-exchanged ZSM-5,[129–131] however due to disparity between zeolite samples, no consistent conclusions have been reached. It is notable that typical cation sites observed vary between zeolite framework types, (a brief overview of typical cation positions found in some of the most common and industrially important zeolites can be found in reference 10) indicating

that Al distribution is non-random. However, whilst these approaches are capable of determining the exact location of counter cations within the framework, they can only infer that Al atoms are in close proximity to these cations, and offer no explicit information about the exact distribution of Al across the framework T-sites.

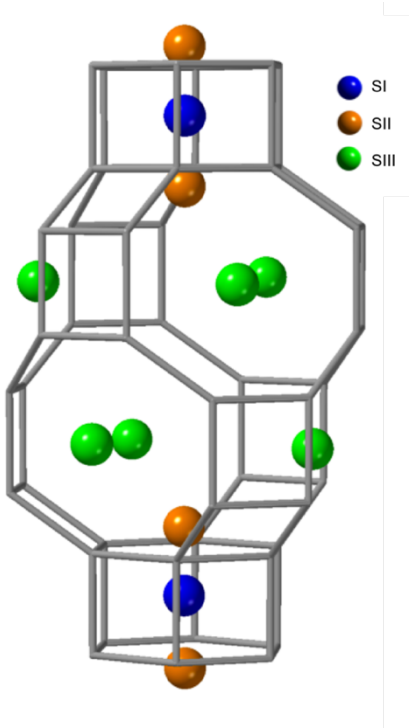

Figure 1.10 *The known cation sites present within the CHA framework; the SI site, located at the centre of the D6R; the SII site, which caps the face of the D6R; and the SIII site, located at the centre of the 8-ring windows of the cha cage.*

Direct and accurate determination of cation and aluminium distribution in protonated zeolite structures is even more problematic. Whilst there are reports of powder neutron diffraction investigations, for example that of Smith *et al.* who report the successful elucidation of acid sites in high-silica deuterated SSZ-13,[132] most researchers have turned to the wide variety of computational methods currently available,[133–138] these methods and their limitations are discussed in further detail in subsequent chapters. However, it is apparent that across all approaches there is an alarming amount of disagreement concerning aluminium's most preferential framework position in zeolites.

This is a common problem in this area of zeolite science, variations between zeolite samples, in terms of Si/Al ratio, structure, density and crystallinity can all affect the distribution of aluminium throughout the framework. In 2014 Vjunov *et al.* confirmed that even seemingly identical zeolites may have substantially different Al distributions

over T-sites.[136] Variation in the distribution of Al over T-sites is known as a short-range inhomogeneous Al distribution, whereas long-range inhomogeneous distributions refer to that on a longer length scale, for example clustering and zoning. Aluminium zoning in ZSM-5 (MFI) was first observed by von Ballmoos and Meier in 1981,[139] the pair used scanning transmission X-ray microscopy, noting Al to be invariably concentrated at the rim of the ZSM-5 crystals. Since then a range of ZSM-5 studies have arisen corroborating von Ballmoos and Meier's work.[140–144] In recent works by Perea *et al.* and Schmidt *et al.*[120,145] atom probe tomography (APT) was used to evaluate both short-range and long-range aluminium distribution. In the former work the authors found short-range Al distribution to be non-random, and on steaming – a post-synthesis dealumination technique – observed a heterogeneous long-range redistribution of Al, forming distinct Al clusters. The authors note that clustering is more pronounced in regions where molecular diffusion barriers exist, *i.e.* grain boundaries, and postulate that these alumina-rich boundaries act as "highways" for the transport of alumina to the surface of the crystal, leading to the formation of extra-framework Al.[126,127]

1.2.6.1 Löwenstein's and Dempsey's rules

A further problem in determining aluminium's location within the zeolite framework is that there are no well-developed design rules that can be used to deduce aluminium's location exactly. However, it is generally agreed that two rules conceptualised over 50 years ago remain largely adhered to for all zeolite types.

The first and most important of these rules is Löwenstein's rule,[146] which states that there is a disinclination for aluminium atoms to exist adjacent to one another, linked by a bridging oxygen atom. Hence forbidding the formation of -Al-O-Al- linkages and restricting the maximum Si/Al ratio of any zeolite to unity.[146] The rule was introduced by Walter Löwenstein in 1954, and since then there have only been a handful of reports that suggest violations of the rule are possible.[147–154]

The first of which is a 1981 report by Bursill *et al.*, who through the use solid state NMR and X-ray diffraction techniques, demonstrated that at a Si/Al ratio of unity, by virtue of its 3:1 ordering scheme Zeolite A (LTA) must contain Löwenstein 'forbidden' Al-O-Al linkages.[147] A year later Klinowski and co-workers confirmed this result for Zeolite A, noting that the same deviation away from Löwensteinian 4:0 ordering also occurs in Losod (LOS), sodalite (SOD) and cancrinite (CAN), although Al-O-Al linkages were not observed in zeolite Li-A(BW) (ABW) and eucryptite, a lithium-containing aluminosilicate

analogue of quartz.[148] A later work by the same authors used the same SS NMR approach and observed the same ordering in ultramarines, blue coloured aluminosilicate pigments with an SOD-type framework.[150] However, the original work by Bursill *et al.*[147] has since been proven to be incorrect; first denounced in print by Smith and Pluth[155] and later disproven beyond doubt by Cheetham *et al.* using a Rietveld neutron powder-profile approach.[156] Zeolite A is hence now recognised as containing strictly alternating Si and Al in accordance with Löwenstein's rule. Further examples of crystalline materials with non-Löwensteinian Al ordering exist only in non-zeolitic silicates and glasses.[151–154]

Aside from the aforementioned reports, the only other examples of non-Löwensteinian ordering in zeolite materials is in all-alumina SOD-type zeolites synthesised by non-hydrothermal approaches, for example by the use of a transition metal catalyst. Although this is only ever alluded to in the literature, the formation of -Ga-O-Ga- linkers in gallosilicate SOD has been demonstrated using a similar methodology.[153] Similar -Ga-O-Ga- linkages have also been proposed to exist in hydrothermally synthesised gallosilicates. A 2009 paper by Shin *et al.* suggested that, based on extensive X-ray and electron diffraction data, the structure of potassium gallosilicate PST-1 (NAT) must contain non-Löwensteinian ordered gallium atoms, although further investigation using ^{17}O SS MAS NMR was required to confirm this finding.[149]

The wealth of literature in favour of Löwenstein's rule,[13,157–162] compared to the little evidence that it may be violated,[147–154] has caused the rule of "aluminium avoidance" to become a fundamental law of zeolite science and hence, the possibility of non-Löwensteinian ordered zeolites are often dismissed. This is true of most theoretical studies where the omission of non-Löwensteinian frameworks is considered a simple way to reduce unnecessary computational expense by decreasing the number of potential configurations.[128,133,159,163,164] However, it is also common practice in experimental work, where employing Löwenstein's rule can assist in understanding results, this was the case in a 1996 ^{29}Si SS MAS NMR study by Akporiaye *et al.*, where possible combinations of two and three aluminium atoms in the six-ring units of CHA were limited to next nearest neighbour (NNN), or next-next nearest neighbour (NNNN) combinations, in accordance with Löwenstein's rule.[159]

A second commonly cited rule is Dempsey's rule.[165] Developed in the late 1960s by Dempsey *et al.*, Dempsey's rule states that on the basis of electrostatics, negatively charge alumina ions are inclined to position themselves as far from one another as

possible within the zeolite framework.[165,166] In general, Dempsey's rule is less highly regarded than Löwenstein's rule, and whilst true of some frameworks it has been shown to be violated in a number of different zeolites both experimentally and theoretically.[162,164,167]

1.3 Aim of study

Aluminium is the essential element that introduces charge, and hence catalytically active sites, to the aluminosilicate zeolite framework and it is well understood that both the concentration of Al and its distribution throughout the framework directly influence the stability and catalytic functionality of a zeolite material. At present, it is impossible to accurately predict the location of aluminium within a given zeolite framework, moreover, it is also impossible to precisely control the distribution of Al throughout a zeolite during synthesis. The aim of this study is to determine the most thermodynamically stable distributions of Al throughout a variety of industrially important zeolites at a range of Si/Al ratios. In this work, computational methods are used to investigate:

- Aluminium's preferred framework location in a range of zeolite frameworks
- Löwenstein's and Dempsey's rules
- The surface segregation of aluminium within zeolites
- The influence both the organic template and charge-compensating cations on aluminium distribution
- The effect of Si/Al distribution on the identity of the catalytically active species during MDA over Mo/H-ZSM-5

The motivation for this thesis is to increase the fundamental understanding of Al distribution in zeolites and thus impact subsequent research towards the controlled design and synthesis of new industrially important zeolite catalysts with improved lifetimes and activities.

1.4 References

1. Gottardi, G. & Galli, E., *Natural Zeolites*, (Springer-Verlag, 1985).
2. de St Claire Deville, H. *Compt. Rend. Se´ances Acad. Sci.* **54,** (1862).
3. Baerlocher, C., McCusker, L., Olson, D.H. *Atlas of Zeolite Framework Types* (2007).
4. International Zeolite Association. *Structure Commission of the International Zeolite Association* (2016). Available at: http://www.iza-structure.org/IZA-SC_FTC.htm.
5. Cronstedt, A.F. *Akad. Handl. Stock.* (1756).
6. Kallo, D. & Sherry, H. *Occurrence, properties and utilization of natural zeolites* (Akademiai Kiado Budapest, 1988).
7. Flanagan, D.M. *U.S. Geological Survey 2015 Minerals Yearbook* (2016).
8. Flanigen, E.M. Zeolites and Molecular Sieves an Historical Perspective in *Studies in Surface Science and Catalysis* **137,** 11–35 (Elsevier, 2001).
9. Payra, P. & Dutta, P.K. Zeolites: A Primer in *Handbook of Zeolite Science and Technology* (eds. Auerbach, S.M., Carrado, K.A. & Dutta, P.K.) **35,** 1–19 (CRC Press, 2003).
10. Broach, R.W. Zeolite Types and Structures in *Zeolites in Industrial Separation and Catalysis* (Wiley- VCH Verlang GmbH &Co. KGaA, 2010).
11. Barrer, R.M. & White, E.A.D. *J. Chem. Soc.* 1267 (1951).
12. Thompson, R. W. Nucleation, growth and seeding in zeolite synthesis in *Verified Syntheses of Zeolitic Materials* 13–15 (2009).
13. Yang, C.-S., Mora-Fonz, J.M., Catlow, C.R.A. *J. Phys. Chem. C* **115,** 24102–24114 (2011).
14. Schaack, B.B. PhD thesis: The Solid State Formation of Zeolitic Materials Studied by Mass Spectrometry (Ruhr Universität Bochum, 2009).
15. IZA. *IZA Commission on Natural Zeolites: Chabazite* Available at: http://www.iza-online.org/natural/Datasheets/Chabazite/chabazite.htm.
16. Meier, W.M. *Z. Krist.* **115,** 439–450 (1961).
17. IZA. *IZA Commission on Natural Zeolites: Mordenite* Available at: http://www.iza-online.org/natural/Datasheets/Mordenite/Mordenite.html.
18. Martens, J. & Jacobs, P. Synthesis of High-Silica Aluminosilicate Zeolites in *Studies in Surface Science and Catalysis* (Elsevier, 1987).
19. van Koningsveld, H. *IZA: Schemes for Building Zeolite Framework Models* Available at: http://www.izastructure.org/databases/ModelBuilding/Introduction.pdf.

20. Smith, R. L., Svelle, S., Fuglerud, T., Arstad, B., Lind, A., Chavan, S., Attfield, M.P., Akporiaye, D.E., Anderson, M.W. *Chem. Mater.* **27,** 4205–4215 (2015).
21. Smith, R.L., Svelle, S., del Campo, P., Terje Fuglerud, Arstad, B., Lind, A., Chavan, S., Attfield, M.P., Akporiaye, D.E., Anderson, M.W. *Appl. Catal. A* **505,** 1–7 (2015).
22. Jacobs, P.A., Flanigen, E. M., Jansen, J.C., van Bekkum, H. (Elsevier, 2001).
23. Baur, W.H. & Fischer, R.X. MFI in *Zeolite-Type Crystal Structures and their Chemistry. Framework Type Codes LTA to RHO 1–31* (Springer Berlin Heidelberg 2006).
24. Cundy, C.S. & Cox, P.A. *Microporous Mesoporous Mater.* **82**, 1–78 (2005).
25. Wright, P.A. *Microporous Framework Solids* (The Royal Society of Chemistry, 2008).
26. Mullin, J.W. *Crystallisation* (Butterworth Heinemann, 2001).
27. Cubillas, P. & Anderson, M.W. *Synthesis Mechanism: Crystal Growth and Nucleationin Zeolites and Catalysis* (Wiley-VCH Verlag GmbH & Co. KGaA, 2010).
28. Knight, C.T.G., Kinrade, S.D., Kirschock, C.E.A., Ravishankar, Raman, Verspeurt, F. Grobet, P.J., Jacobs, P.A., Martens, J.A. *Journal of Physical Chemistry B* **106**, 3329–3334 (2002).
29. Kirschhock, C. E. A., Ravishankar, R., Verspeurt, F., Grobet, P.J., Jacobs, P.A., Martens, J.A. *J. Phys. Chem. B* **103**, 4965–4971 (1999).
30. Mora-Fonz, M.J., Catlow, C.R.A., Lewis, D.W. *Angew. Chemie - Int. Ed.* **44**, 3082–3086 (2005).
31. Weitkamp, J. *Solid State Ionics* **131**, 175–188 (2000).
32. Barrer, R.M. *J. Chem. Soc.* 127–132 (1948).
33. Cundy, C.S.& Cox, P. A. *Chem. Rev.* **103**, 663–701 (2003).
34. Barrer, R.M., Hinds, L., White, E.A. *J. Chem. Soc.* 1466–1475 (1953).
35. Singh, R. & Dutta, P.K. MFI: A Case Study of Zeolite Synthesis in *Handbook of Zeolite Science and Technology* (eds. Auerbach, S. M., Carrado, K. A. & Dutta, P. K.) 21–64 (CRC Press, 2003).
36. Corma, A. & Davis, M.E. *ChemPhysChem* **5**, 304–313 (2004).
37. van Santen, R.A., Ooms, G., Ouden, den, C.J.J., van Beest, B.W.H., Post, M.F.M. Computational studies of zeolite framework stability in *Zeolite Synthesis* in *ACS Symposium Series*, **389**, 617–633 (1989)
38. Navrotsky, A., Petrovic, I., Hu, Y., Chen, C.-Y., Davis, M.E. *Microporous*

Mater. **4**, 95–98 (1995).

39. Pope, C. G. *Microporous Mesoporous Mater.* **21**, 333–336 (1998).
40. Tosheva, L. & Valtchev, V.P. *Chemistry of Materials* **17**, 2494–2513 (2005).
41. Wakihara, T. & Okubo, T. *Chem. Lett.* **34**, 276–281 (2005).
42. Catlow, R., Coombes, D.S., Slater, B., Lewis, D.W., Carlos, J., Pereira, G. Modeling Nucleation and Growth in Zeolites in *Handbook of Zeolite Science and Technology* (eds. Auerbach, S. M., Carrado, K. A. & Dutta, P. K.) (2003).
43. Yang, C.-S., Mora-Fonz, J.M., Catlow, C.R.A. *J. Phys. Chem. C* **117**, 24796–24803 (2013).
44. Klamt, A. & Schüürmann, G. *J. Chem. Soc., Perkin Trans. 2*, **0**, 799–805 (1993).
45. Lupulescu, A. I. & Rimer, J.D. *Science* **16** 16729-732 (2014)
46. Kumar, M., Choudhary, M. K., Rimer, J. D. *Nat. Commun.* **9**, 1–9 (2018).
47. Grand, J., Awala, H. & Mintova, S. *CrystEngComm* **18**, 650–664 (2016).
48. Slater, B., Ohsuna, T., Liu, Z., Terasaki, O. *Faraday Discussions* **136** 125-141 (2007).
49. de Moor, P.-P.E.A., Beelen, T.P.M, Komanschek, B., Beck, L.W., Wagner, P., Davis, M.E., van Santen, R.A. *Chem. Eur. J.* **5**, 2083–2088 (1999).
50. Lewis, D.W., Willock, D.J., Catlow, C.R.A., Thomas, J.M., Hutchings, G. J. *Nature* **382**, 604–606 (1996).
51. Lewis, D.W., Freeman, C.M., Catlow, C.R.A. *J. Phys. Chem.* **99**, 11194–11202 (1995).
52. Barrer, R.M. & Denny, P.J. *J. Chem. Soc.* **0**, 971–982 (1961).
53. Kubota, Y., Helmkamp, M. M., Zones, S.I., Davis, M. E. *Microporous Mater.* **6**, 213–229 (1996).
54. Lewis, D.W., Catlow, C.R.A.,Thomas, J.M. *Chem. Mater.* **8**, 1112– 1118 (1996).
55. Lewis, D.W. Template-Host Interaction and Template Design in *Computer Modelling of Microporous Materials* (ed. C.R.A. Catlow, Berend Smit, R. A. van S.) 298 (Elsevier, 2004).
56. Lewis, D.W., Sankar, G., Wyles, J.K., Thomas, J.M., Catlow, C.R.A., Willock, D.J. *Angew. Chemie Int. Ed. English* **36**, 2675–2677 (1997).
57. Lok, B.M., Cannan, T.R. & Messina, C.A. *Zeolites* **3**, 282–291 (1983).
58. Flanigen, E.M., Khatami, H., Szymanski, H.A. in *Molecular Sieve Zeolites-I* (eds. Flanigen, E. M. & Sand, L. B.) 201–229 (1973).
59. Meise, W. & Schowochow, F.E. *Adv. Chem. Mol. Seives* **121**, 169–178 (1973).

60. Burkett, S.L. & Davis, M.E. *Microporous Mater.* **1**, 265–282 (1993).
61. International Zeolite Association. *Zeolite Synthesis Directory* (2001).
62. Fletcher, R.E., Wells, S.A., Leung, K.M., Edwards, P.P., Sartbaeva, A. *Acta Cryst. B.* **71**, 641–7 (2015).
63. Nearchou, A. & Sartbaeva, A. *CrystEngComm* **17**, 2496–2503 (2015).
64. Song, J., Dai, L., Ji, Y., Xiao, F.S. *Chemistry of Materials* **18** 2775-2777 (2006)
65. Goel, S., Zones, S.I., Iglesia, E. *Chem. Mater.* **27**, 2056–2066 (2015).
66. Wang, Y., Wu, Q., Meng, X., Xiao, F.-S. *Engineering* **3**, 567–574 (2017).
67. Wang, H., Holmberg, B.A., Yan, Y. *J. Am. Chem. Soc.*, **125** 9928–9929 (2003).
68. Leonard, R.S. *US 4066394 A: Reusable zeolite water softener for clothes washing* (1974).
69. Rieck, H.-P. *US 4664839 A: Use of crystalline layered sodium silicates for softening water and a process for softening water* (1985).
70. Chollet, J.-F., Joly, G., Magnoux, P. *US 20130327103: Use of zeolites in supplying micronutrients* (2013).
71. Chojnacki, A., Chojnacka, K., Hoffmann, J., Górecki, H. *Miner. Eng.* **17**, 933–937 (2004).
72. Blackbourne, L.H., Baer, D.G., Eastridge, B.J., Kheirabadi, B., Kragh, J.F., Cap, A.P., Dubick, M.A., Morrison, J.J., Midwinter, M.J., Butler, F.K., Kotwal, R.S., Holcomb, J.B. *J. Trauma Acute Care Surg.* **73**, S372–S377 (2012).
73. Weller, R. B. *Journal of Investigative Dermatology* **129**, 2335–2337 (2009).
74. Neidrauer, M., Ercan, U.K., Bhattacharyya, A., Samuels, J., Sedlak, J., Trikha, R., Barbee, K.A., Weingarten, M.S., Joshi, S.G. *J. Med. Microbiol.* **63**, 203–209 (2014).
75. Fox, S. Wilkinson, T.S., Wheatley, P.S., Xiao, B., Morris, R.E., Sutherland, A., Simpson, A.J., Barlow, P.G., Butler, A.R., Megson, I.L., Rossi, A.G. *Acta Biomater.* **6**, 1515–1521 (2010).
76. Csicsery, S.M. *Zeolites* **4**, 202–213 (1984).
77. Vermeiren, W. & Gilson, J.P. *Top. Catal.* **52**, 1131–1161 (2009).
78. Marcilly, C. *Acido-basic catalysis: application to refining and petrochemistry* (Editions Technip, 2006).
79. Guisnet, M. & Gilson, J.-P. *Zeolites for cleaner technologies in Catalytic Science Series 3*, (Imperial College Press, London, 2002).
80. Stöcker, M. *Microporous Mesoporous Mater.* **29**, 3–48 (1999).
81. Keil, F.J. *Microporous Mesoporous Mater.* **29**, 49–66 (1999).

82. Chang, C.D. *Catal. Rev.* **25**, 1–118 (1983).
83. International Energy Agency. *World Energy Outlook Special Report on Unconventional Gas* (2012).
84. McFarland, E. *Science* **338**, 340–342 (2012).
85. Lunsford, J.H. *Catal. Today* **63**, 165–174 (2000).
86. Deimund, M.A., Harrison, L., Lunn, J.D., Liu, Y., Malek, A., Shayib, R., Davis, M.E. *ACS Catal.* **6**, 542–550 (2016).
87. Zones, S.I. *US 4544538: Zeolite SSZ-13 and its method of preparation* (1985).
88. Zones, S.I. & Van Nordstrand, R. A. *Zeolites* **8**, 166–174 (1988).
89. Dai, W., Wang, X., Wu, G., Guan, N., Hunger, M., Li, L. *ACS Catal.* **1**, 292–299 (2011).
90. Haw, J.F. & Marcus, D. M. *Top. Catal.* **34**, 41–48 (2005).
91. Dusselier, M., Deimund, M.A., Schmidt, J.E., Davis, M.E. *ACS Catal.* **5**, 6078–6085 (2015).
92. Abrams, L, Corbin, D.R., Shannon, *R.D. US 4814503: Zeolite rho and ZK-5 catalysts for conversion of methanol and ammonia to dimethylamine* (1985).
93. Ismagilov, Z.R., Matus, E.V., Tsikoza, L.T. *Energy Environ. Sci.* **1**, 526–541 (2008).
94. Kosinov, N., Coumans, F.J.A.G., Uslamin, E.A., Wijpkema, A.S.G., Mezari, B., Hensen, E.J.M. *ACS Catal.* **7**, 520–529 (2017).
95. Weckhuysen, B. M., Wang, D., Rosynek, M. P. & Lunsford, J. H. *Angew. Chemie Int. Ed. English* **36**, 2374–2376 (1997).
96. Shu, J., Adnot, A., Grandjean, B. P. A. *Indust. Eng. Chem.Research* **38**, 3860-3867 (1999).
97. Mériaudeau, P., Tiep, L.V., Ha, V.T.T., Naccache, C. & Szabo, G. *J. Mol. Catal. A Chem.* **144**, 469–471 (1999).
98. Mériaudeau, P., Ha, V.T.T., Van Tiep, L. *Catal. Letters* **64**, 49–51 (2000).
99. Li, W., Meitzner, G.D., Borry, R.W. & Iglesia, E. *J. Catal.* **191**, 373–383 (2000).
100. Kim, Y.-H., Borry, R.W., Iglesia, E. *Microporous Mesoporous Mater.* **35**, 495–509 (2000).
101. Zhou, D., Ma, D., Liu, X., Bao, X. *J. Chem. Phys.* **114**, 9125–9129 (2001).
102. Xing, S., Zhou, D., Cao, L., Li, X. *Chinese J. Catal.* **31**, 415–422 (2010).
103. Lezcano-Gonzalez, I., Oord, R., Rovezzi, M., Glatzel, P., Botchway, S.W., Weckhuysen, B.M., Beale, A.M. *Angew. Chemie - Int. Ed.* **55**, 5215–5219 (2016).
104. Spivey, J.J. & Hutchings, G. *Chem. Soc. Rev.* **43**, 792–803 (2014).

105. Gao, F., Kwak, J.H., Szanyi, J., Peden, C.H.F. *Top. Catal.* **56**, 1441–1459 (2013).

106. Beale, A.M., Gao, F., Lezcano-Gonzalez, I., Peden, C.H.F. & Szanyi, J. *Chem. Soc. Rev.* **44**, 7371–7405 (2015).

107. Calderón-Garcidueñas, L. & Villarreal-Ríos, R. *Lancet* 675-677 (2017).

108. Iwamoto, M., Furukawa, H., Mine, Y., Uemura, F., Mikuriya, S.-I., Kagawa, S. *J. Chem. Soc. Chem. Commun.* 1272 (1986).

109. Iwamoto, M. & Hamada, H. *Catal. Today* **10**, 57–71 (1991).

110. Chen, H.-Y. & Sachtler, W.M. . *Catal. Today* **42**, 73–83 (1998).

111. Boorse, S. & Dettling, *US 7998423: SCR on low thermal mass filter substrates J. C.* (2011).

112. Hun Kwak, J., Zhu, H., Lee, J.H., Peden, C.H.F., Szanyi, J. *Chem. Commun.* **48**, 4758–60 (2012).

113. Borfecchia, E. Lomachenko, K.A., Giordanino, F., Falsig, H., Beato, P., Soldatov, A.V., Bordiga, S., Lamberti, C. *Chem. Sci.* **6**, 548–563 (2015).

114. Asedegbega-Nieto, E., Díaz, E., Vega, A., Ordóñez, S. *Catal. Today* **157**, 425–431 (2010).

115. Gosiewski, K., Matros, Y.S., Warmuzinski, K., Jaschik, M. & Tanczyk, M. *Chem. Eng. Sci.* **63**, 5010–5019 (2008).

116. Walker, G. *Solid-State Hydrogen Storage: Materials and Chemistry* (Elsevier, 2008).

117. Hattori, H. & Ono, Y. *Solid acid catalysis: from fundamentals to applications* (CRC Press, 2015).

118. Vennestrøm, P.N.R. Katerinopoulou, A., Tiruvalam, R.R., Kustov, A., Moses, P.G., Concepcion, P., Corma, A. *ACS Catal.* **3,** 2158–2161 (2013).

119. Kucherov, A. V. & Slinkin, A. A. *Zeolites* **6**, 175–180 (1986).

120. Perea, D.E. Arslan, I., Liu, J., Ristanović, Z., Kovarik, L., Arey, B.W., Lercher, J.A., Bare, S.R., Weckhuysen, B.M. *Nat. Commun.* **6**, 7589 (2015).

121. McEwen, J.-S. Anggara, T., Schneider, W.F., Kispersky, V.F., Miller, J.T., Delgass, W.N., Ribeiro, F.H. *Catal. Today* **184**, 129–144 (2012).

122. Zhang, Y., Drake, I.J., Bell, A.T. *Chem. Mater.* **18**, 2347–2356 (2006).

123. Liu, D.-J. & Robota, H. J. *J. Phys. Chem. B* **103**, 2755–2765 (1999).

124. Rouse, R. C. & Peacor, D. R. *Am. Mineral.* **71**, 1494–1501 (1986).

125. Calligaris, M., Nardin, G., Randaccio, L., Chiaramonti, P. C. *Acta Cryst. B* **38**, 602–605 (1982).

126. Fickel, D.W. & Lobo, R.F. *J. Phys. Chem. C* **114**, 1633–1640 (2010).

127. Deka, U.J.A., Eilertsen, E.A., Emerich, H., Green, M.A., Korhonen, S.T., Weckhuysen, B.M., Beale, A. M. *J. Phys. Chem. C* **116**, 4809–4818 (2012).
128. Andersen, C.W. Bremholm, M., Vennestrøm, P.N.R., Blichfeld, A.B., Lundegaard, L.F., Iversen, B.B. *IUCrJ* **1**, 382–6 (2014).
129. Lin, J.C., Chao, K.J., Wang, Y. *Zeolites* **11**, 376–379 (1991).
130. Olson, D.H., Khosrovani, N., Peters, A. W. & Toby, B.H. *J. Phys. Chem. B* **104**, 4844–4848 (2000).
131. Mentzen, B.F. & Bergeret, G. *J. Phys. Chem. C* **111**, 12512–12516 (2007).
132. Smith, L.J., Davidson, A., Cheetham, A. K. *Catal. Letters* **49**, 143–146 (1997).
133. Lo, C. & Trout, B. *J. Catal.* **227**, 77–89 (2004).
134. Ghorbanpour, A., Rimer, J.D., Grabow, L.C. *Catal. Commun.* **52**, 98–102 (2014).
135. Liu, R., Zhang, J., Sun, X., Huang, C., Chen, B. *J. Theor. Comput. Chem.* **13**, 1450019 (2014).
136. Vjunov, A. Fulton, J.L., Huthwelker, T., Pin, S., Mei, D., Schenter, G.K., Govind, N., Camaioni, D.M., Hu, J.Z., Lercher, J.A. *J. Am. Chem. Soc.* **136**, 8296–306 (2014).
137. Grajciar, L., Areán, C.O., Pulido, A., Nachtigall, P. *Phys. Chem. Chem. Phys.* **12**, 1497–506 (2010).
138. Fujita, H., Kanougi, T., Atoguchi, T. *Appl. Catal. A Gen.* **313**, 160–166 (2006).
139. von Ballmoos, R. & Meier, W. M. *Nature* **289**, 782–783 (1981).
140. Chao, K. & Chern, J. *Zeolites* **8**, 82–85 (1988).
141. Althoff, R., Schulz-Dobrick, B., Schüth, F., Unger, K. *Microporous Mater.* **1**, 207–218 (1993).
142. Karwacki, L., Kox, M.H.F., de Winter, M., Drury, M.R., Meeldijk, J.D., Stavitski, E., Schmidt, W., Mertens, M., Cubillas, P. Neena, J.m Chan, A., Kahn, N. Bare, S.R., Anderson, M.W., Kornatowski, J. Weckhuysen, B.M. *Nat. Mater.* **8**, 959–965 (2009).
143. Danilina, N., Krumeich, F., Castelanelli, S.A., van Bokhoven, J. A. *J. Phys. Chem. C* **114**, 6640–6645 (2010).
144. Ristanović, Z., Hofmann, J.P., Deka, U., Schülli, T.U., Rohnke, M., Beale, A.M., Weckhuysen, B.M. *Angew. Chemie Int. Ed.* **52**, 13382–13386 (2013).
145. Schmidt, J. E. Poplawsky, J.D., Mazumder, B., Attila, Ö., Fu, D., DeWinter, D.A.M., Meirer, F., Bare, S.R., Weckhuysen, B.M. *Angew. Chemie Int. Ed.* **55**,11173–11177 (2016).
146. Loewenstein, W. *Am. Mineral.* **39**, 92–96 (1954).

147. Bursill, L.A., Lodge, E.A., Thomas, J.M., Cheetham, A.K. *J. Phys. Chem.* **85**, 2409–2421 (1981).

148. Klinowski, J., Thomas, J.M., Fyfe, C. A., Hartman, J.S. *J. Phys. Chem* **85**, 2590–2594 (1981).

149. Shin, J., Kim, S.H., Camblor, M.A., Waarender, S.J., Miller, S.R., Zhou, W., Wright, P.A., Hong, S.B. *Dalt. Trans.* **39**, 2246–2253 (2010).

150. Tarling, S.E., Barnes, P. & Klinowski, J. *Acta Cryst. B* **44**, 128–135 (1988).

151. Putnis, A., Fyfe, C. A., Gobbi, G. C. *Phys. Chem. Miner.* **12**, 211–216 (1985).

152. Fyfe, C.A., Gobbi, G.C., Putnis, A. *J. Am. Chem. Soc*. **108**, 3218–3223 (1986).

153. Dann, S.E., Mead, P.J., Weller, M.T. *Angew. Chemie Int. Ed. English* **34**, 2414–2416 (1995).

154. Florian, P., Veron, E., Green, T.F.G., Yates, J. R. & Massiot, D. *Chem. Mater.* **24**, 4068–4079 (2012).

155. Smith, J.V., Pluth, J.J. *Nature* **291**, 265–266 (1981).

156. Cheetham, A.K., Eddy, M.M., Jefferson, D.A. & Thomas, J.M. *Nature* **299,** 24–26 (1982).

157. Bell, R.G., Jackson, R. A., Catlow, C.R.A. *Zeolites* **70**, 870–871 (1992).

158. Catlow, C.R.A., George, A.R., Freeman, C.M. *Chem. Commun.* 1311–1312 (1996).

159. Akporiaye, D.E., Dahl, I.M., Mostad, H.B. & Wendelbo, R. *J. Phys. Chem.* **100**, 4148–4153 (1996).

160. Melchior, M., Vaughan, D., Jacobson, A. *J. Am. Chem. Soc.* **104**, 4859–4864 (1982).

161. Soukoulist, C.M. *J. Phys. Chem*. **88,** 4898–4901 (1984).

162. Schroeder, K.P. & Sauer, J. *J. Phys. Chem.* **97**, 6579–6581 (1993).

163. Muraoka, K., Chaikittisilp, W., Okubo, T. *J. Am. Chem. Soc*. **138**, 6184–6193 (2016).

164. Zokaie, M., Olsbye, U., Lillerud, K.P., Swang, O. *Microporous Mesoporous Mater.* **158**, 175–179 (2012).

165. Dempsey, E., Kuehl, G.H., Olson, D.H. *J. Phys. Chem.* **73**, 387–390 (1969).

166. Dempsey, E. *J. Catal.* 115–119 (1977).

167. Ruiz-Salvador, A.R., Grau-Crespo, R., Gray, A.E., Lewis, D.W. J. *Solid State Chem.* **198**, 330–336 (2013).

Chapter 2: Theory and Methodology

2.1 Overview

This chapter outlines the underlying theory and functionality of the simulation techniques that were used throughout this study. Density Functional Theory is discussed in detail as it is used most routinely. Hartree Fock, *ab initio* molecular dynamics and inter-atomic potential approaches are also included for completeness.

2.2 Electronic structure methods

2.2.1 *Ab initio* fundamentals and Hartree Fock

Ab initio is a Latin term meaning "from the beginning", and refers to approaches which describe chemical systems from theoretical principles, rather than from experimental observations. The term applies to many quantum theories for the treatment of molecular systems, the most common quantum approaches are Hartree Fock (HF) and Density Functional Theory (DFT). Although DFT is not considered to be entirely *ab initio*, the *ab initio* fundamentals provide a basis to understanding this computational approach.

The starting point for any explanation of quantum mechanics is the Schrödinger equation, $H\psi = E\psi$, where H is the Hamiltonian operator and ψ is a set of solutions, or eigenstates, to the Hamiltonian. Each eigenstate, ψ_n has an associated eigenvalue, E_n.[1–4]

The full time independent, nonrelativistic form of the Schrödinger equation for molecular systems is

$$\left[-\frac{\hbar}{2m}\sum_{i=1}^{N}\nabla_i^2 + \sum_{i=1}^{N}\mathrm{V}(r_i) + \sum_{i=1}^{N}\sum_{j<i}U(r_i, r_j)\right]\psi = E\psi \qquad (2.1)$$

Here, the three bracketed terms represent the kinetic energy of each electron, the nucleus-electron interaction energy, and the electron-electron interaction energy, respectively. Collectively these terms make up the Hamiltonian, which contains the kinetic and potential energy contributions of a system. Here ψ is the many-electron wavefunction, a function of each of the spatial coordinates of each of the N electrons, and E is the ground state energy of the electrons in the system.[1–4]

Two immediate approximations are widely employed to the Schrödinger equation. The first is the Born-Oppenheimer approximation which states that since the resting mass

of a proton is 1836 times greater than the resting mass of an electron, the nuclei can be regarded as static relative to the movement of the electrons. Hence, the nuclei and electrons can be considered separately. The second assumption is that gravity, strong and weak forces are neglected from calculations and only electronic forces and kinetic energy, those forces most prominent in chemical processes, are of interest.

Although chemistry is generally concerned with polyelectronic systems of atoms and molecules, the Schrödinger equation cannot be solved for systems with more than one electron. This is due to the complexity of the many-electron wave-function, ψ. In principle, understanding the electronic forces on an electron is simple, as the fundamental interactions are well-defined. However, introducing additional electrons to the system becomes a problem, as electronic behaviours are inherently coupled due to coulombic interactions, the solutions to each of the wave-functions must be solved simultaneously. The non-linear scaling of this problem means that solving each of these equations quickly becomes intractable. This is known as the 'many-body problem'.

The many-body problem can be avoided by employing the 'Hartree approximation',[5] which states that the many-electron wave function can be approximated to by a set of single-electron wave functions. This is the first of two fundamental assumptions associated with the Hartree Fock approach, the first practical method for calculating the ground-state energy of an assembly of atoms with fixed nuclei. The second assumption is the 'mean field approximation', which assumes that in a wave function of N electrons, each of the electrons have no effect on one another and instead are assumed to be interacting with an external field, hence reducing the many-body problem to a one-body problem.

Therefore, the Hamiltonian for the electrons may be written as

$$H = \sum_{i=1}^{N} h_i \qquad (2.2)$$

where h describes the kinetic and potential energy of electron i. Based on this Hamiltonian, the Schrödinger equation for a single electron is

$$h\chi = E\chi \qquad (2.3)$$

The one electron wave functions defined by this equation are spin orbitals, and are equivalent to a single-electron atomic orbital.

For each single-electron equation there are multiple one-electron wave functions, which define a set of spin orbitals $\chi_j(\mathbf{x}_i)(j = 1, 2, \dots)$ where $\mathbf{x}_i$ is a vector of coordinates that defines the position of an electron, i and its respective spin state, either up or down. We can describe the total Hamiltonian H as a sum of one-electron Hamiltonian operators h_i, and therefore the wave function of H can be described as the product of the one-electron spin orbitals;

$$\psi(\mathbf{x}_1, \dots, \mathbf{x}_\mathrm{N}) = \chi_{J_1}(\mathbf{x}_1)\chi_{J_2}(\mathbf{x}_2) \dots \chi_{J_N}(\mathbf{x}_\mathrm{N}) \qquad (2.4)$$

The energy of this wave function is the sum of the spin orbital energies, this is the Hartree product.[1,2]

However, the Hartree product does not satisfy the antisymmetry principle, which requires the wave functions to change sign when two electrons exchange places. A solution to this problem was first proposed by John Slater in 1929, who showed that expressing the overall wave function as the determinant of a matrix of one-electron wave functions provides an inherent physical description of electron exchange. Hence the multi-electron wave function satisfies both the antisymmetry principle and the condition of orthonormality, which implements the Pauli exclusion principle.

Single-electron wave functions, can be treated as atomic orbitals for a hydrogenic atom and are sometimes referred to as basis functions. Chemistry requires the use of molecular orbitals to describe bonding. Molecular orbitals can be constructed through an approximate linear combination of these orbitals (LCAO).

In computational chemistry, we describe these molecular orbitals through linear combinations of a limited set of mathematical functions, known as the basis set. We assume that the chosen basis set allows for the construction of adequate functions, with respect to the exact solution. Increasing the size of the basis set increases the accuracy of a given calculation, however it also increases the complexity, and hence the computational cost, of the calculation.

In a Hartree-Fock (HF) calculation the Schrödinger equation for each electron can be written as

$$\left[-\frac{h^2}{2m}\nabla^2 + V(\mathbf{r}) + V_H(\mathbf{r})\right]\chi_j(\mathbf{x}) = E_j\chi_j(\mathbf{x}) \qquad (2.5)$$

where the bracketed term includes the kinetic energy, the interaction between the nuclei and the electrons and the Hartree potential, respectively. The Hartree potential is the electronic interaction energy expressed as an average.[1,2]

2.2.2 Density functional theory

2.2.2.1 Principles

In recent years, DFT has become the primary quantum mechanical approach for materials modelling, surpassing its antecedent the Hartree Fock method as the most accurate electronic structure technique.

One major pitfall in Hartree Fock theory is the mean field approximation. Whilst assuming all electrons in a system interact independently of one another simplifies the quantum problem, it is inherently incorrect. In reality, all of the electrons in a system are correlated. Instead of ignoring electron correlation completely, in DFT, the magnitudes of electron exchange and correlation are obtained from the concept of the uniform electron gas (UEG), where the electrons of a system are treated as entirely free particles contained within a given volume.

The preliminary ideas of DFT come from the Thomas Fermi model,[6,7] which defined the UEG, although major developments in the field are considered to have arisen in two pivotal works published in the 1960s, the first by Hohenberg and Kohn in 1964,[8] followed by another by Kohn and Sham in 1965.[9] Walter Kohn was awarded the Nobel prize in 1998 for his contribution to DFT.

The 1964 work by Hohenberg and Kohn[8] defined two theorems. The first of which states that *the ground-state energy of a system can be expressed as a unique functional of the electron density.* And the second that, *the 'true electron density', equivalent to the solution to the Schrödinger equation, is that which minimizes the energy of the functional*. And hence the energy functional described by Hohenberg and Kohn can be written in terms of the single-electron wave function, such that

$$E[\{\psi\}] = E_{known}[\{\psi_i\}] + E_{XC}[\{\psi_i\}] \qquad (2.6)$$

where

$$E_{known}[\{\psi_i\}] = -\frac{\hbar}{m}\sum_i \int \psi_i^* \nabla^2 \psi_i d^3r + \int V(\mathbf{r}) n(\mathbf{r}) d^3r + \frac{e^2}{2}\int\int \frac{n(\mathbf{r})n(\mathbf{r'})}{|\mathbf{r}-\mathbf{r'}|} d^3r d^3r' + E_{ion} \qquad (2.7)$$

The right-hand terms that contribute to $E_{known}[\{\psi_i\}]$ in Equation 2.7 are kinetic energy and Coulomb interactions between electrons and the nucleus, pairs of electrons and pairs of nuclei, respectively. $E_{XC}[\{\psi_i\}]$ is the exchange-correlation functional, which is defined to include all the 'unknown' terms. It includes not only contributions due to exchange and correlation, but also contributions due to discrepancies between the true

kinetic energy of the system and that which is given by $-\frac{\hbar}{m}\sum_i \int \psi_i^* \nabla^2 \psi_i d^3r$, which soley defines the kinetic energy of the independent electrons, and neglects to include the kinetic energy contributions of interacting electrons.[1,2,10]

Describing the contributions of energy in terms of functionals† directly linked to electron density is advantageous, because unlike the elusive wave function, electron density is an observable property with only three as opposed to infinite dimensions. It is hence far simpler to calculate.

The second part of DFT came from the work of Kohn and Sham,[9] who proposed that the minimum energy of a functional (equivalent to the ground state energy of the system) could be calculated by iteratively solving a set of single-particle equations for a defined electron density until the arrival of a self-consistent solution. These equations are known as the Kohn-Sham equations. The full form of which (Equation 2.8), is not dissimilar to the full Schrödinger equation (Equation 2.1), although because the solutions to the Kohn-Sham equations are single-electron wave functions, which depend only on three spatial variables, the summations present in the Schrödinger equation are not required. In the Kohn-Sham equations, energy is comprised of the summation of three potentials, the exact potential resulting from the interaction between an electron and the nuclei, V, the Hartree potential, V_H, and V_{XC} a functional derivative of the exchange-correlation energy.[1]

$$\left[-\frac{\hbar}{2m}\nabla^2 + V(\mathbf{r}) + V_H(\mathbf{r}) + V_{XC}(\mathbf{r})\right]\psi_i(\mathbf{r}) = \varepsilon_i\psi_i(\mathbf{r}) \qquad (2.8)$$

Here the Hartree potential describes the Coulomb repulsion between a single electron and the total electron density of the system. However, it also includes an unphysical term known as the self-interaction contribution, which describes the interaction between an electron and itself. A correction for this interaction is added to the 'unknown' portion of the energy, the exchange correlation term V_{XC}, a functional derivative of the exchange-correlation energy.[1,10]

† In mathematics, a functional is a function of a function, where a function is an expression dependent on a number of variables.

2.2.2.2 Implementation

2.2.2.2.1 The exchange-correlation functional

Solving the Kohn-Sham equations is not straightforward. Iterative solution methods are required as the Hartree potential, necessary to solving the equations, can only be defined using the electron density. However, calculating this term requires the single-electron wave functions to be known, which can only be done by solving the Kohn-Sham equations.

A further challenge is the identity of the exchange-correlation functional which cannot be identified exactly for any system other than the UEG. Hence, further approximations, based on the UEG, are made to obtain a suitable exchange-correlation functional for a particular system. The earliest approach is the local density approximation (LDA), in which the exchange-correlation potential at each position is set to equal the known exchange-correlation potential from the UEG, such that:

$$V_{XC}(\mathbf{r}) = V_{XC}^{UEG}[n(\mathbf{r})] \qquad (2.9)$$

Despite its rudimentary formulation LDA is surprisingly effective for certain systems, although it has been shown that its accuracy is due to a cancellation of errors in the exchange and correlation terms. However, LDA poorly represents the exact electron density of a system, which is unsurprising as the approximation is based on the use of the exact XC functional for the UEG. The functional also tends to overestimate binding energies, typically by 20 – 30% for many molecules and solids, predicting shorter bond lengths.[1,10,11] A later, and more frequently used approximation in chemistry is the generalized gradient approximation (GGA), which like LDA, uses information about the local density, but also incorporates information about the local gradient in the electron density. The additional degrees of freedom incorporated in GGA mean that unlike LDA, there is no single approximation, but instead a group of related approximations, some of the most common functionals include PBE, BLYP and PW91.[12–15] GGA functionals are particularly effective for modelling crystalline solids, and systems where the local density varies rapidly. One major limitation of both LDA and GGA functionals is that they do not capture van der Waals (dispersion) interactions. Due to the ubiquity of van der Waals (vdW) bonding in all chemical systems, methods have been developed to solve this problem, the two most prominent approaches are adding semi-empirical pairwise interactions, or employing an analytically derived functional which accurately represents the physics.[1,10]

The accuracy of a functional, in terms of the ability of a functional to reproduce the properties of a chemical system, can be vastly improved by including exact electron exchange from the Hartree Fock method. These functionals are referred to as hybrid functionals, because they are derived from both DFT and HF methods. Although hybrid functionals are often thought of as simply replacing the exchange part of the DFT XC functional with the HF exchange term, this is not in fact the case. Instead hybrid functionals include a fraction of exact exchange from HF. Some examples of popular hybrid functionals include PBE0 and B3LYP[13,14,16–19]. Hybrid functionals are essential for calculating band gaps, and calculating electronic energy differences reliably, but unfortunately they often underestimate the densities of solid structures. [1,2,10]

John Perdew, responsible for the formulation of the PBE functional and other XC functional developments, has likened the evolution of DFT functionals to "Jacob's Ladder".[20] Starting at the bottom with LDA, and moving up to GGA functionals, meta-GGA functionals – which utilize the second derivative of electron density, and hybrid functionals, with each functional improving in both accuracy and reliability. The final 'rung' of the 'ladder' is fully non-local functionals, although these functionals are yet to be formulated.[10,20]

Whilst, if selected carefully, modern exchange-correlation functionals are generally considered reliable in accurately representing the ground state energy of particular systems, recent work has shown that many fail in accurately representing the true electron density. This is due to a trend in fitting to physical energy measurements, rather than attempting to fit to the exact functional.[21]

2.2.2.2.2 Representing the electrons

Though it is certainly more accurate to consider the total number of electrons in a system when calculating its ground state, the total number of electrons is typically very large and causes the DFT calculation to be enormously computationally expensive. Fortunately, it is possible to simplify the calculation by only considering electrons which are involved in bonding, the *valence electrons*. The *core electrons*, which are scarcely affected by the atomic environment, are replaced by a pseudopotential, an effective potential which replaces both the full nuclear potential and the core electrons, approximating a screened atomic nucleus.[10]

Basis sets were briefly introduced in section 2.2.1 and can broadly be regarded as a numerical representation of wave functions and orbitals. The main requirements of a basis set are that it should be efficient, compact and accurate. There are two main types of basis set; *plane-waves* and *atomic orbitals*. It is important to note that basis sets used in electronic structure calculations are not complete, that is they cannot perfectly represent any wave function in the space they span. However, whilst this is true, most properties of molecules converge within a relatively small number of functions.[10,22]

Plane-waves are the popular choice of basis set for calculations on periodic systems, because this representation is equivalent to a Fourier series. Each orbital wavefunction is expressed as a linear combination of plane waves, which differ by reciprocal lattice vectors, **G**:

$$\psi_i^{\mathbf{k}}(\mathbf{r}) = \sum_{\mathbf{G}} a_{i,\mathbf{k}+\mathbf{G}}\, e^{i(\mathbf{k}+\mathbf{G})\cdot\mathbf{r}} \qquad (2.10)$$

Here, a is a factor of the periodicity, and **k** is a wavevector. This representation of the wavefunction applies Bloch's theorem, which states that the wavefunction of a periodic system can be written as the product of a supercell-periodic factor, a, and a phase factor, the periodic plane wave.[23] Plane-waves are systematic and can be expanded, that is made more complete by increasing the maximum value of the wavevector. Plane-waves are characterized by a cutoff energy, defined as $(\hbar^2/2m)|\mathbf{k}+\mathbf{G}|^2$. The energy of the wavefunction is also proportionately related to its curvature, and hence rapidly varying functions require high energy cutoffs for accurate representation. Unscreened, or hard nuclear potentials lead to rapidly varying wavefunctions and hence require large energy cutoffs. Therefore, most DFT codes will use pseudopotentials alongside plane-waves as a means of softening the nuclear potential. Despite being the solution for free electrons, plane-waves are an impressively efficient form of basis set and have been shown to be effective for modelling a wide range of materials. However, it should be noted that plane-waves fill all space, and can be considered uneconomical for modelling systems with large volumes of vacuum, for example low density materials such as zeolites and metal organic frameworks (MOFs).[2,10,22,23]

Atomic-like orbitals are another common form of basis, popular examples of such basis sets are Gaussians and Slater-type orbitals. These basis sets consist of a radial

function centered on an atom, multiplied by a spherical harmonic. Atom-centered functions are well-adapted, and require very few functions, however unlike plane-waves they are hard to converge systematically and there is generally poor computational scaling with the size of the basis.[1,2,10]

2.2.2.3 CP2K

Due to the countless iterations involved in solving the Kohn-Sham equations, and the complexity of the numerical solution schemes required, DFT calculations are implemented in computer codes, often run on high performance computers (supercomputers) so calculations can run over many processors, increasing the rate at which calculations are solved. There are many different DFT codes to choose from, with varying speed and precision depending on the approximations made in approaching the problem, codes also tend to vary in accessibility and convenience, some being more straightforward to use than others.[24]

This thesis primarily utilizes the CP2K code, first officially released in 2011. CP2K is distinctive in its approach to calculating the Hartree potential (Equation 2.8) and orthogonalising wave functions. CP2K uses a Gaussian and plane wave method (GPW), which is implemented in 'Quickstep' part of the CP2K code.[25–27] This method combines the Gaussian and plane wave basis functions, described in the previous section, to represent the valence electrons, the core electrons are represented by norm-conserving pseudopotentials. This method allows for near-linear scaling of systems exceeding thousands of atoms.[25–27] This level of performance is impressive when compared to other popular DFT codes which typically operate through purely plane wave or Gaussian approaches.[24] Whilst these codes function perfectly well in small systems of <100 atoms, performance does not scale linearly with the number of atoms, hence there is often a considerable computational cost associated with modeling larger systems. CP2K, however, is capable to dealing with up to a million atom supercells.[25–28]

2.3 *Ab initio* molecular dynamics

Ab initio molecular dynamics was first introduced by Car and Parrinello in 1985.[29] The pair developed the technique by combining classical molecular dynamics (MD), and density functional theory. This amalgamation of concepts vastly expanded the range of classical MD beyond the use of the pair-potential approximation.[29]

Both *ab initio* MD (AIMD) and classical MD rely on Newton's second law of motion ($F = ma$) to describe the movement of atoms in a system. Successive configurations of a system can be generated in this way, which is useful to understanding the conformational rearrangements of atoms in a system, including reproducing a system's flexibility, and the interactions of a system with other atoms or molecules, this is especially useful in determining host-guest relationships and reactions.

For an array of nuclei, which are treated as classical point-masses with an interaction energy $E[\{\boldsymbol{R}_I\}]$, where $\{\boldsymbol{R}_I\}$ is the position of the particles, the equation of motion can be written such that

$$M_I \ddot{\boldsymbol{R}}_I = -\frac{\delta E}{\delta \boldsymbol{R}_I} = \boldsymbol{F}_I[\{\boldsymbol{R}_J\}] \qquad (2.11)$$

These equations can be solved through the use of discrete timesteps, t. At each of these timesteps, the position of each atomic nucleus is moved to the next timestep $t + \Delta t$ based upon forces generated by nearby nuclei at that given time step.[27]

$$\ddot{\boldsymbol{R}}_I(t + \Delta t) = 2\boldsymbol{R}_I(t) + \boldsymbol{R}_I(t - \Delta t) + \frac{\Delta t}{M_I} \boldsymbol{F}_I[\{\boldsymbol{R}_J(t)\}] \qquad (2.12)$$

The method described above is known as the Verlet algorithm, an approach that has become well-established in classical MD.[29,30]

Although classical MD and AIMD share the same fundamental principles, discussed above, the difference between the two methods arises in the approach to calculating the forces on the nuclei. Forces on nuclei are determined by nuclei-electron interactions and nuclei-nuclei interactions. In classical MD these forces are typically calculated using classical interaction potentials. Whilst this method performs well for rare gas atoms and indeed simulating the properties of many microporous systems, it struggles to accurately simulate covalently bonded and metallic systems, which are often of intense interest to the scientific community and also fails to provide any insight into the electronic properties of the system. In AIMD the forces are calculated through electronic structure approaches, which allow the forces to be obtained directly from the electrons. Hence bonding, charge transfer and polarization effects are treated intrinsically in this method. [29,30]

In general terms, AIMD relies on two separate approaches; firstly, classical mechanics, which is used to describe ionic motion; and secondly, the Born-Oppenheimer approximation (described in Section 2.2.1), which is used to separate the nuclear and electronic coordinates, as it is in Hartree Fock theory.[29,30]

Following Kohn-Sham DFT, the total energy of the system of ions and electrons is given by

$$E[\{\psi_i\},\{\boldsymbol{R}_I\}] = 2\sum_{i=1}^{N}\int \psi_i^{*}(r)\left(-\frac{1}{2}\nabla^2\right)\psi_i(\mathbf{r})d\mathbf{r} + U[n] + E_{II}[\{\boldsymbol{R}_I\}], \qquad (2.13)$$

$$U[n] = \int d\mathbf{r}\, V_{ext}(\mathbf{r})n(\mathbf{r}) + \frac{1}{2}\int\int d\mathbf{r}d\mathbf{r}'\frac{n(\mathbf{r})n(\mathbf{r}')}{|\mathbf{r}-\mathbf{r}'|} + E_{XC}[n], \qquad (2.14)$$

$$n(\mathbf{r}) = 2\sum_{i=1}^{N}|\psi_i(\mathbf{r})|^2, \qquad (2.15)$$

$$\boldsymbol{F}_I = -\frac{\delta E}{\delta \boldsymbol{R}_I} \qquad (2.16)$$

where $\boldsymbol{F}_I$ is the force, $\boldsymbol{R}_I$ are the ion positions, ψ_i are the single-electron wave functions, E_{II} is the ion-ion interaction energy, $n(\mathbf{r})$ is the electronic charge density, V_{ext} is the electron-ion interaction and $E_{XC}[n]$ is the exchange-correlation energy contribution.[29,30]

The AIMD approach requires these equations to be solved very efficiently. The first method for solving these equations was the Car-Parrinello approach. Following the work of Car-Parrinello, several improvements to the original *ab initio* molecular dynamics method were made, and alternative methods developed. Modifications made within these methods included improvements to the original approach when calculating the ground states of fixed ionic systems, and the speed of the calculations.[31,32] However, even with efficient DFT codes, *ab initio* MD is still several orders of magnitude slower than classical MD. It can however, be used to model dynamics based on forces which are not parameterised for a particular system.

Whilst AIMD was used in this thesis to examine the effect of increasing temperature on small subsets of stable structures that had previously been optimised using DFT, it was not an electronic structure method used frequently throughout this work. For this reason, the details of the Car-Parrinello approach and subsequent *ab initio* MD approaches have been omitted from this thesis for conciseness, but are detailed in the literature.[30–34]

2.4 Interatomic potential models

As the name suggests, quantum mechanical electronic structure methods include all the electrons in a system when calculating its ground state energy. And, whilst methods such as DFT are only concerned with certain electrons, the *valence electrons*, the

number of electrons in the system can still be too large to model particular systems of interest.[2]

Force field (FF) methods neglect the electronic motions present within a system and instead use nuclear coordinates alone to calculate the system's energy. Omitting the electrons in this way allows FF approaches to calculate energies in a fraction of the computer time, and can hence be used as an inexpensive and efficient way to model extremely large systems. [2,35]

One inherent pitfall of FF approaches is the inability to reproduce the properties of a system that are derived from a molecules electronic distribution. Hence, it is not uncommon for FF approaches to be used as coarse-grain sifting methods, which allow a low energy structures to be identified before re-optimisation of these structures using a QM approach, such as DFT. This approach minimises the computational expense, whilst ensuring electronic properties of a system are captured. Another inexpensive solution to this problem is QM/MM, or the embedded cluster method. In these types of approaches, only the site of interest is treated quantum mechanically (QM), and the surrounding framework is treated classically, where MM refers to molecular mechanics, a type of force field approach appropriate for modelling covalently bonded systems. Whilst these approaches minimize computational expense, compared to full quantum mechanical approaches, embedded cluster approaches other problems, including the assignment of the QM/MM boundary.[2]

Like many quantum mechanical approaches, FF approaches require a series of assumptions to be made. The first of which is the Born-Oppenheimer approximation (first explained in section 2.2.1), which is arguably the most important assumption as it permits the energy of a system to be written as a function of nuclear positions. A molecular mechanics force field is constructed to mimic the basic interactions within a system, including contributions from processes such as the stretching and bending of, and rotations around bonds. A good quality force field will be one that is transferable to a variety of systems, as it allows a set of parameters developed and tested on a small subset of structures to be applied to a much larger range of systems. It is also notable to mention that force fields are empirical, that is the parameters contained within each individual force field will have been derived from a given set of observations, that may be physical, for example from experimental data, or theoretical, derived from data obtained using DFT or another molecular modelling technique. This

means that there is no *'one size fits all'* force field, instead, it is typical for one force field to be favoured for a given problem.[2,35]

A straightforward force field can be thought of as comprising four main contributions, that of bond stretching, bond bending, bond rotation and non-bonding interactions. These four contributions are treated in different ways. Deviations from equilibrium bond lengths or angles are assigned energetic penalties, a function describes how energy changes with bond rotation, and specific terms which describe the interactions between non-bonded parts of the system are included within the force field. Most molecular mechanics force fields will follow this form, however more advanced force fields will typically include additional terms.[2,35]

In this thesis, the use of interatomic potential models as a high-throughput screening method was explored to minimise the computational expense associated with DFT. However, due to poor correlation between the two levels of theory, the data is excluded from this thesis and other coarse-grain sifting methods were investigated.

2.5 Calculation settings used in this thesis

As explained, DFT is the approach used most frequently to model structures in this thesis. DFT calculations were implemented using the CP2K code.[25] Models were routinely geometry optimised, in these geometry optimisations both the atomic coordinates and the cell parameters were allowed to fully relax.[†] In general, geometry optimisations were performed using the PBE functional[12] and the high quality TZV2P basis set[††] at an energy cutoff of 650 Ry. Benchmark calculations also involved the use of other functionals including BLYP[13,14] and revPBE,[36] and hybrid functionals PBE0[16,17] and B3LYP.[18,19] It should be noted that *k*-point sampling was only made possible in CP2K during the latter part of this thesis. Hence, to ensure methods were consistent throughout, *k*-space was only sampled at the Γ-point.

AIMD simulations were also performed using the CP2K code. These simulations were run in the NVT ensemble at a timestep of 1 fs. The temperature of the AIMD simulations varied throughout the study.

[†] The geometry optimisation of surface models, included in Chapter 4, involved the relaxation of atomic coordinates within fixed cell parameters

[††] The MOLOPT basis set was used to optimise Mo/MFI structures in Chapter 6

All calculations were performed on the UK's national high performance computing service, ARCHER.[37] The ARCHER hardware consists of the Cray XC30 MPP supercomputer. Typical calculations were run on 8-10 cores, totalling 192-240 processors. Using CP2K each geometry optimisation calculation took 20 minutes to an hour, depending on the zeolite framework type.

2.6 References

1. Sholl, D.S. & Steckel, J. *Density Functional Theory: A Practical Introduction* (John Wiley & Sons, Inc., 2009).
2. Leach, A.R. *Molecular Modelling: Principles and Applications* (Pearson Education Limited, 2001).
3. Schrödinger, E. *Phys. Rev.* **28,** 1049–1070 (1926).
4. Schrödinger, E. *Ann. Phys.* **384,** 361–376 (1926).
5. Hartree, D.R. & Hartree, W. *Proc. R. Soc. London A Math. Phys. Eng. Sci.* **150,** (1935).
6. Thomas, L.H. *Math. Proc. Cambridge Philos. Soc.* **23,** 542 (1927).
7. Fermi, E. *Rend. Accad. Lincei* **6,** 602 (1927).
8. Hohenberg, P. *Phys. Rev.* **136,** B864–B871 (1964).
9. Kohn, W. & Sham, L.J. *Phys. Rev.* **140,** A1133–A1138 (1965).
10. Brázdová, V. & Bowler, D.R. *Atomistic computer simulations : a practical guide* (Wiley-VCH, 2013).
11. Catlow, C.R.A., Kotomin, E., *Computational Materials Science* (IOS Press, 2003).
12. Perdew, J.P., Burke, K. & Ernzerhof, M. *Phys. Rev. Lett.* **78,** 1396–1396 (1997).
13. Becke, A.D. *Phys. Rev. A* **38,** 3098–3100 (1988).
14. Lee, C., Yang, W., Parr, R.G. *Phys. Rev. B* **37,** 785–789 (1988).
15. Burke, K., Perdew, J.P. & Wang, Y. Derivation of a Generalized Gradient Approximation: The PW91 Density Functional in *Electronic Density Functional Theory* 81–111 (Springer US, 1998).
16. Adamo, C. & Barone, V. *J. Chem. Phys.* **110,** 6158 (1999).
17. Ernzerhof, M. & Scuseria, G. E. *J. Chem. Phys.* **110,** 5029 (1999).
18. Stephens, P.J., Devlin, F.J., Chabalowski, C.F. & Frisch, M.J. *J. Phys. Chem.* **98,** 11623–11627 (1994).
19. Vosko, S.H., Wilk, L. & Nusair, M. *Can. J. Phys.* **58,** 1200–1211 (1980).
20. Perdew, J.P. & Schmidt, K. Jacob's ladder of density functional approximations for the exchange-correlation energy in *AIP Conference Proceedings* **577,** 1–20 (AIP, 2001).

21. Medvedev, M.G., Bushmarinov, I. S., Sun, J., Perdew, J.P. & Lyssenko, K.A. Science, **355**, 49-52 (2017
22. Singh, D.J. & Nordstrom, L. *Planewaves, Pseudopotentials and the LAPW Method* (Springer US, 2006).
23. Hasnip, P.J. Refson, K., Probert, M.I.J., Yates, J.R., Clark, S.J., Pickard, C.J. *Philos. Trans. A. Math. Phys. Eng. Sci.* **372** (2014).
24. Lejaeghere, K. *et al. Science* **351,** 3000 (2016).
25. CP2K. Available at: https://www.cp2k.org/.
26. VandeVondele, J., Krack, M., Mohamed, F., Parrinello, M., Chassaing, T., Hutter, J. *Comput. Phys. Commun.* **167,** 103–128 (2005).
27. Lippert, G., Hutter, J., Parrinello, M. *Mol. Phys.* **92,** 477–488 (1997).
28. Bethune, I., Carter, A., Guo, X. & Korosoglou, P. Million Atom KS-DFT with CP2K, *Partnership for Advanced Computing in Europe* 2011
29. Car, R. & Parrinello, M. *Physical Review Letters*, **55,** (1985).
30. Martin, R.M. Quantum molecular dynamics (QMD) in *Electronic Structure* 371–386 (Cambridge University Press 2004).
31. Payne, M.C., Joannopoulos, J.D., Allan, D.C., Teter, M.P., Vanderbilt, D.H. *Phys. Rev. Lett.* **56,** 2656–2656 (1986).
32. Payne, M.C., Teter, M.P., Allan, D.C., Arias, T.A., Joannopoulos, J.D. *Rev. Mod. Phys.* **64,** 1045–1097 (1992).
33. Iftimie, R., Minary, P., Tuckerman, M.E. *Proc. Natl. Acad. Sci. U. S. A.* **102,** 6654–9 (2005).
34. Marx, D. & Hutter, J. *Ab Initio Molecular Dynamics: Basic Theory and Advanced Methods* (Cambridge University Press, 2012).
35. Bowen, J.P. & Allinger, N.L. *Molecular Mechanics: The Art and Science of Parameterization* (Wiley-Blackwell, 2007).
36. Zhang, Y. & Yang, W. *Phys. Rev. Lett.* **80,** 890–890 (1998).
37. ARCHER HPC. Available at: http://www.archer.ac.uk

Chapter 3: Violations of Löwenstein's Rule in Zeolites

3.1 Overview

As outlined in Chapter 1, over the last 60 years zeolites have had a bigger impact on the petroleum and petrochemical industry than any other single catalytic material. Now, at a time of dwindling traditional fuel sources and heightened concern for the environment, the development of efficient zeolite catalysts has never been of more importance to the energy industry. It is therefore no surprise that a large proportion of recent zeolite science is aimed at optimizing zeolite catalysts in terms of both lifetime and activity. Thus far, the approach to this has been predominantly experimental, involving time consuming trial-and-error based experiments in which synthesis conditions and Si/Al ratios are varied until an optimal balance between turnover, longevity and regeneration cost is reached. There is an opportunity for computational simulation to be used as a tool to guide experiment by informing on the factors that influence catalytic behaviour, circumventing the need for lengthy initial analysis processes, and moving us closer to the design of process-tailored catalysts.

To begin optimising zeolite catalysts, it is first imperative to understand their catalytic activity in terms of the distribution of Brønsted and Lewis acid sites throughout the framework. However, this requires a comprehensive understanding of the most favourable framework aluminium distributions in specific zeolites. As mentioned in section 1.1.6 of Chapter 1, despite extensive efforts to elucidate aluminium distribution in zeolites, there is still widespread disagreement concerning aluminium's preferred and precise framework location. This is largely attributed to limitations in analytical methodology and disparity between zeolite samples.

The work contained within this chapter aims to examine the long-standing question concerning aluminium distribution within zeolite frameworks, using periodic DFT implemented in the software package CP2K. Focusing solely on extra-framework cation containing frameworks, representing the calcined form of the zeolite, the most thermodynamically favourable and thermally accessible framework Al distributions over framework T-sites are evaluated. Long-range Al distributions and the influence of templates as charge-compensating and space-filling agents are addressed in subsequent chapters.

Although there have been previous computational attempts to elucidate aluminium's preferred position exactly, many have been limited by the level of theory employed, or

in assumptions made to reduce what was, until recently, the large computational cost associated with modelling zeolite systems. Many initial theoretical studies used a 'cluster approach' to investigate this problem.[1,2] In this approach only the site of interest and its direct surroundings (the 'cluster') are considered, and 'dangling bonds' at the bounds of the area are satisfied by atoms of appropriate size and charge. This method was popular in early quantum mechanical studies as the system size is greatly reduced from the entire crystal to only a few tens of QM atoms or smaller. Early DFT codes struggled to compute systems exceeding 100 atoms, especially before the arrival of widespread high performance supercomputing services with tens of thousands of processors. For many zeolite frameworks, the number of atoms contained within the unit cell exceeds 100 atoms, and hence for a long while cluster approaches were the only way to inspect zeolite systems quantum mechanically. However, whilst providing a useful method to avoid computational expense, 'dangling bonds' can be a problem, as they lack the ability to mimic the complexity of the surrounding zeolite framework accurately, particularly confinement effects and long-range interactions.[3] For a long time embedded cluster, or QM/MM, approaches[4–6] were considered a solution to this problem. However, whilst these approaches minimize computational expense compared to full quantum mechanical approaches and improve the representation of long-range interactions compared to cluster approaches, full quantum mechanical methods are more appropriate for the problems addressed in this thesis.[3–5] Although it should be noted that QM/MM approaches are superior to full quantum mechanical methods when simulating the diffusion and adsorption of reactant and product species during a zeolite catalysed reaction. This is due to the considerable computational expense associated with these simulations.

This study utilizes a periodic density functional theory (DFT) approach. Periodic DFT eliminates artefacts encountered at the boundaries between QM and MM regions that can influence the relaxation of species, which in turn can affect geometry and reactivity. However, introducing periodicity, defined by the unit cell or supercell, can be a problem. To capture realistic geometries cell size needs to be carefully considered as cells which are too small will hinder relaxation. By utilising supercomputer architectures and efficient DFT codes, in this work sufficiently large cells were considered, allowing relaxation to be captured accurately. Periodic DFT has proved to be a reliable method for modelling zeolite systems and their behaviours, and its use in elucidating the most favourable aluminium distribution in a range of frameworks has been demonstrated by several groups over the past decade. The remainder of this section provides an

overview of pertinent literature in which periodic DFT and other theoretical methods are used to investigate Al distribution in zeolites.

In 2006 Fujita *et al.*[7] explored the protonated form of zeolite Beta (H-BEA), a widely used petrochemical zeolite catalyst, using periodic DFT implemented in the numerical basis set code DMol^3.[7] The work was a continuation of previous work from the same group concerning the identity and stability of H-BEA Brønsted acid sites with 1 Al per unit cell, which provided the four 2 Al per unit cell models, on which the authors based their study. The models were optimised to equilibrium using the local density approximation (LDA) and subsequent single point energies were calculated using the generalized gradient approximation (GGA) functional PBE. Contrary to Dempsey's rule[8] (section 1.3.1.1.1), the authors concluded that the most stable model was that containing two Brønsted acid sites in close proximity, they attributed this to hydrogen bonding interactions between the protons and framework oxygen.[7] A later work by Meeprasert *et al.* [9] also used the DMol^3 code to explore Brønsted acid site distribution in the LTL framework, however their approach involved cell optimisations using only the GGA derived functional, HTCH. The work explored the sensitivity of Brønsted acid site location to heteroatom identity, elucidating the most stable proton positions surrounding the two distinct T-sites in the framework, in Al, B and G substituted LTL. The authors concluded that whilst the T2 site is most stable for B substitution, when substituting Si for Al or Ga the T1 site is favoured and charge-balancing protons reside at the same oxygen site. They suggest that the Al and Ga atoms at the T1 site are more accessible than the B at the T2 site by virtue of their position in the 12-ring window, and that in practice, this site would be the most stable for all heteroatom substitutions. The remainder of their work is concerned with the implications of tetrahedral cation substitution in terms of acidity and the adsorption of common industrial substrates, and although higher heteroatom concentrations are explored, only next-nearest neighbour (NNN), Löwensteinian ordered Al distributions were considered, presumably to reduce computational expense.[9]

One of the most detailed computational investigations in this area is a 2014 van der Waals (vdW) corrected periodic DFT study by Ghorbanpour *et al.* which focuses on H-ZSM-5 (MFI).[3] DFT does not account for vdW interactions; however, there are functionals available that include a correction factor, in this report the authors used the plane wave code VASP and a range of functionals, including vdW-functionals DFT-D2 and vdW-DF. MFI has a large unit cell size, containing 12 crystallographically distinct T-sites across 288 atoms in its all-silica orthorhombic form. For this reason, the authors

focused only on singly substituted ZSM-5 (Si/Al = 95) in an attempt to decipher which T-site is more preferential for Al substitution. Concluding that the T7 site is the most stable site for Al substitution, and the T9 to be the least stable site. According to DFT energy difference between these two sites is 0·38 eV, approximately 15 *k*T at room temperature and 10 *k*T at synthesis temperature (~ 453 K).[3] The preference for the T7 site is in keeping with PXRD data for fully Cs^+ exchanged ZSM-5 reported by Kim *et al*.,[10] and a QM/MM study by Brändle and Sauer[11] in which Al substitution at the T7 site was compared to substitution at the T12 site. The T12 site is the site most frequently chosen for Al substitution in computational studies concerning catalytic reactions over ZSM-5 due to the accessibility of this site.[12–17]

Although there are several reports which have employed periodic DFT to elucidate the identity of single Brønsted acid sites in zeolites, and the reaction mechanisms that occur over them,[18–20] few focus on frameworks with more than one aluminium substituted T-site. One 2004 study by Lo and Trout examines CHA aluminium distribution in natural Chabazite with Si/Al ratios of 11 and 5, corresponding to 1 and 2 Al atoms per rhombohedral CHA unit cell. [21] The authors' approach involved the CPMD code at the GGA level of theory,[22] and the majority of the work is focused on elucidating the most stable Brønsted acidic site in the single aluminium substituted protonated Chabazite unit cell model. Following the labelling by Calligaris *et al.,*[23] the authors conclude that the most preferential proton position is at the O2 oxygen site, a finding that contradicts many previous theoretical works and neutron diffraction work by Smith *et al.*, all of which concur that the most stable proton site at O1.[6,18–20,22] Only a small portion of Lo and Trout's report is concerned with 2 Al per unit cell substitutions and the effect that the two Brønsted acid sites, positioned relative to one another, has on acidity and substrate adsorption. The work neglects to account for possible non-Löwensteinian configurations, and only includes three models with aluminium atoms positioned *'ortho'*, *'meta'* or *'para'* to one another in the 8-ring.[21] The authors conclude that the *'ortho'* and *'para'* models were more stable than the *'meta'* model.[21]

Complementary DFT calculations included in the 2014 PXRD-Rietveld/MEM analysis of Cu-CHA by Andersen *et al.,*[24] explored all combinations of two aluminium atoms per CHA unit cell, excluding Al pairs as nearest neighbours in accordance with Löwenstein's rule. The authors found there to be specific Löwensteinian configurations with energies approximately 50 kJ mol^{-1} lower than all other configurations explored in their study, approximately 20 *k*T at room temperature, and 13 *k*T at synthesis temperature. These structures contained aluminium atoms positioned in the 6-ring as

next nearest neighbours (NNN) and next-next nearest neighbours (NNNN), with the associated copper ion positioned at the centre of the ring. This is in line with the experimental work of Akporiaye and co-workers[25] and early computational work by Schroeder *et al.,*[26] in which lattice energy minimizations based on classical potentials and large scale quantum chemical *ab initio* calculations were used to demonstrate the enhanced stability of aluminium pairs at NNN positions in the protonated FAU framework, compared to 'traditional' Dempsey ordering.[26]

The CHA framework has been the focus of the majority of the computational studies in which multiple framework Al are considered due to the fact that in its hexagonal form, the unit cell contains a single crystallographically distinct T-site. Hence, modelling permutations of multiple aluminiums across the T-sites is facile compared to more complex framework types like MFI, which contains 12 distinct T-sites. However, due to the importance of Al pairs to ZSM-5 (MFI) catalysis, there are a number of computational studies that assess the stability of different Al pair arrangements in the MFI framework.[17] One example is an early SCF-MO cluster study by Hass *et al.*,[27] which focussed on the relative stability of $(OH)_2$T-O-T$(OH)_2$ clusters, where T is equal to different combinations of Si and Al, in Al-containing clusters the negative charge was balanced by either Li^+ or Be^{2+}. The authors concluded that $(OH)_2$ Al-O-Al$(OH)_2$ clusters were unstable, in accordance with Löwenstein's rule.[28] A later, more comprehensive work by Ruiz-Salvador *et al.*[29] investigated Al distributions in monoclinic ZSM-5 through a force field approach. In this study the authors focused on the incorporation of Al atoms to the MFI framework in the absence of charge-balancing protons. Extra-framework species were replaced by a charge-correction, applied as a mean field. These simulations mimic the conditions of synthesis at the stage in which Al incorporation occurs, and situations where there is no site-specific interaction between the charge-compensating species and a framework T-site, for example when cationic species move rapidly. The removal of extra-framework cations also allows the role of Al-Al interactions on framework Si/Al distribution to be explored in isolation. The authors found that framework Al distributions may deviate from Dempsey's rule[8] due to anisotropy in the zeolite lattice, and that the distribution of Al across framework T-sites is primarily determined by two competing factors: the thermodynamic preference for Si → Al substitution at a single site, and Al-Al separation, driven by coulombic repulsions between negatively charged $(AlO_4)^-$ units (*i.e.* Dempsey's rule).[29] Arguably, the most comprehensive study in this area is a 2017 DFT study by Xing *et al.*[30] In this study the authors used the vdW-corrected functional PBE-D3 and the plane wave-based code VASP to model Al substitution at Si/Al ratios of 95, 46, 31 and 23,

equivalent to 1 to 4 Al per orthorhombic unit cell. The authors found T7 and T3 sites to be the most stable for Al substitution at Si/Al of 95, this is in line with previous vdW-corrected DFT work by Ghorbanpour *et al.*[3] On the addition of a second Al the authors note a distinct preference for Al to exist at the T3 and T11 sites, and on increasing the Al content further they found Al to be located at the T3 site in all cases, concluding this site to be the most preferable site for Al substitution in ZSM-5.[30]

It should be noted that computational methods have also been used to investigate Al distribution in other, non-zeolite aluminosilicates, and in the 1990s Dove and co-workers used the Monte Carlo method of statistical thermodynamics to investigate enthalpy and degree of Si/Al ordering in the aluminosilicate mineral gehlenite;[31] to determine the number of Al-O-Al linkages from ^{29}Si MAS NMR of Cs exchanged leucite and the zeolite analcime;[32] and to determine the phase transition temperature for Si/Al ordering in sillimanite, gehlenite, cordierite, and leucite.[33]

Despite extensive research in this area, there appears to be little consistency across the literature concerning aluminium's preferred framework location, and it is clear that differences in zeolite framework-type, Si/Al ratio and the identity of the counter-cation have a profound effect on Al distribution. Discrepancies not only exist between experiment and theory, but also between theoretical studies concerned with modelling Al distribution in a specific zeolite framework. However, this is most likely due to differences in approach or simulation settings. Studies which use similar approaches, give similar results. For example, both Ghorbanpour *et al.*[3] and Xing *et al.*[30] predict the T7 site to be a stable site for single Al substitution in H-ZSM-5, and report similar total energy ranges $\Delta E(E_{\text{global maximum}} - E_{\text{global minimum}})$ for Al substitution across the 12 T-sites. $\Delta E(E_{\text{global maximum}} - E_{\text{global minimum}})$ is 36·6 kJ mol^{-1} and 35·6 kJ mol^{-1} according to Ghorbanpour *et al.* and Xing *et al.,* respectively. Both studies use vdW-corrected periodic DFT and the plane-wave code VASP, although different vdW-corrected functionals are used in these studies, Ghorbanpour *et al.* use the vdW-DF functional and Xing *et al.* use PBE-D3.

However, in general, across the computational studies surveyed in this section, there seems to be good agreement that Al pairs prefer to be in the NNN or NNNN positions. Whilst this violates Dempsey's rule, there is a wealth of experimental evidence to support this conclusion.[7,9,24–26,29,34] Furthermore, Löwenstein's rule of aluminium avoidance is adhered to in all the computational studies discussed, in line with the vast majority of the experimental work in this area. Although it should be noted that all the

discussed studies neglect to include non-Löwensteinian ordered frameworks in their simulations.

In this chapter, DFT implemented in the CP2K code is used to elucidate the most thermodynamically favourable Si/Al distribution over the T-sites of catalytically active zeolite frameworks. Although this work includes a variety of zeolite frameworks with marked differences in both density and topology, it is primarily concerned with small-pore zeolite catalyst SSZ-13 (CHA), due to intense interest in this zeolite at present. All possible arrangements of framework aluminium in SSZ-13 are investigated, including non-Löwensteinian ordered distributions, surveying aluminium distribution at Si/Al ratios of 17, 11 and 8, in both Brønsted acidic H-SSZ-13 and as-synthesised Na-SSZ-13, the lithium form of the zeolite is also briefly examined as a means of comparison. A similar approach is extended to high-silica forms of the LTA, RHO, ABW, AEI and MOR frameworks; the DFT data obtained for these zeolite types is used to highlight and support the conclusions drawn for SSZ-13 (CHA). The implications of the most thermodynamically preferred Si/Al distributions on catalysis is considered, particularly emphasising the effect of different Al distributions on Brønsted acidity in H-SSZ-13. As outlined, work of this nature has been attempted previously, however, to my knowledge, this is the only exhaustive study of zeolite framework aluminium distribution with different Si/Al ratios at this fully periodic quantum mechanical level of theory.

3.2 Approach

Since the substitution of a single Al into a zeolite unit cell yields four potential proton positions (at the four apical oxygens of the alumina tetrahedra), before examining Al ordering in SSZ-13 (CHA), it is necessary to first establish whether there is a significant thermodynamic preference for a proton to reside in any one of these positions. To do this, a single Al, Al1, was substituted into one of the 36 available T-sites. Since all T-sites in CHA are crystallographically equivalent, an arbitrary T-site near the centre of the hexagonal CHA unit cell was selected. This substitution was accompanied by the addition of a single proton, covalently bound one of four available alumina oxygen sites – yielding four unique structures, each with a Si/Al ratio of 36.

To methodically explore all the permutations of Al ordering at a Si/Al ratio of 17, a typical Si/Al ratio for commercial SSZ-13 catalysts, the position of Al1 was maintained and a second Al, Al2, was sequentially substituted into the remaining 35 T-sites. To maintain charge-neutrality, each individual aluminium substitution was accompanied

by the tandem substitution of a charge compensation by a cationic moiety, either H^+, Na^+ or Li^+. For H-SSZ-13, each proton was placed at one of the four oxygen sites surrounding both Al1 and Al2, yielding a total of 560 combinations of 2 Al per unit cell. For the sodium form of the zeolite, each Na^+ cation was placed in a cavity space in close proximity to the corresponding Al. The same methodology was used to explore the lithium form, which was used to further explore cation-dependent trends in Al distribution. The high-silica protonated and sodium-containing forms of the LTA, RHO and ABW frameworks at Si/Al ratios of 11, 23 and 3, respectively, were also examined using this methodology. The same approach was not appropriate for the MOR and AEI frameworks as both contain more than one crystallographically unique T-site; MOR contains four, and AEI contains three. Hence, for these frameworks only the protonated forms were investigated, containing two aluminium ions at the nearest neighbour (NN) and next-nearest neighbour (NNN) positions for each of the distinct T-sites. All initial framework structures were obtained in their all-silica form from the database of zeolite structures, the majority of structures were optimised as 1x1x1 unit cells, however ABW and MOR were optimised as 2x2x2 unit cells due to their small unit cell sizes.[35]

On investigation of lower silica forms of SSZ-13 (CHA) calculating the prohibitively large number of combinations of 3 Al per unit cell (Si/Al = 11) and 4 Al per unit cell (Si/Al = 8) SSZ-13 was avoided by employing a method of stepwise aluminium incorporation. In this approach, 2 Al per unit cell global minimum structures, per the prior DFT, were used as the initial structures. A single Al, Al3, was sequentially introduced into each of the remaining Si T-sites, and the appropriate counter-cation positioned at one of the four apical oxygen sites, totalling 136 distinct framework arrangements. Using the 3 Al per unit cell (Si/Al = 11) global minimum as the new initial structure, the 4 Al per unit cell (Si/Al = 8) SSZ-13 structures were then investigated in the same way.

As discussed in Chapter 1, many industrial catalysts are proton-compensated zeolites. Since proton position is directly determined by the position of Al within the framework, it follows that the distribution of Al will have a direct effect on the Brønsted acidity of the zeolite. To test the relative Brønsted acidity between relaxed structures with different Al distributions, an acetonitrile probe was employed, using the adsorption energy, ΔE_{ads}, between the framework structure and the probe as a quantitative measure of Brønsted acidity. To calculate the ΔE_{ads}, each probe containing framework was geometry optimised to equilibrium, the framework and probe structures were then separated and single point energy calculations were performed on both structures,

providing the energy contributions for each. The energies were then input into the following equation, to give the ΔE_{ads}:

$$\Delta E_{ads} = E_{ads} - E_{framework} - E_{probe} \qquad (3.1)$$

ΔE_{ads} has been used in many previous Brønsted acidity studies, and is known to be a reliable Brønsted acidity descriptor.[36,37]

The majority of the periodic DFT calculations were performed using the CP2K code,[38–40] although the 1 Al per unit cell (Si/Al = 36) CHA calculations were performed using both CP2K and CASTEP in order to test the GPW basis set quality of CP2K against a purely plane wave basis, and ensure the suitability of CP2K for further use in this investigation. Additional benchmark calculations for energetics and solid-state NMR were also performed using the CASTEP code.[41] Throughout the investigation results were calculated using the PBE[42] functional, although further calculations using a other functionals were included to verify the initial 2 Al per unit cell (Si/Al = 17) CHA findings, these functionals included revPBE[43], BLYP[44,45], van der Waals corrected functionals vdW-DF2[46] and PBE+D3[47], and the hybrid functional PBE0[48,49]. Hybrid DFT calculations were carried out in CP2K using auxiliary density matrix methods (ADMM), and due to the computational demand associated with hybrid methods, the PBE0 calculations were performed as simple single point energy calculations. Individual models were fully geometry optimised to equilibrium density, with variable lattice parameters in CP2K as 1x1x1 cells using the high quality TZV2P basis set and an energy cutoff of 650 Ry. Only the ABW and MOR frameworks were optimised as a 2x2x2 supercell, due to their small unit cell sizes. A selection of larger 2x2x2 supercells were also tested for each of the frameworks, although no meaningful change was observed in the relative energies using the larger cells.[50]

3.3 Aluminium distribution in SSZ-13 (CHA)

3.3.1 Si/Al ratio = 35

To determine the relative stability of the four possible Brønsted acid sites in a 1 Al per unit cell CHA framework (Si/Al = 35) four unique structures were constructed as described in the previous section. The unit cell parameters for each of the initial structures were ***a,b*** = 13·68 Å and ***c*** = 14·77 Å, giving a cell volume of 2391·54 Å^3.[35] These parameters are idealized CHA cell parameters obtained from DLS refinement as reported by the IZA.[35,51] Each of the four CHA structures contained a single Al and proton. For each model the proton was assigned a different oxygen site designated

O1-4 in accordance with the labelling scheme of Calligaris *et al.*,[23] where sites O1 and O4 are part of the 6-ring, and O2 and O3 part of the larger 8-ring.

Following geometry optimisation, the cell parameters of each of the structures increased, and a mean volume increase of 2.7 % was observed. The increase in cell parameters is due to the introduction of Al. The results for the geometry optimisations (Table 3.1) show that the O1 site is the most favourable proton site, with a relative energy (relative to the mean energy) of -5·2 kJ mol^{-1} per unit cell (U.C.). The O3 site is the least stable proton site with a relative energy of -1·2 kJ mol^{-1} per U.C. These results are concordant with three previous theoretical studies, a 1997 DFT study by Shah *et al.* and two separate studies conducted in 1998, one *ab initio* study by Jeanvoine *et al.*[20] and one 'embedded cluster' study by Brändle *et al.*[6] However, these results are contradictory to the work of Trout and Lo, who postulated that the O2 site is the most stable proton position. Although, unlike other theoretical studies, including this one, Trout and Lo used deprotonation energy as an indication of site stability, which could be the cause of disagreement between results. [21]

	Relative Energy / kJ mol^{-1}
O1	-5·2
O2	-2.4
O3	-1·2
O4	-1·5

Table 3.1 *Relative energies of each of the 1 Al per unit cell H-SSZ-13 structures in which the acidic proton is positioned at oxygen sites O1-4.*

Whilst the structure containing a proton at the O1 proton position is the most stable, it is important to consider the energy range, which is only 7·6 kJ mol^{-1} per U.C. This energy range is in keeping with those reported by Shah *et al.* (8·7 kJ mol^{-1}) and Jeanvoine *et al.* (8·8 kJ mol^{-1}) and is equivalent to ~3 *k*T (where *k* is the Boltzmann constant) at room temperature. At SSZ-13 synthesis temperature, 433·15 K,[52] the thermodynamic preference for O1 would be greatly reduced, hence we can assume that all positions, O1-4, are likely to be occupied during synthesis. This is contrary to conclusions made in a 1997 neutron diffraction study by Smith and co-workers[22] who reported that only the O1 and O2 sites are occupied. This may indicate that proton

siting in real samples is controlled by the accessibility of the site during the exchange process, rather than thermodynamics. However, it is noteworthy that the O1 and O2 sites are the most stable sites predicted by DFT, in line with results of Smith *et al.*[22] Furthermore, Smith *et al.* only analysed a single H-SSZ-13 sample – it is possible that other preparations and samples might yield population of the other sites.

3.3.2 Si/Al ratio = 17

Catalytic samples of SSZ-13 typically have a Si/Al ratio of 17, equal to 2 Al per hexagonal CHA unit cell. Since, for a single Al substitution, all potential proton sites are likely to be occupied at synthesis temperature, it was important to consider all possible permutations of both the aluminium atoms and the protons in the 2 Al per unit cell model. The approach to methodically investigating each of the unique H-SSZ-13 and Na-SSZ-13 configurations was discussed in section 3.2.

The DFT data for 2 Al per unit cell SSZ-13 (CHA) in both its protonated and sodium-containing forms is shown in Figure 3.1, where the relative energy per unit cell (U.C.) (with respect to the average total energy) is given as a function of framework aluminium separation.

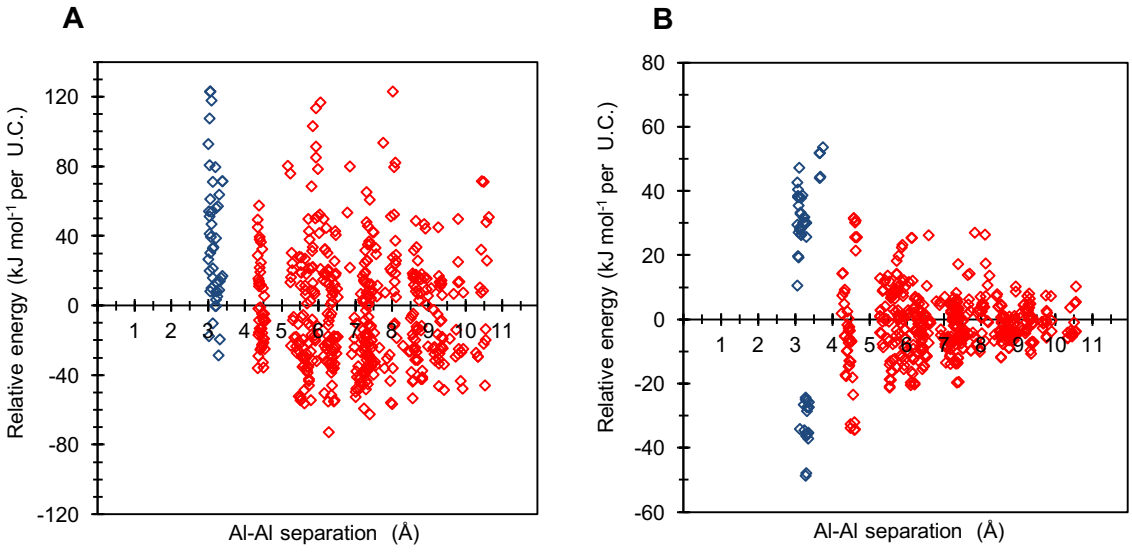

Figure 3.1 *Relative energy distribution (kJ mol^{-1} per U.C.) against framework aluminium separation for* ***a)*** *Na-SSZ-13 and* ***b)*** *H-SSZ-13. Frameworks possessing non-Löwensteinian (NL) ordered aluminium atoms (-Al-O-Al-) are shown in blue.*[50] *(Reproduced from reference 50 with permission from the Royal Society of Chemistry.)*

Assuming Löwenstein's rule[28] of aluminium avoidance is valid, we would expect the SSZ-13 structures containing aluminium atoms at separations equivalent to that of a "forbidden" -Al-O-Al- linkage to be the least stable, and therefore the structures with the highest energy. We would also expect structures to become increasingly stable with increasing aluminium separation, in accordance with Dempsey's rule.[53] As predicted by Löwenstein's rule, the majority of H-SSZ-13 and Na-SSZ-13 configurations containing adjacent aluminium atoms, with Al-Al separations of approximately 3 Å (Figure 3.1), are unstable. However, beyond this separation the relative energy landscapes for the two forms of the zeolite become strikingly different.

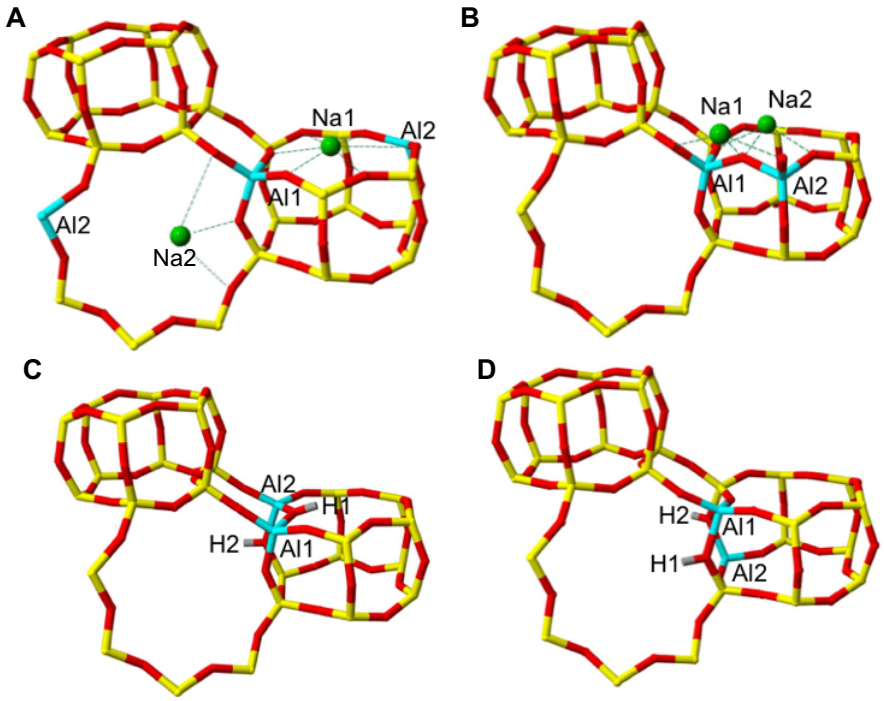

Figure 3.2 *Global minima L and NL 2 Al per U.C. SSZ-13 structures predicted by DFT.* ***a)*** *Global minimum Na-SSZ-13 structure, with Löwensteinian ordered aluminium atoms at the NNNN position,* ***b)*** *lowest energy NL Na-SSZ-13 structure,* ***c)*** *Global minimum NL H-SSZ-13 structure, with protons oriented trans to one another* ***d)*** *lowest energy Löwensteinian ordered structure with Al at NNN position. Where; silicon (yellow), oxygen (red), aluminium (light blue), sodium (green), hydrogen (grey)*[50] *(Reproduced from reference 50 with permission from the Royal Society of Chemistry.)*

In accordance with Löwenstein's rule, and what has already been widely observed in sodium-containing zeolites, the Na-SSZ-13 global minimum (Figure 3.2a) contains

aluminium pairs as next-next nearest neighbours (NNNN).[25] The energy penalty for forming the most stable non-Löwensteinian (NL) structure (Figure 3.2b) $\Delta E(NL_{global\ minimum} - L_{global\ minimum}$ is +44·3 kJ mol^{-1} per U.C., ~12 *k*T at typical synthesis temperature. This suggests the formation of Löwensteinian forbidden -Al-O-Al- linkages to be very unfavourable. In this Löwensteinian global minimum structure, aluminium atoms are separated by 6·18 Å, with associated Na^+ cations in two discrete positions; one at the parameters of the 8-ring aperture of the *'cha'* cavity (the SIII site), and another capping the face of the D6R (SII) (cation sites in CHA are shown in Figure 1.10 of Chapter 1). This is in line with recent work by Zhao *et al.*, who demonstrated that there is a preference for Na^+ to exist in both the SII and SIII sites in 2 Al per hexagonal unit cell structures through ^{23}Na solid state MAS NMR and complementary DFT.[54] Figure 3.2a shows that the energy penalty for bringing Al pairs together to 5·5 Å separations (+18·5 kJ mol^{-1}) is greater than the energy penalty for separating Al pairs to 7·40 Å (+10·4 kJ mol^{-1}), this is because separations of 5·50 Å correlate to NNN ordering, where an Al separation of 7·4 Å correlates to NNNN ordering across different D6Rs.

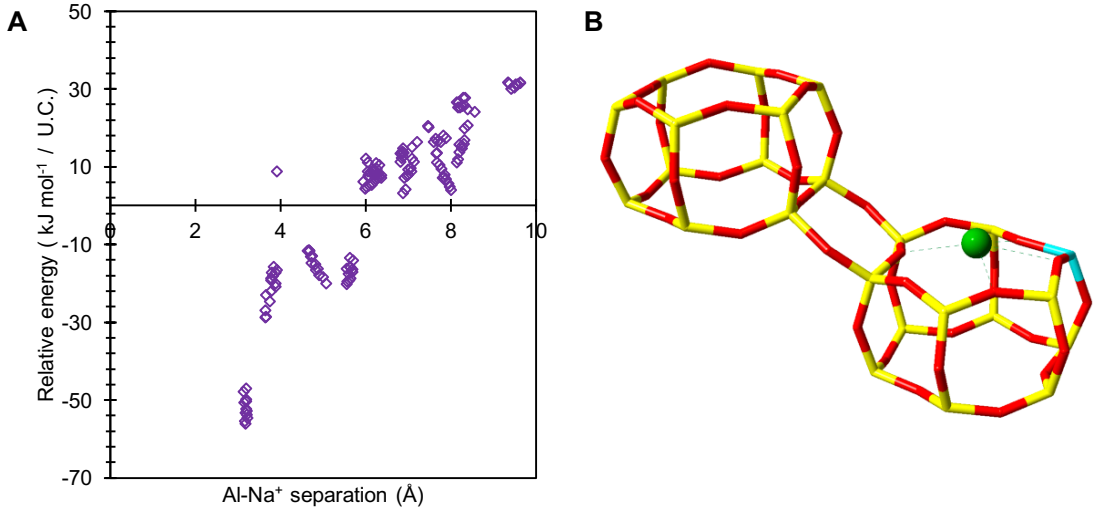

Figure 3.3 a) *Relative energy distribution (kJ mol^{1} per U.C.) against Al-Na^+ separation for 1 Al per U.C. Na-SSZ-13* ***b)*** *Global minimum structure for 1 Al per U.C. Na-SSZ-13 predicted by DFT, in this structure the Na^+ cation resides at the SII position.*

To investigate the relative stability of the SII site versus the SIII site, 1 Al per U.C. Na-SSZ-13 structures (Si/Al = 35) were generated in which the charge-compensating cation is positioned at the SII site, capping the face of the D6R; or the SIII site, at the

8-ring windows of the *'cha'* cage. Each of the structures were geometry optimised using DFT at the same level of theory used throughout this chapter. There is a positive correlation between Al-Na^+ separation and the energy of the structure (Figure 3.3a), and the global minimum structure, Figure 3.3b, was found to contain the Na^+ cation at the SII position. This structure is 27·4 kJ mol^{-1} per U.C. more stable than the lowest energy structure in which Na^+ is at the SIII site. This is contrary to what is reported in much of the crystallographic data in literature, which indicates that the SIII position should be preferred at such low Na loadings.[55,56] However, these findings are in line with a 2003 Hartree Fock study by Civalleri *et al.*,[57] and a recent combined NMR and DFT study by Zhao *et al.*,[54] both which reported the SII site to be the preferred Na^+ site.

XC Functional	Cation Site	FD / T / 1000 Å	Total Energy / kJ mol^{-1}	ΔE (SII-SIII) / kJ mol^{-1}
PBE	**SII**	14·6	-3536568·4	-27·4
	SIII	14·7	-3536541·0	
PBE+D2	**SII**	14·7	-3537284·1	-33·2
	SIII	14·9	-3537250·9	
PBE+D3	**SII**	14·7	-3537126·6	-17·4
	SIII	14·8	-3537109·2	
BLYP	**SII**	14·5	-3532743·1	-27·9
	SIII	14·5	-3532715·2	

Table 3.2 *Calculated energy penalties for forming the less stable SIII site over the SII site in 1 Al per U.C. Na-SSZ-13 using a range of XC functionals.*

In a 2015 DFT study by Fischer *et al.*[58] the SIII site was reported to be the most stable Na^+ position in CHA at the PBE level of theory, however, when introducing dispersion corrections to the functional, PBE+D2, the authors noted a change in the relative order of stability of the cation sites. Considering this, the SII and SIII 1 Al per U.C. Na-SSZ-13 global minimum structures were reoptimised with a range of functionals, including PBE+D2, PBE+D3 and BLYP. No change in the order of stability between the SII and SIII sites was observed, however the energy penalty for forming the less stable SIII

structure, ΔE (SII-SIII), varied across the different levels of theory (Table 3.2). Although the SIII structures tend to be slightly more dense, the data shows little change in the density across the different structures, indicating that cation ordering is dominated by short-range interactions rather than changes in density. Discrepancies between these results and those of Fischer *et al.* are most likely because Fischer and co-workers' simulations involved fixed cell optimisations, where here, the cell geometries were allowed to fully relax.

The H-SSZ-13 global minimum structure (Figure 3.2c) is remarkably different to the Na-SSZ-13 global minimum structure – illustrating the influence of counter-cation identity on framework aluminium location. The lowest energy H-SSZ-13 structure contains adjacent aluminium atoms positioned along the edge of the 6-ring at a separation of only 3·28 Å, in violation of Löwenstein's rule. In this structure the two associated protons, H1 and H2, are separated by 4·36 Å and arranged '*trans'* to one another; H1, which mediates the aluminium ions, is directed into the plane of the 6-ring, and H2, positioned at the connecting edge of the D6R, is oriented away from H1, and directed into the 8-ring window of the *'cha'* cavity. In this 'trans' orientation unfavourable proton-proton repulsions are minimized. The most stable Löwensteinian (L) structure (Figure 3.2d) contains aluminium ions positioned as NNN along the diagonal of a 4-ring, at a 'non-Dempsey' separation of 4·60 Å. Here, both protons are directed into separate 8-ring windows of the central *'cha'* cavity.

The energy penalty for forming the L structure, over the NL structure is +14·2 kJ mol^{-1} per U.C., approximately 4 *k*T at typical synthesis temperature. The $\Delta E(NL_{global\ minimum} - L_{global\ minimum})$ for Na-SSZ-13 is +44·3 kJ mol^{-1} per U.C., whilst $\Delta E(NL_{global\ minimum} - L_{global\ minimum})$ for H-SSZ-13 is -14·2 kJ mol^{-1} per U.C., this suggests there is a strong enthalpic incentive to adopt 'traditional' Löwensteinian ordering in sodium-containing frameworks, and a modest enthalpic incentive for the formation of non-Löwensteinian linkages in protonated frameworks.

Zero point energies (ZPE) for the NL and L global minimum structures were calculated from predictive vibrational frequency data using CP2K (Appendix B). This data was then compared with data obtained for equivalent NL and L structures in the smaller 12 T-atom rhombohedral CHA cell (Si/Al = 5) using CASTEP. The ZPE data is included in Table 3.3.

		ZPE	ΔZPE (NL-L)	ΔE (NL-L)	ΔE (NL-L) + ZPE
Si/Al = 17 *(CP2K)*	**NL**	1123·3	3·4	-14·2	-10·8
	L	1119·9			
Si/Al = 5 *(CASTEP)*	**NL**	398·4	0·2	-9·1	-8·9
	L	398·2			

Table 3.3 *ZPE data for NL and L 2 Al per U.C. structures. CP2K was used to calculate data for the hexagonal 36 T-atom unit cell (Si/Al = 17) and CASTEP was used to calculate the data for the rhombohedral 12 T-atom unit cell (Si/Al = 5). All energies are reported in kJ mol^{-1}.*

The absolute ZPE difference between the CASTEP data with a 12 T atom unit cell is slightly lower than that obtained using CP2K for the larger 36 T atom unit cell. This is due to a combination of the lower Si/Al ratio and differences in the pseudopotential and basis sets used. The key point is that the enthalpy difference for NL-L still favours NL by ~10 kJ mol^{-1}.

CASTEP was then used to carry out an assessment of the free energy difference between smaller NL and L rhombohedral CHA cells (Si/Al = 5). Taking account of the vibrational entropy differences within the static, harmonic approximation with a cutoff of 800 eV. In these calculations, phonon frequencies were sampled at four different *k*-points in the Brillouin zone. The Helmholtz free-energy difference between configurations as a function of temperature is shown in Figure 3.4. These calculations show that the relative stability of the L and NL H-SSZ-13 configurations is maintained beyond typical synthesis temperatures demonstrating a clear thermodynamic preference for non-Löwensteinian structures, over Löwensteinian structures in H-SSZ-13.

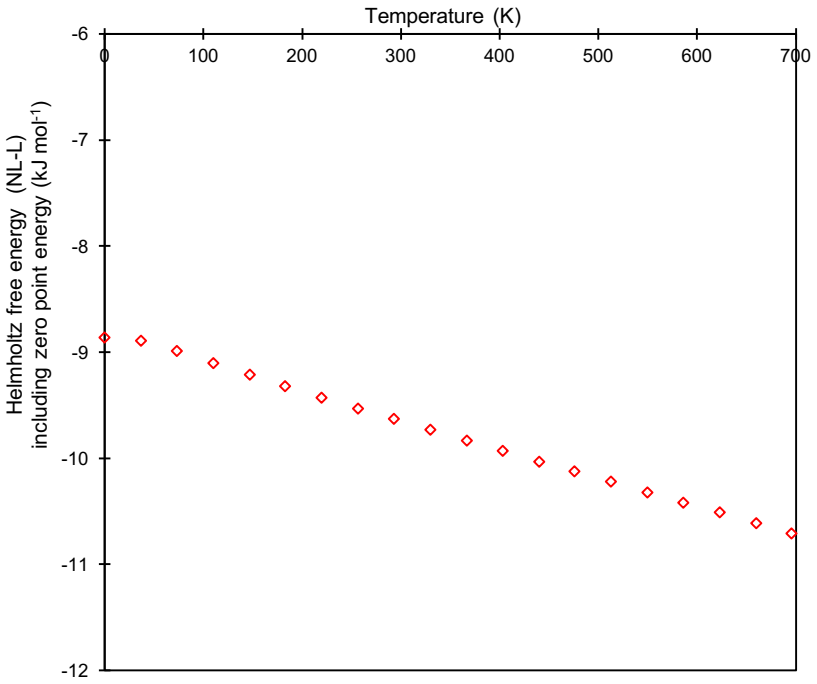

Figure 3.4 *Helmholtz free-energy difference between configurations as a function of temperature for NL and L H-SSZ-13 12T atom rhombohedral unit cell structures at a Si/Al ratio of 5.*

Furthermore, *ab initio* molecular dynamics (AIMD) calculations were performed on the two hexagonal H-SSZ-13 NL and L global minimum structures. AIMD simulations were run using 1 fs timestep, in the NVT ensemble at 500 K. The results are included in Figure 3.5. Over the production ranges of 500 – 1000 fs the mean energy difference between NL and L is -13·2 kJ mol^{-1}, the mean energy difference is the same over the production range of 750 – 1000 fs. This confirms that the total energy differences found at 0 K (-14·2 kJ mol^{-1}) is maintained at elevated temperature.

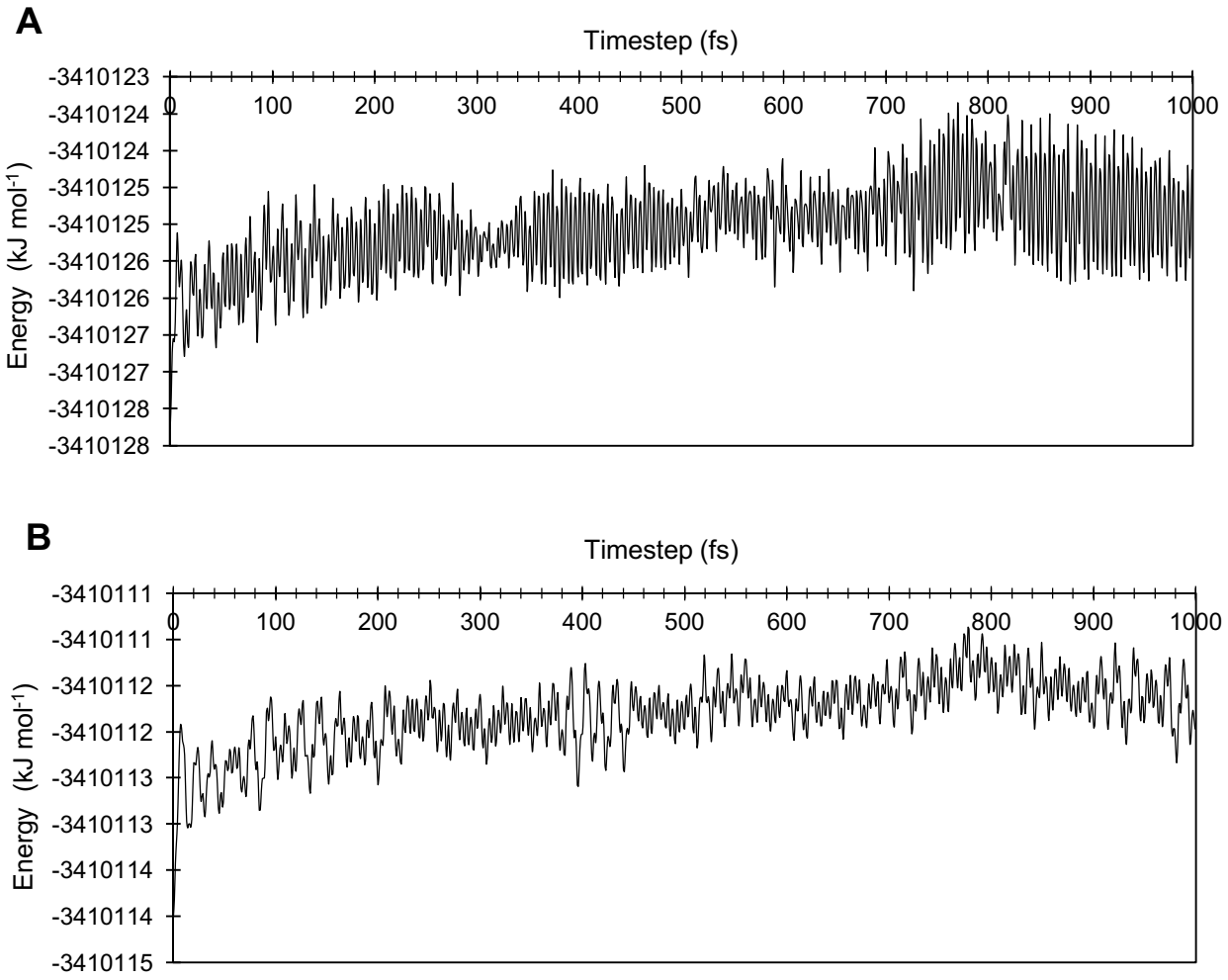

Figure 3.5 *AIMD data at 500 K for the 2 Al per U.C. (Si/Al = 17) H-SSZ-13* ***a)*** *NL global minimum structure and* ***b)*** *L global minimum structure.*

It is notable that the NL global minimum H-SSZ-13 is not unique. Figure 3.1b shows seven other NL ordered frameworks (excluding the global minimum structure) with lower energies than the L global minimum. Each of these structures contain proton arrangements similar to those displayed in the NL global minimum structure (Figure 3.2c), in which a proton sites at the oxygen site mediating the two aluminium ions.[50]

To verify the unexpected H-SSZ-13 result the 12 lowest energy structures were further investigated using the higher level hybrid functional PBE0[48,49] and van der Waals corrected functionals vDW-DF2 and PBE+D3. The results these calculations are

shown in Figure 3.6. The relative energies calculated using these methods show good correlation with those calculated using the standard PBE functional, confirming the robustness of the predictions.

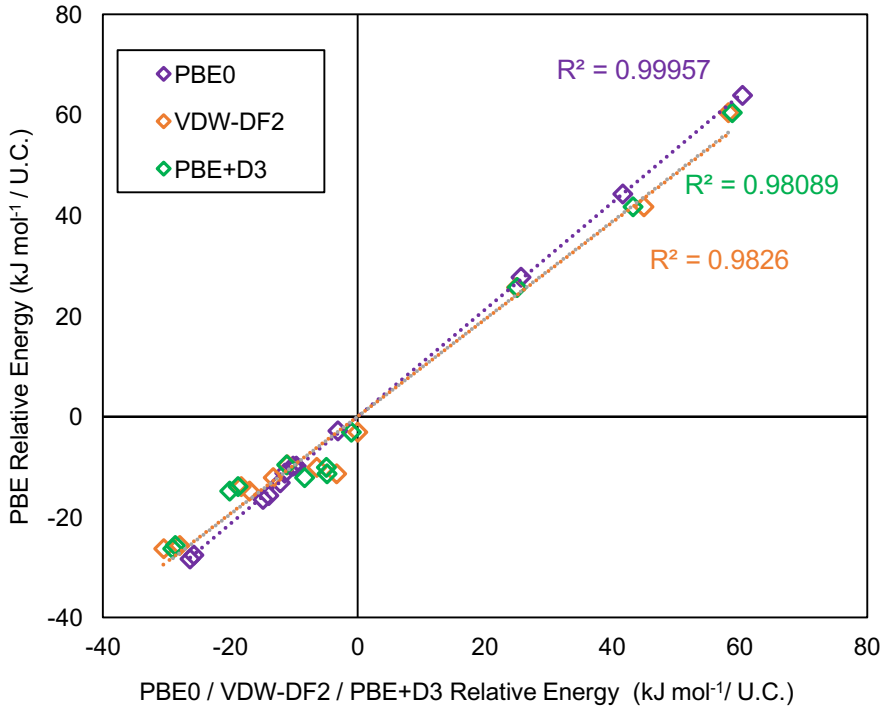

Figure 3.6 *Correlation between the relative energies of the 12 most stable 2 Al per unit cell (Si/Al = 17) H-SSZ-13 (CHA) structures calculated using standard PBE and the PBE0 hybrid functional,* and *Van der Waals corrected functionals vdW-DF2 and PBE+D3.*

Whilst there seems to be a clear thermodynamic preference for non-Löwensteinian ordering in the protonated from of the zeolite, and Löwensteinian ordering in the sodium-containing form, it is noteworthy that Dempsey's rule[8] is violated in the global minimum structures of both forms of the zeolite.

The literature contains several reports of violations of Dempsey's rule in zeolites,[7,25,26] and it has been established that non-covalent interactions, present between framework oxygen and extra-framework cations, may distort aluminium distributions away from true Dempsey-ordering.[7] On close inspection, violations of Dempsey's rule in Na-SSZ-13 can be rationalized by simple electrostatics. As shown in the global minimum

structure for 2 Al per unit cell (Figure 3.2a), there is a preference for Na^+ cations to maximize their coordination with framework oxygen whilst minimizing unfavourable cation-cation interactions – as illustrated by the collection of unusually high energy structures (with aluminium separations of 5·80 - 8·20 Å) in Figure 3.2a, all of which contain Na^+ cations at unfavourably short separations, causing these structures to be destabilized compared with what would be expected from Dempsey's rule.

Rationalizing the non-Dempsey aluminium distribution in sodium-containing frameworks is straightforward, whilst untangling the thermodynamic preference for NL ordering in protonated frameworks is more complex. As demonstrated by sodium-containing frameworks, non-covalent interactions play a significant role in determining aluminium distribution. Fujita *et al.* demonstrated that hydrogen bonding interactions cause aluminium atoms to reside in close proximity to one another in zeolite Beta.[7] The separation between framework oxygen and H1 and H2 in 2 Al per unit cell H-SSZ-13 indicates the existence of two hydrogen bonds (O-H---O < 2·5 Å) per aluminium in both the global minimum structure and the lowest energy Löwensteinian structure. Given the possibility that hydrogen-bonding interactions could be the cause of the unanticipated stability of the NL ordering in H-SSZ-13 the robustness of the order of stability predicted in this work was examined using other density functionals. A representative subset of structures were selected and re-optimised with the revPBE[43] and BLYP functionals,[44,45] which have been shown to underbind hydrogen bonding interactions in water and ice structures (whilst PBE overbinds).[59] The results, Figure 3.7, show that decreasing the hydrogen bonding strength in this way has no qualitative effect on the results and little quantitative effect, indicating that whilst hydrogen bonding must play a part in stabilizing the H-SSZ-13 structures, it is not the decisive factor that controls whether NL is favoured over L. In a 1993 computational study, Schroeder *et al.*,[26] found NNN Al ordering to be considerably more stable than Dempsey ordering in H-FAU. They concluded the stability of NNN ordered structures compared to those with more dispersed Al to be due to the minimization of local framework distortion. Whilst the authors found Al-O-Al to be considerably unstable, similar conclusions could be drawn from the results of this study.

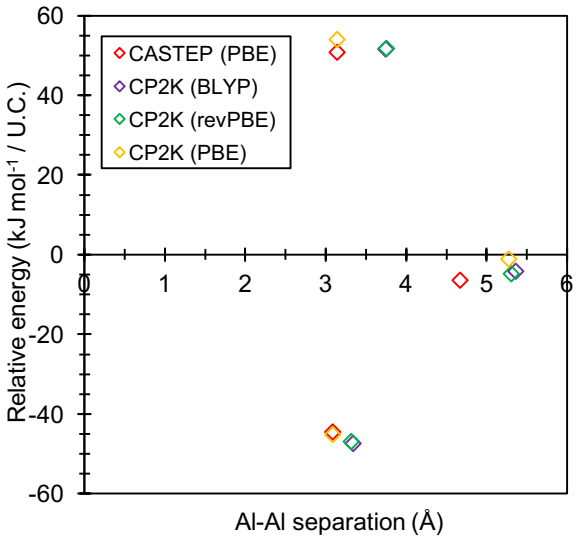

Figure 3.7 *The relative of stabilities of a collection of high-, mid-, and low-energy 2 Al per unit cell (Si/Al = 17) H-SSZ-13 (CHA) configurations, geometry optimised using CP2K with PBE, BLYP and revPBE functionals, and CASTEP at the PBE level of theory.*[50] (*Reproduced from reference 50 with permission from the Royal Society of Chemistry)*

To ascertain whether the thermodynamic preference of Löwensteinian structures, compared to non-Löwensteinian structures in Na-SSZ-13 can be attributed to electrostatic or steric factors, the framework Al distribution in Li-SSZ-13 was investigated. The ionic radius of Li^+ is intermediate to that of H^+ and Na^+, however, interactions between Li^+ and the framework are predominantly electrostatic as is the case for Na^+. The DFT data for Li-SSZ-13 is shown in Figure 3.8a, and is remarkably similar to that of Na-SSZ-13, with a thermodynamic preference for Löwensteinian aluminium ordering over non-Löwensteinian ordering, where ΔE ($NL_{global\ minimum} - L_{global\ minimum}$) = +51·2 kJ mol^{-1} per U.C. However, the global minimum for the Li-SSZ-13 (Fig. 3.8b) contains aluminium atoms at a slightly greater separation (7·34 Å) than what was calculated for Na-SSZ-13 (6·18 Å). However, for both Li-SSZ-13 and Na-SSZ-13 global minimum structures, Al pairs exist as NNNN. In Li-SSZ-13 the Li^+ cations are positioned at the SII site, capping both faces of the D6R. This is in line with what was reported in a previous Hartree Fock study by Civalleri *et al.,*[57] and in experimental studies by Smith *et al.*[55,56] We can assume that the diminished size of Li^+ compared to Na^+ is what causes two SII sites to be occupied, as opposed to one SII site and one SIII site. In this position Li^+ can maximize bonding with framework oxygen in the consequently puckered 6-ring of the D6R.

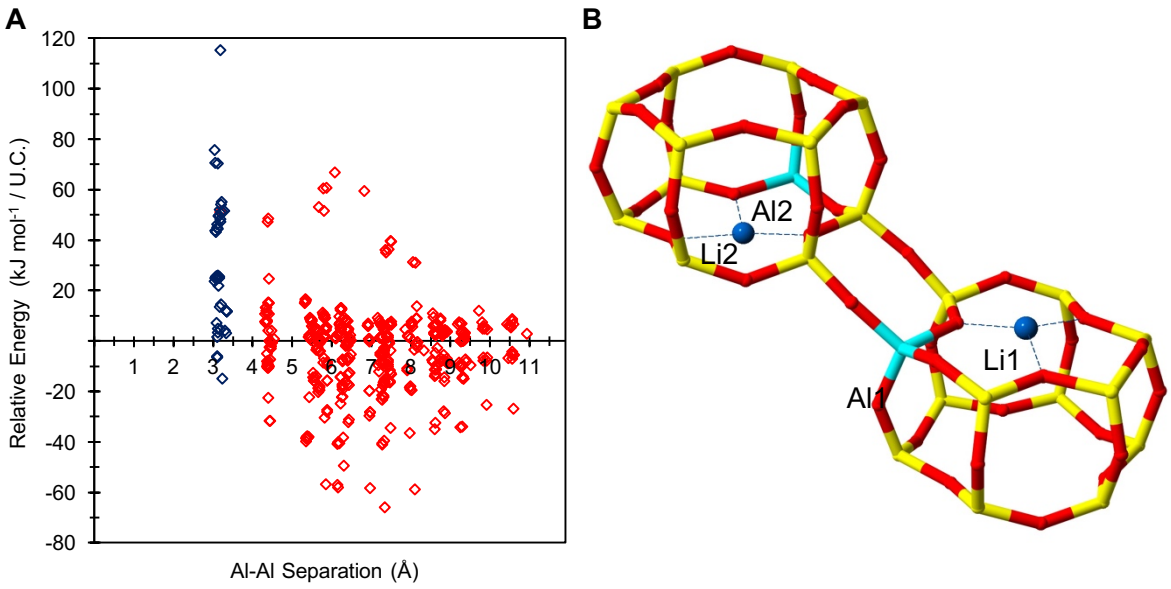

Figure 3.8 a) *Relative energy distribution (kJ mol^{-1} per U.C.) against framework aluminium separation for Li-SSZ-13. Frameworks possessing non-Löwensteinian (NL) ordered aluminium atoms (-Al-O-Al-) are shown in blue.* ***b)*** *NL global minima for 2 Al per U.C. Li-SSZ-13, where; silicon (yellow), oxygen (red), aluminium (light blue), lithium (dark blue).*[50] (*Reproduced from reference 50 with permission from the Royal Society of Chemistry)*

The similarities between the Li-SSZ-13 and Na-SSZ-13 data qualitatively illustrate that aluminium distribution is broadly governed by the electrostatic contributions of the charge-balancing cations, although steric factors may control differences between global minimum structures. To quantify these qualitative findings, the charge distributions in both the Na- and H-SSZ-13 structures were considered.

Table 3.4 contains charge distribution data for the protonated and sodium-containing forms of SSZ-13, obtained through two different charge-partitioning approaches; Bader charge analysis and Mulliken population analysis.

On comparison of the charges for 2 Al per unit cell Na- and H-SSZ-13 (Table 3.4), the charge on the Na^+ cation in the Löwenstein Na-SSZ-13 structure is far greater than that of the proton in the H-SSZ-13 non-Löwenstein structure, is because H^+ is predominantly covalently bonded to framework oxygen whereas bonding between Na^+ and framework oxygen is purely electrostatic. Consequently, the charge on the

framework oxygen atoms covalently bound to the protons is diminished in comparison to the corresponding oxygen atoms in the Na-SSZ-13 structure. It should be noted that whilst there are discrepancies between the absolute charge values obtained through the two charge partitioning methods, this is to be expected, and the overall trend between the values remains constant for both approaches.

Structure	Atom	Charge	
		Bader	**Mulliken**
H-SSZ-13	**H^+**	+0·66	+0·42
	O	-1·47	-0·71
Na-SSZ-13	**Na^+**	+0.92	+1.07
	O	-1·60	-1.08

Table 3.4 *Comparison of the Bader and Mulliken charges for the H- and Na-SSZ-13 global minimum structures. For H-SSZ-13 the charge on the proton and the framework oxygen atom it is covalently bound to are shown. For Na-SSZ-13, the charge on the corresponding framework oxygen atom is shown, along with the charge on the Na^+ cation.*

In zeolites, Al–O bonds are typically longer and weaker than Si–O bonds. Since Al^{3+} has a smaller absolute charge than Si^{4+}, and hence Si–O bonds tend to be shorter, stronger and more ionic than Al–O bonds, due to the higher charge on Si^{4+} compared to Al^{3+}. Furthermore, T–OH bonds (where T is Si or Al) will be longer than T–O bonds, due to the diminished charge on the protonated oxygen caused by covalent bonding between the oxygen and the proton. For the H-SSZ-13 structure with 2 Al per U.C. Al–OH bonds are 11% longer compared to Al–O, stretched to a maximum of 1·90 Å, compared to an average Al–O bond length of approximately 1·71 Å. Si–OH bonds are only 7% longer than Si–O, stretched to a maximum bond length of 1·74 Å, compared to a framework average of approximately 1·63 Å.

It is notable that each of the stable NL H-SSZ-13 structures contain a hydroxyl species mediating two aluminium ions, these structures therefore contain a total of three long Al–OH bonds, and a single long silanol Si–OH bond. In the high-energy NL structures and all L structures, there are two Al–OH bonds, and two comparatively unfavourable

long Si–OH bonds. Adopting the NL configuration minimises the number of long Si–OH bonds and maximises the number of the short, strong, more ionic Si–O bonds – this is the driving force for non-Löwensteinian ordering in H-SSZ-13. It is also likely that the mediating hydroxyl in Al-O(H)-Al shields the charge of the two adjacent Al^{3+} ions, allowing them to be positioned nearer to one another than predicted by Löwenstein's and Dempsey's rules.

In the sodium-loaded zeolite, the interaction between Na^+ and framework oxygen is primarily electrostatic and there is complete charge transfer between Na^+ and framework oxygen, as reflected by the computed Na^+ charge. Therefore, the difference in charge/ionicity between a framework oxygen coordinated to Na^+ and those not coordinated to Na^+ is rather small and so the alumina units favour NNNN positions.

Attempts were made to estimate the electrostatic contribution of the energy differences between the NL and L H- and Na-SSZ-13 configurations through the use of the atoms in molecules (AIM) approach and interatomic potential models. However, the AIM approach produced unphysical charges for Na^+ cations despite intensive investigation and potential models were unable to qualitatively reproduce the total energy differences between NL and L H-SSZ-13 configurations obtained through DFT.

3.3.3 Si/Al ratio = 11

Employing the method of stepwise aluminium incorporation described in section 3.2, the 3 Al per unit cell structures of SSZ-13 (CHA) (Si/Al = 11) were explored, using the NL and L ordered 2 Al per unit cell global minima structures as the initial configurations. A total of 136 distinct framework arrangements were created in this way for each NL and L initial global minimum structure (272 calculations for both Na^+ and H^+ containing zeolites).

Interestingly, both the 2 Al per U.C. NL and L H-SSZ-13 initial configurations gave the same NL 3 Al per U.C. global minimum structure (Figure 3.9). This structure contains a chain of three oxygen linked aluminium atoms, $[O\text{-}Al\text{-}O]_3$, with each charge-compensating proton located at a bridging oxygen and arranged *trans* to its neighbour(s). Clustering of Al in this way minimises the number of long, unstable silanol linkages and maximises the number of short, strong and stable Si-O.

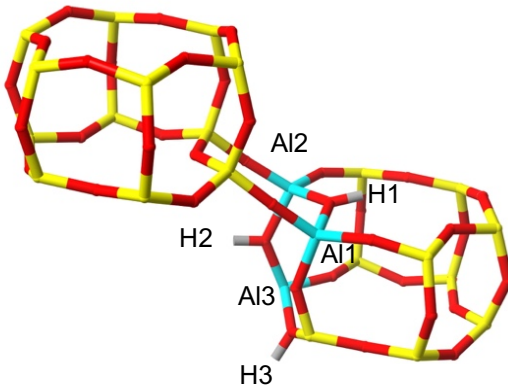

Figure 3.9 *Global minima for 3 Al per U.C. SSZ-13 (CHA) in its protonated form (NL).*[50] *Reproduced from reference 50 with permission from the Royal Society of Chemistry)*

However, for Na-SSZ-13 with 3 Al per unit cell, each initial structure yielded two different global minimum structures. As was the case for the sodium-containing zeolite with 2 Al per unit cell, both structures contained Löwensteinian ordered aluminium distributions, however the initial Löwensteinian structure favoured the third aluminium at the NNN position,[26] where the non-Löwensteinian structure favoured Al at the NNNN position. The corresponding figures for these structures are shown in Figure 3.10.

The difference in aluminium ordering between the two structures further highlights the importance of cations in determining the distribution of framework aluminium throughout a zeolite. In the Löwensteinian structure, the NNN Al position is favoured, and the associated Na^+ cations occupy one SII site, and two SIII sites. However, the NNNN Al position is favoured for the non-Löwensteinian global minimum structure, in which the Na^+ cations occupy only two SII sites and one SIII site. Hence the NNNN site is the only aluminium position that can satisfy the Na^+ coordination requirements, whilst minimising unfavourable Na-Na interactions. Further supporting conclusions that the distribution of framework aluminium and extra-framework sodium cations are inherently linked. Due to the fact that the non-Löwensteinian structure contains an -Al-O-Al- linkage, which is unstable in Na-SSZ-13 structures, the Löwensteinian structure is the most stable structure by 16·1 kJ mol^{-1} per U.C. [50]

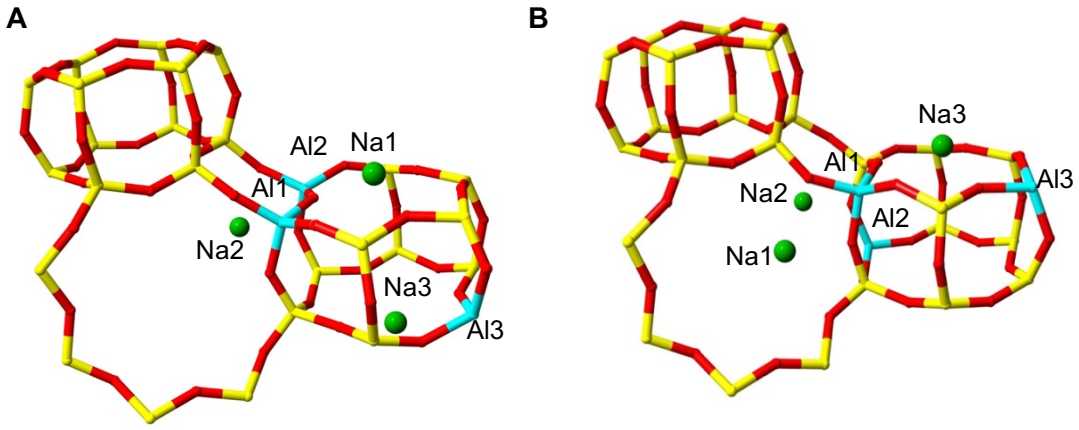

Figure 3.10 *Global minima for 3 Al per U.C. SSZ-13 (CHA) in its* ***a)*** *sodium form, from the NL 2 Al per U.C. initial structure* ***b)*** *sodium form, from the L 2 Al per U.C. initial structure.*[50] (*Reproduced from reference 50 with permission from the Royal Society of Chemistry)*

3.3.4 Si/Al ratio = 8

As outlined in section 3.2, the H-SSZ-13 (Si/Al = 11) global minimum was then used as the new initial structure to investigate 4 Al per unit cell, equivalent to a Si/Al ratio of 8. The global minimum structure, shown in Figure 3.11a, contains a chain of four oxygen linked aluminium atoms arranged in a 4-ring, with protons arranged *trans* to one another. It appears that as the aluminium content of the zeolite is increased, the aluminium clusters into zones of concentrated -Al-O-Al-, this is contrary to the general belief that that aluminium is reasonably well dispersed throughout the frameworks of real samples.[50,60,61]

In the sodium form of this structure, Figure 3.11b, the fourth Al resides in the next-nearest neighbour position (NNN), again in accordance with Löwenstein's rule, and what has already been documented for similar zeolites.[26] All four sodium cations position themselves near to the aluminium ions, occluding two SII sites and two SIII sites, where they can maximise their coordination with framework oxygen, whilst minimising unfavourable Coulomb repulsions.[50]

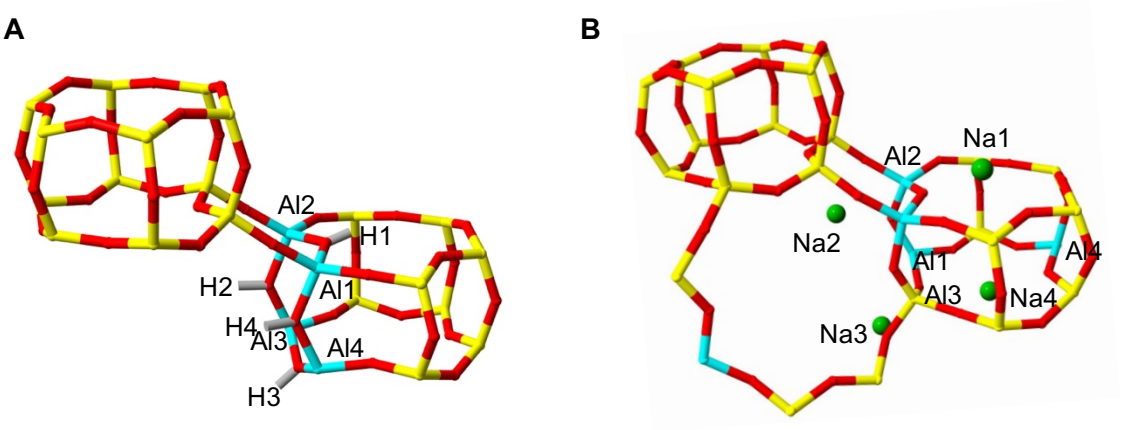

Figure 3.11 *Global minima for 4 Al per U.C. SSZ-13 (CHA) in it's* ***a)*** *protonated form (NL),* ***b)*** *sodium form, from the NL 3 Al per U.C. initial H-SSZ-13 structure.*[50] (*Reproduced from reference 50 with permission from the Royal Society of Chemistry)*

3.4 Other zeolite frameworks (LTA, RHO, ABW, MOR AEI)

To ascertain whether the unexpected findings of this study manifest in other framework structures, the following framework-types were investigated by the same methods discussed previously: LTA, RHO, ABW, MOR and AEI.

These framework-types were selected due to their prevalence in industry[62–65] and due to differences between their structures, densities, and SBUs. Although some are more structurally alike than others, for example CHA, LTA, RHO, and AEI all contain 6-membered ring systems, ABW and MOR are made up from distinct SBUs, hence allowing examination into whether preference for NL ordering over L can be extended to other ring systems (each of these framework structures are discussed in detail Chapter 1). Only materials with reasonably sized unit cells and minimal crystallographically distinct T-sites were considered to reduce computational expense. Like CHA, LTA, RHO and ABW contain a single distinct T-site, these frameworks were examined using the same methodology that was employed for CHA. AEI and MOR have three and four crystallographically distinct T-sites, respectively, and hence in these structures the approach was modified and aluminium pairs were explored as nearest neighbours and next-nearest neighbours at each of the individual T-sites (as described in section 3.2).

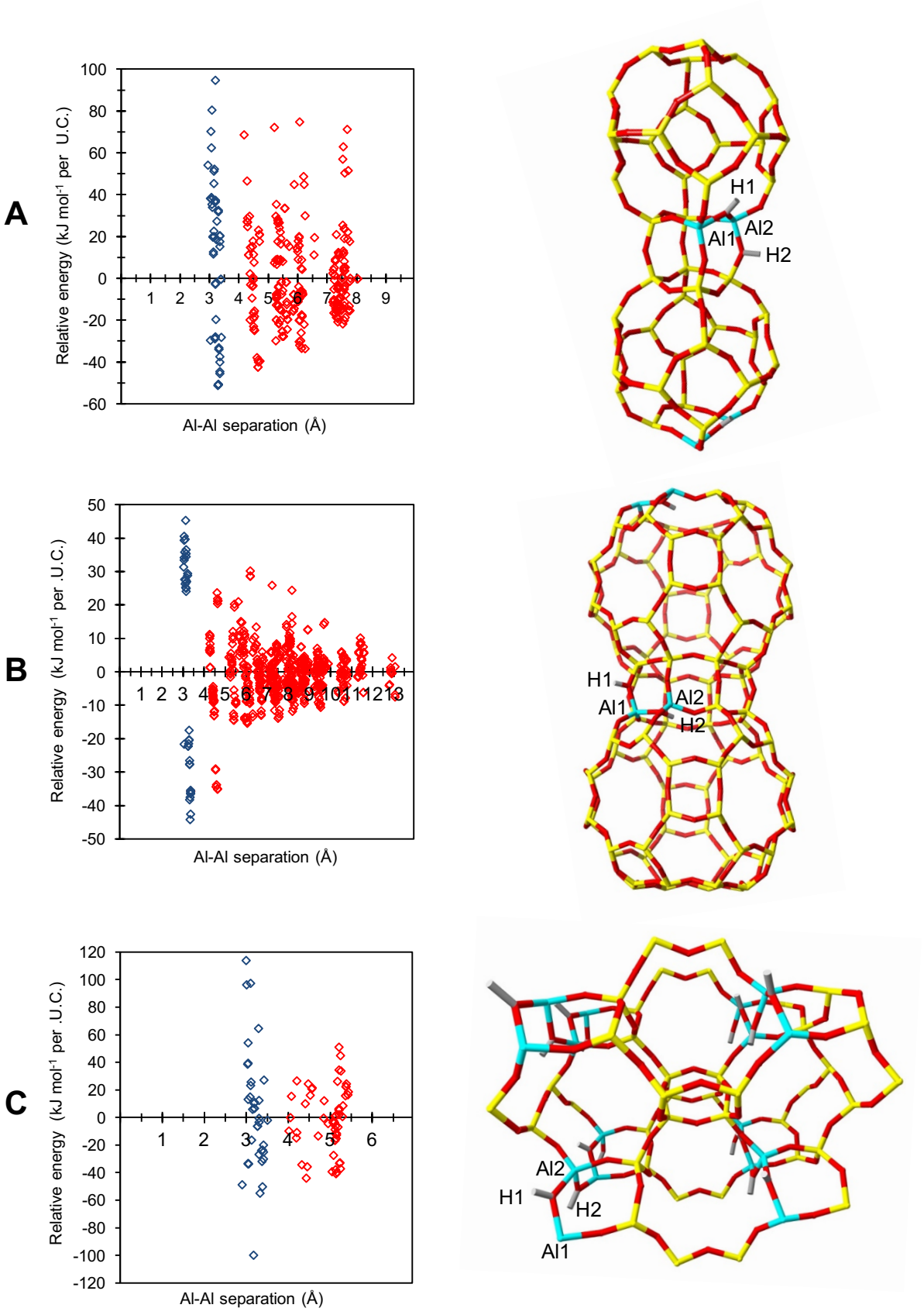

Figure 3.12 *Relative energy dispersion (kJ mol^{1} per U.C.) against framework aluminium separation and NL global minima for 2 Al per U.C. protonated forms of* ***a)*** *LTA (1x1x1)* ***b)*** *RHO (1x1x1)* ***c)*** *ABW (2x2x2)*[50]

The DFT data for each of the frameworks with 2 Al per unit cell LTA, RHO and ABW, corresponding to Si/Al ratios of 11, 23 and 3, respectively, is shown in Figure 3.12. Like CHA, all three framework types possess NL global minimum structures in their protonated forms, with protons arranged in the same *'trans'*-like orientation. The energy penalty for forming the L structure (ΔE ($NL_{global\ minimum}$-$L_{global\ minimum}$)) for each framework is correlated to the respective densities of each framework. For low density H-LTA (14·2 T/1000 $Å^3$) this value is +8·3 kJ mol^{-1} per U.C., +9·2 kJ mol^{-1} per U.C. for H-RHO (14·1 T/1000 $Å^3$), +14·4 kJ mol^{-1} per U.C. for H-CHA (15·1 T/1000 $Å^3$), and is +55·7 kJ mol^{-1} per U.C. for high density H-ABW (17·6 T/1000 $Å^3$). Contrary to what might be expected, these results suggest that 'forbidden' NL linkages are more strongly preferred in denser zeolites, although this is consistent with the fact that NL motifs have been observed in denser aluminosilicate minerals.[66] However, despite this, even for LTA, the lowest density framework, the energy penalty for forming L structures is ~2 *k*T at typical synthesis temperatures (~450 K).

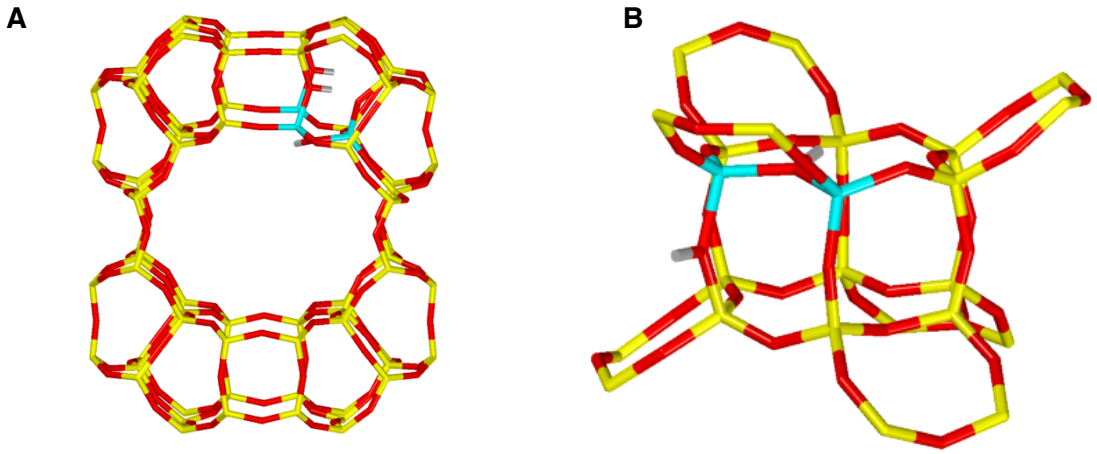

Figure 3.13 *Fragments of the frameworks of the NL global minima for 2 Al per U.C. protonated forms of* ***a)*** *MOR (2x2x2) Si/Al = 23* ***b)*** *AEI (1x1x1) Si/Al = 23*

The DFT data for H-MOR and H-AEI (both Si/Al = 23) also showed NL ordering to be favoured over L ordering in these structures (Figure 3.13), where the energy penalty for forming the L structure over the NL structure (ΔE ($NL_{global\ minimum}$-$L_{global\ minimum}$)) is -16·1 kJ mol^{-1} per U.C. for MOR and -16·0 kJ mol^{-1} per U.C. for AEI, the framework densities for these structures are 17·2 T/1000 $Å^3$ and 14·8 T/1000 $Å^3$, respectively. These values are consistent with the observed trend between density and preference for the formation of Al-O-Al, it can be assumed that NL linkages are preferred in denser

structures due to the increased stability of these structures compared to those with more open frameworks. Furthermore, this data confirms that non-Löwensteinian Al ordering is not unique to CHA-type zeolite frameworks, and that there is also no obvious preference for the formation of NL linkages in a particular ring-system.

3.5 Brønsted acidity of non-Löwensteinian frameworks

In many zeolite catalysed reactions the catalytically active sites are Brønsted acidic protons covalently bound to oxygen sites at the vertices of the alumina tetrahedra. The work contained in this chapter demonstrates that framework aluminium distribution is directly determined by the arrangement of the extra-framework counter cations, and *vice versa*. Given that Brønsted acidity arises from the presence of charge-balancing protons, it follows that the Brønsted acidity of a zeolite catalyst, and indeed the catalytic activity of the zeolite, will also be determined by the distribution of framework aluminium.

The interdependence of Al distribution and Brønsted acidity has been demonstrated in several recent computational studies. A 2017 study by He *et al.*,[67] showed the Brønsted acidity of FER to be strongly dependent on both the stability of the T-site for Al substitution, in accordance with the existing literature,[68,69] and the stability of the Brønsted acid site, demonstrating that stable Al arrangements, in which Brønsted acidic protons are part of hydrogen bonding networks with nearby framework oxygens exhibit the weakest Brønsted acidity. Furthermore, the authors concluded that Brønsted acidity increases with increasing Al-Al separation, noting NNNN arrangements to be far more acidic that NNN arrangements, and that Brønsted acidity decreases with increasing Al content, in line with what has been found in previous experimental studies[70] and more recent computational studies by Li *et al.* and Liu *et al*.[37,69]

Due to the lack of evidence that Löwenstein's rule can be violated in real zeolite samples, these studies only consider Löwensteinian ordered structures. The data for H-SSZ-13 shows that nearest neighbour and next-nearest neighbour Al arrangements are far more stable than Al arrangements with greater Al separations; the energy penalty for forming the lowest energy structure with Al at the NNNN position over the L global minimum is +12 kJ mol^{-1} per unit cell. The relative Brønsted acidity between NL and L ordered H-SSZ-13 at Si/Al ratios of 17, 11 and 8, equivalent to 2, 3 and 4 Al

per U.C., respectively was hence considered. Basic molecules are typically used as experimental probes to gauge zeolite Brønsted acidity. Pyridine is a popular probe molecule, however, there are significant limitations to the diffusion of pyridine throughout the small-pore CHA channel system in SSZ-13, hence in these simulations a smaller acetonitrile probe was used, which has been used to measure Brønsted acidity in similar computational studies.[71] The acetonitrile probe was placed in four discrete positions within the zeolite framework, each position was labelled Ac1-4 (Figure 3.14).

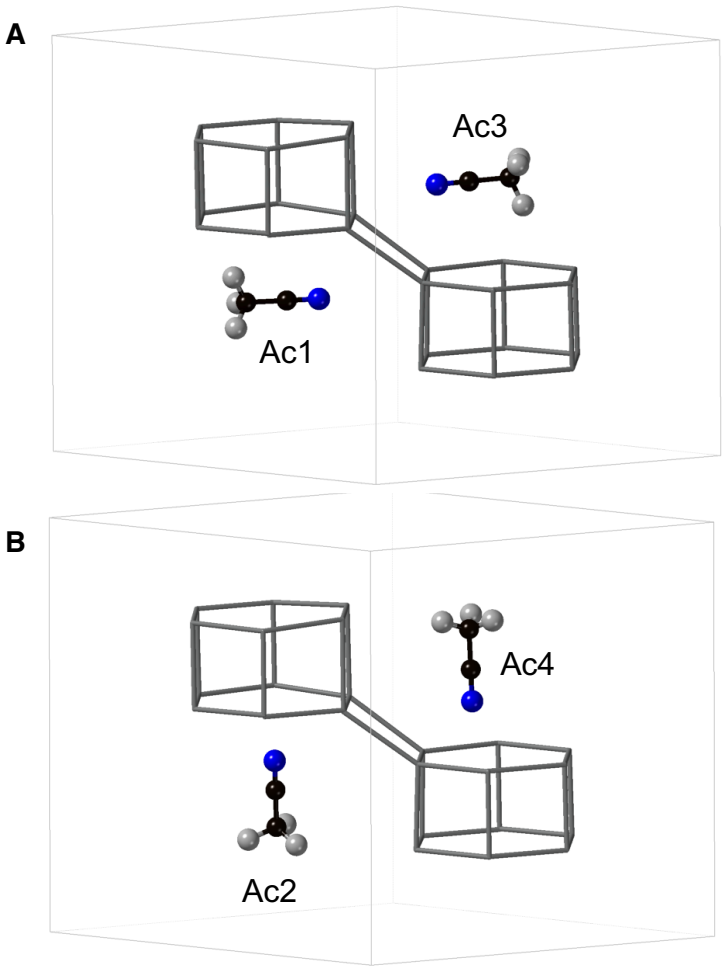

Figure 3.14 *The four discrete acetonitrile positions investigated, Ac1, Ac2, Ac3 and Ac4. Whilst these positions may seem symmetry related, introduction of Al breaks framework symmetry, yielding four discrete framework positions. Where: carbon (black), hydrogen (grey) and nitrogen (blue); the geometry of the framework is represented by an all-silicon structure.*

ΔE_{ads} between the acetonitrile probe and the framework was used as a quantitative measure of Brønsted acidity, where the most negative ΔE_{ads} indicates the highest Brønsted acidity. The calculated adsorption energies for each of the structures are shown in Figure 3.15. The most negative ΔE_{ads} for NL ordered frameworks are those with the acetonitrile probe in the Ac1 position, and those in the Ac1 and Ac4 positions for the Löwensteinian framework. The stability of the structures with probes in these positions is due to the ability of the nitrogen of the probe to bind more strongly with the acidic protons. This is reflected in the N-H bond distances, which are shorter in structures with more negative ΔE_{ads}. Furthermore, this indicates that the initial orientation and location of the probe has a significant impact on the overall stability of the framework+probe complex. Considering this, it is notable that this study was not exhaustive as only four probe positions were investigated. Given the influence of the probe's position on the resultant asorption energy it is possible that the structures with the most negative ΔE_{ads} were not captured in the simulations.

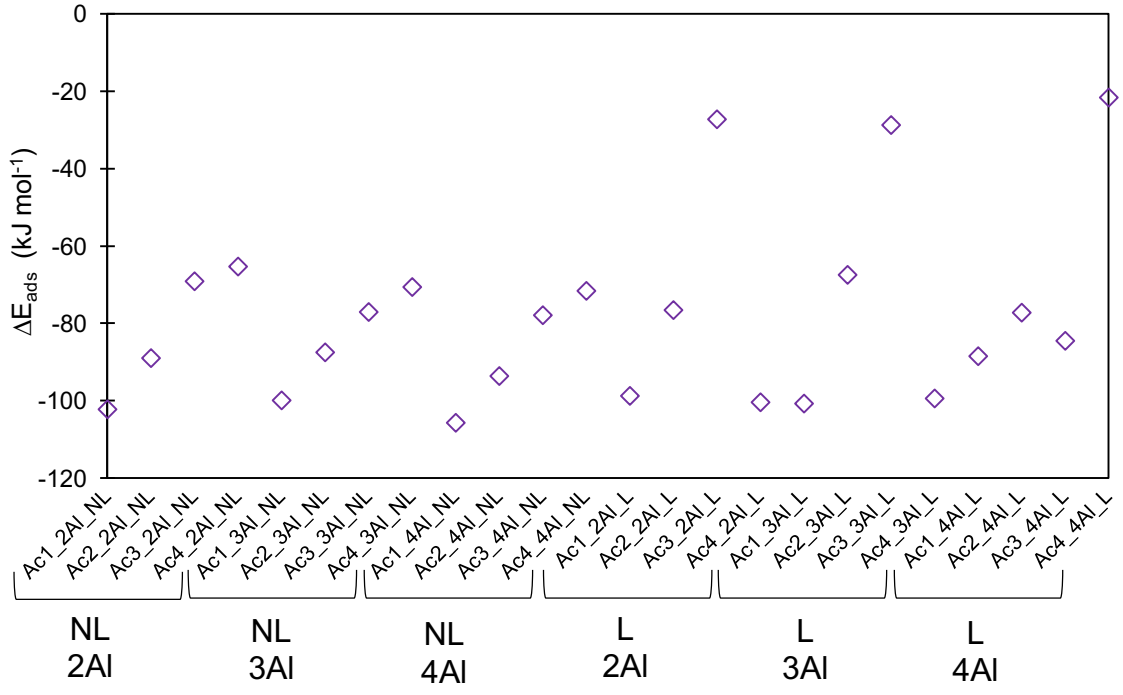

Figure 3.15 *ΔE_{ads} for each of the probe-containing structures. Where NL or L indicates whether the structure is non-Löwensteinian or Löwensteinian; 2Al, 3Al or 4Al is the number of Al atoms per unit cell; and Ac1-4 is the position of the acetonitrile probe within the framework.*

The Löwensteinian structures give the most positive ΔE_{ads}, this is to be expected as these structures are inherently less stable than the NL global minimum structures according to DFT. However, there is no other discernible correlation between Al content and binding energy, and across the three Si/Al ratios the ΔE_{ads} is almost consistent for frameworks in which the probe is in the same position. Despite what has been reported in the literature,[67–70] there is no apparent relationship between Al-Al separation and Brønsted acidity. In fact, contrary to what has been reported previously,[67–70] the NL frameworks with aluminium in the NN positions have slightly more negative ΔE_{ads}, and therefore slightly higher Brønsted acidities than those L frameworks with Al at the NNN position.

3.6 Characterising non-Löwensteinian ordering in zeolites

An intriguing question is whether the NL linkages predicted in this work are present in existing samples, and if so, what signatures could be used to unambiguously identify these -Al-O-Al- sequences. ^{29}Si MAS NMR shifts and vibrational frequencies were predicted for the global minimum NL and L H-SSZ-13 structures (Si/Al = 17) to discern whether spectroscopic signatures exist that would be indicative of the presence of non-Löwensteinian ordering. At a Si/Al ratio of 17, typical for SSZ-13, the predicted ^{29}Si NMR data shows that there is a slight decrease in the negativity of the chemical shift values for -Al-O-Al- containing frameworks. However, these shifts are well within the anticipated range for a zeolite at this Si/Al ratio, and far too similar to the chemical shifts of the surrounding Si atoms to be used practically as a characterisation method (further information is included in the Appendix). Similarly, predicted vibrational frequencies indicate that characteristic stretches would not be detectable due to overlap of Al–O(H)–Al stretches (3699·9 cm^{-1}) with that of Si–O(H)–Al (3665·6 cm^{-1}, 3696·1 cm^{-1} and 3699·4 cm^{-1}), and other broad stretches. Hence Al-O(H)-Al stretches would not be uniquely distinguishable using FT-IR.

To discern whether an acetonitrile probe molecule could be used experimentally to aid differentiation between NL and L ordered zeolite frameworks, CP2K was used to predict the vibrational frequencies and the FT-IR spectra of probe-containing structures with the lowest adsorption energies: Ac1_2Al_NL, Ac1_4Al_NL, Ac1_3Al_L, and Ac4_2Al_L. These structures gave adsorption energies within 5 kJ mol^{-1} of one another. The predicted IR spectra for these structures are included in the Appendix.

The O-H stretching frequencies are slightly red-shifted in structures containing NL clusters of four Al atoms, compared to NL structures with higher Si/Al ratios. However, there is considerable overlap between the red-shifted Al-O(H)-Al stretching frequencies and Si-O(H)-Al frequencies predicted for L ordered structures. Furthermore, a discernible difference in the vibrational frequencies between the protons interacting with the acetonitrile probe compared to the frequencies predicted for the same frameworks in which the probe was omitted was found, the O-H stretching frequencies for protons interacting with the probe are also red-shifted. For example, the stretching frequency for Si-O(H)-Al proton, which is the proton interacting with the probe in Ac1_2Al_NL is 2353.2 cm^{-1} in the presence of the probe, and 2800.3 cm^{-1} in the probe-free framework. However, as this example illustrates, the data shows no preference for Al-O(H)-Al protons to interact with the probe over Si-O(H)-Al protons. Therefore, the use of an acetonitrile probe cannot be used to aid the characterisation Al-O(H)-Al linkages through FT-IR.

3.7 Conclusions

The work contained in this chapter provides evidence that it is thermodynamically favourable for Löwenstein's rule to be violated in protonated zeolite frameworks. All stable NL ordered frameworks contain adjacent Al^{3+} ions linked by a bridging hydroxyl moiety, this bridging hydroxyl stabilises the framework by maximising the number of long Al-OH linkages, hence minimising the number of short, strong and stable Si-O linkages present within the framework. Violations of Löwenstein's rule are preferred in a range of proton-containing frameworks with varying densities and ring systems, and it can be concluded that violations of Löwenstein's rule are preferred in higher density framework types. At lower Si/Al ratios, there is a preference for the formation of discrete aluminium clusters. Despite Al clustering, Brønsted acidity tests indicate no apparent decrease in Brønsted acidity in H-SSZ-13, contrary to much of the accepted wisdom in this area. However, the Brønsted acidity predictions were not exhaustive, and only considered a single probe molecule in four discrete framework positions. The data shows the initial orientation and location of the acetonitrile probe to have a significant influence on the resultant adsorption energy between the probe and the framework, it is therefore possible that the lowest adsorption energies have not been captured in this investigation, and further sampling would be necessary to make definitive conclusions. Furthermore, whilst acetonitrile has been used in similar computational studies[71], its proton affinity is much lower than that other basic probes, such as ammonia or pyridine.

A 2017 DFT study by Liu *et al.*[37] demonstrated that whilst different probes gave internally consistent orders of Brønsted acidity in FAU at a range of Si/Al ratios, there were significant differences in sensitivity between the probes due to differences in proton affinity. As this study was confined to differences between NN and NNN ordered structures, it is possible that a probe with a greater proton affinity and dimensions small enough to access the internal structure of the zeolite, such as ammonia, could provide a clearer picture of the relationship between Al distribution and Brønsted acidity.[37]

Such findings cannot be extended to sodium-containing zeolites, for which all the global minimum structures are Löwensteinian ordered frameworks. In structures with 2 Al per U.C. there is a preference for pairs of Al to exist as NNNN. The results demonstrate that the SII site is most favoured in SSZ-13 structures with low Na^+ content, and population of both SII and SIII cation sites becomes more favourable at higher concentrations of Na^+. This is in accordance with a recent combined ^{23}Na SS NMR and DFT study by Zhao *et al.*[54] The marked differences between the most thermodynamically stable aluminium distributions of protonated and sodium-containing zeolites demonstrate the influence of counter-cation identity on framework aluminium location, and *vice versa*. However, it is noteworthy that Dempsey's rule[8] is violated in the global minimum structures of all investigated frameworks. Given that real samples of SSZ-13 are typically synthesised from a sodium solution in the presence of an SDA, the most likely distribution of Al in these samples will be most similar to that predicted for Na-SSZ-13.

The direct synthesis of proton compensated zeolites has not yet been achieved, hence protonated zeolites tend to be generated through a two-step cation exchange process, as discussed in Chapter 1. In the case of SSZ-13, the initial Na-SSZ-13 form of the zeolite will contain Löwensteinian ordered Al, according to the predictions contained within this chapter. Assuming these alumina units are fixed throughout the exchange process, following the exchange, the predictions suggest that resultant H-SSZ-13 will contain alumina units in a thermodynamically unstable Löwensteinian arrangement. This structure can be considered kinetically stable, exhibiting a thermodynamically 'frustrated' framework Al distribution. Post-synthesis framework Al re-arrangement is a known phenomenon, and is typically initiated by steaming the zeolite. This has been demonstrated experimentally in two recent studies on ZSM-5 by Holzinger *et al.*[72] and Perea *et al.*[60] In the former study the authors demonstrated that following

dealumination by aggressive steam treatment, softer steam treatment (≤ 300˚C) of the dealuminated zeolite could 'heal' the framework. Suggesting that there is an activation barrier to Al re-inserting itself to the framework, and that this barrier can be easily overcome at moderate temperatures in the presence of water molecules.[72] Long-range redistribution of framework Al on steaming was also observed in the latter study.[60] It is therefore conceivable that more stable NL Al arrangements could be achieved through post-synthesis treatment of the exchanged protonated zeolite.

The formation of -Al-O-Al- might be facilitated *via* two post-synthetic methods. The first is to use water, which has been shown to facilitate the making and breaking of -Si-O-Si- and -Al-O-Si- in its liquid form,[73] as well as facilitating dealumination in its vapour form.[60,72] Long-term steeping of H-SSZ-13 in liquid water could be expected to lead to the redistribution of Al in the framework, yielding -Al-O-Al- as the thermodynamically preferred arrangement. Potentially, very slightly acidic or basic water might enhance the rate of rearrangement without dealumination or desilication of the zeolite framework. A second potential approach is "reverse-dealumination"; placing a zeolite crystal in a solution containing an excess of alumina units with the assumption that for high alumina zeolites, the aluminium content will rise, increasing the likelihood of alumina units situated adjacent to one another. Previously, this has been achieved in high-silica ZSM-5 through $AlCl_3$ vapour treatment, and in very low-silica zeolite Y using non-crystallisation inducing alkaline solutions (*e.g.* KOH) in the presence of large concentrations of extra-framework aluminium.[74,75]

If the proposed post-synthetic techniques or alternative synthesis strategies are successful in realising zeolites with NL framework aluminium distributions, as predicted by this work, these materials would be potentially invaluable for the development of new zeolite catalysts. Despite the advantages of using zeolites in catalysis, for example, specificity and size exclusion properties, it is well documented that the catalytic efficiency of microporous materials is often limited by restricted access to active sites. Introducing ordered, controllable meso- and macroporosity to the framework provides a solution to mass transport limited diffusion through the porous zeolite network. The introduction of hierarchy has also been shown not only enhance catalytic activity, but also stability in a range of zeolite frameworks. A variety of both bottom-up and top-down strategies have proved successful for hierarchically ordered zeolite synthesis. The post-synthetic introduction of mesoporosity by the extraction of

framework atoms is a particularly popular method, and can be achieved by acid, base or steam treatment of the zeolite material.[76,77] One can imagine how techniques such as these could be used to dealuminate low-silica aluminium cluster-containing materials, similar to those predicted in this work. For example, removing all four alumina units in the 4 Al per unit cell H-SSZ-13 global minimum structure predicted by DFT would increase the 7 Å, 8-ring aperture cavity system, with a void-space of approximately 10 Å in diameter, to up to 17 Å, approaching mesoporosity. Crucially, the calculations indicate that not only is aluminium clustered, but it is also located in predictable, ordered positions, which suggests that introduced porosity *via* selective dealumination could be controllable in H-zeolites.

The reaction mechanisms and deactivation pathways of real catalytic zeolite materials is relatively a poorly understood area of zeolite science, notwithstanding remarkable recent advances.[78,79] In part this is due to a lack of molecular-level information concerning the location of framework alumina and associated counter-cations, which are thought to be integral to the catalytic reaction mechanism. Clustering of aluminium and the associated clustered acid sites, as predicted by the DFT results, is suggestive of new active sites and new reaction pathways which have not yet been considered. Perea *et al.* have shown that the Si/Al distribution can be inhomogeneously distributed throughout the zeolite framework,[60] furthermore, silicon islanding (formation of silicon rich regions that must also give rise to aluminium rich areas) has been shown to be present in SSZ-13's silicoaluminophosphate counterpart SAPO-34.[80] Given this, and the fact that samples containing well-dispersed Al would be considerably frustrated, it is hence plausible that aluminium cluster motifs, including non-Löwensteinian linkages, already exist in real zeolite materials; generated through Al rearrangements facilitated by the high temperatures experienced by the zeolite during calcination and catalysis. Such clusters could impact both the reaction and deactivation pathways operating in real zeolite catalysts.

However, the predictions indicate that if such -Al-O-Al- linkages were to exist in real samples, characterisation of these linkages would be extremely difficult and despite recent advances in characterisation techniques, for example the use of atom probe tomography to evaluate the heterogeneity of Al distribution in zeolites,[60] at present, there is no direct method that can accurately distinguish framework aluminium from framework silicon with Ångström resolution. Although the predictions indicated that ^{29}Si

NMR would not be a suitable technique to differentiate between Al-O(H)-Al and Al-O(H)-Si linkages, there are reports in the literature that other NMR approaches could be capable of characterising Al-O-Al linkages. Firstly, a 2010 work by Shin *et al.*[81] concerning possible non-Löwensteinian structures observed in gallosilicates, discusses the possibility of using of ^{17}O magic angle spinning (MAS) NMR to detect non-Löwensteinian ordering, a method which has been successful in identifying -Al-O-Al- linkages in aluminosilicate glasses.[82] A 2D NMR approach could also prove useful in solving this problem, in a recent 2018 study, Dib *et al.*[83] used a combination of DFT and 2D ^{27}Si-^{29}Al NMR to investigate the preferential incorporation of Al into ZSM-5. The authors propose that this combined approach can precisely determine Al sites in zeolite frameworks.[83]

3.8 References

1. Alvarado-Swaisgood, A.E., Barr, M.K., Hay, P.J., Redondo, A. *J. Phys. Chem.* **95,** 10031–10036 (1991).
2. Chu, Z.K., Fu, G., Guo, W., Xu, X. *J. Phys. Chem. C* **115,** 14754–14761 (2011).
3. Ghorbanpour, A., Rimer, J.D., Grabow, L.C. *Catal. Commun.* **52,** 98–102 (2014).
4. Sklenak, S. Dědeček, J., Li, C., Wichterlová, B., Gábová, V., Sierka, M., Sauer, J. *Angew. Chemie Int. Ed.* **46,** 7286–7289 (2007).
5. Sklenak, S. Dědeček, J., Li, C., Wichterlová, B., Gábová, V., Sierka, M., Sauer, J. *Phys. Chem. Chem. Phys.* **11,** 1237–1247 (2009).
6. Brändle, M., Sauer, J., Dovesi, R., Harrison, N.M. *J. Chem. Phys.* **109,** 10379 (1998).
7. Fujita, H., Kanougi, T., Atoguchi, T. *Appl. Catal. A* **313,** 160–166 (2006).
8. Dempsey, E. *J. Catal.* 115–119 (1977).
9. Meeprasert, J., Jungsuttiwong, S., Namuangruk, S. *Microporous Mesoporous Mater.* **175,** 99–106 (2013).
10. Kim, C.W., Heo, N.H., Seff, K. *J. Phys. Chem. C* **115,** 24823–24838 (2011).
11. Brändle, M. & Sauer, J. *J. Am. Chem. Soc.* **120,** 1556–1570 (1998).
12. Lonsinger, S.R., Chakraborty, A.K., Theodorou, D.N., Bell, A.T. *Catal. Letters* **11,** 209–217 (1991).
13. Kustov, L.M., Kazanskii, V.B., Beran, S., Kubelkova, L., Jiru, P. *J. Phys. Chem.* **91,** 5247–5251 (1987).
14. Joshi, K.L., Psofogiannakis, G., van Duin, A.C.T., Raman, S. *Phys. Chem. Chem. Phys.* **16,** 18433–18441 (2014).
15. Kim, S. Evans, T.J., Mukarakate, C., Bu, L., Beckham, G.T., Nimlos, M.R.,

Paton, R.S., Robichaud, D.J. *ACS Sustain. Chem. Eng.* **4,** 2615–2623 (2016).

16. Charoenwiangnuea, P., Maihom, T., Kongpracha, P., Sirijaraensre, J., Limtrakul, J. *RSC Adv.* **6,** 105888–105894 (2016).
17. Knott, B. C. Nimlos, C.T., Robichaud, D.J., Nimlos, M.R., Kim, S., Gounder, R. *ACS Catalysis* **8,** 770–784 (2018).
18. Shah, R., Gale, J. D., Payne, M. C. *J. Phys. Chem.* **100,** 11688–11697 (1996).
19. Haase, F., Sauer, J., Hutter, J. *Chem. Phys. Lett.* **266,** 397–402 (1997).
20. Jeanvoine, Y., Ángyán, J. G., Kresse, G., Hafner, J. *J. Phys. Chem. B* **102,** 5573–5580 (1998).
21. Lo, C. & Trout, B. *J. Catal.* **227,** 77–89 (2004).
22. Smith, L. J., Davidson, A., Cheetham, A. K. *Catal. Letters* **49,** 143–146 (1997).
23. Calligaris, M., Nardin, G., Randaccio, L., Chiaramonti, P. C. *Acta Crystallogr. B Struct. Crystallogr. Cryst. Chem.* **38,** 602–605 (1982).
24. Andersen, C. W., Bremholm, M., Vennestrøm, P.N.R., Blichfeld, A.B., Lundegaard, L.F. *IUCrJ* **1,** 382–6 (2014).
25. Akporiaye, D.E., Dahl, I.M., Mostad, H.B., Wendelbo, R. *J. Phys. Chem.* **100,** 4148–4153 (1996).
26. Schroeder, K.P. & Sauer, J. *J. Phys. Chem.* **97,** 6579–6581 (1993).
27. Hass, C., Mezey, G., Plath, J. *J. Mol. Struct.* **76,** 389–399 (1981).
28. Loewenstein, W. *Am. Mineral.* **39,** 92–96 (1954).
29. Ruiz-Salvador, A.R., Grau-Crespo, R., Gray, A.E., Lewis, D.W. *J. Solid State Chem.* **198,** 330–336 (2013).
30. Xing, B., Ma, J., Li, R., Jiao, H. *Catal. Sci. Technol.* **7,** 5694–5708 (2017).
31. Thayaparam, S., Dove, M.T., Heine, V. *Phys. Chem. Miner.* **21,** 110–116 (1994).
32. Dove, M.T. & Heine, V. *Am. Mineral.* **81,** 39–44 (1996).
33. Dove, M.T., Thayaparam, S., Heine, V., Hammonds, K.D. *Am. Mineral.* **81,** 349–362 (1996).
34. Zokaie, M., Olsbye, U., Lillerud, K.P., Swang, O. *Microporous Mesoporous Mater.* **158,** 175–179 (2012).
35. Baerlocher, C., McCusker, L., Olson, D.H. *Atlas of Zeolite Framework Types* (2007).
36. Borges, P., Ramos Pinto, R., Lemos, M.A.N.D.A., Lemos, F., Védrine, J.C., Derouane, E.G., Ramôa Ribeiro, F. *J. Mol. Catal. A Chem.* **229,** 127–135 (2005).
37. Liu, C., Tranca, I., Van Santen, R. A., Hensen, E.J.M., Pidko, E.A. *J. Phys. Chem. C* **121,** 23520–23530 (2017).
38. CP2K Available at: https://www.cp2k.org/
39. VandeVondele, J.J., Krack, M., Mohamed, F., Parrinello, M., Chassaing, T.,

Hutter, J. *Comput. Phys. Commun.* **167,** 103–128 (2005)

40. VandeVondele, J. & Hutter, J. *J. Chem. Phys.* **127,** 114105 (2007).
41. Clark, S.J., Segall, M. D., Pickard, C.J., Hasnip, P.J., Probert, M.J., Refson, K., Payne, M.C. *Zeitschrift fuer Krist.* **220,** 567–570 (2005).
42. Perdew, J.P., Burke, K., Ernzerhof, M. *Phys. Rev. Lett.* **78,** 1396–1396 (1997).
43. Zhang, Y. & Yang, W. *Phys. Rev. Lett.* **80,** 890–890 (1998).
44. Becke, A.D. *Phys. Rev. A* **38,** 3098–3100 (1988).
45. Lee, C., Yang, W., Parr, R.G. *Phys. Rev. B* **37,** 785–789 (1988).
46. Lee, K., Murray, É.D., Kong, L., Lundqvist, B.I., Langreth, D.C. *Phys. Rev. B - Condens. Matter Mater. Phys.* **82,** (2010).
47. Grimme, S., Antony, J., Ehrlich, S., Krieg, H. *J. Chem. Phys.* **132,** 154104 (2010).
48. Guidon, M., Hutter, J., VandeVondele, J. *J. Chem. Theory Comput.* **6,** 2348–2364 (2010).
49. Adamo, C. & Barone, V. *J. Chem. Phys.* **110,** 6158 (1999).
50. Fletcher, R.E., Ling, S., Slater, B. *Chem. Sci.* **8,** 7483–7491 (2017).
51. Baerlocher, C., Hepp, A., Meier, W. *DLS-76 : a program for the simulation of crystal structures by geometric refinement* (Zürich : Institute of crystallography and petrography, 1978).
52. International Zeolite Association *Zeolite Synthesis Directory* (2001)
53. Dempsey, E., Kuehl, G.H., Olson, D.H. *J. Phys. Chem.* **73,** 387–390 (1969).
54. Zhao, Z., Xing, Y., Li, Shihan., M, Xiangju., X, F-S., McGuire, R., Parvulescu, A-N., Müller, U., Zhang, W. *J. Phys. Chem. C* **122,** 9973–9979 (2018).
55. Smith, L.J., Eckert, H., Cheetham, A.K. *J. Am. Chem. Soc.* **122,** 1700–1708 (2000).
56. Smith, L.J., Eckert, H., Cheetham, A.K. *Chem. Mater.* **13,** 385–391 (2001).
57. Civalleri, B., Ferrari, A.M., Llunell, M., Orlando, R., Mérawa, M., Ugliengo, P. *Chem. Mater.* **15,** 3996–4004 (2003).
58. Fischer, M., Delgado, M.R., Areán, C.O., Duran, C.O. *Theor. Chem. Acc.* **134,** 1–18 (2015).
59. Gillan, M.J., Alfè, D., Michaelides, A. *J. Chem. Phys.* **144,** 130901 (2016).
60. Perea, D.E. Arslan, I., Liu, J., Ristanović, Z., Kovarik, L., Arey, B.W., Lercher, J.A., Bare, S.R., Weckhuysen, B.M. *Nat. Commun.* **6**, 7589 (2015).
61. Schmidt, J.E. Poplawsky, J.D., Mazumder, B., Attila, Ö., Fu, D., DeWinter, D.A.M., Meirer, F., Bare, S.R., Weckhuysen, B.M. *Angew. Chemie Int. Ed.* **55**,11173–11177 (2016).
62. Leonard, R.S. *US 4066394 A: Reusable zeolite water softener for clothes*

washing (1974).

63. Rieck, H.-P. *US 4664839 A: Use of crystalline layered sodium silicates for softening water and a process for softening water* (1985).
64. Abrams, L., Corbin, D.R. & Shannon, R. *US 4814503: Zeolite rho and ZK-5 catalysts for conversion of methanol and ammonia to dimethylamine* (1989)
65. Vermeiren, W. & Gilson, J. P. *Top. Catal.* **52,** 1131–1161 (2009).
66. Pavón, E., Osuna, F.J., Alba, M.D, Delevoye, L. *Chem. Commun.* **50,** 6984–6986 (2014).
67. He, M., Zhang, J., Liu, R., Sun, X. & Chen, B. *Catalysts* **7,** 11 (2017).
68. Zhao, R., Zhao, Z., Li, S., Zhang, W. *J. Phys. Chem. Lett.* **8,** 2323–2327 (2017).
69. Li, S., Zhao, Z., Zhao, R., Zhou, D., Zhang, W. *ChemCatChem* **9,** 1494–1502 (2017).
70. Zhao, G. Teng, J., Zhang, Y., Xie, Z., Yue, Y., Chen, Q., Tang, Y. *Appl. Catal. A Gen.* **299,** 167–174 (2006).
71. Simperler, A., Bell, R.G., Foster, M.D., Gray, A.E., Lewis, D.W., Anderson, M.W. *J. Phys. Chem. B* **108,** 7152–7161 (2004).
72. Holzinger, J., Beato, P., Lundegaard, L.F., Skibsted, J. *J. Phys. Chem. C* **122,** 15595–15613 (2018).
73. von Ballmoos, R. & Meier, W.M. *J. Phys. Chem.* **86,** 2698–2700 (1982).
74. Liu, X., Klinowski, J., Thomas, J.M. *J. Chem. Soc., Chem. Commun.* (1986).
75. Bezman, R.D. *J. Chem. Soc., Chem. Commun.* **Com. 606,** 1562–1563 (1987).
76. Verboekend, D. & Pérez-Ramírez, J. *Catal. Sci. Technol.* **1,** 879–890 (2011).
77. Möller, K. & Bein, T. *Science* **333,** 297 (2011).
78. de Smit, E. Swart, I., Creemer, J.F., Hoveling, G.H., Gilles, M.K., Tyliszczak, T., Kooyman, P.J., Zandbergen, H.W., Morin, C., Weckhuysen, B.M., de Groot, F.M.F. *Nature* **456,** 222–225 (2008).
79. Buurmans, I.L.C. & Weckhuysen, B.M. *Nat. Chem.* **4,** 873–886 (2012).
80. Sastre, G., Lewis, D.W., Catlow, C.R.A. *J. Phys. Chem. B* **101,** 5249–5262 (1997).
81. Shin, J., Kim, S.H., Camblor, M.A., Warrender, S.J., Miller, S.R., Zhou, W., Wright, P.A., Hong, S.B. *Dalt. Trans.* **39,** 2246–2253 (2010).
82. Stebbins, J.F., Lee, S.K., Oglesby, J.V. *Am. Mineral.* **84,** 983–986 (1999).
83. Dib, E., Mineva, T., Veron, E., Sarou-Kanian, V., Fayon, F., Alonso, B. *J. Phys. Chem. Lett.* **9,** 19–24 (2018).

Chapter 4: Surface Segregation of Aluminium

4.1 Overview

Chapter 3 focused on the short-range ordering of Al over framework T-sites in the bulk. In this chapter, long-range Al distribution throughout the zeolite crystal is explored, specifically, the thermodynamic driving force for bulk to surface and surface to bulk Al migration.

The long-range heterogeneous distribution of Al through a zeolite crystal has been well known for many years[1,2] and is often referred to as 'Al zoning'. Due to the impact that 'zoned' Al has on the accessibility and availability of catalytic active sites, there have been a number of studies concerned with understanding the non-uniform distribution of Al throughout a crystal and the factors that govern it.[3]

Al zoning has been most investigated in ZSM-5 (MFI);[1,2,4–10] there are very few studies dedicated to understanding Al distribution at the surface and in the bulk of other zeolites. The first study on ZSM-5 was conducted by von Ballmoos and Meier in 1981.[1] Using electron microprobe analysis, the pair reported a clear surface enrichment of Al in 40 large (60 to 100 μm) ZSM-5 crystal samples (with Si/Al ratios ranging from 50 to 100. In these samples, the surface of the crystal contained more than 10 times as much Al than the silica-rich core, and all Al zoning was symmetric.[1] The same behaviour was also reported in the same year by Derouane *et al.*,[2] who observed large ZSM-5 crystals (greater than 5μm) to contain a Si-rich core (Si/Al > 95) and an Al-rich crust (Si/Al = 15). A later study by Chao *et al.*[4] also confirmed this result, concluding that enrichment of Al at the rim of the crystal is due to the crystallisation mechanism of ZSM-5. During ZSM-5 synthesis, an Al-rich gel is initially formed at the bottom of the reactor, when most of the alumina is fixed in the gel, the MFI framework nucleates from the Si-rich solution. Al is then released from the gel and increasingly incorporated into the MFI framework at a later stage.[4]

It should be noted that a tetrapropylammonium (TPA) ion template was used in the synthesis of all the aforementioned studies. It is postulated that the observed results are due to the preferential interaction of TPA with silica species in basic media, causing the initial incorporation of these species into the growing ZSM-5 crystal. Synthesis with a different template, or entirely template-free synthesis, can lead to completely

homogeneous distributions of Al throughout the crystal.[5] In a template-free system, the counter-cations are assumed to be the templating species, these cations interact more strongly with the alumina species leading to more uniform Al distributions.

However, there are several contradictory studies, in which TPA-synthesised ZSM-5 samples are reported to have entirely homogeneous Al distributions[7,8] with some studies reporting that it is possible to use TPA to synthesise ZSM-5 with an alumina-depleted surface and a silica-rich rim.[6,9] Derouane *et al.* reported small ZSM-5 crystallites (0·1 – 0·5 μm) with Si/Al ratios of 35 – 40 to exhibit either well-distributed Al or a Si enriched crust.[2] It is therefore clear that Al zoning is dependent on a range of factors in ZSM-5, including Si/Al ratio, crystal size, synthesis conditions (including sources of reagents and concentration of Al in the reactant mixture) and the technique by which the Al distribution is examined and characterised.[3] Furthermore, post-synthesis treatment of the zeolite has also been shown to influence the distribution of Al throughout a zeolite. A recent work by Perea *et al.*[10] used atom probe tomography (APT) to demonstrate that on steaming ZSM-5 there is a long-range heterogeneous redistribution of framework Al forming Al clusters at grain boundaries. As-synthesised zeolites are filled with water molecules and are routinely calcined to high temperatures prior to analysis, it is therefore conceivable that all the examples of zoning discussed are a result of post-synthesis Al redistribution due to steaming arising from the calcination process.

Aluminium zoning also appears to be dependent on the given zeolite framework type. For example, early studies concerning zeolite Beta (BEA) and zeolite X (FAU) indicate that these zeolites contain heterogeneous Al distributions in contrast to what is generally observed in ZSM-5, *i.e.* an Si-rich surface and an Al-rich core.[11,12] For zeolite X it has been postulated that this is due to the fact that alumina is the limiting reagent during zeolite synthesis.[12] Conversely, a handful of studies have shown that Al distributions in zeolite X, along with zeolites A (LTA), Y (FAU) and ZSM-5 (MFI) are entirely homogeneous.[7,13,14] Whereas, an early theoretical study by Corma *et al.*[15] indicated that the surface of zeolite Y crystals are likely to be enriched with aluminium. An XPS study concerned with the influence of the conditions of dealumination on the surface Al enrichment of Y by Kubelková *et al.*[16] suggested that this surface enrichment may be due to extra-framework aluminium. Furthermore, a more recent XPS study by Bare *et al.*[17] demonstrated Al zoning in zeolite Y to be strongly influenced by the post-

synthesis treatment of the zeolite, reporting the surface of as-synthesised Na-Y to be considerably Si-rich, compared to the surfaces of calcined and ammonium exchanged samples. It is plausible that this is caused by heterogeneous aluminium redistributions as described by Perea *et al.,*[10] which arise due to inadvertent steaming.

There have been only a few attempts to simulate the surfaces of zeolite crystal using periodic density functional theory, this is largely due to the computational expense associated with modelling the zeolite slab. The most comprehensive *ab initio* work has been carried out by Bučko *et al.*, who used periodic DFT to model the (011) surface of mordenite (MOR).[18–20] However, these studies are predominantly concerned with discerning qualitative differences between the acid sites at the external surface of mordenite in its fully siliceous and aluminium-containing state, and those in the bulk of the zeolite. These studies are not concerned with aluminium distribution throughout the slab specifically. However, the authors did conclude that Brønsted acidic sites are more stable approaching the surface of the aluminosilicate slab than they are in the bulk, and that there is a destabilisation associated with Si → Al + H substitutions at the external surface compared to the bulk.[18]

Rey *et al.*[21] recently published an extensive study concerned with modelling the external surface structure of zeolite Beta (BEA). The authors examined the external surface of the type A polymorph of zeolite Beta, cleaving the bulk structure at two different heights yielding two different external surfaces with distinct terminating structures. They conclude that Si-O(H)-Al linkages exist at the “open micropores” of the surface, whereas, water molecules adsorbed to Q3 aluminium, Al-(H_2O), exist at the outermost surface of the zeolite.[21] However, whilst this work provides substantial insight into the external surface of zeolites, like the work of Bučko and co-workers, [18–20] it does not address the long-standing questions surrounding the long-range heterogeneous distribution of Al across the surface and the bulk of zeolite crystals.

Although there is a large amount of conflicting information concerning the long-range distribution of Al throughout zeolite crystals, there is a substantial body of literature that indicates there to be a discernible difference between the external surface of the crystal and the zeolite bulk. Understanding these differences is crucial to the catalytic performance of zeolite structures, particularly to the catalytic processes associated with petroleum refining, for example gasoil cracking, which involves large molecules

whose dimensions are often too large to enter the zeolite micropore system. It has hence been rationalised that the initial stages of these processes are catalysed by active sites approaching the external surface of the zeolite crystal, and internal acidity has little to no impact on catalysis.[15,22] The role of the external surface becomes more important in smaller crystallites, which also play a crucial role in the petrochemical industry, this is due to an increased surface-area-to-volume ratio in these crystals compared to larger ones.[23] This also applies to 2D zeolites and zeolite thin films, which are becoming an area of intense interest within the zeolite community.[24–27] It is also noteworthy that surface enrichment of Al, as described in many of the papers concerning ZSM-5, has an effect of the hydrophobicity of the zeolite crystal. Zeolite crystals with Al-rich surfaces and Al-depleted cores will be relatively hydrophobic compared to crystals in which Al is homogeneously dispersed, due to the hydrophobicity of the Si-rich core.[28] Crystals containing zoned Al will display a gradient of hydrophobicity, which may lead to unequal distributions of reagents, products and intermediate transition state species throughout the crystal. Whereas, crystals containing well dispersed Al will have more uniform properties and presumably catalytic behaviours.

The work contained within this chapter is concerned with the use of periodic DFT to study Al-zoning in SSZ-13 (CHA). The purpose of the modelling described herein is to examine whether there is a thermodynamic driving force for Al to be at the surface and if there is, establish the strength of this driving force. To my knowledge this is the first theoretical study dedicated to understanding Al distribution at the surface and in the bulk of in a system containing more than one Al atom, it is also the first study to model Al zoning in SSZ-13. Building on the work containing within Chapter 3, the (001) and (011) surfaces of both H-SSZ-13 and Na-SSZ-13 at a range of Si/Al ratios are examined. The potential implications of the results are discussed in terms of Al zoning in real zeolite samples, specifically in catalysts.

4.2 Approach

Periodic DFT was employed to evaluate surface segregation of Al in SSZ-13. To simulate the surface of the SSZ-13 crystal, a range of CHA slab structures were created through cleavage of the bulk zeolite framework. In previous surface studies, it has been established that that cleaving the least number of T-O bonds in a zeolite slab yields the most stable crystal surface,[29–32] hence two different surfaces were examined,

the (001) and (011), the generation of which involved the equivalent cleavage six T-O bonds at each of the two faces of the crystal. Under synthesis conditions, under-coordinated silicon is presumed to interact with water, which dissociates at the surface giving rise to silanols. Hence both surface structures were terminated by silanol groups.

The (001) face is the most morphologically important CHA surface, hence the (001) terminating slab is the focus of this work. Each of the (001) terminating slabs with varying Si/Al ratios and Al distributions were created from an initial all-silica hexagonal slab structure with an optimised geometry of ***a,b*** = 13·77 Å and ***c*** = 44·69 Å, where ***c*** includes vacuum space above and below the zeolite slab to break periodicity, the actual length of the zeolite slab, measured from proton to proton, is 31·51 Å. The (001) terminating slab is composed of two CHA 'layers', hence the number of permutations of 1, 2 and 3 Al per slab is considerably larger than when considering a single CHA unit cell. To reduce the number of configurations in order to consider a tractable number of models, Al motifs contained within low energy single unit cell structures, determined in Chapter 3, were permuted along the ***c*** parameter of the slab, allowing effect of surface migration of Al on the stability of the zeolite to be investigated.

For the 1 Al per (001) terminating slab (Si/Al = 71), Al was permuted along the ***c*** parameter of the slab at eight distinct distances from the surfaces. For each Al substitution, a single proton or an Na^+ cation was introduced to the framework. As in Chapter 3, the protons were covalently bound to each of the four oxygen sites of the alumina tetrahedra and sodium cations were positioned in cavity spaces near to the location of Al, in either the SII or SIII position.

For the 2 Al per (001) terminating slab (Si/Al = 35), both non-Löwensteinan (NL) and Löwensteinan (L) ordered structures were considered, using the NL and L global minimum (GM) 1 Al per U.C. structures from Chapter 3 as 'guideline' structures. For the NL H-SSZ-13 slab, the Si-O(H)-Al-O(H)-Al atom chain from the 1 Al per unit cell NL GM structure was permuted throughout the zeolite slab, creating seven distinct NL ordered slab structures. For the L case, the Al-O(H)-Si-O-Al-O(H) atom chain from the 1 Al per unit cell L GM structure was permuted throughout the slab in the same way, creating a further seven distinct slab structures. The same methodology was employed for the Na-SSZ-13 slab at this Si/Al ratio, however in this case motifs were taken from

the L and NL global minimum Na-SSZ-13 2 Al per unit cell structures, which differ from those observed for H-SSZ-13 at a Si/Al ratio of 17.

The 3 Al per (001) terminating slab (Si/Al = 23) was created in a similar way. Here, NL and L motifs from the entirely NL and L 3 Al per U.C. global minimum H-SSZ-13 structures (Chapter 3) were reproduced and permuted along the ***c*** parameter of the slab. The sodium form of the zeolite was not investigated at this Si/Al ratio.

The same approach was applied to the (011) terminating slab. All structures created for the (011) terminating slab were made from an initial all-silica triclinic slab structure with an optimised cell geometry of ***a*** = 13·77 Å, ***b*** = 20·28 Å and ***c*** = 40·00 Å, where $\alpha = 90^{\circ}$, $\beta = 90^{\circ}$ and $\gamma = 110^{\circ}$. Only 1 Al and 2 Al containing slabs, with Si/Al ratios of 109 and 54, respectively, were considered for the (011) terminating structures.

All the structures investigated within this chapter, with both (001) and (011) terminating surfaces, were geometry optimised using CP2K at the PBE level of theory using a TZV2P basis. In these geometry optimisations, all atomic coordinates were allowed to change within fixed cell parameters.[†] *Ab initio* MD calculations were performed on geometry optimised structures using CP2K. The AIMD simulations were run using a 1 fs timestep, in the NVT ensemble at 433 K, the synthesis temperature for SSZ-13.[33–35]

4.3 Surface segregation of aluminium

4.3.1 The (001) terminating surface

4.3.1.1 H-SSZ-13

The initial investigation was concerned with the (001) terminated slab at a Si/Al ratio of 71, equivalent to 1 Al per slab. 32 H-SSZ-13 slab models were created as described in the previous section. These models contained aluminium atoms at eight distinct distances from the hydroxyl-terminating surface. Structures containing Al in the bulk of the zeolite are referred to as ‘bulk Q4’ structures, those containing Al at the surface of the zeolite are referred to as ‘surface Q3’ structures. Each of the 32 models were geometry optimised using DFT at the level of theory described in the approach section.

[†] It should be noted that the fixed cell parameters were based on idealised unit cell parameters for the all-silica form of CHA. Al invariably causes lattice expansion, whilst cell parameters remain constrained in these calculations, the cell is large enough to alleviate much of the strain associated with the introduction of Al.

The results (Figure 4.1) show that there is a preference for Q4 Al to be located below the external surface of the zeolite in the lower 6-ring of the terminating D6R, 4·3 Å from the terminating hydroxyls at the surface of the zeolite (Figure 4.2a). The minimum energy penalty for moving subsurface Q4 Al into the bulk of the zeolite (14 Å from the terminating hydroxyls), $\Delta E(E_{bulk} - E_{GM})$ is +7·4 kJ mol^{-1}, approximately 3 *k*T at room temperature and 2 *k*T at typical synthesis temperature, where *k* is the Boltzmann constant. The energy penalty for moving the subsurface Q4 Al to the external surface forming Q3 Al, $\Delta E(E_{surface} - E_{GM})$, is +4·1 kJ mol^{-1}, approximately 1·5 *k*T at standard temperature and 1 *k*T at typical synthesis temperature. It is therefore theoretically more favourable for subsurface Q4 Al to move to the external surface forming surface Q3, than into the bulk of the zeolite crystal in H-SSZ-13 at this Si/Al ratio.

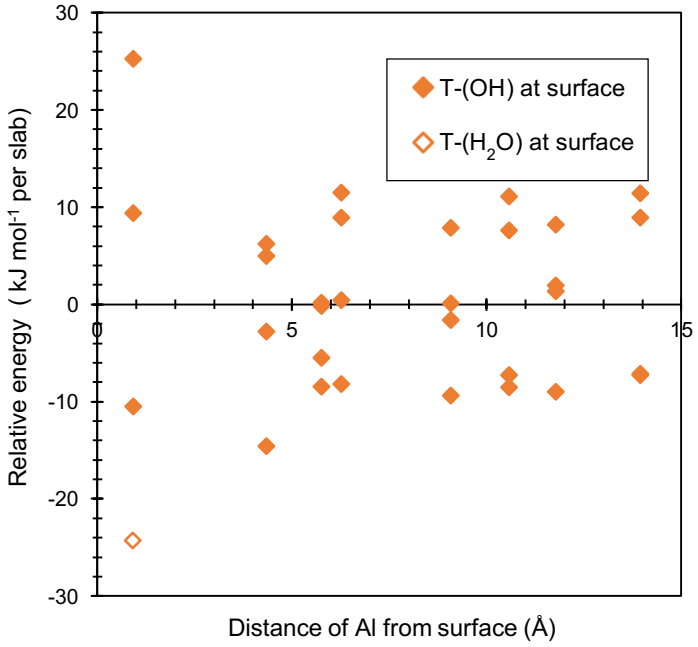

Figure 4.1 *Relative energy distribution (kJ mol^{-1} per slab) against the distance of Al from the surface of the slab (measured as the distance of Al from the terminating OH groups) for H-SSZ-13 (001) terminating slab with a Si/Al ratio of 75, equivalent to 1 Al per slab. Filled in points indicate models in which dangling bonds are satisfied by hydroxyls, the unfilled point denotes the surface model in which the Brønsted acidic proton has migrated to a terminating hydroxyl, forming water at the surface.*

Rey *et al.*[21] demonstrated that the most stable external surface structures in zeolite Beta (BEA) contain water molecules adsorbed to Q3 aluminium, forming Al-(H_2O). To investigate whether the same is true for CHA, the lowest energy surface Q3 model (where the Al is 0·9 Å from the terminating hydroxyls) was reoptimised. In the reoptimised model, the Brønsted acidic proton positioned at one of the four oxygen sites of the surface alumina was migrated to a terminating hydroxyl, forming Q3 Al-(H_2O). In line with what was reported by Rey *et al.*[21], there is a stabilisation energy associated with the migration of the proton to form water at the surface, $\Delta E(E_{Q3Al\text{-}H_2O} - E_{Q3Al\text{-}OH})$ -13·8 kJ mol^{-1}, yielding a new surface Q3 global minimum structure (Figure 4.2b) which is 9·7 kJ mol^{-1} more stable than the original subsurface Q4 global minimum. The total segregation energy, *i.e.* the energy of migrating Al from the lowest energy Q4 bulk position to the lowest energy Q3 surface position, $\Delta E(E_{Q3} - E_{Q4})$ is -11·7 kJ mol^{-1}.

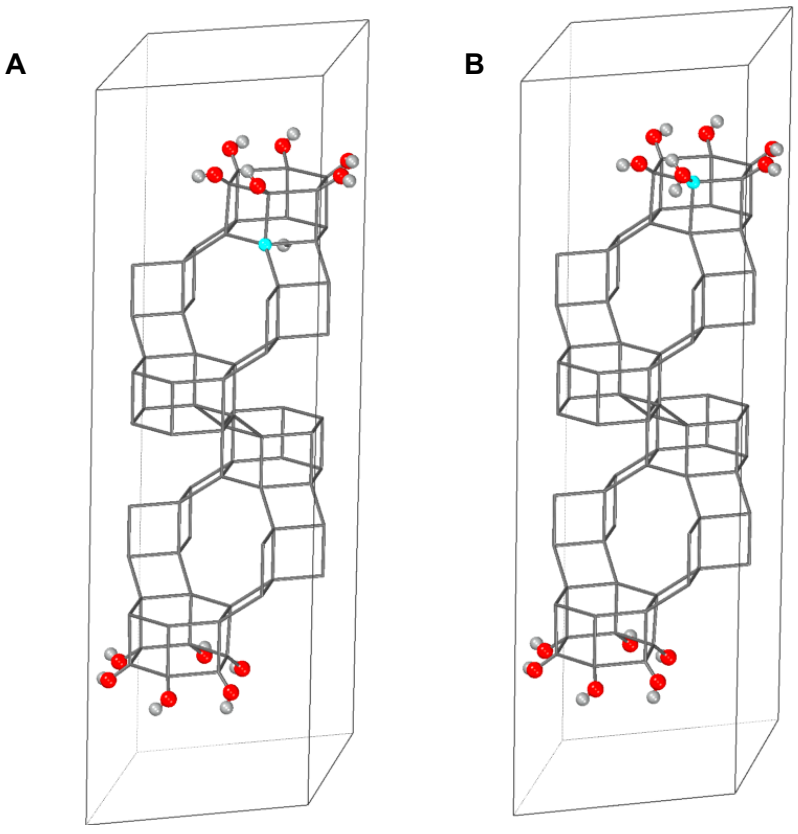

Figure 4.2 *Global minimum structures for the H-SSZ-13 (001) terminating slab with a Si/Al ratio of 75, where* ***a)*** *the surfaces are terminated by hydroxyls, yielding a subsurface Q4 structure and* ***b)*** *the acidic proton has migrated to a terminating hydroxyl, forming water, yielding a surface Q3 structure. The latter structure is the most stable structure at 0 K.*

The stabilisation associated with forming water at the surface could be due to several factors. The addition of another hydrogen atom to the terminating hydroxyl groups of the surface has the potential to increase the number of hydrogen bonds in the hydrogen bonding network, and facilitate the reorientation of hydroxyls improving existing hydrogen bonding interactions. In addition, the formation of uncharged water alleviates repulsions between Q3 Al^{3+}, which formally exhibit a single negative charge with respect to Si^{4+}, and OH^- at the surface.

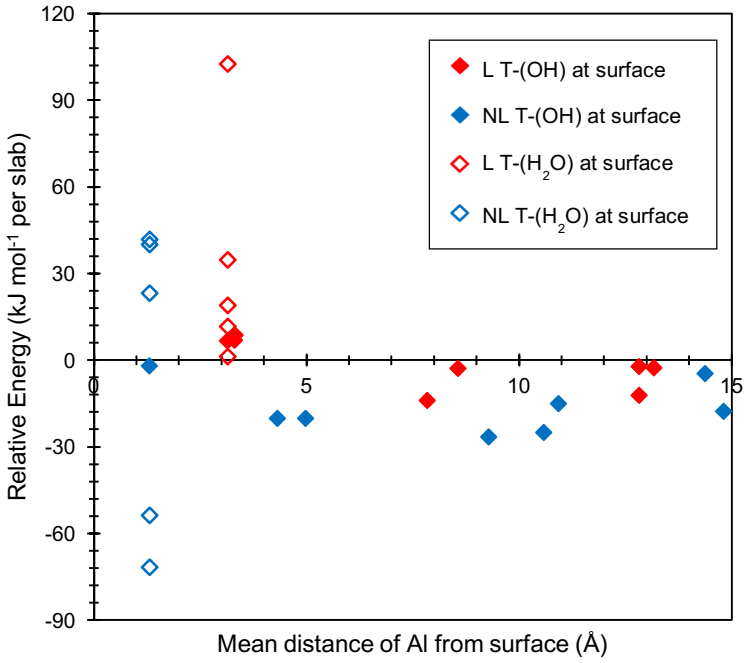

Figure 4.3 *Relative energy distribution (kJ mol^{-1} per slab) against the mean distance of Al from the surface of the slab (measured as the distance of Al from the terminating OH groups) for H-SSZ-13 (001) terminating slab with a Si/Al ratio of 35, equivalent to 2 Al per slab. Where; filled in points indicate models in which dangling bonds are satisfied by hydroxyls; unfilled points indicate the surface models in which the Brønsted acidic protons have migrated to a terminating hydroxyl, forming water at the surface; NL ordered frameworks (blue); and L ordered frameworks (red).*

Having established that there is a thermodynamic preference for the formation of Q3 Al structures, 2 Al per slab structures were then examined to establish whether there is a thermodynamic preference for non-Löwensteinian (NL) motifs to exist at the

surface, over Löwensteinian (L) motifs. As explained in the Approach section, the 2 Al per unit cell H-SSZ-13 NL and L global minimum structures reported in Chapter 3 were used as guideline structures for the generation of 2 Al per slab models (Si/Al ratio = 35), permuting the NL Si-O(H)-Al-O(H)-Al motif and the L Al-O(H)-Si-O-Al-O(H) motif, contained within the guideline global minima structures, along the ***c*** parameter of the H-SSZ-13 slab.

The results for these simulations are shown in Figure 4.3, where relative energy is plotted against the mean distance of Al from the surface. The mean distance is used as these structures contain two Al^{3+} ions. The results show NL structures to be generally more stable than L structures, this is in line with previous findings concerning H-SSZ-13 (Chapter 3). Both NL and L global minimum structures, for slab models in which all terminating T-atoms are satisfied by hydroxyls, are Q4 bulk structures. The global minimum NL structure contains Al at a mean distance of 9·2 Å from the external surface and the L structure contains Al at a mean distance of 7·3 Å. The minimum energy penalties for forming structures with Al in the centre of the bulk $\Delta E(E_{bulk} - E_{GM})$ are +9·1 kJ mol^{-1} and +1·9 kJ mol^{-1} for NL and L, respectively. The minimum energy penalties for forming structures with Al at the external surface, surface Q3 structures, $\Delta E(E_{surface} - E_{GM})$ are +24·7 kJ mol^{-1} and +15·2 kJ mol^{-1}, for NL and L respectively. For both NL and L ordered zeolites, it is hence more favourable for Q4 Al to move deeper into the bulk of the zeolite than to form Q3 Al at the surface.

To test whether the stabilisation energy observed on the formation of Q3 Al-H_2O at the surface applies to slabs with a higher Al content, the proton migration simulations for the 1 Al per slab were replicated using NL and L structures with Al at the surface. It should be noted that NL and L surface structures contain Al atoms at different mean distances from the surface, this is because the NL structure contains two surface Q3 Al and the L structure contains one surface Q3 Al and one subsurface Q4 Al. Hence the mean distance from the surface is larger for L than NL. L structures containing two Q3 Al atoms were not examined.

The two Brønsted acidic protons were migrated to nearby terminating hydroxyls individually, forming a single Q3 T-H_2O and maintaining the position of one of the acidic protons in each case. In keeping with previous findings, there is a stabilisation energy associated with forming water at the surface of the zeolite. However this stabilisation

energy, is far greater for the NL-ordered structure than the L-ordered structure, $\Delta E(E_{Al\text{-}H_2O} - E_{Al\text{-}OH})$ is -69·6 kJ mol^{-1} and -10·6 kJ mol^{-1} for NL and L, respectively. Only in the NL case is the stabilisation associated with formation of Q3 Al-H_2O great enough to create a new global minimum structure containing Al at the external surface of the zeolite, Figure 4.4b. The total segregation energy for the 2 Al slab structure, $\Delta E(E_{Q3} - E_{Q4})$ is -44·9 kJ mol^{-1}.

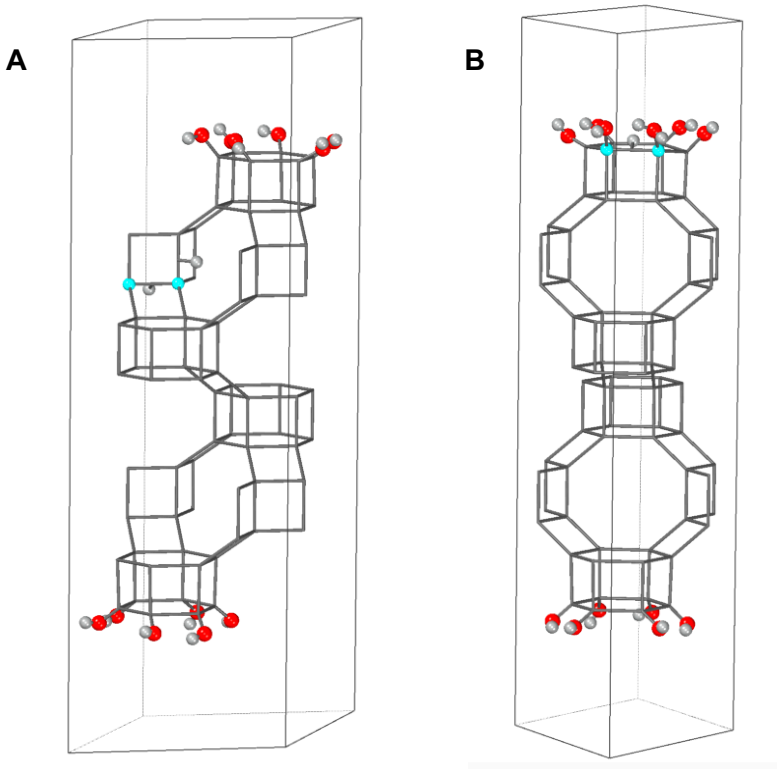

Figure 4.4 *Global minimum structures for the H-SSZ-13 (001) terminating slab with a Si/Al ratio of 35, where* ***a)*** *the surfaces are terminated by hydroxyls, yielding a bulk Q4 structure and* ***b)*** *the acidic proton has migrated to a terminating hydroxyl, forming water, yielding a surface Q3 structure. The latter structure is the most stable structure at 0 K.*

It is noteworthy that there is not a stabilisation energy associated with the formation of Q3 Al-H_2O in all cases. For NL structures, there is only a destabilisation energy associated with the migration of the proton at the oxygen site mediating the two linked aluminium atoms, Al-O(H)-Al. As demonstrated in Chapter 3, this proton is necessary to screen the negative charges on the adjacent alumina tetrahedra from one another,

which is the driving force for non-Löwensteinian ordering. Furthermore, in the L-ordered structure, there is only a stabilisation energy associated with the migration of a Brønsted acidic proton from the surface Al, forming Q3 Al-H_2O, the migration of the proton associated with the Al further in the bulk and the formation of Q3 Si-H_2O are extremely unfavourable processes ($\Delta E(E_{Al\text{-}H_2O} - E_{Al\text{-}OH})$ = +17·9 kJ mol^{-1} and +33·5 kJ mol^{-1}).

The stabilisation energy, $\Delta E(E_{Al\text{-}H_2O} - E_{Al\text{-}OH})$, for the NL-ordered 2 Al per slab structure (-69·6 kJ mol^{-1}) is much larger than both the L-ordered structure (-10·6 kJ mol^{-1}) and the 1 Al per slab structure (-13·8 kJ mol^{-1}). PBE is known to overbind hydrogen bonding interactions, and underestimate the energy barrier for proton transfer between adjacent oxygens. To eliminate the possibility that the increased stabilisation energy is a product of the functional used, a subset of NL-ordered structures were reoptimised with the van der Waals corrected functional BLYP-D3, which is known to underbind hydrogen bonding interactions and accurately mimic the energy barrier to proton migration. No significant change in $\Delta E(E_{Al\text{-}H_2O} - E_{Al\text{-}OH})$ was observed using BLYP-D3, confirming the robustness of these initial calculations, and excluding the possibility that the significant increase in $\Delta E(E_{Al\text{-}H_2O} - E_{Al\text{-}OH})$ is a product of the simulation method. Furthermore, *ab initio* MD simulations calculated at the PBE level of theory showed no proton transfer between neighbouring Al-OH and Al-H_2O. (Data for BLYP-D3 DFT and AIMD calculations is included in the Appendix.) It is possible that the increased stabilisation energy associated with forming Q3 Al-H_2O in the NL structure, compared to the L structure originates from alleviation of the repulsive interaction between nearby protons, Al-O(H)-Al and Al-O(H)-Si, by migrating the latter proton to the surface.

For the 1 Al per slab structure, it was suggested that the stabilisation energy on forming water could be due to the quenching of repulsive forces between negatively charged alumina and terminating hydroxides at the surface. In the NL-ordered structure, repulsive forces are greater as there are two adjacent alumina units in the 6-ring interacting unfavourably with six negatively charged hydroxyls. The increased repulsion is reflected in the difference between the bulk Q4 1 Al and 2 Al per slab global minimum structures; in the 2 Al structure Q4 Al is 4·9 Å further into the bulk than in the 1 Al structure. Hence, diminishing the repulsive forces by converting one hydroxyl to water has a greater net effect on the stability of the structure. Therefore, it should follow that migrating both acidic protons to form two water molecules at the surface from two

individual terminating hydroxyls gives an even greater stabilisation energy in 2Al per slab structures. However, this is not the case, in fact the largest destabilisation energy for both the NL and L structures is associated with the migration of both protons to terminating hydroxyls, forming two Q3 T-H_2O at the external surface ($\Delta E(E_{Al\text{-}H_2O} - E_{Al\text{-}OH})$ = +41·9 kJ mol^{-1} and +101·3 kJ mol^{-1} for NL and L, respectively). For the NL structure, this is because moving both protons involves removing the Al-O(H)-Al proton, which has been demonstrated to be extremely unfavourable. For the L structure, this is because forming two water molecules at the surface involves both the migration of the sub-surface proton and the formation of Q3 Si-H_2O at the external surface, which is also extremely unfavourable.

To ascertain whether the trend of increasing $\Delta E(E_{Al\text{-}H_2O} - E_{Al\text{-}OH})$ stabilisation energy with increasing Al content can be extended to NL-ordered structures containing more than two aluminium atoms, 3 Al per slab models (Si/Al = 23) were examined. These models were constructed using NL and L motifs from the 3 Al per U.C. H-SSZ-13 global minimum structures obtained from simulations in Chapter 3. Two sets of structures were optimised: purely NL ordered structures containing Al-O(H)-Al-O(H)-Al-O(H), in this motif two Q3 Al sit in the upper 6-ring of the D6R and another Q4 Al is positioned in the 6-ring below, occupying three of the four T-site vertices of a 4-ring of the D6R; and purely L ordered structures containing O(H)-Al-O-Si-O(H)-Al-O-Si-O(H)-Al. The structures were geometry optimised at the same level of theory used throughout this chapter.

Results for these simulations are shown in Figure 4.5. Once again, the NL-ordered structures are generally more stable than the L-ordered structures, this is due to the inherent thermodynamic preference for NL over L in H-SSZ-13. The global minimum NL structure contains Q4 Al at a mean distance of 12·6 Å from the external surface, illustrating the increased repulsive forces between the three negatively charged alumina units and the six terminating hydroxyls. The global minimum L structure contains Q4 Al at a mean distance of 8·0 Å as Al is better dispersed throughout the crystal.

In this case $\Delta E(E_{bulk} - E_{GM})$ is 0 kJ mol^{-1} and +11·6 kJ mol^{-1} for NL and L, respectively, and $\Delta E(E_{surface} - E_{GM})$ is +22·3 kJ mol^{-1} and +25·6 kJ mol^{-1}, for NL and L respectively. In accordance with the data for 2 Al per slab, it is more favourable for Q4 Al to move

deeper into the bulk of the zeolite than to form Q3 Al at the surface in both the NL and L-ordered structures.

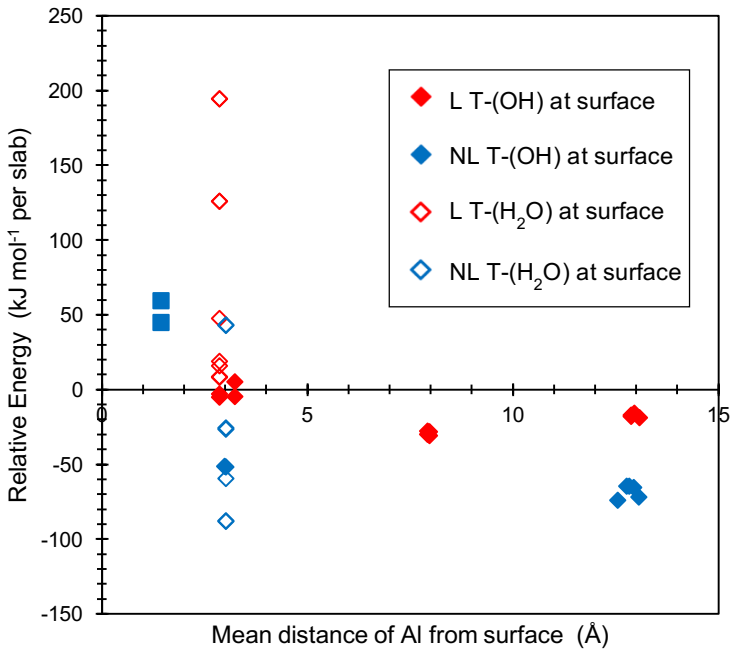

Figure 4.5 *Relative energy distribution (kJ mol^{-1} per slab) against the mean distance of Al from the surface of the slab (measured as the distance of Al from the terminating OH groups) for H-SSZ-13 (001) terminating slab with a Si/Al ratio of 23, equivalent to 3 Al per slab. Where; filled in points indicate models in which dangling bonds are satisfied by hydroxyls; unfilled points indicate the surface models in which the Brønsted acidic protons have migrated to a terminating hydroxyl, forming water at the surface; purely NL ordered frameworks (blue); and purely L ordered frameworks (red); the two square points indicate that the 3 Als are arranged in a chain along a single 6-ring of a surface D6R, these structures are terminated by hydroxyls only.*

It is notable that for the NL structure, $\Delta E(E_{surface} - E_{GM})$ increases to +118·4 kJ mol^{-1} if the global minimum structure is compared to a surface structure in which all three of the Al atoms are Q3 Al, and sit in a chain along the same 6-ring in the terminating D6R. To ascertain why it is more favourable to replace one Q3 Al with Q4 Al, DFT cluster calculations were performed for isolated D6R units. Two 3 Al per D6R clusters were examined, one cluster containing three Al in a chain along a single 6-ring of the D6R, mimicking the three Q3 Al structure (Figure 4.6a) and another containing two Al in a single 6-ring of the D6R and one Al in the 6-ring below, mimicking the two Q3 Al and

one subsurface Q4 Al structure (Figure 4.6b). In both clusters all dangling T-O bonds were satisfied by terminating hydroxyls. The calculations show the latter configuration (Figure 4.6b) to be the most stable by 23·5 kJ mol^{-1}, in line with the surface calculations. This structure is more stable because it minimises local framework distortions introduced by the increased length of Al-O linkages compared to Si-O.

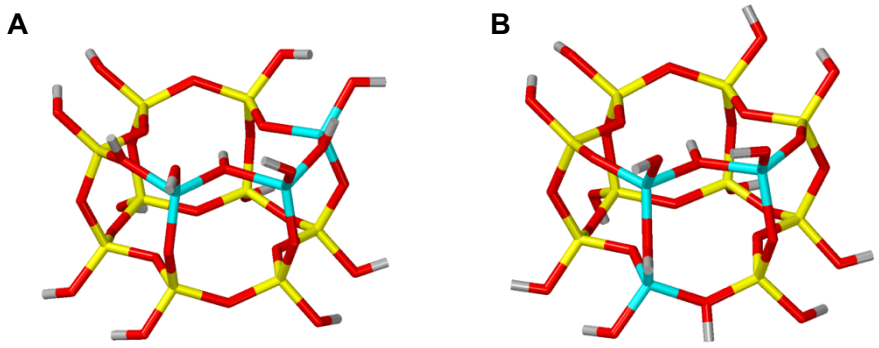

Figure 4.6 *Optimised structures of the D6R clusters containing 3 Al in* ***a)*** *a chain along a single 6-ring of the D6R, and* ***b)*** *a chain in which 3 Al atoms are positioned around a 4-ring of the D6R, with 2 Al atoms in a single 6-ring and another in the 6-ring below, this structure is the most stable.*

Once again, there is a stabilisation energy associated with migrating a single acidic proton from surface alumina to a terminating hydroxyl in the NL-ordered structure, $\Delta E(E_{Al\text{-}H_2O} - E_{Al\text{-}OH})$ = -36·0 kJ mol^{-1}, creating a new global minimum structure with Al at the surface of the crystal (Figure 4.7b). As in the 2 Al per slab simulations, only migrations involving protons which do not mediate two Al atoms are stable. For the 3 Al per slab structure there is no stabilisation associated with the formation of Al-H_2O in the L-ordered structure, $\Delta E(E_{Al\text{-}H_2O} - E_{Al\text{-}OH})$ = +13·4 kJ mol^{-1} due to extreme framework distortions at the surface of the structure. The total segregation energy for the 3 Al slab structure, $\Delta E(E_{Q3} - E_{Q4})$ is -13·7 kJ mol^{-1}. There appears to be no trend in $\Delta E(E_{Q3} - E_{Q4})$ on increasing the Al content in the (001) terminating H-SSZ-13 slab structure.

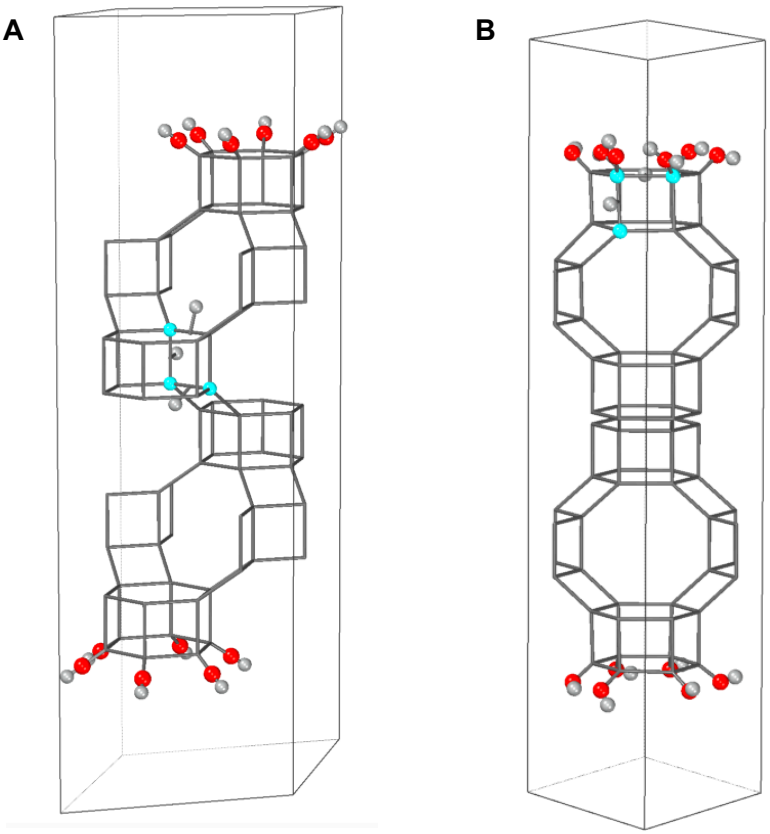

Figure 4.7 *Global minimum structures for the H-SSZ-13 (001) terminating slab with a Si/Al ratio of 23, where* ***a)*** *the surfaces are terminated by hydroxyls, yielding a bulk Q4 structure and* ***b)*** *the acidic proton has migrated to a terminating hydroxyl, forming water, yielding a surface Q3 structure. The latter structure is the most stable structure at 0 K.*

4.3.1.2 Na-SSZ-13

In Chapter 3, bulk SSZ-13 simulations showed that there are marked differences between the short-range Al distributions of H-SSZ-13 and Na-SSZ-13. To ascertain how counter-cation identity influences long-range Al distribution 1 Al and 2 Al Na-SSZ-13 slab structures were investigated.

The 1 Al per slab (Si/Al = 75) Na-SSZ-13 simulations show that there is an increased preference for Al to exist further into the bulk of the crystal than in the H-SSZ-13 at the same Si/Al ratio. The Na-SSZ-13 global minimum structure contains Q4 Al 10·6 Å from the external surface of the zeolite, compared to 4·3 Å in the equivalent H-SSZ-13 structure. In this Na-SSZ-13 global minimum structure, Na^+ is at the SII site, in accordance with what was found for N-SSZ-13 bulk structures in Chapter 3. The minimum energy penalty for moving the Q4 Al from this position into the bulk of the zeolite (14 Å from the terminating hydroxyls), $\Delta E(E_{bulk} - E_{GM})$ is +10·23 kJ mol^{-1}, and

the energy penalty for moving the Q4 Al to the external surface forming Q3 Al, $\Delta E(E_{surface} - E_{GM})$, is +32·8 kJ mol^{-1}. Therefore, it is theoretically more favourable for Q4 Al to move to the bulk, contrary to previous data for the equivalent H-SSZ-13 structure.

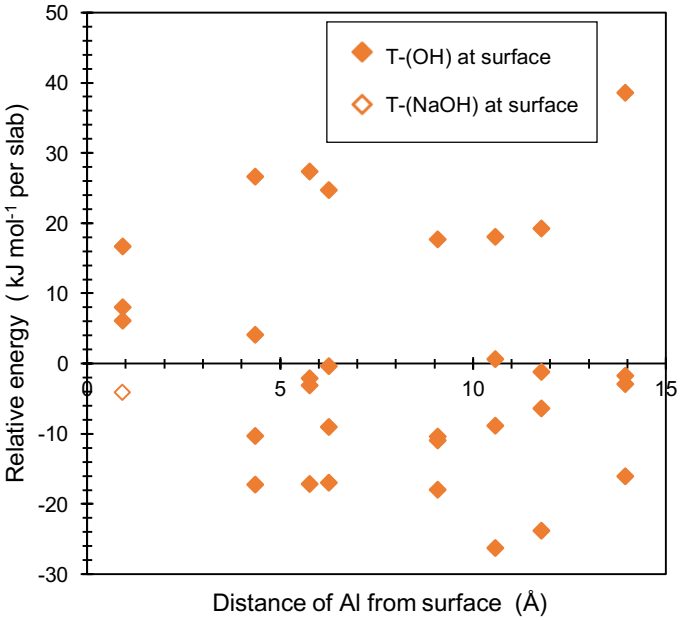

Figure 4.8 *Relative energy distribution (kJ mol^{-1} per slab) against the distance of Al from the surface of the slab (measured as the distance of Al from the terminating OH groups) for Na-SSZ-13 (001) terminating slab with a Si/Al ratio of 75, equivalent to 1 Al per slab. Filled in points indicate models in which dangling bonds are satisfied by hydroxyls, the unfilled point denotes the surface model in which the Na^{+} counter-cation has migrated to a terminating hydroxyl, forming NaOH at the surface.*

There is a stabilisation energy associated with the migration of Na^{+} from the internal *'cha'* cage in the lowest energy Q3 Al surface structure to the external surface of the zeolite, forming NaOH, $\Delta E(E_{Al\text{-}NaOH} - E_{Al\text{-}OH})$ = -10·2 kJ mol^{-1}. However, in contrast to what was observed for H-SSZ-13, the stabilisation energy is not significant enough to yield a new global minimum structure, and the Q3 Al-NaOH structure is still 22·5 kJ mol^{-1} less stable than the initial Q4 Al global minimum structure. The total segregation energy for the 1 Al Na-SSZ-13 slab structure, $\Delta E(E_{Q3} - E_{Q4})$ is +22·2 kJ mol^{-1}

Similar trends can be seen in the DFT data for the 2 Al per slab (Si/Al =35) Na-SSZ-13 simulations (Figure 4.9). At this Si/Al ratio, the global minimum structure is a Löwensteinian structure, containing Q4 Al at a mean distance of 14.5 Å from the external surface, in the centre of the bulk. Contrary to what was seen for H-SSZ-13, for the Na-SSZ-13 structure L-ordering is far more favourable than NL-ordering, this is to be expected according to the bulk Na-SSZ-13 simulations in Chapter 3.

For the 2 Al per U.C. structure, $\Delta E(E_{bulk} - E_{GM})$ is +0·54 kJ mol^{-1} and 0 kJ mol^{-1} for NL and L, respectively, and $\Delta E(E_{surface} - E_{GM})$ is +89·87 kJ mol^{-1} and +31·02 kJ mol^{-1}, for NL and L respectively. In accordance with previous findings it is more favourable for Q4 Al to move deeper into the bulk of the zeolite than to form two Q3 Al atoms at the surface in both the NL and L-ordered structures.

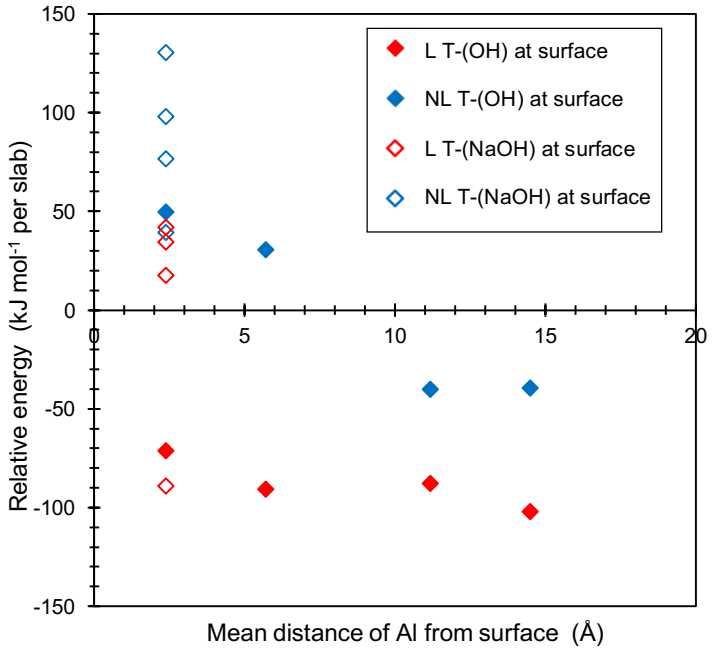

Figure 4.9 *Relative energy distribution (kJ mol^{-1} per slab) against the distance of Al from the surface of the slab (measured as the distance of Al from the terminating OH groups) for Na-SSZ-13 (001) terminating slab with a Si/Al ratio of 35, equivalent to 2 Al per slab. Filled in points indicate models in which dangling bonds are satisfied by hydroxyls, the unfilled point denotes the surface model in which the Na^{+} counter-cation has migrated to a terminating hydroxyl, forming NaOH at the surface.*

In agreement with what has been observed throughout this chapter, there is a stabilisation energy associated with migrating the Na^+ counter-cation to the external surface of the zeolite, forming NaOH, $\Delta E(E_{Al\text{-}NaOH} - E_{Al\text{-}OH})$ is -10·49 kJ mol^{-1} and -17·92 kJ mol^{-1}, for the NL and L-ordered structures, respectively. Although this energy is not significant enough to produce a new Q3 Al global minimum structure, in line with what was seen for the 1 Al per slab Na-SSZ-13 structure. It should be noted that unlike the H-SSZ-13 2 Al per slab structures, both NL and L Na-SSZ-13 surface structures contain two Q3 Al atoms, this is due to differences in the H-SSZ-13 and Na-SSZ-13 bulk global minimum structures (Chapter 3). The total segregation energy for the 2 Al Na-SSZ-13 slab structure, $\Delta E(E_{Q3} - E_{Q4})$ is +13·2 kJ mol^{-1}. It can therefore be concluded that surface enrichment of Al is less favourable in Na-containing zeolite structures than in protonated structures, demonstrating the influence of counter-cation identity on long-range Al distribution throughout the zeolite crystal.

4.3.2 The (011) terminating surface

Having established that counter-cation identity has a strong influence over the long-range distribution of Al in the (001) terminating slab, the (011) terminating slab was examined to determine whether the same trends are observed in crystals with different terminating surface geometries. Following the same methodology, 1 Al and 2 Al per (011) terminating H-SSZ-13 slab structures (Si/Al = 109 and 54, respectively) were investigated.

The DFT data for the 1 Al per (011) terminating H-SSZ-13 slab structures is shown in Figure 4.10. In contrast to the 1 Al per (001) H-SSZ-13 slab structure, in this structure, there is a preference for Q3 Al to reside at the surface of the zeolite in structures where all dangling bonds are satisfied by terminating hydroxyls. The minimum energy penalty for moving the Q3 Al from this position into the bulk of the zeolite forming Q4 Al, $\Delta E(E_{bulk} - E_{GM})$, is +8·4 kJ mol^{-1}, is comparable to what was found for the equivalent (001) terminating global minimum structure ($\Delta E(E_{bulk} - E_{GM})$ = +7·4 kJ mol^{-1}) However, the total energy landscape for the (011) terminating slab structures is significantly narrower than that of the (001) terminating structure; with a total energy range of 23·1 kJ mol^{-1}, compared to 49·6 kJ mol^{-1}.

In keeping with what has been observed throughout this chapter, there is a stabilisation energy associated with the formation of water at the surface *via* the migration of an acidic proton, $\Delta E(E_{Al\text{-}H_2O} - E_{Al\text{-}OH})$ = -3·1 kJ mol^{-1}. As the original global minimum structure is one with Q3 Al at the external surface, the stabilisation energy does not yield a new global minimum structure with an altered Al distribution. The total segregation energy for the 1 Al H-SSZ-13 (011) terminating slab structure, $\Delta E(E_{Q3} - E_{Q4})$ is therefore 0 kJ mol^{-1}.

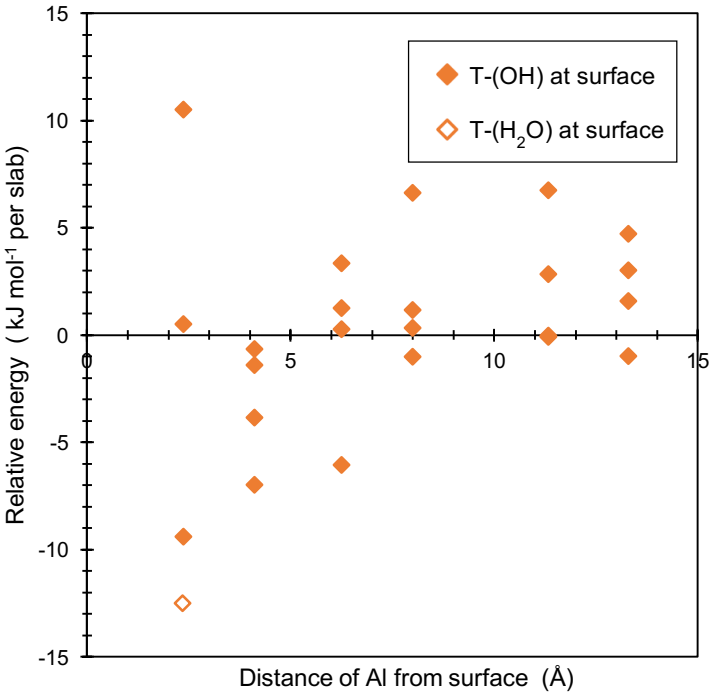

Figure 4.10 *Relative energy distribution (kJ mol^{-1} per slab) against the distance of Al from the surface of the slab (measured as the distance of Al from the terminating OH groups) for H-SSZ-13 (011) terminating slab with a Si/Al ratio of 109, equivalent to 1 Al per slab. Filled in points indicate models in which dangling bonds are satisfied by hydroxyls, the unfilled point denotes the surface model in which the Brønsted acidic proton has migrated to a terminating hydroxyl, forming water at the surface.*

As expected, the non-Löwensteinian ordering is favoured over Löwensteinian ordering in the 2 Al per (011) terminating slab (Figure 4.11), and the global minimum structure is a NL-ordered structure. In this case both the NL and L-ordered global minimum structures contain Q4 Al at a mean distance of 6·1 Å from the external surface. $\Delta E(E_{bulk} - E_{GM})$ is +5·2 kJ mol^{-1} and +2·9 kJ mol^{-1} for NL and L, respectively, and $\Delta E(E_{surface} -$

E_{GM}) is +34·5 kJ mol^{-1} and +9·5 kJ mol^{-1} for NL and L, respectively. In accordance with previous findings, it is more favourable for Q4 Al to move deeper into the bulk of the zeolite than to form Q3 Al at the surface.

The stabilisation energies on forming water at the external surface are vastly different for the NL and L-ordered structures, $\Delta E(E_{Al\text{-}H_2O} - E_{Al\text{-}OH})$, is -78·2 kJ mol^{-1} and -1·1 kJ mol^{-1} for NL and L, respectively. In keeping with previous findings, the stabilisation energy for the L-ordered structure is considerably reduced compared to the NL structures due to the unfavourable formation of Q3 Si-H_2O at the surface. The total segregation energy for the 2 Al H-SSZ-13 (011) terminating slab structure, $\Delta E(E_{Q3} - E_{Q4})$ is -43·7 kJ mol^{-1}, comparable to the value obtained for the (001) terminating slab structure with 2 Al per unit cell ($\Delta E(E_{Q3} - E_{Q4})$ = -44·9 kJ mol^{-1}).

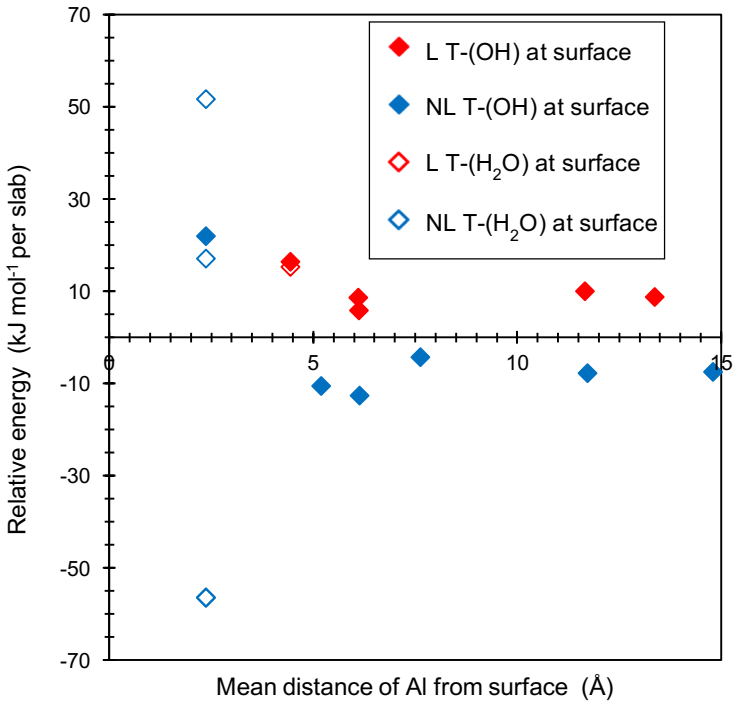

Figure 4.11 *Relative energy distribution (kJ mol^{-1} per slab) against the mean distance of Al from the surface of the slab (measured as the distance of Al from the terminating OH groups) for H-SSZ-13 (011) terminating slab with a Si/Al ratio of 54, equivalent to 2 Al per slab. Where; filled in points indicate models in which dangling bonds are satisfied by hydroxyls; unfilled points indicate the surface models in which the Brønsted acidic protons have migrated to a terminating hydroxyl, forming water at the surface; NL ordered frameworks (blue); and L ordered frameworks (red).*

4.4 Conclusions

Periodic DFT was used to study Al distribution at the surface and in the bulk of SSZ-13 (CHA) through simulations involving slab structures with different terminating surface geometries, Si/Al ratios and counter-cations.

The influence of counter-cation identity on short-range Al distribution over framework T-sites was established in the previous chapter. The work contained within this chapter further demonstrates the Al-directing capability of counter cations, as there is a clear contrast between the surface Al concentrations of H-SSZ-13 and Na-SSZ-13 slab structures. In high-silica structures, there is a preference for surface enrichment of Al in H-SSZ-13 compared to Na-SSZ-13, in structures with terminating silanol surfaces. This preference decreases with increasing Al content due to repulsions between negatively charged alumina units and terminating hydroxyls at the external surface. However, such repulsions can be overcome by the migration of a Brønsted acidic proton from surface alumina to a terminating hydroxyl, forming water. Single proton migrations such as these can stabilise the otherwise unstable Al-rich surface structures at lower Si/Al, provided the migration results in the formation of Q3 Al-H_2O, not Si-H_2O in Löwensteinian (L) ordered structures, and the migrating proton is not one at an oxygen site mediating two aluminium atoms, Al-O(H)-Al, in non-Löwensteinian (NL) systems. The latter finding further validates conclusions made in Chapter 3, concerning the importance of the bridging hydroxyl in stabilising Al-O(H)-Al by maximising the number of stable Si-O linkages in the zeolite framework and screening the charge of neighbouring Al^{3+} ions.[36] These findings are in accordance with work by Rey *et al.*[21] in which the thermodynamically most stable external surface sites of zeolite Beta (BEA) were shown to be Q3 Al-H_2O.[21] In all H-SSZ-13 cases, the formation of water at the surface stabilises NL structures to a greater extent. This is because NL motifs are inherently more stable than L motifs in protonated zeolites, as demonstrated in Chapter 3.[36] These trends are observed in both (001) and (011) terminating H-SSZ-13 slabs. Hence, we can conclude that the most thermodynamically favourable long-range Al distribution in H-SSZ-13 crystals is one where Al exists at the surface and is arranged as nearest neighbours.

The long-range Al distribution is distinctly different for Na-SSZ-13. In these structures, there is an obvious preference for Al to exist in the bulk of the crystal. In accordance with what was observed for H-SSZ-13 slab structures, the energy penalty for forming

Al at the surface of the structure, $\Delta E(E_{surface} - E_{GM})$, increases with increasing Al content. Hence in lower Si/Al ratio Na-SSZ-13 structures, it is more favourable for Al to exist deeper within the bulk of the crystal. In keeping with the data from Chapter 3, L ordered structures are significantly more stable than NL ordered structures. Furthermore, there is a distinct preference for Na^+ to be located at SII sites over SIII sites in the zeolite slab.[36] In accordance with what was found for H-SSZ-13, there is a stabilisation energy associated with the migration of the Na^+ counter-cation to the surface hydroxyls, forming NaOH. This is due to quenching of the negative charge at the surface on forming NaOH, reducing the repulsions between negatively charged alumina units and terminating hydroxyls. However, in contrast with the formation of water in H-SSZ-13, the stabilisation is much less significant, and does not produce a new global minimum structure with Al at the surface. The lowest energy structure hence remains one with Al in the bulk of the crystal. The reason for the differences in stabilisation energy is most likely due to increased stabilisation from improved hydrogen bonding networks in H-SSZ-13, such interactions do not exist on forming NaOH instead of water at the surface.

The work contained within this chapter hence demonstrates the influence of counter-cations on long-range Al distribution in SSZ-13. As in Chapter 3, given that real samples of SSZ-13 are typically synthesised from a sodium solution in the presence of an SDA, the most likely distribution of Al throughout real SSZ-13 crystals is likely to be similar to that reported for Na-SSZ-13, in which Al distribution is Löwensteinian and more homogenous than that which has been observed in real samples of ZSM-5. Since these simulations neglect to include the synthesis template, these findings support the conclusions of Althoff *et al.*,[5] who reported that entirely template-free syntheses, in which cations play the role of the structure-directing species, will yield more homogeneous Al distributions due to favourable interactions between the cations and alumina species present in the initial synthesis gel. This leads to improved Al framework incorporation compared syntheses involving a TPA template, as TPA interacts preferentially with silica.[5] It should be noted that the standard synthesis of SSZ-13, according to the patent by Zones *et al.*,[34,35] also involves the use of an ammonia derived template; N,N,N-trimethyl-1-ammonium adamantane hydroxide. It is therefore conceivable that the long-range Al distribution in real Na-SSZ-13 is more heterogeneous than what is predicted in this chapter, due to impeded Al incorporation due to the presence of the template.

Chapter 3 discussed the possibility that H-SSZ-13 samples, formed *via* cation-exchange from Na-SSZ-13, are 'frustrated' in terms of Al distribution over framework T-sites, as aluminium is suspended in extremely thermodynamically unstable framework positions. Applying the same rationale, the work contained within this chapter indicates that this 'frustration' may in fact be two-fold, as framework Al atoms are likely to be locked into both short-range and long-range Al distributions that are thermodynamically unfavourable.

It is plausible that the implications of this frustration are already observed in real protonated zeolite samples. For example, in the rearrangement of Al species and formation of extra-framework Al. The findings suggest that the removal of Al from the bulk of the zeolite, forming vacant defect sites would be favourable due to the instability of Al within the bulk of the zeolite in protonated zeolites. Such Al extractions could be achieved by heating the zeolite, for example during steaming, which is a well-known dealumination method.[10,37] The results thus far indicate there to be a stabilisation associated with the preservation of strong Si-O linkages. Hence, the formation of extra-framework Al could be due to increased energy barriers to reintroducing extra-framework Al to a more stable framework T-site near the surface *via* Si → Al + H substitution,[18] compared to the initial extraction of framework Al. However, work by Holzinger *et al.*[37] demonstrated that following high temperature steaming, framework annealing was only possible by softer steaming the zeolite at lower temperatures. It is possible that in this case reinsertion of Al into the framework is made feasible by the interaction of water molecules at the surface, which reduce the energy barrier of Si → Al + H substitutions. At high temperatures, the rapid movement of water molecules could hinder adsorption to surface Q3 Al atoms, hence framework healing is not possible.

4.5 References

1. von Ballmoos, R. & Meier, W.M. *Nature* **289,** 782–783 (1981).
2. Derouane, E.G., Gilson, J.P., Gabelica, Z., Mousty-Desbuquoit, C., Verbist, J. *Journal of Catalysis* **71,** 447–448 (1981).
3. van Bokhoven, J.A. & Danilina, N. Aluminum in Zeolites: Where is it and What is its Structure? in *Zeolites and Catalysis* (eds. Čejka, J., Corma, A. & Zones,

S.) 283–300 (Wiley-VCH Verlag GmbH & Co. KGaA, 2010).

4. Chao, K.J. & Chern, J.Y. *Zeolites* **8,** 82–85 (1988).
5. Althoff, R., Schulz-Dobrick, B., Schüth, F., Unger, K. *Microporous Mater.* **1,** 207–218 (1993).
6. Debras, G., Gourgue, A., Nagy, J. B., De Clippeleir, G. *Zeolites* **5,** 369–376 (1985).
7. Suib, S.L., Stucky, G.D., Blattner, R.J. *J. Catal.* **65,** 179–184 (1980).
8. Lin, J. C. & Chao, K. J. *J. Chem. Soc. Faraday Trans. 1 Phys. Chem. Condens. Phases* **82,** 2645–2649 (1986).
9. Hughes, A.E., Wilshier, K.G., Sexton, B.A., Smart, P. *J. Catal.* **80,** 221–227 (1983).
10. Perea, D.E. Arslan, I., Liu, J., Ristanović, Z., Kovarik, L., Arey, B.W., Lercher, J.A., Bare, S.R., Weckhuysen, B.M. *Nat. Commun.* **6**, 7589 (2015).
11. Perez-Pariente, J., A. Martens, J.A., Jacobs, P. *Appl. Catal.* **31,** 35–64 (1987).
12. Weeks, T.J., Passoja, D.E., Corporation, U.C. *Clays Clay Miner.* **25,** 211–213 (1977).
13. Dwyer, J., Fitch, F.R., Machado, F., Qin, G., Smyth, S.M., Vickerman, J.C. *J. Chem. Soc. Chem. Commun.* **0,** 422 (1981).
14. Dwyer, J., Fitch, F.R., Qin, G., Vickerman, J.C. *J. Phys. Chem.* **86,** 4574–4578 (1982).
15. Corma, A., Melo, F.V., Rawlence, D. *Zeolites* **12,** 261–264 (1992).
16. Kubelková, L., Dudíková, L., Bastl, Z., Borbély, G., Beyer, H.K. *J. Chem. Soc. Faraday Trans. 1 Phys. Chem. Condens. Phases* **83,** 511–516 (1987).
17. Bare, S.R., Knop-Gericke, A., Teschner, D., Hävacker, M., Blume, R., Rocha, T., Schlögl, R., Chan, A.S.Y., Blackwell, N., Charochak, M.E., Ter Veen, R., Brongersma, H.H. *Surf. Sci.* **648,** 376–382 (2016).
18. Bučko, T., Benco, L., Demuth, T., Hafner, J. *J. Chem. Phys.* **117,** 7295–7305 (2002).
19. Bučko, T., Benco, L., Hafner, J. *J. Chem. Phys.* **118,** 8437–8445 (2003).
20. Bučko, T., Hafner, J., Benco, L. *J. Chem. Phys.* **120,** 10263–10277 (2004).
21. Rey, J., Raybaud, P., Chizallet, C. *ChemCatChem* **9,** 2176–2185 (2017).
22. Thomas, C.L. & Barmby, D.S. *J. Catal.* **12,** 341–346 (1968).
23. Mintova, S., Gilson, J.P., Valtchev, V. *Nanoscale* **5,** 6693–6703 (2013).
24. Roth, W.J., Nachtigall, P., Morris, R.E., Čejka, J. *Chemical Reviews* **114,** 4807–4837 (2014).

25. Boscoboinik, J.A., Yu, X., Yang, B., Fischer, F.D., Wodarczyk, R., Sierka, M., Shaikhutdinov, S., Sauer, J., Freund, H.J. *Angew. Chemie - Int. Ed.* **51,** 6005–6008 (2012).
26. Rybicki, M. & Sauer, J. *Phys. Chem. Chem. Phys.* **17**, 27873-27882 (2015).
27. Choi, M*.,* Na, K., Kim, J., Sakamoto, Y., Terasaki, O., Ryoo, R. *Nature* **461,** 246–249 (2009).
28. Paparatto, G., Moretti, E., Leofanti, G., Gatti, F. *J. Catal.* **105,** 227–232 (1987).
29. Chiu, M.E., Slater, B., Gale, J.D. *Angew. Chemie Int. Ed.* **44,** 1213–1217 (2005).
30. Meza, L.I., Anderson, M.W., Slater, B., Agger, J.R. *Phys. Chem. Chem. Phys.* **10**, 5066-5076 (2008).
31. Mistry, M. PhD Thesis: The surface structure and growth of natural zeolites (University of London, 2005).
32. Jelfs, K. PhD Thesis: Modelling the growth of zeolitic materials (UCL, 2010).
33. International Zeolite Association. *Zeolite Synthesis Directory* (2001).
34. Zones, S.I. & Van Nordstrand, R.A. *Zeolites* **8,** 166–174 (1988).
35. Zones, S.I. *US 4544538: Zeolite SSZ-13 and its method of preparation* (1985).
36. Fletcher, R.E., Ling, S., Slater, B. *Chem. Sci.* **8,** 7483–7491 (2017).
37. Holzinger, J., Beato, P., Lundegaard, L. F., Skibsted, J. *J. Phys. Chem. C* **122,** 15595–15613 (2018).

Chapter 5: The effect of an organic template on Al distribution

5.1 Overview

The work in the preceding chapters has demonstrated the distribution of framework Al throughout the zeolite crystal to be decidedly non-random and dependent on several factors. For example, the identity of neighbouring T-atoms, the nature and distribution of charge-compensating cations, and whether Al is located at the surface or within the bulk of the zeolite crystal. The idea that Al distribution is not governed by statistical factors is in line with the generally accepted wisdom in this area. It is well understood that the conditions under which a zeolite crystal is synthesised have a marked effect on Al distribution and it has been demonstrated that the choice of Si and Al sources, mineralizing agents, the SDA, and synthesis time and temperature all influence the final arrangement of Al in the resultant zeolite.[1–4]

The work contained in Chapters 3 and 4 involved simulations in which the only variables considered were the locations of framework Si and Al, and extra-framework cations. Whilst these models have proven useful in disentangling the influence of certain framework components on Al arrangement, they are in no way comprehensive and neglect to include important factors that are known to affect the position of Al within the framework during synthesis. In this chapter, the models are extended to include both the synthesis template and water, to better mimic real as-synthesised zeolite samples. The influence of these components on framework Al distribution is examined, making reference to the work contained in Chapters 3 and 4 and the literature. The templating effect of the SDA, and the qualities of successful templating molecules were discussed in detail in Chapter 1. This chapter focuses on the Al-directing capabilities of the templating molecule, as opposed to the structure-directing capabilities, the remainder of this section provides an overview of pertinent literature in this area.

It is well known that altering the templating molecule during the synthesis of a specific zeolite framework allows a range of Si/Al ratios to be attained.[5,6] This can be explained by the size-excluding properties of large organic SDAs, which limit the number of extra-framework counter cations per characteristic zeolite cavity, and hence the number of negatively charged framework alumina units present within the framework. In some cases, the organic templating molecule may be a charge-bearing species, capable of acting as the sole charge-compensating species within the framework, using large

cationic species as templating molecules is often useful for the synthesis of high-silica zeolites (Si/Al > 5).[7,8] The earliest examples of high-silica zeolite syntheses involve the use of tetramethyl ammonium, TMA, templates. [9–12] Since then quaternary ammonium salts have become the preferred templates for high-silica zeolite synthesis. However, recently the use of di-quaternary ammonium salts has become more prevalent. This is because the increased charge on these structures reduces the hydrophobicity of the template, which is known to impact a template's structure directing ability, whilst maintaining the template's dimensions.[8,13,14]

The use of co-templates during synthesis has been demonstrated to be a potentially useful method for controlling the distribution of Al throughout a zeolite framework. The method exploits the existence different void architectures within certain zeolite frameworks, using two or more different SDA molecules with distinct dimensions, which will have a preference to be reside within pores of the appropriate size. Using a mixture of charge-neutral and charged templates of different sizes it is possible to 'guide' Al into a T-site location associated with a specific cavity-space within the framework. This has been demonstrated experimentally by Pérez-Pariente and co-workers,[15,16] who synthesised Ferrierite (FER) (Si/Al = 15) from cation-free gels in fluoride media and in the presence of a range of different SDA molecule combinations: pyrrolidine, pyrrolidine + tetramethylammonium (TMA) and TMA + benzylmethylpyrrolidinium (BMP). The FER framework is composed of 10-ring channels that run parallel to the crystallographic [001] direction, these channels are intersected by 8-ring channels, which run parallel to the [010] direction. Furthermore, 6-ring channels also run along the [001] direction, and these channels form characteristic 'ferrierite cavities' where they intersect with the 8-ring channels. The authors demonstrated that during synthesis, when acting as the sole SDA, pyrrolidine is contained within both the ferrierite cavity and the 10-ring channel. When FER was synthesised using pyrrolidine + TMA, pyrrolidine is found in the same framework locations, the TMA cation can also reside in the ferrierite cavities, but not in the 10-ring channels. When using TMA + BMP, TMA is exclusively located within the cavities, and BMP within the 10-ring channels. The authors also demonstrated that the accessibility of the active sites to pyridine decreased in the order TMA + BMP > TMA + pyrrolidine > pyrrolidine, finding there to be a good correlation between active site accessibility and catalytic activity for a series of catalytic reactions, demonstrating that acid site, and hence Al, distribution can be effectively controlled through by rationally selecting an SDA or combination of SDAs with suitable structure and dimension.[15,16] A similar phenomena has been demonstrated in ZSM-5 (MFI); when ZSM-5 is synthesised with tetrapropylammonium

(TPA) and no other charge-balancing cations, Al tends to be located at T-sites near the intersections, as TPA^+ is too large to be accommodated elsewhere in the framework. However, when ZSM-5 is synthesised with both TPA^+ and Na^+, Al can be found in T-sites at the parameters of both intersections and the straight/sinusoidal channels. It is also notable that when ZSM-5 is synthesised with pentaerythritol (PET) in combination with Na^+ as PET is uncharged, Al are only found surrounding the straight/sinusoidal channel systems.[5,6,17,18]

Whilst there is a wealth of computational work in the literature that is dedicated to understanding zeolite-template interactions,[19–22] there are very few studies that focus specifically on the Al-directing ability of templating molecules. One of the earliest studies is a 2002 study by Sastre *et al.*,[23] in which the authors use force field atomistic simulations, employed in GULP, to investigate the preferential arrangement of both Al and associated protons in zeolite ITQ-7 (ISV). They found that the template plays a significant role in controlling framework Al arrangement, noting that "SDA accommodation within the microporous space acts not only as a structure director but also as a director of the Al distribution". The authors hence conclude the energetics of the SDA - framework interactions that occur during synthesis to be the principal factor determining the distribution of Al throughout the resultant zeolite, rather than the energy of the final framework.[23] Later work by Gómez-Hortigüela *et al.*[24] utilized a similar force field approach to confirm these findings in FER, noting the Al-directing ability of a given zeolite to be directly determined by the capacity of the organic SDA molecule to form strong hydrogen bonds with framework oxygen. This work was later expanded on by Pinar and co-workers who demonstrated that such hydrogen bonding interactions could be used in the design of successful template molecules to yield zeolites with specific Al arrangements.[25]

In this chapter, periodic DFT is used to examine the most thermodynamically favourable Al distribution in SDA-containing SSZ-13 structures. The relative Al-directing ability of the SDA with that of the charge-balancing extra-framework cations is examined in both the as-synthesised form of the zeolite, SDA-containing Na-SSZ-13, and the hypothetical Brønsted acidic SDA-containing H-SSZ-13. Finally, water is introduced to the SDA-containing Na-SSZ-13 models to examine the relative Al-directing ability of the fully-hydrated form of the cation compared to the bare form of the cation and the SDA. The results are discussed in terms of previous findings and existing experimental work on SSZ-13.

5.2 Approach

The typical synthesis template for SSZ-13 is N,N,N-trimethyl-1-ammonium adamantane hydroxide.[26–28] To investigate the Al-directing ability of the SDA, in these simulations the SDA was considered to be its cationic form (Figure 5.1). Due to considerable size restrictions in small-pore SSZ-13, the SDA is generally thought to sit in the characteristic *'cha'* cage of the CHA framework. Each hexagonal CHA unit cell contains three *'cha'* cages, shown in Figure 5.2. A single SDA cation can fit comfortable in one of these cavities, although there is very little room for rotation.

To examine the effect of the SDA on aluminium distribution, initial simulations were concerned with models containing a single SDA cation. To generate these structures, a single Al was positioned at each of the 36 framework T-sites. The N,N,N-trimethyl-1-ammonium adamantane cation was treated as the sole charge-compensating species, and positioned within each of the three *'cha'* cages individually, yielding a total of 108 different structures, each with an Si/Al ratio of 35.

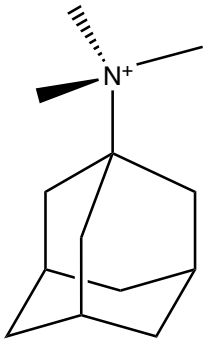

Figure 5.1 *The N,N,N-trimethyl-1-ammonium adamantane cation*.

To examine the effect of the SDA on Al distribution at lower Si/Al ratios, SSZ-13 models containing 2 Al per U.C. (Si/Al = 17) and two SDA cations per U.C. were investigated. To generate all the possible permutations of 2 Al per U.C. in these structures, the same methodology used in Chapter 3 was employed. To limit the number of possible permutations, and hence computational expense, the SDA cations were only contained within two of the three *'cha'* cages per unit cell. For simplicity the two 'full' *'cha'* cages at opposite vertices of the unit cell were chosen to contain the SDA cations (Figure 5.2). Using this methodology, a total of 35 2 Al per U.C. SDA/SSZ-13 structures were considered.

The combined effect of the SDA and other counter-cations on aluminium distribution was then explored. Once again, these simulations were concerned with SSZ-13 models at a Si/Al ratio of 17, equivalent to 2 Al per U.C. To establish which charge-balancing moiety has the greatest influence on Al arrangement, in each of the models one negatively charged alumina tetrahedra was compensated by the cationic SDA and the other compensated by either Na^+ or H^+. In keeping with previous methodology, the number of possible permutations was limited by only considering the SDA to be present in one of the two 'full' *'cha'* cavities per unit cell (Figure 5.2). As in previous chapters, protons were covalently bound to one of the four possible oxygen sites per alumina tetrahedra, and Na^+ cations were placed in either the SII or SIII positions. A total of 140 discrete SDA/Na-SSZ-13 structures and 280 SDA/H-SSZ-13 structures were generated in this way. To better mimic real as-synthesised zeolite samples, six water molecules were then introduced to each of the 140 SDA/Na-SSZ-13. The molecules were positioned around the Na^+ cation, to simulate the cation in its fully-hydrated form $[Na(H_2O)_6]^+$.

Each of the initial structures were obtained from the IZA's database of zeolite structures.[29] Models generated from these structures were geometry optimised with the CP2K code,[30,31] using the PBE[32] XC functional and a TZV2P basis set.

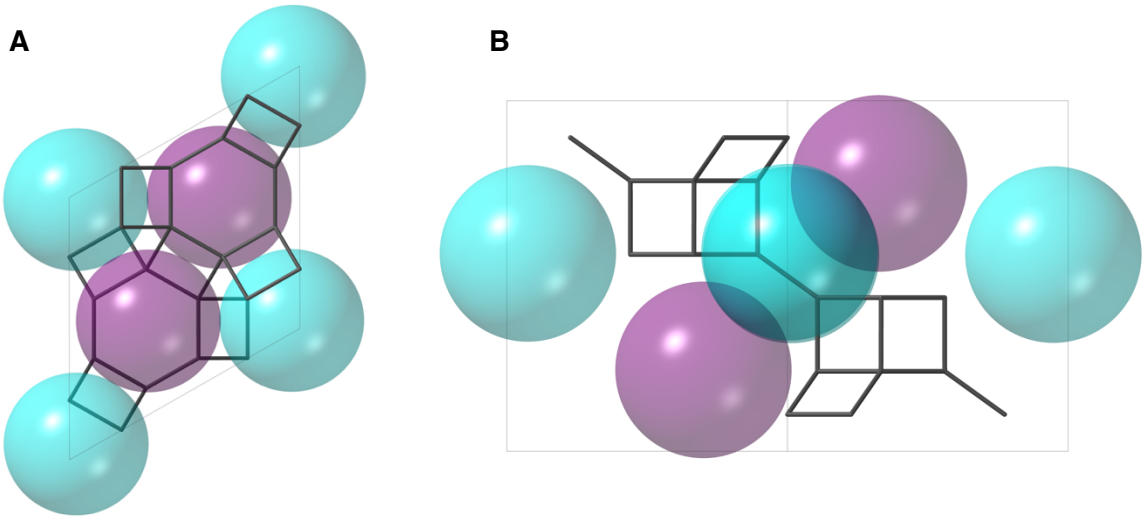

Figure 5.2 *The large (> 8 Å) cavity spaces present within the CHA framework, equivalent to three 'cha' cages shown along* ***a)*** *the [001] and* ***b)*** *the [110]. The purple cavity spaces are those 'cha' cages in which the SDA molecules were contained in the 2 Al per U.C. structures. The turquoise cavities make up the third 'cha' cage, which exists in four quarters per hexagonal CHA unit cell.*

5.3 The effect of the SDA on Al distribution where the SDA is the sole charge-compensating species

5.3.1 1 Al per CHA unit cell with 1 SDA

The initial investigation was concerned with the effect of a single SDA cation (N,N,N-trimethyl-1-ammonium adamantane), positioned in one of the three *'cha'* cavities, on aluminium location in SSZ-13 (CHA). The results are shown in Figure 5.3a, where the relative energy of each of the 1 Al per unit cell SSZ-13 structures is plotted against the separation between the negatively charged aluminium tetrahedral unit and the charge-compensating SDA cation. The charge associated with the SDA is formally denoted to be on the nitrogen atom, hence, for simplicity, the separation between the SDA and Al is defined as the shortest distance between the positively charged nitrogen of the SDA and framework Al. However, in real as-synthesised samples, it is likely that the charge is spread across the entire templating molecule.

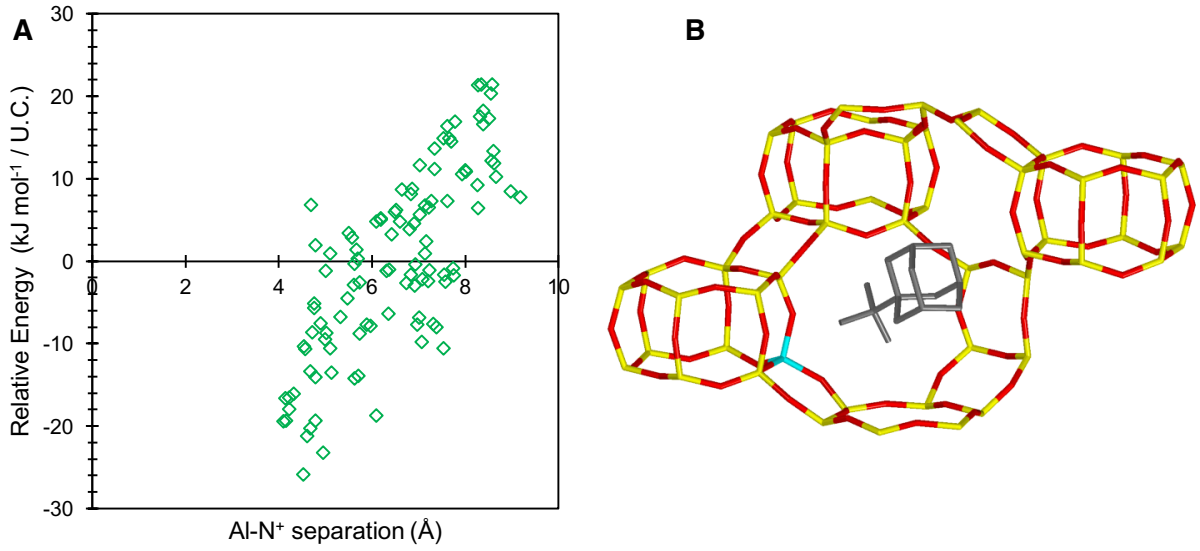

Figure 5.3 a) *DFT data showing the relative energy (defined relative to the mean energy) distribution of, and* ***b)*** *the global minimum structure for 1 Al per unit cell SSZ-13 (CHA) (Si/Al = 35) where the negative charge introduced by Al is solely compensated by a single SDA cation.*

The DFT data shows that there is a positive correlation (R^2 = 0·609) between energy and the separation between the charge-balancing SDA and the negatively charged aluminium. Therefore, the closer the charge-balancing SDA cation is to the negatively charged alumina unit, the more stable the structure and *vice versa*. The global minimum structure, Figure 5.3b, contains Al and the SDA separated by 4·5 Å. The minimum energy penalty for forming this structure over one in which there is maximum separation between the SDA and Al (9·2 Å) is 33·6 kJ mol^{-1}, 9 *k*T at synthesis temperature. Such a large energy difference over such short distances indicates that the SDA has a significant framework Al-directing ability.

5.3.2 2 Al per CHA unit cell with 2 SDAs

The introduction of a second Al and SDA cation to the framework (Si/Al = 17) yields a distinctly different Al distribution to what was reported for both Na-SSZ-13 and H-SSZ-13 at the same Si/Al (Chapter 3). The relative energy landscape shows that aluminium arrangement adheres to both Löwenstein's and Dempsey's rule, as illustrated in Figure 5.4a, which displays relative energy as a function of Al-Al separation. Comparing this data to that where the relative energy is given as a function of the separation between Al and the SDA (Figure 5.4b) we see a very weak correlation (R^2 = 0·062) between the stability of the structure and the Al-SDA separation. This trend is less pronounced than in 1 Al per U.C. structure due to the small unit cell size of the CHA framework, which restricts the maximum separation between a single Al and an SDA molecule. However, at both Si/Al ratios, the most stable SDA/SSZ-13 structures are those which contain the SDA at the shortest separation from Al.

The preference for Löwensteinian and Dempsey ordering can be attributed to the confinement of SDA molecules in cavities at opposite vertices of the unit cell. Such SDA molecules are considerably restricted in terms of orientation, this is illustrated in Figure 5.4c, which shows the total change in N^+-N^+ separation across all of the structures to be 1 Å. The Al atoms hence prefer to be at a maximum framework separation of 10·3 Å, where both Al^{3+} ions can interact more strongly with nitrogen atoms of the two SDA cations. This is illustrated in the SDA/SSZ-13 global minimum structure, displayed in Figure 5.4d. The Al arrangement in this structure is distinctly different from that in the sodium-compensated structure at the same Si/Al ratio in Chapter 3. Here, Al pairs are positioned as 5th nearest neighbours, whereas the 3rd nearest neighbour (NNNN) position was preferred for Na-SSZ-13.

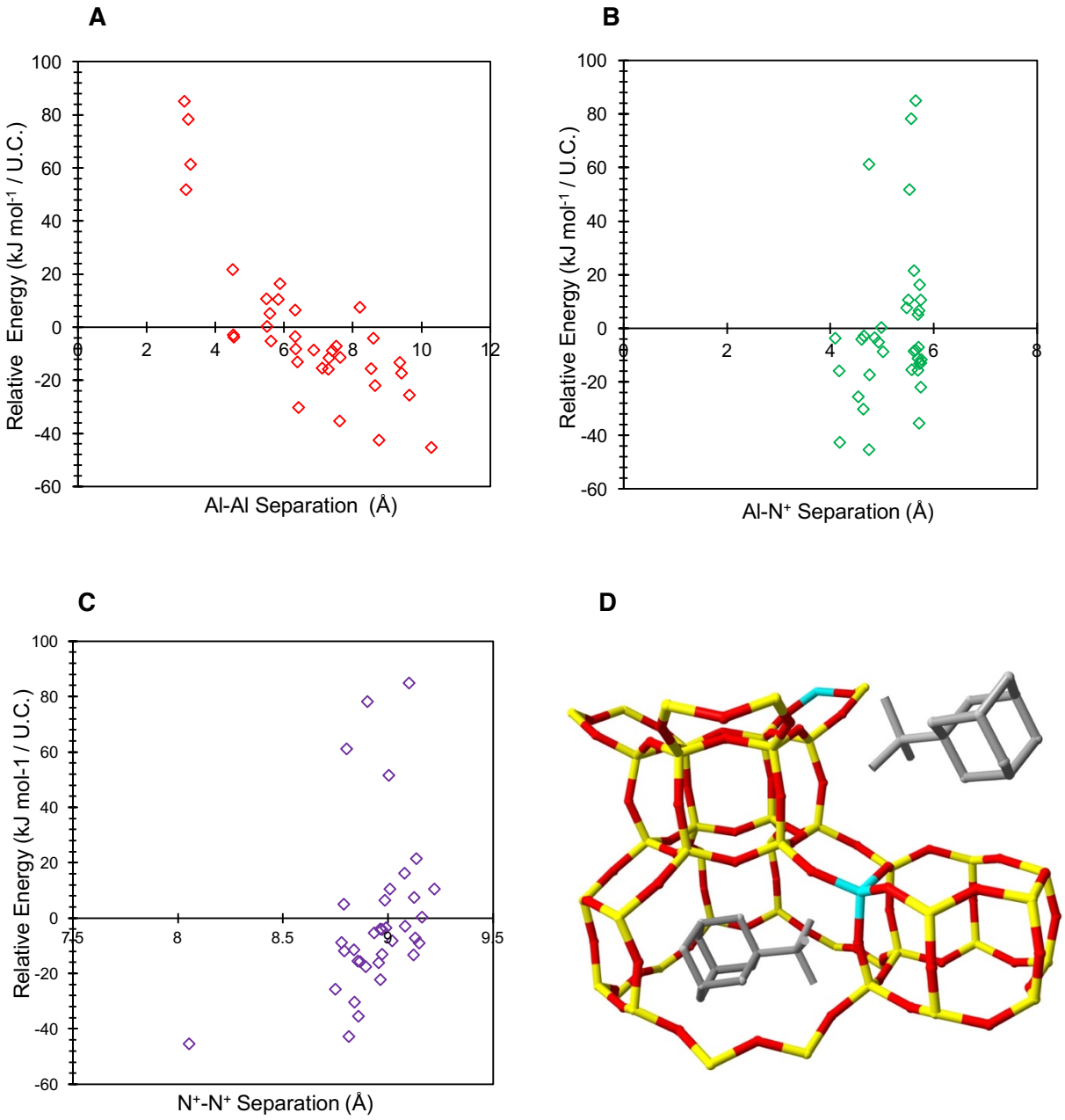

Figure 5.4 *DFT data for 2 Al per unit cell SSZ-13 where the charge from Als is countered by two SDA cations, where relative energy (defined relative to the mean energy) per DFT is shown as a function of* ***a)*** *Al-Al separation,* ***b)*** *Al-N^+ separation, and* ***c)*** *N^+-N^+ separation.* ***d)*** *The global minimum structure according to this data.*

Contrary to what might be expected, according to Figure 5.4c, the lowest energy structures contain SDA molecules at the shortest N^+-N^+ separation. This is due to the fact that more stable structures are denser. For example the total volume of the global minimum structure is 2507·1 $Å^3$, whereas the global maximum structure has a total volume of 2538·5 $Å^3$. The increase in volume comes from framework distortions along

a single parameter introduced by unfavourable Al-O-Al linkages. The data shown in Figure 5.4 hence indicates that Al-Al interactions influence Al distribution more strongly than other atom-atom interactions.

5.4 The effect of the SDA on Al distribution in the presence of other extra-framework counter-cations

5.4.1 Sodium cation

The purpose of this work is to gain insight into the Al directing function of the components present during zeolite synthesis, hence the relative Al-directing capabilities of the SDA and the synthesis cation were evaluated in tandem. As discussed in previous chapters, SSZ-13 is typically synthesised from a sodium solution in the presence of the N,N,N-trimethyl-1-ammonium adamantane hydroxide template. Therefore, initial SDA/cation simulations involved SDA/Na-SSZ-13 models containing 2 Al atoms per unit cell (Si/Al = 17). As explained in the Approach section of this chapter, each models contained a single SDA cation and a single Na^+ cation. In keeping with previous simulations, the SDA was positioned in two of the three available *'cha'* cages, and the Na^+ cation was positioned at the SII and SIII cation sites.

The DFT data for the SDA/Na-SSZ-13 simulations is shown in Figure 5.5. The relative energy distribution as a function of Al-Al separation is shown in Figure 5.5a. The same energy distribution is given as a function of Al-N^+ separation and Al-Na^+ separation in Figures 5.5b and c, respectively. There are striking similarities between Figure 5.5a and the energy landscape that was obtained in Chapter 3 for 2 Al per U.C. Na-SSZ-13. In both cases, there is a clear preference for Löwensteinian (L) ordering over non-Löwensteinian (NL) ordering. However, the energy penalty for forming the most stable NL structure over the L global minimum structure ($\Delta E(NL_{global\ minimum} - L_{global\ minimum})$) is +62·3 kJ mol^{-1} per U.C. for SDA/Na-SSZ-13, compared to +44·3 kJ mol^{-1} per U.C for the purely Na-compensated structure. Indicating that non-Löwensteinian ordering is more strongly disfavoured in SDA-containing frameworks. In both cases the global minimum structure is a non-Dempsey ordered structure with Al atoms at a separation of 6.4 Å.

In the SDA/Na-SSZ-13 global minimum structure, Figure 5.6, the pair of Al atoms are arranged as NNNN, and '*para'* to one another along a single 6-ring of the D6R, this Al arrangement was also found to be the most favourable in purely Na-compensated SSZ-13 at the same Si/Al in Chapter 3.[33] Na^+ is located in the SII position, capping the face

of the D6R. The observed preference for the SII site over the SIII site is in keeping with the results of 1 Al per U.C. Na-SSZ-13 simulations in Chapter 3, and a recent combined ^{23}Na SS MAS NMR and DFT study by Zhao *et al.*[34] It is likely that the preference for the SII site over the SIII site in this structure is due to the ability of the Na^+ cation to interact with both alumina units in the 6-ring in this position.

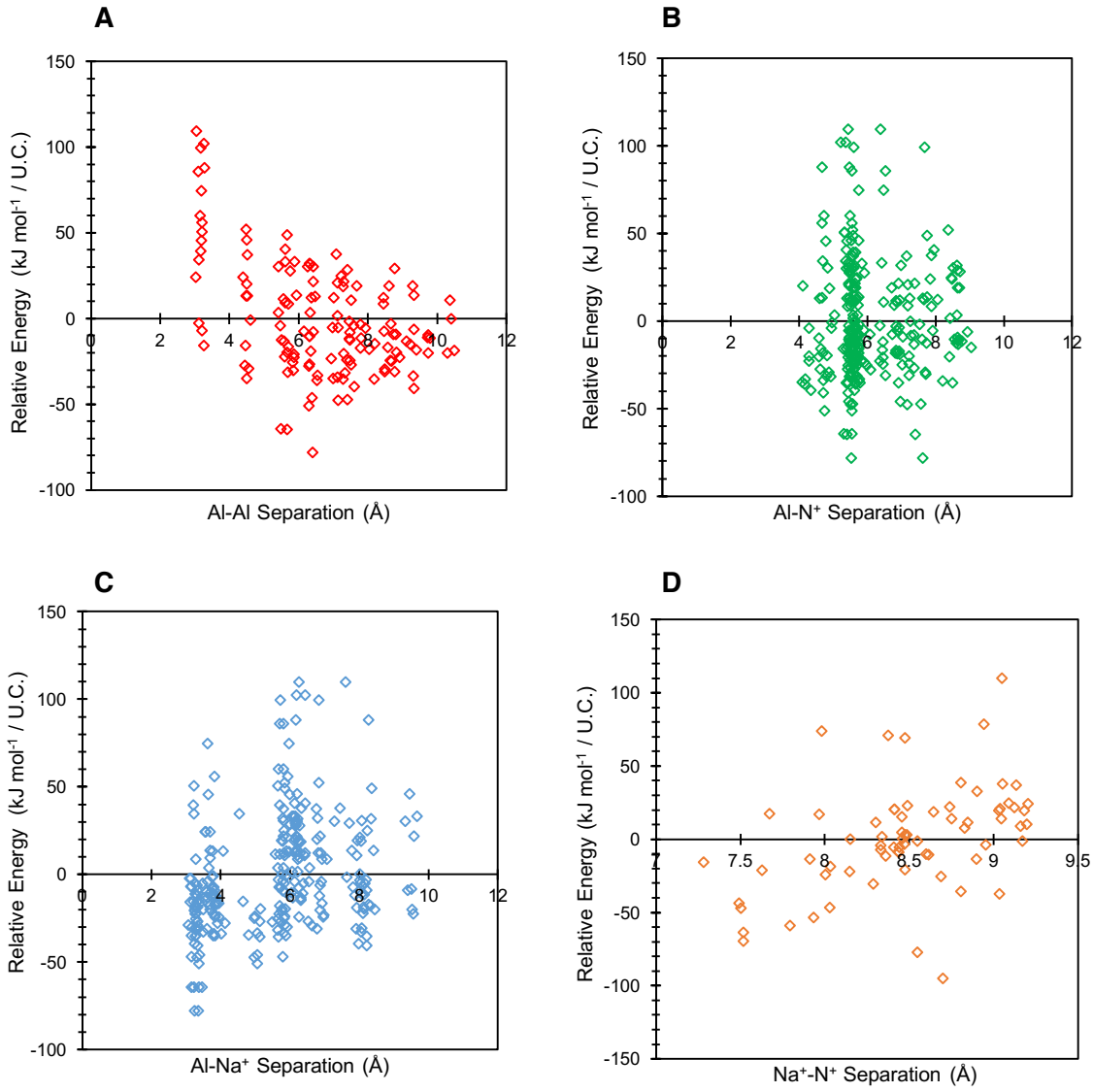

Figure 5.5 *DFT data for 2 Al per unit cell SSZ-13 where the charge from Als is countered by a single SDA cation and a single Na^+ cation, where relative energy (defined relative to the mean energy) per DFT is shown as a function of* ***a)*** *Al-Al separation,* ***b)*** *Al-N^+ separation,* ***c)*** *Al-Na^+ separation and* ***d)*** *Na^+-N^+ separation*

Given the qualitative similarity between the energy landscapes and global minimum structures for both the SDA/Na-SSZ-13 and Na-SSZ-13 structures at a Si/Al of 17, and the dissimilarity of the SDA/Na-SSZ-13 structure and that in which two SDA cations are the sole charge-compensating species, it is evident that the Na^+ cation has greater Al-directing ability than the SDA cation. Comparing Figures 5.5b and c, we can see this quantitatively. Figure 5.5c shows a distinct positive correlation between Al-Na^+ separation and the energy of the SDA/Na-SSZ-13, in which the lowest energy structures are those with the shortest Al-Na^+ separations, and *vice versa*. This is in accordance with what was observed for 1 Al per U.C. Na-SSZ-13 in Chapter 3. There is no discernible trend between the stability of the structures and the Al-N^+ separations (Figure 5.5b). Furthermore, Figure 5.5d shows that there is a weak correlation between Na^+-N^+ separation and the relative energy of the structure (R^2 = 0·196). Lower energy structures tend to contain the SDA nearest the Na^+ cation, this is contrary to what might be expected. This could suggest that the charge of the SDA is not confined to the nitrogen atom (as defined here) and is instead spread over the entire organic molecule. However, given the fact that the global minimum structure contains the Na^+ cation and the SDA at a relatively large separation of 8·7 Å, indicating that SDA-cation interactions do influence the stability of the structure, this is unlikely. It is more plausible that short Na^+-N^+ separations are favoured as these separations allow structures to contain the more favourable Al-Al and Al-Na^+ separations. Increased correlation of Al-Al and Al-Na^+ separations with energy suggest that these interactions influence Al and cation distribution more strongly than Na^+-N^+ interactions, in keeping results for the SDA/SSZ-13 structure at the same Si/Al ratio.

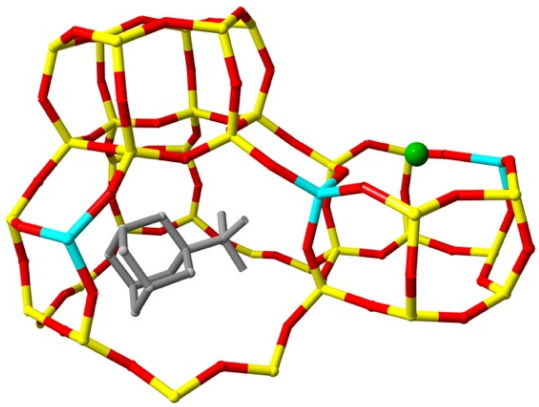

Figure 5.6 *The global minimum structure according to DFT for 2 Al per unit cell SSZ-13 where the charge from Als is countered by a single SDA cation and a single Na^+ cation.*

5.4.2 Protons

2 Al per U.C. structures in which both Al atoms are charge-compensated by a single SDA cation and a single proton, were then considered. It is notable that an SSZ-13 structure containing both these species is entirely hypothetical. As explained in Chapter 1 and 3, SSZ-13 is generally synthesised from a sodium solution in the presence of an the N,N,N-trimethyl-1-ammonium adamantane hydroxide SDA. To attain the protonated form of the zeolite, the zeolite undergoes calcination to remove the template, followed by ion exchange, hence the two components would not realistically co-exist in a physical sample of SSZ-13. However, the aim of this study was to further understand the relative Al-directing ability of the cation compared to the SDA.

In accordance with the SDA/Na-SSZ-13 data, the data for SDA/H-SSZ-13 (Figure 5.7) clearly illustrates that the proton exhibits a greater Al-directing ability than the SDA cation. The relative energy landscape for SDA/H-SSZ-13 plotted against Al-Al separation (Figure 5.7a), is very similar to that reported for purely proton-compensated SSZ-13 with 2 Al per unit cell in Chapter 3. In keeping with previous work, there is a clear preference for non-Löwensteinian, non-Dempsey Al ordering. The global minimum structure (Figure 5.7d) is almost identical to the H-SSZ-13 global minimum structure, containing a NL Al-O-Al linkage, with a single proton at the oxygen site mediating the two Al atoms. This finding further validates conclusions made in Chapters 3 and 4, concerning the fact that the preference for non-Löwensteinian ordering, and indeed Al clustering, in protonated zeolites is driven by maximising the number of Al-OH linkages in order to maximise the number stable Si-O linkages within the framework, and shielding the negative charges from adjacent alumina units.

$\Delta E(NL_{global\ minimum} - L_{global\ minimum})$ for SDA/H-SSZ-13 is -35·1 kJ mol^{-1} per U.C, compared to -14·2 kJ mol^{-1} per U.C in the purely H-SSZ-13 case at this Si/Al ratio, indicating non-Löwensteinian ordering is more strongly preferred in the SDA-containing form of the zeolite. Despite the marked differences in Al distribution between SDA/Na-SSZ-13 and SDA/H-SSZ-13, $\Delta E(NL_{global\ minimum} - L_{global\ minimum})$ values are increased in both structures compared to analogous SDA-free structures (Chapter 3). The reason for such inflated values is likely because in these structures the counter-cation species has the highest charge/radius ratio, the most efficient way for the single cation to compensate the two individual negative charges introduced by 2 Al is for the cation reside in a position where it can interact with both Al (and *vice versa*), in SDA/H-SSZ-13 this yields a structure containing an Al-O(H)-Al linkage.

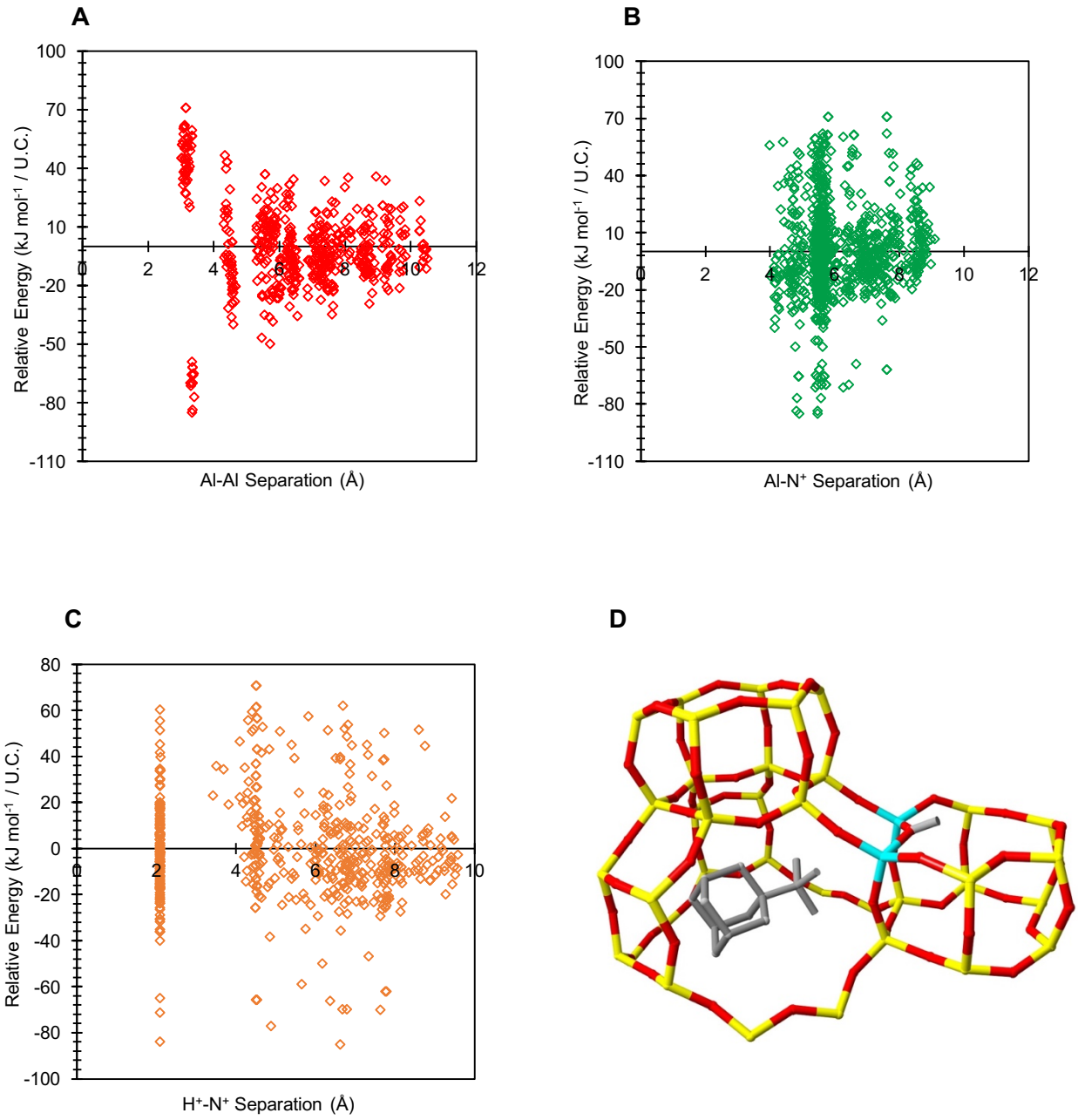

Figure 5.7 *DFT data for 2 Al per unit cell SSZ-13 where the charge from Als is countered by a single SDA cation and a single proton, where relative energy (defined relative to the mean energy) per DFT is shown as a function of* ***a)*** *Al-Al separation and* ***b)*** *Al-N^+ separation and* ***c)*** *H^+-N^+ separation.* ***d)*** *The global minimum structure*

There is no apparent trend between the stability of the SDA/H-SSZ-13 structures and the separation between Al and the SDA (Figure 5.7b). Moreover, there is also no discernible trend between the energy of the structures and proton-SDA separation (Figure 5.7c). It can therefore be concluded that despite the presence of the SDA cation, Al-Al interactions determine Al arrangement in SDA/H-SSZ-13.

5.4.3 In the presence of water

As-synthesised zeolites contain copious amounts of water. Given this, and the work contained in Chapter 4, in which water was demonstrated to stabilise otherwise unstable zeolite structures, the effect of small quantities of water on the relative stability of SDA-containing SSZ-13 structures was examined.

Since SSZ-13 is typically synthesised from a sodium solution in the presence of the N,N,N-trimethyl-1-ammonium adamantane hydroxide template, the SDA/Na-SSZ-13 structure is most likely to represent real SSZ-13 samples. Sodium cations were positioned at the SII and SIII sites with six water molecules arranged around them, mimicking the hydrated form of the cation, $[Na(H_2O)_6]^+$. Each of these structures were then geometry optimised at the same level of theory used throughout this chapter.

The results for the geometry optimisations are included in Figure 5.8. There are distinct similarities between the energy landscapes for the hydrated cation structure (Figures 8a, b and c) and the SDA/Na-SSZ-13 structures in which Na^+ cations are bare (Figure 5. 5). In accordance with what has been seen for all Na-SSZ-13 structures in this thesis, there is a preference for Löwensteinian, non-Dempsey ordering. On comparison of Figures 5.9 and 5.6, it is clear that hydrating the cation does not change the position of Al or Na^+ in the global minimum structure. In keeping with our previous results Na^+ exists in the SII site, and Al pairs exist at NNNN positions, '*para*' to one another along the 6-ring of the D6R. However, the energy penalty for forming the lowest energy NL structure over this global minimum structure ($\Delta E(NL_{global\ minimum} - L_{global\ minimum})$) is +70·3 kJ mol^{-1} per U.C., therefore it is 8 kJ mol^{-1} less favourable to form the NL structure in frameworks containing hydrated cations, than those containing bare cations. It seems that Löwensteinian ordering becomes more favourable with the addition of framework components that would be present in real as-synthesised samples.

On comparison of the energy landscape given as a function of Al-Na^+ separation for the hydrated-cation containing structure (Figure 5.8c) with that for the dehydrated SDA/Na-SSZ-13 structure (Figure 5.5c), we see that correlation between Al-Na^+ and

the energy of the structure becomes less pronounced for the hydrated structure. This is to be expected, as the charge on the cation is screened from Al due to the presence of six water molecules. Furthermore, in line with what was observed for the dehydrated structure, there is a very weak correlation between Na^+-N^+ separation and the energy of the structure (Figures 5.8c and 5.5c). This correlation is slightly stronger than in the dehydrated structure (R^2 = 0·201), and contrary to what might be expected the global minimum structure contains Na^+-N^+ at a minimum separation of 8·2 Å. The improved correlation is likely due to screening of the Na^+ charge by the water molecules. Moreover, these results confirm that Al-Al interactions influence atom arrangement more strongly than other atom-atom interactions.

Similarities between the energy landscape for the water-containing SDA/Na-SSZ-13 with those obtained water-free SDA/Na-SSZ-13 and purely Na-compensated SSZ-13 (Chapter 3), indicate that even when fully hydrated, the Na^+ cation has a greater Al-directing ability than the SDA cation in SSZ-13. However, there are key differences between the energy landscapes for the hydrated SDA/Na-SSZ-13 structure (Figure 5.8a) and the SDA/Na-SSZ-13 structure containing bare Na^+ cations (Figure 5.5a). Firstly, the 'energy well' containing the global minimum structure and other low energy structures has significantly shallowed on the introduction of water. Where the energy difference between the global minimum structure and the next lowest energy structure was +13·7 kJ mol^{-1} in the dehydrated structure, in the hydrated structure the energy difference is +1·2 kJ mol^{-1}. In fact, there are multiple global minima structures with comparable energies (four structures within 4·5 kJ mol^{-1} of one another). These structures contain Al pairs at separations of 6·3 Å to 10·4 Å, therefore, whilst NNNN (3rd NN) Al arrangement exists in the global minimum structure, Al pairs at 4th NN and 5th NN positions are also thermally accessible. Once again, this is due to the fact that Al-Al interactions influence the arrangement of atoms in these structures more strongly than any other atom-atom interactions present within the framework, hence Dempsey-like ordering is more accessible than predicted for purely Na-compensated structures at the same Si/Al ratio, in which Na^+-Al interactions dominate (Chapter 3).

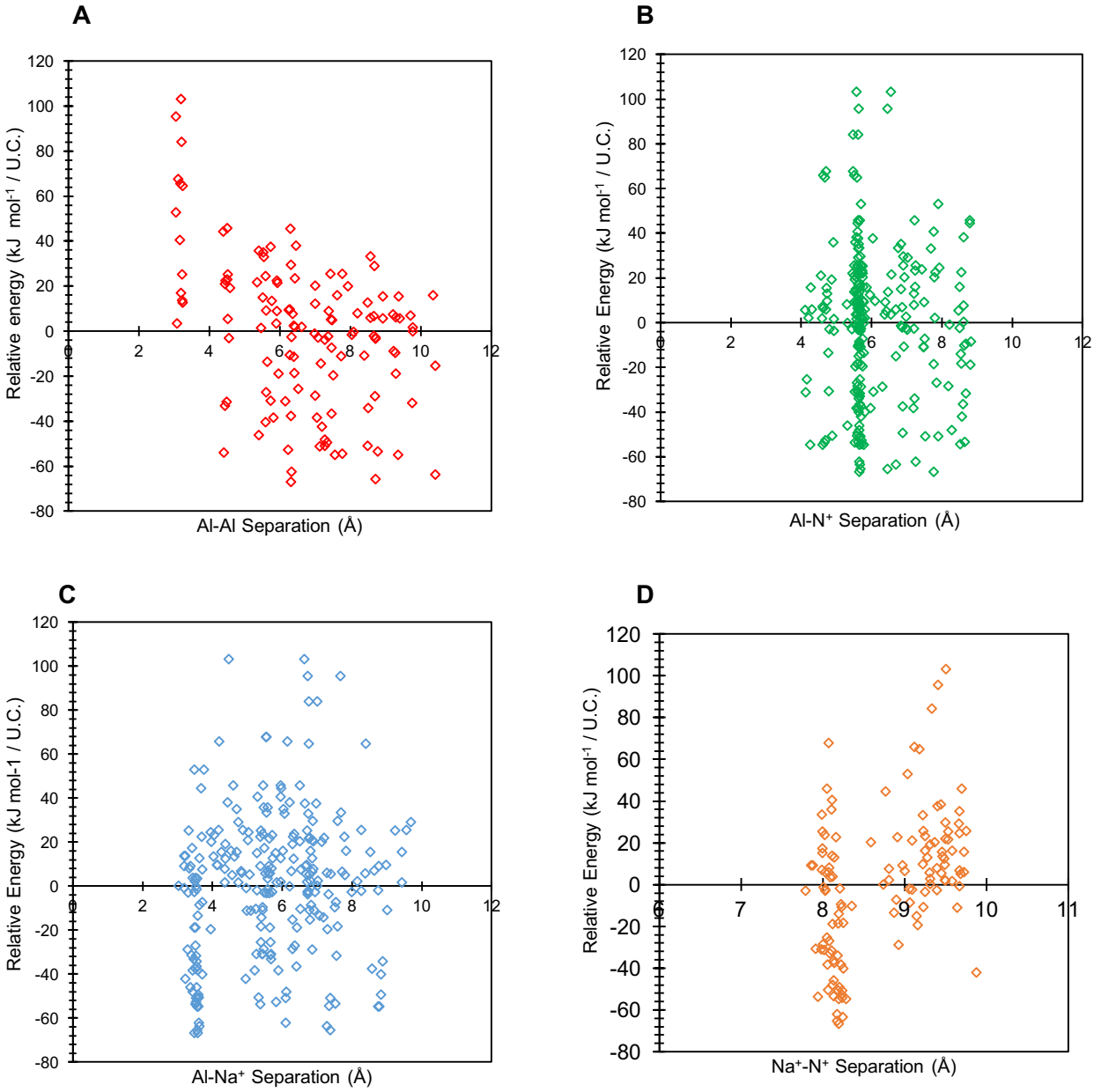

Figure 5.8 *DFT data for 2 Al per unit cell SSZ-13 where the charge from Als is countered by a single SDA cation and a single fully-hydrated Na^+ cation, where relative energy (defined relative to the mean energy) per DFT is shown as a function of* ***a)*** *Al-Al separation,* ***b)*** *Al-N^+ separation and* ***c)*** *Al-Na^+ separation and* ***d)*** *Na^+-N^+ separation*

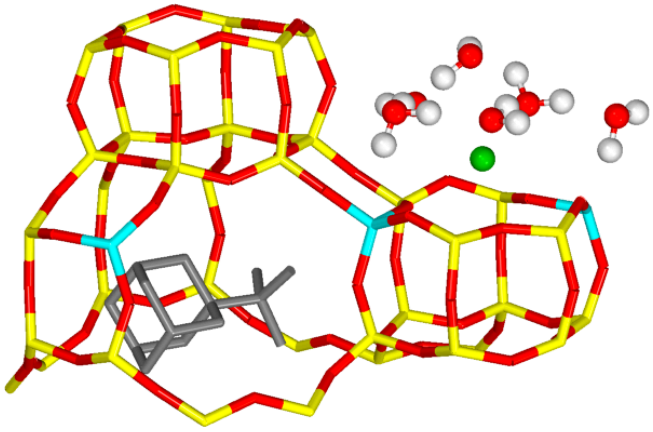

Figure 5.9 *The global minimum structure according to DFT for 2 Al per unit cell SSZ-13 where the charge from Als is countered by a single SDA cation and a single fully-hydrated* Na^+ *cation* $[Na(H_2O)_6]^+$

5.5 Conclusions

In this chapter, periodic DFT was used to simulate the energies and geometries of more complex SSZ-13 structures than those included in previous chapters. Such simulations allowed the relative influence of the SDA and cations over Al distribution to be examined.

The work contained within this chapter demonstrates that whilst the SSZ-13 synthesis SDA, N,N,N-trimethyl-1-ammonium adamantane hydroxide, has Al-directing capabilities, as demonstrated in 1 Al per U.C. SSZ-13 structures in which the SDA is the only charge-compensating species (Figures 5.3 and 5.4), the SDA's influence over Al arrangement is greatly reduced when a second Al and a counter-cation (Na^+ or H^+) are introduced to the framework. It is notable that Al-Al interactions are the dominating interaction present across all framework types, although Al-Al interactions dominate Al distribution in different ways depending on the charge balancing species present.

In the presence of typical synthesis components, *i.e.* the SDA and Na^+ cations, Löwensteinian ordering is preferred. This is primarily due to interactions between the Na^+ cation, which sits in the SII position, and the oxygens of the alumina units. No change in the global minimum structure was observed on fully hydrating the Na^+ cation. These results are in accordance with work contained in previous chapters, where the

SII site has been demonstrated to be the most favourable cation position in SSZ-13 at low Na^+ loadings. This is in keeping with the results of a recent combined ^{23}Na SS NMR and DFT work by Zhao *et al.*[34] It should be noted that the energy penalty for forming the lowest energy non-Löwensteinian structure significantly increased with the addition of the SDA and water molecules, hence it can be deduced that Löwensteinian ordering is more strongly preferred in real SSZ-13 samples than predicted in Chapter 3. However, it should be noted that in the presence of water, the Al-directing ability of the Na^+ is dampened, due the charge on the cation being screened by the water molecules. In these structures the Al-Al repulsive interaction becomes more important, and structures containing Al pairs at greater separations become more thermally accessible than predicted from structures in which Al is compensated solely by Na^+ cations (Chapter 3).

To confirm whether the findings for the relative Al-directing abilities of the SDA and cations could be extended to other counter-cation types, entirely hypothetical SSZ-13 structures, in which both exchanged protons and the SDA exist within the same CHA framework, were examined. These simulations showed there to be a preference for non-Löwensteinian ordering, hence validating our work from previous chapters. These simulations also demonstrate that the cation has a greater Al-directing ability than the SDA, in accordance with the SDA/Na-SSZ-13 data.

The diminished Al directing ability of the SDA compared to the counter-cations reported in this chapter is most likely due to increased charge/size ratio of the SDA cation. N,N,N-trimethyl-1-ammonium adamantane is a bulky organic molecule, which is restricted from interacting with framework Al due to sterics. The bare cations are small and can interact with negatively charged alumina units more strongly than the SDA, hence they have a stronger Al-directing ability.

The increased influence of Al-Al interactions on introducing counter-cations to the framework can also be attributed to sterics, and the diffuse charge over the SDA. In these structures one Al is formally compensated by the counter-cations and the other by the SDA, however, as demonstrated in SDA/H-SSZ-13 and SDA/Na-SSZ-13 simulations, the single cation endeavours to counter the charge of both Al atoms and hence NNNN ordering is preferred in SDA/Na-SSZ-13 and NN ordering is preferred in SDA/H-SSZ-13. The increased preference for NL ordering in the SDA/H-SSZ-13 structure compared to the H-SSZ-13 structure at the same Si/Al ratio (Chapter 3) is

due to the instability associated with Al molecules being further apart. Protons are known to counter the charge introduced by framework Al by covalently binding to an oxygen site at the apices of an alumina tetrahedra, the charge-compensating capability of a proton is considerably short-range, hence on moving Al pairs further apart, one of the Al^{3+} ions is no longer charge compensated. One inference of this finding is that Al-O-Al linkages could be encouraged to form in real structures during synthesis through the use of use of two different templates. The purpose of the first template would be to direct the formation of the final framework, for example N,N,N-trimethyl-1-ammonium adamantane hydroxide. The purpose of the second template molecule would be to act as a sacrificial proton donor to direct the formation of Al-O-Al linkages, a suitable molecule for this purpose would be pyridinium or ammonium. Following synthesis both templates would be removed from the structure, either by calcination or by washing in the case of ammonia, yielding a CHA framework structure containing an Al-O(H)-Al linkage.

The explanation as to why the Löwensteinian ordering is more favoured in SDA/Na-SSZ-13 structures compared to structures compensated by Na^+ alone (Chapter 3) is more involved, and relies on findings by Ruiz-Salvador *et al.*,[35] who reported that in the absence of any charge-compensating species Al distribution in ZSM-5 is determined by Al-Al interactions, in accordance with Dempsey's rule.[36] In the hydrated SDA/Na-SSZ-13 structure, we see proof of this concept. In this structure the SDA has little charge-compensating ability, and much the charge on Na^+ is screened from Al by the water molecules, hence in this structure the negative charge from framework Al is not sufficiently compensated, Al-Al interactions therefore dominate and Al distributions containing large Al-Al separations become more thermally accessible, in accordance with Dempsey's rule. In the dehydrated structure, whilst Al pairs exist in non-Dempsey positions as NNNN, the destabilisation associated with forming non-Löwensteinian structures increases due increased repulsions between practically un-compensated negatively charged Al pairs.

5.6 References

1. Dědeček, J., Sobalík, Z., Wichterlová, B. *Catalysis Reviews - Science and Engineering* **54,** 135–223 (2012).
2. Dědeček, J., Kaucký, D., Wichterlová, B. *Chem. Commun.* **0,** 970–971 (2001).
3. Han, O.H., Kim, C.-S., Hong, S.B. *Angew. Chemie Int. Ed.* **41,** 469–472 (2002).

4. van Bokhoven, J.A., Lee, T.L., Drakopoulos, M., Lamberti, C., Thiess, S., Zegenhagen, J. *Nat. Mater.* **7,** 551–555 (2008).
5. Van Der Gaag, F.J., Jansen, J.C., Van Bekkum, H. *Appl. Catal.* **17,** 261–271 (1985).
6. Biligetu, T., Wang, Y., Nishitoba, T., Otomo, R., Park, S., Mochizuki, H., Kondo, J.N., Tatsumi, T., Yokoi, T. *Journal of Catalysis* **353**, 1-10 (2017).
7. Jacobs, P.A. & Martens, J.A. *Studies in Surface Science and Catalysis* **33,** (Elsevier, 1987).
8. Burton, A. Catalysis Reviews, **60**, 132-175(2017).
9. Barrer, R.M. & Denny, P. J. *J. Chem. Soc.* **0,** 971–982 (1961).
10. Barrer, R.M. & Denny, P. J. *J. Chem. Soc.* **0,** 983–1000 (1961).
11. Kerr, G.T. *Inorg. Chem.* **5,** 1537–1539 (1966).
12. Aiello, R. & Barrer, R.M. *J. Chem. Soc. A Inorganic, Phys. Theor. Chem.* **0,** 1470–1475 (1970).
13. Casci, J.L. Bis-quaternary ammonium compounds as templates in the crystallisation of zeolites and silica molecular sieves in *Studies in Surface Science and Catalysis* **28,** 215–222 (Elsevier, 1986).
14. Corma, A. Towards a rationalization of zeolite and zeolitic materials synthesis in *Studies* in *Surface Science and Catalysis* **154,** 25-40 (Elsevier, 2004).
15. Pinar, A.B., Márquez-Álvarez, C., Grande-Casas, M., Pérez-Pariente, J. *J. Catal.* **263,** 258–265 (2009).
16. Márquez-Alvarez, C., Pinar, A.B., García, R., Grande-Casas, M., Pérez-Pariente, J. *Top. Catal.* **52,** 1281–1291 (2009).
17. Lok, B.M., Cannan, T.R., Messina, C.A. *Zeolites* **3,** 282–291 (1983).
18. Yokoi, T., Mochizuki, H., Biligetu, T., Wang, Y., Tatsumi, T. *Chem. Lett.* **46,** 798–800 (2017).
19. Turrina, A. & Cox, P.A. Molecular Modelling of Structure Direction Phenomena in *Structure and Bonding* 75–102 (Springer, Cham, 2017).
20. Lewis, D.W., Catlow, C.R.A., Thomas, J.M. *Chem. Mater.* **8,** 1112–1118 (1996).
21. Lewis, D.W., Willock, D.J., Catlow, C.R.A., Thomas, J.M., Hutchings, G.J. *Nature* **382,** 604–606 (1996).
22. Lewis, D.W. Template-Host Interaction and Template Design in *Computer Modelling of Microporous Materials* (ed. Catlow, C.R.A., van Santen, R.A. & Smit, B.) 298 (Elsevier, 2004).
23. Sastre, G., Fornes, V., Corma, A. *J. Phys. Chem. B* **106,** 701–708 (2002).
24. Gómez-Hortigüela, L., Pinar, A.B., Corà, F., Pérez-Pariente, J. *Chem. Commun.*

46, 2073 (2010).

25. Pinar, A.B., Gómez-Hortigüela, L., McCusker, L.B., Pérez-Pariente, J. *Chem. Mater.* **25,** 3654–3661 (2013).
26. International Zeolite Association. *Zeolite Synthesis Directory* (2001).
27. Zones, S.I. *US 4544538: Zeolite SSZ-13 and its method of preparation* (1985).
28. Zones, S.I. & van Nordstrand, R.A. *Zeolites* **8,** 166–174 (1988).
29. IZA-SC. *IZA Structure Database* Available at: http://www.iza-structure.org/databases/
30. CP2K Available at: https://www.cp2k.org/.
31. VandeVondele, J., Krack, M., Mohamed, F., Parrinello, M., Chassaing, T., Hutter, J.
    Comput. Phys. Commun. **167,** 103–128 (2005).
32. Perdew, J.P., Burke, K., Ernzerhof, M. *Phys. Rev. Lett.* **78,** 1396–1396 (1997).
33. Fletcher, R.E., Ling, S., Slater, B. *Chem. Sci.* **8,** 7483–7491 (2017).
34. Zhao, Z., Xing, Y., Li, S., Meng, X., Xiao, F-S., McGuire, R., Parvulescu, A-N., Müller, U., Zhang, W. *J. Phys. Chem. C* **122,** 9973–9979 (2018).
35. Ruiz-Salvador, A.R., Grau-Crespo, R., Gray, A.E., Lewis, D.W. *J. Solid State Chem.* **198,** 330–336 (2013).
36. Dempsey, E. *J. Catal.* 115–119 (1977).

Chapter 6: Mo speciation during methane dehydroaromatisation over Mo/MFI catalysts

6.1 Overview

Methane upgrading over zeolites was introduced in section 1.2.5.1.2 of Chapter 1. In this chapter, the topic is revisited, focussing specifically on the direct conversion of methane to aromatic products through methane dehydroaromatisation (MDA). The advantages of direct methane conversion processes are discussed, as are the proposed mechanisms for MDA over Mo-exchanged zeolites. Finally, through the combined use of computational simulation and experimental analysis, a series of stable intermediate structures generated during MDA over an alternative Mo/silicalite (MFI) catalyst are identified, and a rational scheme is proposed for the evolution of the active Mo species during MDA over this catalyst. Results are compared with analogous simulations of Mo/ZSM-5 and the recent literature.

As discussed in Chapter 1, due to a general increase in oil prices and the emergence of fracking over the past few decades, recent renewed interest in methane as both a fuel and chemical feedstock has caused the natural gas market to flourish. However, whilst methane is certainly abundant and available, and in many cases, unused or wasted, there are significant obstacles that prevent natural gas from surpassing crude oil as the principal feedstock used for chemical production. Firstly, methane is an extremely thermodynamically stable molecule, causing the direct activation of methane to be especially difficult. Hence, all currently commercialised methane conversion processes, for example MTO, are indirect and proceed *via* the formation of synthesis gas (syngas), a mixture of carbon monoxide and hydrogen. The generation of syngas from natural gas, which is typically achieved through a combination of steam reforming and partial oxidation, is costly and the expense associated with this conversion is currently a major deterrent for the mass commercialisation of gas to liquid fuel conversion processes. Hence, developing a direct methane conversion process, which omits expensive syngas production, would be extremely lucrative.[1,2]

A promising direct methane conversion process is methane dehydroaromatisation (MDA), which involves direct generation of benzene from methane as follows:

$$6CH_{4(g)} \rightarrow C_6H_{6(g)} + 9H_{2(g)} \quad \Delta G_r^\circ = +433\ kJmol^{-1} \quad \Delta H_r^\circ = +531\ kJ\ mol^{-1} \quad (6.1)$$

This is a thermodynamically unfavourable endothermic process. The thermodynamics (which can be found in reference 1) dictate that benzene production can only be achieved under limited conditions, which involve impractably high temperatures, this reaction also tends to be kinetically driven to produce unwanted carbon.[1]

The use of a Mo-exchanged zeolite catalyst, typically Mo/H-ZSM-5, has been demonstrated to considerably improve the efficiency of the MDA reaction, circumventing the use of impractical reaction conditions by activating C-H bonds in methane. However, as explained in Chapter 1, there is still a lot of uncertainty surrounding whether MDA is catalysed by a monofunctional mechanism, where Mo carbide activates a C-H bond in methane, and converts the resulting CH_x to either ethylene or acetylene, subsequent aromatization then takes place exclusively over Mo carbide;[3,4] or a bi-functional mechanism, in which initial activation over the Mo carbide or oxycarbide active site is followed by oligomerisation and cyclisation at nearby Brønsted acid sites (Figure 1.8).[2,5–7]

Untangling the catalytic mechanism of MDA has been attempted by many researchers over the years. One popular method of demonstrating the bifunctional nature of the catalysis mechanism is to physically separate the proposed methane activation components (*i.e.* Mo species) from the proposed cyclisation components (*i.e.* Brønsted acid sites), this has been achieved using Mo/SiO_2 Mo_2C and $Mo_2C/\alpha Al_2O_3$.[8–10] In all these examples the authors reported considerable synergy between the Mo-species and the Brønsted acid sites when compared to the individual components. However, Kosinov *et al.*[2] have since reported that Mo/silicalite (MFI) is suitable for efficient MDA. Silicalite is the all-silica form of ZSM-5, and hence does not contain any Brønsted acidic protons. At first glance, it seems that these conclusions invalidate the long-established bifunctional mechanism theory, however by preparing physical mixtures of H-ZSM-5 and different Mo-oxide precursors on a range of supports, the authors showed that the Brønsted acid does indeed play an integral role in MDA, once again reporting significant synergy when compared to the individual components. The authors postulate that the role of the protons is to encourage the migration of Mo oxide species towards the Brønsted acid sites, into the shape-selective microporous regions of the zeolite. They conclude by demonstrating that the reason Mo/silicate functions as an efficient MDA catalyst is that in this catalyst the Mo oxide species is already contained within a shape selective environment within the zeolite framework.[2]

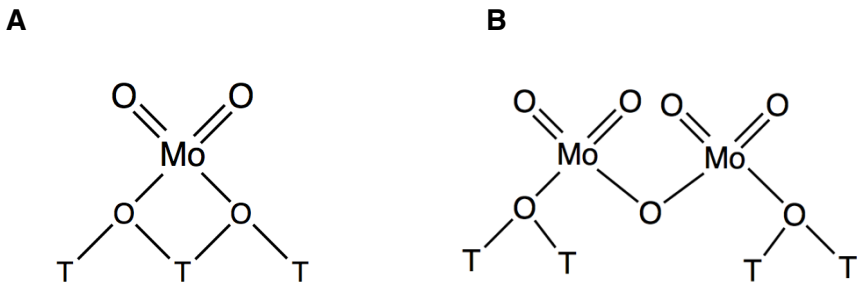

Figure 6.1 *Generally accepted proposed structures of the Mo-oxo species present during MDA over Mo/H-ZSM-5. Shown grafted to the framework the* ***a)*** *$[MoO_2]^{2+}$ monomer, and* ***b)*** *$[Mo_2O_5]^{2+}$ dimer, framework T-sites are labelled T.*

Despite significant advances in understanding the mechanism by which MDA proceeds, there is still considerable conflict concerning the identity of Mo species and its evolution throughout the catalytic process. It is generally accepted that the Mo active species originates from a Mo oxide species, which has been proposed to take the form of $[MoO_2]^{2+}$ monomers or $[Mo_2O_5]^{2+}$ dimers, depending on the chemical composition of the surrounding zeolite framework.[11–17] An early study by Li *et al.*[11] combined the use of Raman spectroscopy and X-ray absorption spectroscopy to investigate the identity of Mo oxide in H-ZSM-5. Raman spectroscopy was used to determine the type of Mo-O bonding in the MoO_x species, and both XANES and EXAFS were used to distinguish between octahedral and tetrahedral Mo. Using these methods, the authors confirmed the Mo oxide species to be in its dimeric form, $[Mo_2O_5]^{2+}$, in which each tetrahedral Mo centre has two Mo=O double bonds, is individually bound to framework oxygen and is linked to the adjacent Mo centre by bridging oxygen (Figure 6.1b).[11] A study in the same year by Kim *et al.*[12] also used Raman and X-ray absorption spectroscopy alongside ^{27}Al SS NMR and confirmed the same result.[12] A recent study by Lezcano-González *et al.*[16] used operando time-resolved combined X-ray diffraction (XRD) and high energy resolution fluorescence detection (K_a-detected) X-ray absorption near-edge spectroscopy (HERFD-XANES) during the MDA reaction over H-ZSM-5 and demonstrated that Mo oxide is in its monomeric $[MoO_2]^{2+}$ form, although they note that small amounts of dimer species cannot be excluded. The authors propose the evolution of the Mo species to proceed according to Figure 6.2.[16]

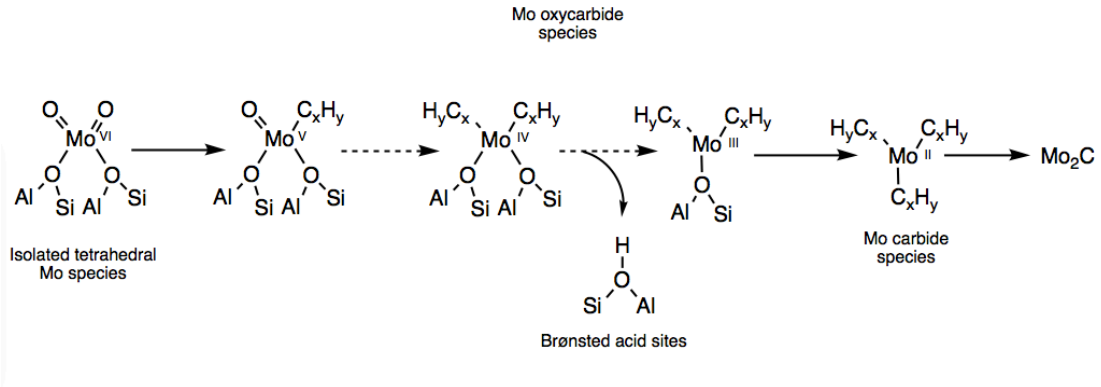

Figure 6.2 *Proposed evolution of the active Mo species during MDA over Mo-ZSM-5. Figure recreated from the work of Lezcano-González et al.*[16]

Over the past two decades there have been several theoretical studies focused on better understanding the mechanism of MDA over Mo exchanged ZSM-5. One of the first is a 2001 study by Zhou *et al.*,[13] in which the authors use a DFT cluster approach to investigate the interactions between the $[MoO_2]^{2+}$ monomer and the MFI framework. They investigated the geometry of the monomer, which they conclude to be di-coordinated to the zeolite framework, where terminal bonds are double Mo=O bonds, in line with the wealth of experimental data in this area. They propose that this binding is achieved though initial transformation of Mo oxide to molybdate, $MoO_2(OH)_2$, which binds to the framework through condensation reactions with adjacent Brønsted acid sites. [13]

In a later 2007 study by the same authors,[14] a similar approach was utilised to investigate both the geometric and electronic structures of the $[MoO_2]^{2+}$ monomer and $[Mo_2O_5]^{2+}$ dimer. The Mo oxide species were optimised in 6T clusters of H-ZSM-5, and the authors found there to be a thermodynamic preference for the dimer species to be positioned at T6T6 and T6T9 sites, through simulated Raman spectroscopy and natural bond orbital analysis they propose that this dimer contains four Mo≡O triple bonds, and is bound to four framework oxygens (Mo-O_F) though σ donations of the p orbitals of framework oxygen to antibonding orbitals in Mo-O bonds. They note that whilst the terminal Mo≡O bond lengths predicted by DFT are in line with experiment, the Mo-O_F bond lengths are longer than predicted by EXAFS data. The authors conclude that these discrepancies arise because XRD measures the distances between the electron density centroids, which is what is being represented by the DFT,

and EXAFS measures the distances between neighbouring electron clouds – hence the measured data underestimates the actual interatomic distances between nuclei. They also postulate that such discrepancies could be due to real samples of the MDA catalyst also containing the monomeric Mo-oxo species, which they predict to be triple bound to three framework oxygens with a formal charge of +5, contrary to their earlier work.[14]

In 2010 Xing *et al.*[15] published a DFT study, based on the earlier work of Zhou and co-workers,[13,14] that focused on identifying the Mo carbide species present during MDA over a Mo/H-ZSM-5 catalyst. The group simulated four different active site models: $Mo(CH_2)_2$/ZSM-5, $Mo(CH_2)_2CH_3$/ZSM-5, $Mo_2(CH_2)_4$/ZSM-5 and $Mo_2(CH_2)_5$/ZSM-5. The authors note all the proposed models to be reasonable, per DFT, and that all structures contain $Mo{=}CH_2$ bonds, they also report the system to exist with considerable π orbital conjugation. Since the calculated activation energy for C-H activation was considerably lower for $Mo_2(CH_2)_5$/ZSM-5, the authors postulate that this structure is the most likely Mo carbide species during MDA catalysis.[15]

One of the most comprehensive studies in this area is a combined experimental and theoretical study by Gao *et al.*[17], in which the authors used DFT coupled with multiple spectroscopic techniques to determine the nature of Mo-oxo species in ZSM-5, considering not only monomeric and dimeric MoO_x species, but also other MoO_x nanostructures. Following calcination, experimental evidence showed Mo to be in its +6 oxidation state. Through DFT, the authors demonstrated that neutral MoO_3 anchored to the framework was unstable, concluding that Al sites are necessary for binding the Mo-oxo species to the framework. Given this, and assuming Löwenstein's rule is valid, the authors state that $[MoO_2]^{2+}$ monomers cannot exist due to the inability of such a small molecule to bridge two Al sites that are not nearest neighbours, furthermore the DFT indicates that only Al atoms as NNN neighbours (Al-O-$(SiO)_2$-Al) can serve as anchoring sites for $[Mo_2O_5]^{2+}$ dimers, but only if these third neighbours exist in the same channel. However, using Raman spectroscopy, the authors demonstrate that this double anchoring is only viable at suitably low Si/Al ratios, at higher Si/Al ratios, where Al is scarce there is a preference for $Mo(O_2)OH$ to be di-coordinated to a single framework Al site. This structure contains two Mo=O bonds, and three Mo-O bonds, one to the hydroxyl oxygen (Mo-OH) and two to framework oxygen (Mo-O_F). In extremely siliceous frameworks they postulate that $[MoO_2]^{2+}$ monomers double anchor to two individual Si atoms at the external surface of the

zeolite crystal, however this binding is far less favourable than the double anchoring of the dimer species across third neighbour Al sites.[17]

Despite the abundance of studies that have been undertaken in this area, there is still a great deal of uncertainty regarding the identity of the catalytically active Mo species present during MDA over Mo/ZSM-5. Understanding the evolution of the Mo species is necessary to understanding the mechanism by which MDA proceeds, and henceforth improving the efficiency of MDA in terms of promoting MDA catalysis and impeding deactivation of the catalyst. The latter is particularly important, as deactivation by coking of the catalyst during MDA is currently the main limitation to the commercialisation of the MDA process. In this chapter, DFT is used to simulate the intermediate structures that evolve from Mo-oxide over the course of MDA over Mo/silicalite, the all-silica analogue of ZSM-5. Since silicalite contains no aluminium, it is thermodynamically more stable than ZSM-5, which is advantageous since MDA is generally carried out at high temperatures (973 K). DFT is also used to simulate the effect of the local framework environment on these species, focusing specifically on the presence of Al and silanol defects. The simulations were informed by experimental data provided by Professor Andrew Beale and his group at UCL, including Dr Ines Lezcano-Gonzalez and Miren Agote-Aran.[16,18]

6.2 Approach

In accordance with recent claims by Kosinov *et al.*[2] and Guo *et al.*,[19] Beale and co-workers found evidence of efficient MDA over Mo-containing silicalite (MFI). As silicalite contains no aluminium and hence no protons, such findings indicate that Brønsted acid sites are not essential for the aromatisation of methane. It follows that the reaction must proceed *via* a mono-functional mechanism over purely siliceous catalysts. This is contrary to much of the accepted wisdom in this area, and indicates that the molybdenum species plays a more significant role in catalysis than originally postulated. The aim of the work contained within in this chapter is to aid the understanding of the evolution of the molybdenum species in Mo/silicalite during MDA, and deduce whether there is any meaningful difference in the evolution of the Mo species in Mo/silicalite compared to Mo/ZSM-5.

Agote-Aran prepared a Mo-containing (4 wt% Mo) silicalite (Mo/silicalite) sample by mixing MoO_3 with the zeolite in an agate mortar. Following calcination, the sample was consequently analysed using a range of techniques. XRD showed the zeolite to be in

its orthorhombic form. UV-vis and XAS measurements were used to determine the initial geometry of the Mo-oxo species, both approaches indicated Mo to be octahedral and in its +6 oxidation state, *i.e.* MoO_3. XAS studies for *in situ* calcination of Mo/silicalite suggested evolution of the MoO_3 into isolated tetrahedral Mo-oxo species above 600 °C. Such findings are indicative of a $[MoO_4]^{2-}$ monomer species, containing two Mo=O double bonds and two Mo-O_F single bonds, and are consistent with previous findings for Mo/ZSM-5.[18]

The initial computational component of this investigation involved the geometry optimisation of a single orthorhombic MFI unit cell (Si/Al = ∞), obtained from the IZA zeolite structure database,[20] using CP2K[21,22] at the PBE[23] level of theory with a DZVP-MOLOPT basis. Following optimisation, the structure of the initial $[MoO_4]^{2-}$ tetrahedral species supported on the silicalite framework was investigated. The $[MoO_4]^{2-}$ species is known to have a similar structure to molybdate, $MoO_2(OH)_2$, hence molybdate was geometry optimised as an isolated cluster using the Orca code (PBE functional and SVP basis), to give a sensible starting geometry for $[MoO_4]^{2-}$. It is generally accepted that the initial Mo-oxo species exists in the framework interstitial sites of MFI, and is di-coordinated to the walls of the interstitial, hence $[MoO_2]^{2+}$ was grafted to two framework oxygen atoms (O_F) across the T5 site, forming $[MoO_4]^{2-}$. This structure was geometry optimised at the same level of theory as the empty silicalite framework.

Simulations for the evolution of this initial $[MoO_4]^{2-}$ species during MDA were based on the evolution scheme in Figure 6.2, proposed by Lezcano-Gonzalez *et al.* in a 2016 study on Mo/H-ZSM-5.[16] Despite previous computational work, which had focussed solely on simulating $MoOCH_2$ and $Mo(CH_2)_2$ intermediates, Agote-Aran found no evidence of Mo=C bonding in the Mo carbide/oxycarbide intermediates during MDA, hence such motifs were excluded from the simulations and only $MoOCH_3$ and $Mo(CH_3)_2$ models were considered.[18] All intermediate structures were geometry optimised using CP2K at the PBE level of theory.

FTIR studies suggested the initial migration and dispersion of the Mo-oxo species into the zeolite pores to be driven by the interaction between the metal centre and silanol defects present within the framework.[18] A similar phenomenon is observed between the Brønsted acidic sites and the metal centre in Mo/ZSM-5, as reported by Kosinov *et al.*[2] To simulate the effect of silanol nests on Mo-oxo evolution during MDA, Si was removed from the T5 sites in the initial empty silicalite structure satisfying the four

dangling Si-O bonds generated with terminating protons. The resultant structure was then geometry optimised at the same level of theory used throughout. Following this, $[MoO_2]^{2+}$ was re-introduced to the same position as before, removing the two protons from the framework oxygens bound to Mo, mimicking the condensation reaction that is proposed to occur when the initial mobile Mo-oxo species, generally accepted to be molybdate, is di-coordinated to the walls of the framework.[24]

In Mo/silicalite, the Mo-oxo species can be bound across terminal or vicinal silanol nests (Figure 6.3.). In the simulations described above, $[MoO_2]^{2+}$ is bound across two terminal silanol defects of a silanol nest, where in each case, a single OH is bound to a single Si atom. Vicinal defects are formed when two terminal silanols are adjacent to one another connected by bridging oxygen. It has been reported that the binding of $[MoO_2]^{2+}$ to non-vicinal silanols is more stable than vicinal hydroxyls in amorphous silica.[24] To investigated whether the same is true for microporous silicalite, vicinal and non-vicinal silanol defects were simulated by removing Si from the T5 and T9 in both the vicinal and non-vicinal case. $[MoO_2]^{2+}$ was then grafted cross the defects, removing two protons to mimic condensation reactions. The two structures were geometry optimised at the same level of theory used throughout this chapter.

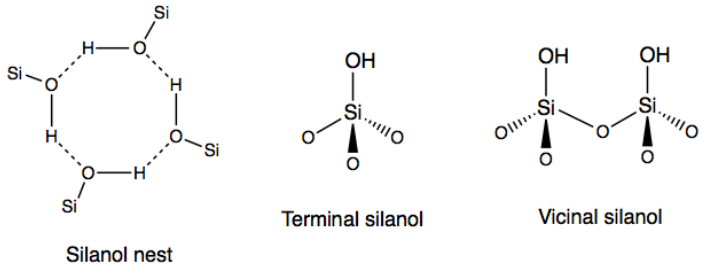

Figure 6.3 *Types of silanol defects that the Mo-oxo species has been proposed to bind across in silicates and aluminosilicate catalysts*

Whilst Mo/silicalite has been shown to catalyse MDA,[2,19] Mo/ZSM-5 is still the most efficient catalyst and is more resistant to coking than Mo/silicalite, especially compared to Mo/silicalite structures containing a high density of silanol defects. The Mo-oxo species–containing silicalite models were hence compared with that of Mo/ZSM-5 by introducing a single Al to each of the 12 crystallographically distinct framework T-site present in orthorhombic MFI. Brønsted acidic protons were not included in these simulations to mimic the liberation of water which is proposed to occur on binding of the initial Mo-oxo species to the walls of the framework. The Mo-oxo species remained

in the same position, grafted across the T5 site. To simulate the evolution of the Mo species in ZSM-5, hydrocarbon groups were introduced to each of the $[MoO_2]^{2+}$ oxygen sites sequentially. Each structure was geometry optimised at the same level of theory used throughout.

Only monomeric species were considered in this study as Beale and co-workers found no substantial evidence of dimeric species in their experimental analysis.

6.3 Characterisation of Mo species formed during MDA catalysis over Mo/MFI

6.3.1 Mo/silicalite

6.3.1.1 The structure of the initial Mo-oxo species

Previous experimental and computational studies have suggested that the initial Mo-oxo species present within the MFI framework during MDA over Mo/ZSM-5 is a di-coordinated $[MoO_2]^{2+}$ structure.[13,16] Hence, initial simulations were concerned with the optimisation of this structure. The fully geometry optimised structure is shown in Figure 6.4. This structure contains $[MoO_2]^{2+}$ grafted to the walls of the MFI framework intersection through two Mo-O_F bonds, where Mo is bound to two framework oxygen atoms across the T5 site. The Mo-oxo structure is a pseudo-tetrahedral structure (θ(O-Mo-O) = 118˚ and θ(O_F-Mo-O_F) = 63˚) containing two short Mo-O bonds with bond lengths of 1·73 Å and two longer Mo-O_F bonds with bond lengths of 2·33 Å. These bond lengths comparable to those observed experimentally in Mo/silicalite by Agote-Aran who reported Mo-O and Mo-O_F to be 1.69 Å and 2.31 Å, respectively.[18] In a 2001 Mo/ZSM-5 DFT study by Zhou *et al.*,[13] Mo-O and Mo-O_F bond lengths in the initial Mo-oxo were reported to be 1·72 Å and 2·11 Å. Whilst the there is good agreement between the Mo-O bond lengths, the Mo-O_F bond lengths reported by Zhou *et al.*,[13] are slightly shorter than those reported in this chapter. Discrepancies such as this could be due to differences in simulation method, Zhou and co-workers used the LDA functional, or because of the presence of Al. According to work by Agote-Aran, experimental values for Mo/ZSM-5 are shorter than those for Mo/silicalite, Mo-O = 1·69 Å and Mo-O_F =1·8 Å,[18] this is presumably due to interactions between the Mo-oxo species and aluminium or Brønsted acid sites.

It is generally accepted that this di-coordinated $[MoO_2]^{2+}$ species contains two double Mo=O bonds, and is bound to framework oxygen by two single Mo-O bonds. To establish whether bond lengths observed in these simulations equate to two Mo=O double bonds and two Mo-O single bonds, the bond lengths were compared to those

in molybdate, $MoO_2(OH)_2$. Molybdate is generally accepted to be the initial mobile Mo-oxo species present during MDA, and formally contains two double Mo=O bonds and two single Mo-O bonds. $MoO_2(OH)_2$ was geometry optimized as a cluster using DFT implemented the ORCA code at the PBE level of theory.[25] In accordance with the accepted theory, the optimised molybdate molecule contains two short Mo=O bonds with bond lengths of 1·71 Å, and two longer Mo-OH bonds with bond lengths of 1·93 Å. There is good agreement between the shorter bond lengths in the Mo-oxo/silicalite species and molybdate, hence it can be assumed that the Mo-oxo/silicalite species contains two Mo=O double bonds, in accordance with the literature.[13,16] However, there is a 0·40 Å discrepancy between the longer bonds in molybdate and the Mo-oxo/silicalite structure. These findings suggest that Mo-O_F bond length is too long to be considered a real bond. However, the Mulliken charges on the two framework oxygens 'bonded' to Mo (Mo-O_F) are more negative than charges on other framework oxygens, (-0·55 compared to a mean charge of -0·45 for the remaining framework oxygens). This indicates that an electrostatic interaction exists and crucially that charge transfer occurs between framework oxygens and Mo. It is notable that in a previous DFT study, Zhou *et al.*[13] also reported only weak bonding between framework oxygen and Mo, forming weak Mo-O_F covalent bonds with a large amount of ionic character. In this conformation, Mo has an oxidation state of +6.

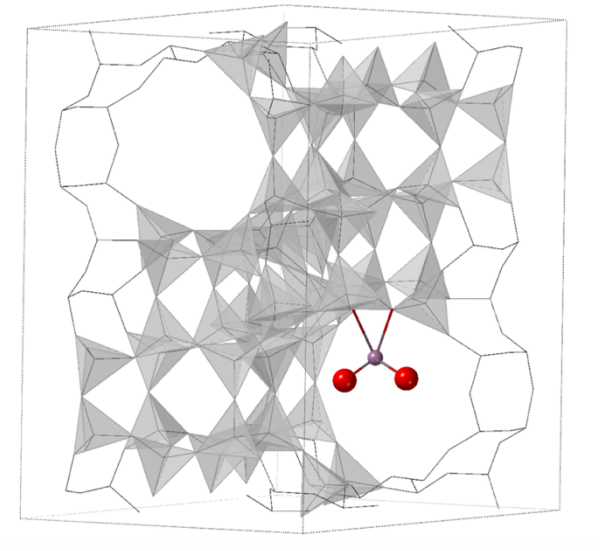

Figure 6.4 *Fully optimised structure of the initial Mo-oxo species supported on silicalite. In this structure* $[MoO_2]^{2+}$ *contains two double Mo=O bonds and is di-coordinated to the walls of the all-silica MFI framework by two long Mo-*O_F *bonds. Where the framework is represented by grey tetrahedra, Mo is purple and oxygen is red.*

6.3.1.2 The evolution of molybdenum oxide intermediates during catalysis

The formation of Mo oxycarbide structures from the di-coordinated Mo-oxo/silicalite according to the evolution scheme in Figure 6.2 were then examined. Inspection of the initial Mo oxycarbide $[MoOCH_3]^{2+}$ involved the generation of two distinct models from the optimised Mo-oxo/species, with the methyl group substituted into the one of the two available oxygen sites. The fully geometry optimised forms of these structures are shown in Figure 6.5.

Prior to optimisation, the $MoOCH_3$ components of each structure were seemingly identical in terms of geometry, and only differed in the relative position of the methyl group and double-bonded oxygen. However, following optimisation one of the structures, Figure 6.5a, is 6·6 kJ mol^{-1} more stable than the other, 0·8 *k*T at typical working catalytic temperatures (973 K). It is therefore likely that these structures would degenerate at catalytic temperatures.

In both structures, Mo-O has a bond length of 1·78 Å, and hence can be regarded as a Mo=O double bond, this is in accordance with what has been reported in the literature. For the lower energy structure (Figure 6.5a), the Mo-O_F bond lengths are 2·09 Å, 3·04 Å. Mulliken population analysis suggests that in both cases only a single framework oxygen is interacting with Mo, hence $MoOCH_3$ is mono-coordinated to the walls of the framework, this is contrary to what is postulated in the literature.[15,16] Given the enhanced stability of the structure shown in Figure 6.5a, there seems to be a preference for the formation of a shorter, stronger Mo-O_F bond, rather than the formation of two much weaker, longer bonds. Mulliken population analysis also indicates that a nearby silicon is interacting directly with Mo (Mo-Si = 2·56 Å) in both structures; the charge on nearby Si is slightly more negative than the mean charge on the other framework Si atoms (the Si charge is +0·78 compared to a mean Si charge of +0·90). The Mo-Si interactions cause severe framework distortions, stretching the adjacent Si-O linkage to ~1·88 Å in both frameworks. In real systems, it is likely that such distorted bonds would break and interact with water molecules present within the framework. Similar interactions between Al and Mo in Mo-oxo/ZSM-5 structure were observed by Zhou and co-workers. The authors concluded these interactions to be due to outer-orbital overlap between Al and Mo.[13] The Mo-C bond lengths (2·10 Å) are comparable with those reported for single Mo-C bonds in previous theoretical studies,[15] hence in this conformation Mo has a formal oxidation state of +4, contrary to what is shown in the evolution scheme in Figure 6.2.[16]

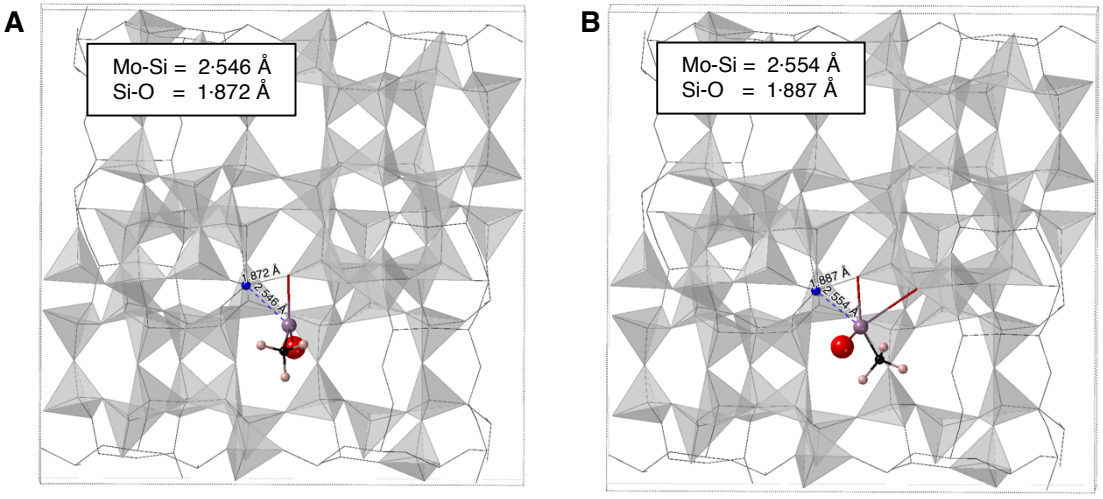

Figure 6.5 *Fully optimised structures of the initial Mo oxycarbide species formed during MDA over Mo/silicalite. Structure* ***a*** *is the most stable structure. In both structures* $MoOCH_3$ *contains one double Mo=O bond and is mono-coordinated to the walls of the all-silica MFI framework by one long Mo-*O_F *bond, although a second framework oxygen is within bonding distance in structure* ***b****. There is also an interaction between a nearby framework Si atom and Mo in both structures, this interaction causes significant framework distortions, particularly in the stretching of an Si-O bond. Where the framework is represented by grey tetrahedra, Mo is purple, oxygen is red, carbon is black and hydrogen is pink.*

Using both structures (Figure 6.5a) as initial structures, evolution of the $MoOCH_3$ species to one containing two methyl groups, $Mo(CH_3)_2$, was examine. Figure 6.6 shows the structures of the two $Mo(CH_3)_2$ models following geometry optimisation.

Curiously, the structure derived from the slightly less stable structure (Figure 6.6b) is the global minimum structure by 5·0 kJ mol^{-1}, although both structures would likely be degenerate at working catalytic temperatures ($\Delta E = 0{\cdot}6\ kT$ at 973 K). As was the case for the $MoOCH_3$ species, bond distances in both $Mo(CH_3)_2$ containing structures indicate that only one framework oxygen is bound to framework oxygen, Mo-O_F is 1·90 Å in both cases, this bond length is comparable with a single Mo-OH bond in molybdate. However, Mulliken population analysis suggest that there is no interaction between Mo and the surrounding framework oxygen atoms. However, in accordance with what was found for the $MoOCH_3$ species and the work of Zhou *et al.*,[13] Mulliken

population analysis suggests that there is a strong interaction with a nearby framework Si (Si charge is +0·71 compared to a mean Si charge of +0·90). The Mo-Si separation is 2·47 Å, slightly shorter than in the $MoOCH_3$/silcalite structure, framework distortions in this structure are also greater, and in this structure the Si-O linkage with a nearby oxygen is stretched to approximately 2·9 Å in both structures. This suggests that the interaction of Mo with Si is favourable enough to overcome the breaking of framework Si-O bonds.

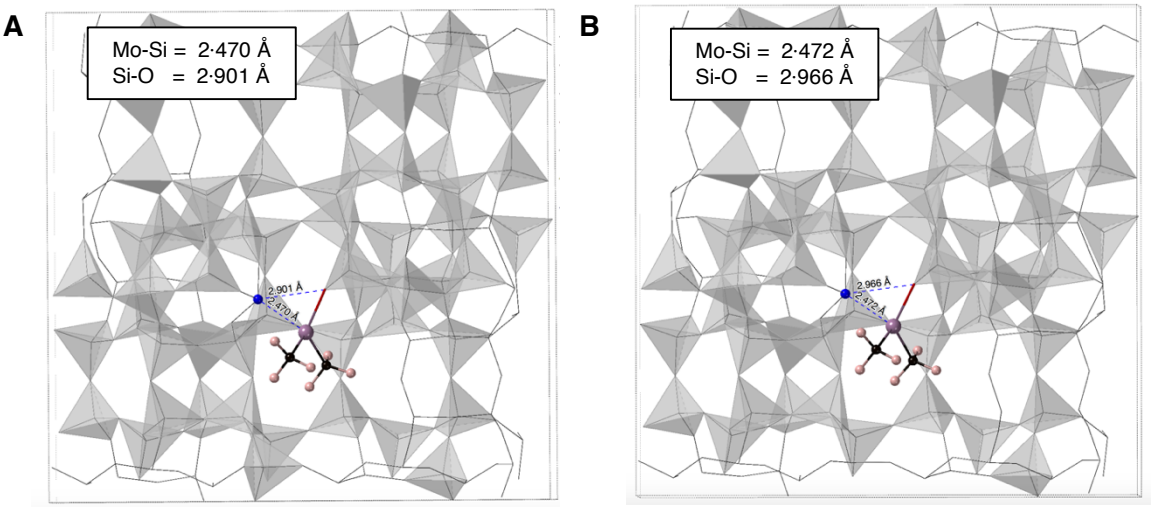

Figure 6.6 *Fully optimised structures of the second Mo oxycarbide species formed during MDA over Mo/silicalite. Here, structure* ***b*** *is the most stable structure. In both structures $Mo(CH_3)_2$ contains one double Mo=O bond and is mono-coordinated to the walls of the all-silica MFI framework by one long Mo-O_F bond. There is also an interaction between a nearby framework Si atom and Mo in both structures, this interaction causes significant framework distortions, particularly in the stretching of an Si-O bond. These distortions are more severe than those shown in the $MoOCH_3$/silicalite structure shown in Figure 6.5. Where the framework is represented by grey tetrahedra, Mo is purple, oxygen is red, carbon is black and hydrogen is pink.*

6.3.1.3 The effect of silanol defects

Silanol defects are known to exist in real silicalite samples[18] and many other zeolites.[26–30] To ascertain the effect of silanol defects on the binding of the initial Mo-oxo to the walls of the framework, a range of silanol-containing Mo/silicalite structures were examined.

As explained in the Approach section of this chapter, the presence of silanol nests were simulated through the removal of a single Si atom from the T5 sites. The four dangling Si-O bonds generated by the introduction of the vacant site were satisfied by the presence of hydroxyls. $[MoO_2]^{2+}$ was then di-coordinated across the now vacant T5 site, with the removal of two protons, simulating binding across two terminal silanol defects by condensation reaction. The fully geometry optimised form of this structure is shown in Figure 6.7. This structure contains two short Mo=O bonds with equivalent bond lengths of 1·69 Å, comparable to those reported for the Mo-oxo species supported on silanol-free silicalite in section 6.3.1 (Mo-oxo/silicalite Mo=O = 1·73 Å) and with that of experiment.[18] However, Mo-O_F bond lengths are much shorter than those reported for the Mo-oxo species supported on silanol-free silicalite in section 6.3.1 (Mo-oxo/silicalite Mo-O_F = 2·33 Å), with one bond slightly longer than the other, Mo-O_F = 1·90 Å and 1·88 Å. These bond lengths are in accordance with the single Mo-OH bond lengths present in geometry optimized molybdate (Mo-OH = 1·93 Å). However, these lengths are shorter than the Mo-O_F bond lengths reported for the initial Mo-oxo species in silicalite by Beale *et al.* Hence, it can be assumed that in these samples, the Mo-oxo species is bound to a different type silanol defect site.

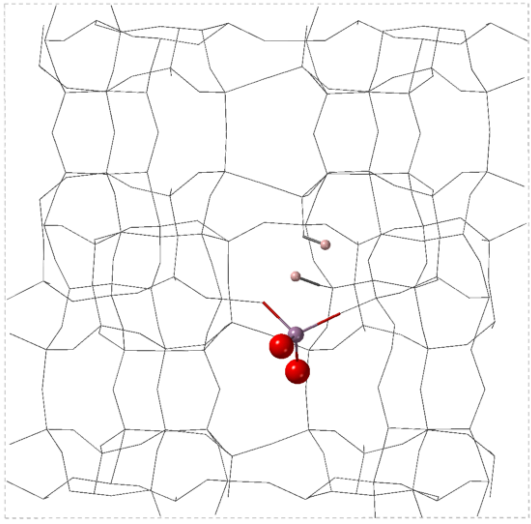

Figure 6.7 *The fully geometry optimised form of the initial Mo-oxo species bound across two terminal silanol defects in a silanol nest in Mo/silicalite. Here,* $[MoO_2]^{2+}$ *contains two Mo=O double bonds and is di-coordinated across the vacant T5 site by two short Mo-*O_F *bonds. Where the framework is shown as stick bonds, Mo is purple, oxygen is red and hydrogen is pink.*

A 2014 DFT study by Guesmi *et al.*[24] demonstrated that non-vicinal silanol defects are the most stable sites for the binding of molybdenum monomeric oxide species in amorphous silica. The authors concluded that the preference for anchoring at non-vicinal silanol groups is due to the increased flexibility of these sites compared to vicinal sites and geminal silanol defects. To establish whether the same trends can be extended to zeolitic systems, the relative stability of Mo-oxo coordination at different silanol defects in silicalite was examined. Guesmi and co-workers reported geminal sites to be highly unstable due to their rigidity,[24] hence only vicinal and non-vicinal sites were considered.

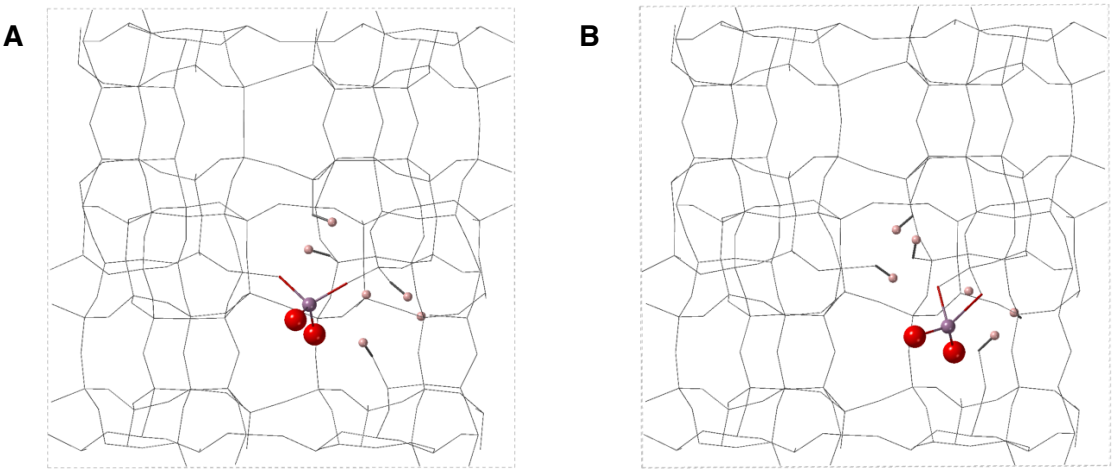

Figure 6.8 *The fully geometry optimised form of the initial Mo-oxo species bound across two silanol nests, at the T5 and T9 sites in different ways* ***a)*** *across vicinal defects* ***b)*** *across non-vicinal defects. In both structures* $[MoO_2]^{2+}$ *contains two Mo=O double bonds and is di-coordinated across the vacant T-sites by two short Mo-*O_F *bonds. Where the framework is shown as stick bonds, Mo is purple, oxygen is red and hydrogen is pink.*

The fully optimised structures of $[MoO_2]^{2+}$ bound across vicinal and non-vicinal silanol groups are shown in Figure 6.8. In these structures, Si has been removed from the T5 and T9 sites and the resulting dangling bonds are satisfied by hydroxyls, simulating the presence of two silanol nests per MFI unit cell. The calculations suggest that bonding to vicinal OHs is more stable than non-vicinal by 52 kJ mol^{-1}, contrary to the work by Guesmi *et al.*[24] The bond lengths in these structures are Mo=O = 1·70 Å and Mo-O_F = 1·90 Å and 1·88 Å for binding across the vicinal site and Mo=O = 1·70 Å and Mo-O_F = 1·97 Å and 2·08 Å. Mulliken population analysis suggests that Mo is interacting with

both framework oxygens, hence it appears that binding at vicinal sites is preferred due stronger, more equal coordination to the framework. The Mo-O_F bonds in these simulations are also shorter than those observed in real Mo/silicalite samples by Agote-Aran (Mo-O = 1·69 Å and Mo-O_F =2·11 Å).[18] These simulations hence suggest that it is unlikely that the Mo-oxo species is exclusively bound across silanol defect sites in these samples. However, it should be noted that MDA catalysis proceeds at high temperatures (973 K), it is therefore likely that during MDA catalysis the Mo-oxo species is located further from the framework than suggested in these calculations, which are performed at 0 K.

6.3.2 Mo/ZSM-5

Mo/silicalite has only been demonstrated to catalyse MDA in recent years, and the majority of the existing data concerning the identity of Mo species in MDA catalysts is predominantly focused on Mo/ZSM-5. To examine effect of Al on Mo speciation during MDA over Mo/MFI, the evolution of the Mo species in Mo/ZSM-5 was simulated using the same methodology used for Mo/silicalite.

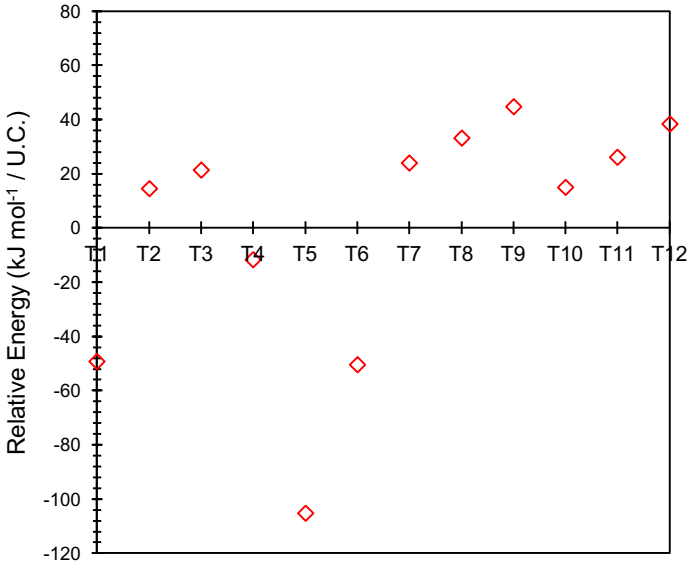

Figure 6.9 *Relative energy distribution of 12 different Mo-oxo/ZSM-5 structures. Each zeolite structure contains 1 Al per U.C. positioned at one of the 12 crystallographically distinct framework T-sites present in MFI. T1-12 denotes the T-site at which Al is located.*

As explained in the Approach section of this chapter, Al was introduced into each of the 12 crystallographically distinct T-sites present in the orthorhombic MFI unit cell.

The initial Mo-oxo species was then introduced to the framework in the form of $[MoO_2]^{2+}$ di-coordinated across the T5 site.

The DFT data for the Mo-oxo species supported 1 Al per U.C. ZSM-5 is shown in Figure 6.9. According to this data, the global minimum structure (Figure 6.10a) contains Al at the T5 site. In accordance with what was observed for the initial Mo-oxo species in Mo/silicalite, the $[MoO_2]^{2+}$ species contains two The Mo=O double bonds with bond lengths of are 1·70 Å and is bound across the T5 site by two Mo-O_F bonds. In this case the Mo-O_F bonds are 2·13 Å, slightly shorter than the 2·33 Å bonds observed in the analogous Mo/silicalite structure. These results are in keeping with experimental data by Agote-Aran who reported the Mo-O_F bonds to be shorter in the initial Mo-oxo species in Mo/ZSM-5 (Si/Al = 15) than in Mo/silicalite.[18]

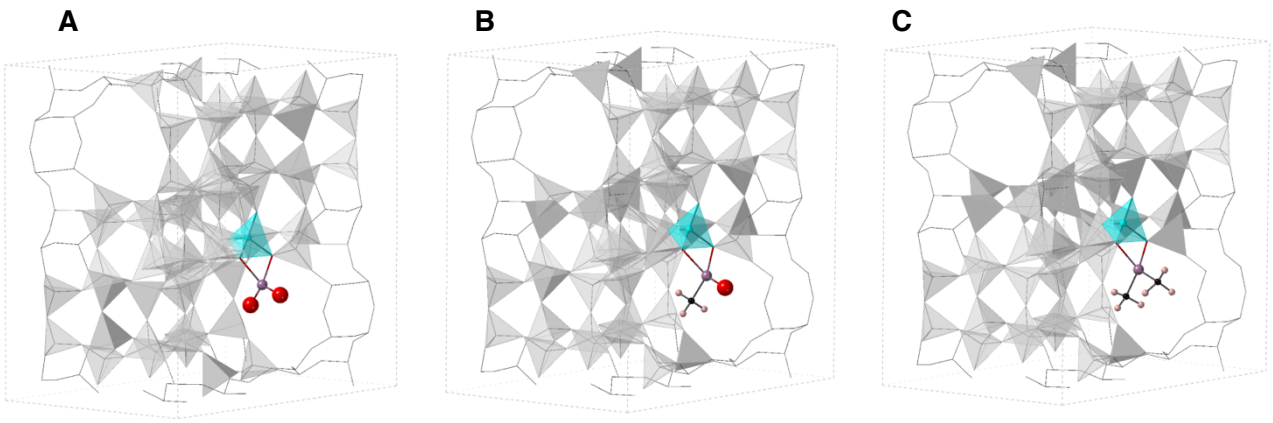

Figure 6.10 *Evolution of the initial Mo-oxo species into $MoOCH_3$ and $Mo(CH_3)_2$ oxycarbide species during MDA over Mo/ZSM-5 according to DFT. In each structure, the Mo species is di-coordinated to the walls of the zeolite framework across Al which prefers to sit at the T5 site.*

Further simulations show that there are marked differences between the evolution of the initial Mo-oxo species into $MoOCH_3$ and $Mo(CH_3)_2$ oxycarbide species (Figure 6.10) during MDA over Mo/ZSM-5 compared to Mo/silicate. Contrary to what was found for Mo/silicalite, the formation of the oxycarbide structures in Mo/ZSM-5 proceeds according to the evolution scheme shown in Figure 6.2.[16] Both $MoOCH_3$ and $Mo(CH_3)_2$ oxycarbide species are di-coordinated to the framework, with Mo-O_F bonds of 2·18 Å and 2·19 Å for $MoOCH_3$/silicalite, and 2·15 Å and 2·17 Å for $Mo(CH_3)_2$/silicalite.

Furthermore, there are no discernible interactions between the Mo oxycarbide species and framework silicon in Mo/ZSM-5. Such distinct differences in the evolution of the two structures illustrates the influence of framework Al on the orientation and identity of Mo species in MDA catalysts.

All Mo/ZSM-5 simulations showed the T5 site to be the most stable site for Al substitution. This is in accordance with experimental work by Mentzen *et al.*[31,32] who showed the T5, T7, T9 and T12 sites to be the most preferred sites for Al substitution in ZSM-5. Whilst there are several studies which suggest that Al substitution at other T-sites is more stable, there no suggestions in the literature that the T5 site is the most unstable site for Al substitution.[33–38] It is noteworthy to mention that the T12 site is the site most frequently chosen for Al substitution in ZSM-5 catalysis studies,[36,39–44] however the DFT data in this section shows the T12 site to be particularly unstable. Differences between the literature and the DFT data included in this section are most likely due to the position of the Mo species being maintained across the T5 site all Al-containing structures throughout these simulations.

6.4 Conclusions

In this chapter, DFT was used to model the evolution of the active Mo species during MDA catalysis over Mo/silicalite. MDA typically proceeds over Mo/ZSM-5, however, at present, the MDA process is yet to be commercialised due to rapid deactivation of the catalyst by coking. Besides rapid coking of the catalyst, MDA is also a thermodynamically unfavourable endothermic process, hence high temperatures (973 K) are required to produce a sufficient yield of benzene. Mo/silicalite, which has been shown to catalyse MDA despite the absence of Brønsted acidic sites, is considered to be a viable alternative to Mo/ZSM-5. All-silica silicalite is more thermally stable than aluminium-containing ZSM-5, hence, MDA over Mo/silicalite can theoretically be run at higher temperatures, increasing the product yield.

Whilst MDA catalysis over Mo/ZSM-5 has been known for the past few decades,[2,19] the ability of aluminium-free systems to catalyse such reactions is a relatively new finding. One that provides direct evidence that it is possible for MDA to proceed in the absence of Brønsted acid sites, widely thought to be integral to catalysis, which is generally accepted to proceed *via* a bi-functional mechanism. Catalysis over Mo/silicalite hence provides evidence that MDA can proceed efficiently *via* a mono-functional mechanism, and furthermore that neither Brønsted acidic sites nor

aluminium are required for the catalytically active Mo species to bind to the walls of the framework. The DFT simulations contained within this chapter provide further evidence that the binding of the Mo species to the all-silica framework is not only stable, but favoured in all cases. This is contrary to the recent work of Gao *et al.* who reported Al to be necessary for anchoring of the Mo-oxo species in ZSM-5.[17]

There is good correlation between the theoretical data and that provided by Agote-Aran for the structure and binding of the Mo-oxo species to the walls of the silicalite framework.[18] Simulations of silanol-containing frameworks show a distinct decrease in the Mo-O_F bond length compared to that where Mo is bound to a defect-free portion of the framework. It is unclear why there is such a pronounced decrease in the Mo-O_F bond length in silanol-containing structures compared to defect-free structures, however it could be due to increased framework flexibility introduced by the vacant T-site. The discrepancies between theory and experiment suggest that the Mo-oxo species is not exclusively coordinated to silanol defects in experimental samples. However, it is plausible that at catalytic temperatures the Mo-oxo species resides further away from the framework than indicated from these simulations.

The DFT data indicates that the evolution of the Mo species proceeds *via* the scheme shown in Figure 6.11 during the initial stages of MDA catalysis over Mo/silicalite. The initial Mo-oxo species is identical to that proposed for Mo/ZSM-5 by Lezcano-Gonzalez *et al.*[16] in Figure 6.2. However, subsequent evolution of the Mo-oxo species to Mo oxycarbide species is distinctly different in Mo/silicalite. Mono-coordination is preferred on the formation of the Mo oxycarbide species, forming a +4 Mo species immediately from the +6 Mo-oxo species.

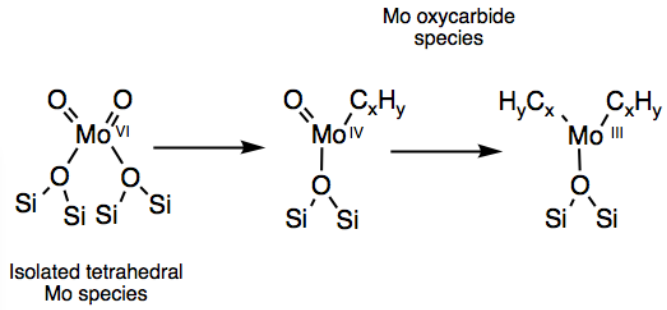

Figure 6.11 *Evolution of the Mo species during the initial stages of MDA over Mo/silicalite according to DFT*

Simulations of Mo speciation in Mo/ZSM-5 corroborate the findings of Lezcano-Gonzalez *et al.*[16] Marked differences between the evolution of the Mo-species during MDA over Mo/silicalite and Mo/ZSM-5, shown in Figures 6.11 and 6.2, respectively, demonstrate the strong influence of Al over Mo speciation in MDA catalysts. Experimental work by Agote-Aran demonstrated Mo/ZSM-5 to be a more efficient MDA catalyst than Mo/silicalite, as this catalyst was found to be more resistant to deactivation through the formation of carbonaceous deposits. Agote-Aran postulated that deactivation of the catalyst is caused by migration of the Mo species to the external surface of the crystal, hence rapid deactivation is observed in Mo/silicalite compared to Mo/ZSM-5 due to the instability of molybdenum active species grafted to the walls of the zeolite. The work contained within this chapter indicates that differences in the relative stabilisation of the molybdenum active species inside the zeolite pores may be due to differences in coordination mode for Mo/ZSM-5 and Mo/silicalite. The DFT data shows that there is a preference for Mo oxycarbide species to be mono-coordinated to the walls of silicalite, and di-coordinated to the walls of ZSM-5. Liberation of the Mo species is therefore likely to be easier in Mo/silicalite than in Mo/ZSM-5, leading to rapid catalyst deactivation.

6.5 References

1. Spivey, J.J. & Hutchings, G. *Chem. Soc. Rev.* **43,** 792–803 (2014).
2. Kosinov, N., Coumans, F.J.A.G., Uslamin, E.A., Wijpkema, A.S.G.,Mezari, B., Hensen, E.J.M. *ACS Catal.* **7,** 520–529 (2017).
3. Mériaudeau, P., Tiep, L.V., Ha, V.T.T., Naccache, C., Szabo, G. *J. Mol. Catal. A Chem.* **144,** 469–471 (1999).
4. Mériaudeau, P., Ha, V.T.T., Tiep, L. Van. *Catal. Letters* **64,** 49–51 (2000).
5. Ismagilov, Z.R., Matus, E.V, Tsikoza, L.T. *Energy Environ. Sci.* **1,** 526–541 (2008).
6. Weckhuysen, B.M., Wang, D., Rosynek, M.P., Lunsford, J.H. *Angew. Chemie Int. Ed. English* **36,** 2374–2376 (1997).
7. Shu, J., Adnot, A., Grandjean, B.P.A. *Ind. Eng. Chem. Res.* **38,** 3860–3867 (1999).
8. Liu, S., Wang, L., Ohnishi, R., Ichikawa, M. *J. Catal.* **181,** 175–188 (1999).
9. Solymosi, F., Cserényi, J., Szöke, A., Bánsági, T., Oszkó, A. *J. Catal.* **165,** 150–161 (1997).
10. Honda, K., Chen, X., Zhang, Z. G. *Catal. Commun.* **5,** 557–561 (2004).
11. Li, W., Meitzner, G.D., Borry, R.W. & Iglesia, E. *J. Catal.* **191,** 373–383 (2000).

12. Kim, Y.-H., Borry, R.W., Iglesia, E. *Microporous Mesoporous Mater.* **35,** 495–509 (2000).
13. Zhou, D., Ma, D., Liu, X., Bao, X. *J. Chem. Phys.* **114,** 9125–9129 (2001).
14. Zhou, D., Zhang, Y., Zhu, H., Ma, D., Bao, X. *J. Phys. Chem. C* **111,** 2081–2091 (2007).
15. Xing, S., Zhou, D., Cao, L., Li, X. *Chinese J. Catal.* **31,** 415–422 (2010).
16. Lezcano-Gonzalez, I. Oord, R., Rovezzi, M., Glatzel, P., Botchway, S.W., *Angew. Chemie - Int. Ed.* **55,** 5215–5219 (2016).
17. Gao, J., Zheng, Y., Jehng, J.-M., Tang, Y., Wachs, I.E., Podkolzin, S.G. *Science* **348,** 686–690 (2015).
18. Agote-Aran, M. PhD thesis: Identification of structure-activity relationships in molybdenum and iron-containing zeolites used in methane dehydroaromatisation and NO_x reduction (UCL, 2018).
19. Guo, X. Fang, G., Li, G., Ma, H., Fan, H., Yu, L., Ma, C., Wu, X., Deng, D., Wei, M., Tan, D., Si, R., Zhang, S., Li, J., Sun, L., Tang, Z., Pan, X., Bao, X. *Science* **344,** 616–619 (2014).
20. IZA-SC. *Database of zeolite structures* Available at: http://www.iza-structure.org/databases/
21. CP2K: Available at: https://www.cp2k.org/.
22. VandeVondele, J., Krack, M., Mohamed, F., Parrinello, M., Chassaing, T., Hutter, J. *Comput. Phys. Commun.* **167,** 103–128 (2005).
23. Perdew, J.P., Burke, K., Ernzerhof, M. *Phys. Rev. Lett.* **78,** 1396–1396 (1997).
24. Guesmi, H., Gryboś, R., Handzlik, J., Tielens, F. *Phys. Chem. Chem. Phys.* **16,** 18253–18260 (2014).
25. Neese, F. *Rev. Comput. Mol. Sci* **2,** 73–78 (2012).
26. Kobe, J.M., Gluszak, T.J., Dumesic, J.A., Root, T.W. *J. Phys. Chem.* **99,** 5485–5491 (1995).
27. Dzwigaj, S., Massiani, P., Davidson, A., Che, M. *J. Mol. Catal. A Chem.* **155,** 169–182 (2000).
28. Janin, A., Maache, M., Lavalley, J.C., Joly, J.F., Raatz, F., Szydlowski, N. *Zeolites* **11,** 391–396 (1991).
29. Hunger, M., Kärger, J., Pfeifer, H., Caro, J., Zibrowius, B., Bülow, M., Mostowicz, R. *J. Chem. Soc. Faraday Trans. 1 Phys. Chem. Condens. Phases* **83,** 3459 (1987).
30. Kondo, J.N., Yoda, E., Ishikawa, H., Wakabayashi, F., Domen, K. *J. Catal.* **191,** 275–281 (2000).

31. Mentzen, B.F., Bergeret, G., Emerich, H., Weber, H.-P. *J. Phys. Chem. B* **110,** 13741–52 (2006).
32. Mentzen, B. F. & Bergeret, G. *J. Phys. Chem. C* **111,** 12512–12516 (2007).
33. Ghorbanpour, A., Rimer, J.D., Grabow, L.C. *Catal. Commun.* **52,** 98–102 (2014).
34. Ruiz-Salvador, A.R., Grau-Crespo, R., Gray, A.E., Lewis, D.W. *J. Solid State Chem.* **198,** 330–336 (2013).
35. Fripiat, J.G., Andr, F.B.J., Derouanet, E.G. **3,** 306–310 (1983).
36. Lonsinger, S.R., Chakraborty, A.K., Theodorou, D.N., Bell, A.T. *Catal. Letters* **11,** 209–217 (1991).
37. Yokoi, T., Mochizuki, H., Namba, S., Kondo, J.N., Tatsumi, T. *J. Phys. Chem. C* **119**, 15303–15315 (2015).
38. Xing, B., Ma, J., Li, R., Jiao, H. *Catal. Sci. Technol.* **7,** 5694–5708 (2017).
39. Brändle, M. & Sauer, J. *J. Am. Chem. Soc.* **120,** 1556–1570 (1998).
40. Kustov, L. M., Kazanskii, V. B., Beran, S., Kubelkova, L., Jiru, P. *J. Phys. Chem.* **91,** 5247–5251 (1987).
41. Joshi, K.L., Psofogiannakis, G., van Duin, A.C.T., Raman, S. *Phys. Chem. Chem. Phys.* **16,** 18433–18441 (2014).
42. Kim, S., Evans, T.,J., Mukarakate, C., Bu, L., Beckham, G.T., Nimlos, M.R., Paton, R.S., Robichaud, D.J. *ACS Sustain. Chem. Eng.* **4,** 2615–2623 (2016).
43. Charoenwiangnuea, P., Maihom, T., Kongpracha, P., Sirijaraensre, J., Limtrakul, J. *RSC Adv.* **6,** 105888–105894 (2016).
44. Knott, B.C., Nimlos, C.T., Robichaud, D.J., Nimlos, M.R., Kim, S., Gounder, R. *ACS Catalysis* **8,** 770–784 (2018).

Chapter 7: Conclusions and outlook

The intention of this study was to investigate the most thermodynamically stable Al distributions in industrially important zeolites at a range of Si/Al ratios. Al arrangement was examined at different levels in the zeolite structure, starting with short-range Al distribution over framework T-sites and progressing on to long-range Al distribution throughout the zeolite crystal. Initial simulations involved rudimentary models, in which the only extra-framework species considered were counter-cations. This approach allowed the relative effects of cation identity, Si/Al ratio and framework-type on Al distribution to be established before moving on to more complex models in which other extra-framework materials, such as the synthesis template and water, were included. In the final chapter of this study, the effect of the presence of Al, or lack thereof, on Mo speciation during the process of methane dehydroaromatisation (MDA) over Mo/MFI zeolites was examined, these simulations were informed by experimental data for real Mo/MFI catalysts provided by experimental collaborators.

Chapter 3 involved the systematic study of Al distribution across framework T-sites in zeolite frameworks. Although a range of zeolite types were investigated in this chapter, the majority of the work was concerned with Al arrangement in small-pore zeolite SSZ-13 (CHA) in its protonated and alkali metal-containing forms at a range of Si/Al ratios. Contrary what has generally been accepted in zeolite science for the past 60 years, the work contained within this chapter provides evidence that the most thermodynamically favourable and thermally accessible Al distributions in protonated zeolites are non-Löwensteinian distributions. It is important to note that Al-O-Al linkages are actually unstable in these frameworks, and only frameworks containing Al-O(H)-Al linkages, where adjacent Al^{3+} ions are linked by a bridging hydroxyl moiety are stable. This bridging hydroxyl stabilises the framework by maximising the number of long Al-OH linkages, hence minimising the number of short, strong Si-O linkages present within the framework. It is likely that the bridging hydroxyl also shields the negative charges, arising from Al on either side, from one another, permitting Al pairs to be positioned nearer to one another than predicted by Löwenstein's and Dempsey's rule.[1,2] Clustering of Al at lower Si/Al corroborates these conclusions.[3]

Such findings cannot be extended to alkali metal-containing frameworks, which show a preference for Löwensteinian ordering. In both Na-SSZ-13 and Li-SSZ-13 at a Si/Al

ratio of 17, equivalent to 2 Al per hexagonal CHA unit cell, there is a distinct preference for Al pairs to be arranged in the next-next nearest neighbour (NNNN) position. However, for Li-SSZ-13 the two Al atoms are located in different D6R units, whereas in Na-SSZ-13 they are arranged along a single 6-ring of a D6R. Furthermore, there are marked differences in cation site preference; both Li^+ cations are positioned in the SII position, where the two Na^+ cations are positioned at the SII and SIII positions. In higher silica structures, there is a preference for Na^+ to reside at the SII position. Such findings are in keeping with recent work in this area.[4]

The distinct differences between the most thermodynamically stable aluminium distributions in protonated frameworks compared to alkali-metal containing frameworks demonstrates the influence of counter-cation identity on framework aluminium location. Furthermore, because SSZ-13 is typically synthesised from a sodium solution in the presence of an SDA, according to the predictions contained in Chapter 3 the most likely distribution of Al in real SSZ-13 samples will be most similar to that predicted for Na-SSZ-13. Given that the direct synthesis of proton compensated zeolites has not yet been achieved, and assuming Al rearrangement does not occur during the cation-exchange process, the predictions contained in Chapter 3 indicate that real H-SSZ-13 samples obtained through ion-exchange from as-synthesised Na-SSZ-13 samples exhibit thermodynamically 'frustrated' framework Al distributions.

The work contained in Chapter 4 provides evidence that 'frustrated' Al distributions in protonated zeolites may in fact be two-fold, indicating that both the short-range distribution of Al over T-sites and the long-range distribution of Al throughout the zeolite crystal are thermodynamically disfavoured. In keeping with the findings of Chapter 3, this is due to differences in long-range Al distribution between protonated and sodium-containing SSZ-13 crystals. The DFT data indicates that Al prefers to be more homogenously distributed and deeper into the bulk of Na-containing SSZ-13 crystals, whereas there is a preference for Al-zoning in protonated SSZ-13 crystals. The heterogeneity in the distribution of Al in protonated frameworks originates from the thermodynamic preference for Al clustering in these zeolites, as established in Chapter 3. The preference for Al clusters to exist at the external surface of the protonated-form of the zeolite is driven by the stabilisation of structures containing surface Al on the formation of water at the external surface, *via* the migration of Brønsted acidic protons to terminating hydroxyl groups. Such findings are in keeping with previous computational work by Rey *et al.*[5] in which the thermodynamically most stable external

surface sites of zeolite Beta (BEA) were shown to be Q3 Al-H_2O. It should be noted that similar stabilisations were not observed on forming NaOH at the surface of sodium-containing zeolite structures.

It is well established that post-synthesis treatment methods, such as steaming, can facilitate solid-state framework Al rearrangements in real zeolite samples.[6,7] Following this notion, it is hence conceivable that frustrated framework Al distributions in protonated zeolites may be overcome by steaming the zeolite. Furthermore, it is also conceivable that such atom rearrangements could be facilitated by inadvertent steaming of the zeolite during routine calcination. In Chapter 4, the possibility that such phenomena are responsible for the existence of extra-framework Al is rationalised in terms of the relative ease of removing 'frustrated' Al from the framework compared to reinsertion of Al into framework T-sites that are already occupied by silicon. However, at present this argument is only speculative. Further investigation, involving the quantification of the energy barriers to Al → vacancy and Si → Al + H substitutions, is required to affirm this postulation.

Whilst the DFT work contained within Chapters 3 and 4 is extensive relative to previous theoretical studies on Al distribution, the models included in those chapters neglect to include the presence of the synthesis template. Typical synthesis of SSZ-13, according to the recipe by Zones *et al.*,[8–10] involves an N,N,N-trimethyl-1-ammonium adamantane hydroxide template, which prevents the formation of more stable competing phases, such as analcime or quartz, during synthesis.[10] It has been demonstrated that short-range Al distribution over T-sites can be controlled through an adept choice of template during zeolite synthesis,[11–16] furthermore, the synthesis template is also known to influence the long-range distribution of Al throughout the zeolite crystal.[5] Hence, for completeness, the short-range Al distribution in SSZ-13 was re-examined using models containing the synthesis template in its cationic form, allowing the relative Al directing ability of the SDA in relation to the counter-cations (Na^+ and H^+) to be established. The results for these simulations (Chapter 5) demonstrated that whilst the SDA possesses some Al directing ability, in the presence of Na^+ and H^+ counter-cations the influence of the SDA on Al arrangement is greatly reduced. The diminished influence of the SDA over Al distribution compared to the Na^+ and H^+ counter-cations is primarily due to sterics and the decreased charge/size ratio of the SDA. Moreover, simulations of SDA/Na-SSZ-13 structures in which the Na^+ cation is considered to be in its fully-hydrated form $[Na(H_2O)_6]^+$ also showed a preference for Löwensteinian

ordering, in keeping with the DFT data for the purely sodium-compensated structures in Chapter 3. In this structure, Al pairs are arranged as NNNN and Na^+ is located in the SII site, in accordance with the work contained in Chapter 3, and the recent literature.[4] It is noteworthy that the preference for Löwensteinian ordering in both the hydrated and dehydrated SDA/Na-SSZ-13 structure is increased compared to the structure purely compensated by Na^+ at the same Si/Al ratio. This is due to increased influence of Al-Al repulsions in these structures which can be attributed to the poor Al-compensating ability of the SDA and the hydrated Na^+ cation, such observations are in accordance with Dempsey's rule[2] and the work of Ruiz-Salvador *et al.*[19] Furthermore, an increased preference for non-Löwensteinian ordering was observed in the SDA/H-SSZ-13 this is also due to the poor Al-compensating ability of the SDA and the short-range Al-compensating ability of the proton, which encourages the formation of Al-O(H)-Al. Considering these results a key open question is whether Al-O(H)-Al linkages can be generated in real zeolites samples through dual-template synthesis, in which one of the templates functions as a structure directing agent, and the other as a proton-donor. Furthermore, it would be interesting to examine the influence of the uncharged form of the SDA, in which the hydroxide moiety is included, on Al-directing ability and identify how interactions between the hydroxide and water or charge-compensating cations affect results obtained Chapter 5.

Whilst Chapters 3-5 focus on the impact of extra-framework species on Al distribution, the work contained within Chapter 6 clearly illustrates the impact of Al and framework defect sites such as silanol groups on extra-framework species. In this chapter, simulations of the speciation of the Mo active species during MDA over Mo/MFI catalysts corroborated experimental findings concerning the fact that Mo/silicalite is more prone to rapid deactivation during catalysis than Mo/ZSM-5. The simulations show that the evolution of the initial Mo oxo species into Mo oxycarbide species to proceed differently when supported on the all-silica and aluminosilicalite forms of MFI, silicalite and ZSM-5, respectively. The Mo oxycarbide species is mono-coordinated to the walls of the zeolite in Mo/silicalite, whereas di-coordination is observed in Mo/ZSM-5. At catalytic temperatures, it is hence easier for the oxycarbide species to be liberated and migrate to the surface in Mo/silicalite in Mo/ZSM-5. This is the reason for more rapid deactivation of Mo/silicalite catalyst compared to Mo/ZSM-5. However, it is important to note that only ZSM-5 with a Si/Al ratio of 95 was inspected in this chapter, typical experimental Mo/ZSM-5 catalysts have Si/Al ratios of ~15. It would be interesting to expand this study to firstly establish the most preferable Al distribution in

ZSM-5 at this Si/Al ratio, and then examine how this Al distribution affects Mo speciation during MDA. However, the MFI framework contains 12 crystallographically distinct T-sites in its orthorhombic form. Examining all the possible permutations of six Al per 96 T-site unit cell at the level of theory used throughout this thesis is currently out of the bounds of possibility due to the large computational expense associated with DFT calculations. Expansion of this study hence requires the development of an inexpensive coarse-grain sifting method that can operate with DFT-level accuracy.

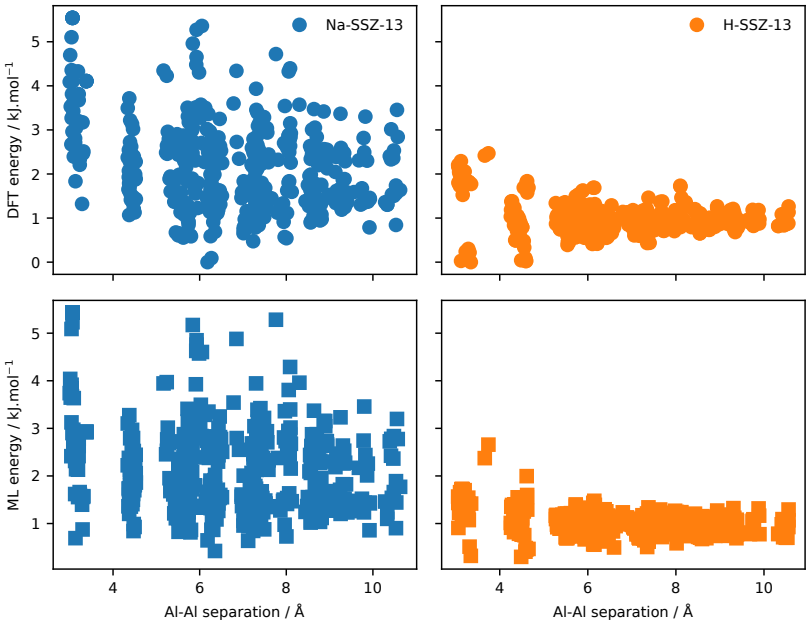

Figure 7.1 *Energy landscapes for H- and Na-SSZ-13 at a Si/Al ratio of 17 (equivalent to 2 Al per U.C.) according to ML and DFT, here relative energy is plotted against Al-Al separation (Å). Data for Na-SSZ-13 is plotted in blue and data for H-SSZ-13 is plotted in orange. Circular points indicate energies according to DFT and square points indicate energies according to the ML model.*

Machine learning has been demonstrated to be a useful tool for the high-throughput screening of large systems, including zeolites.[20] The development of a predictive machine learning model which provides insight into the formation energy of zeolites with different Al distributions is currently in progress. This work is part of a collaborative project with Dr Jack Evans at TU Dresden, who has developed the predictive model using DFT data included in this thesis. The predictive model was constructed using a simple random forest regressor using the Python *scikit-learn* package,[21] the orbital field

matrix (OFM) method[22] was used to describe the structural attributes of the zeolite structure.

The accuracy of this machine learning approach was initially tested on the SSZ-13 DFT data (Chapter 3), this data included both Na- and H-compensated structures at a range of Si/Al ratios. Good correlation was seen between the energies generated by the machine learning model (ML) and the DFT data. On comparison of the energies generated by the ML model for 2 Al per U.C. for Na-SSZ-13 and H-SSZ-13 with those according to DFT (Figure 7.1), we see that the ML model is capable of accurately reproducing the energy landscape generated by DFT. Most importantly, the ML model captures the preference for Löwensteinian ordering in Na-SSZ-13 and non-Löwensteinian ordering in H-SSZ-13.

In the results discussed above the ML model was both trained and tested on the same DFT data for SSZ-13. However, in order for the predictive model to be useful it is imperative that it is transferable, *i.e.* capable of dealing with all zeolite framework types having only been trained on a subset of framework types. Hence, the training set was extended to include DFT data for LTA, AEI, ABW and RHO, expanding the total data set to include ~1600 structures. Having not been trained on any DFT data for the MOR framework, the ability of the ML model to predict the energies of different Al distributions in unseen H-MOR was then tested. The data for this test is included in Figure 7.2, and shows good correlation between the energies predicted by ML and DFT. Such tests confirm the transferability of this model and prove that this model is capable of predicting the formation energies of different Al distributions in unseen zeolite frameworks with near-DFT level accuracy in a fraction of the time. Such methods could be used to investigate Al distribution in ZSM-5 at a Si/Al of 15 in order to further examine Mo speciation during MDA in Chapter 6. The model could also be used to further expand the number of frameworks evaluated in Chapter 3, allowing a more realistic picture of the most thermodynamically favourable Al distribution in zeolites to be painted.

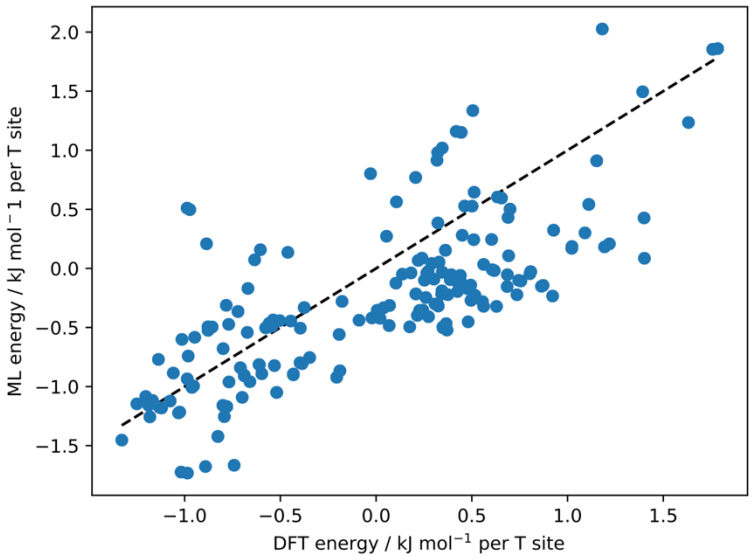

Figure 7.2 *Correlation plot of the predicted energies for H-MOR at a Si/Al ratio of 23 (equivalent to 2 Al per U.C.) according to the machine learning model and DFT.*

Furthermore, the simulations in Chapter 3 involved the geometry optimisation of a subset of frameworks optimised using 1x1x1 unit cells through fully periodic DFT. Whilst a subset of 2x2x2 supercells were tested, these supercells were generated from smaller unit cells and contained Al distributions identical to those present within the smaller unit cell structures from which the supercells were generated. Real zeolites have been demonstrated to contain heterogeneous Al distributions. Large supercells are required to examine the relative stability of these heterogeneous Al distributions compared to homogenous distributions. Once again, exhaustively examining the all the possible permutations of Al in these large supercells would be extremely time consuming and expensive using DFT. The dataset was extended again to include 2x2x2 and 3x3x3 supercell data for Na-SSZ-13 and H-SSZ-13. In keeping with results for 1x1x1 cells, energies provided by the machine learning model showed good correlation with those according to DFT. Confirming that the model can not only handle larger supercell structures but is also capable of accurately predicting the energies of different Al distributions within large supercell structures having only been trained on smaller unit cell structures.

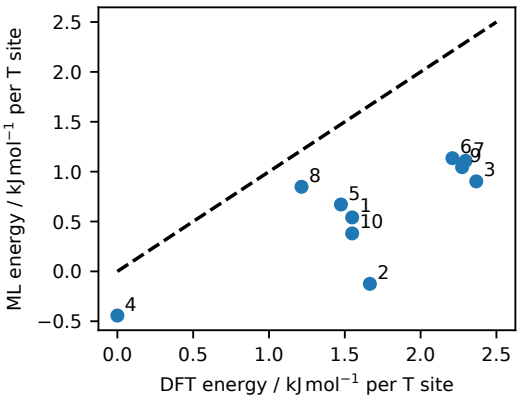

	Al distribution	
1	NNN	
2	all alumina centre	non-Löwensteinian
3	NNNN	
4	4 x 4 rings	non-Löwensteinian
5	NNN	
6	NNNN	
7	NNNN	
8	isolated Al-O-Al linkages	non-Löwensteinian
9	random	
10	3 x 4 rings + 4 isolated Als	non-Löwensteinian

Figure 7.3 *Correlation plot for the energies of 10 unseen 2x2x2 H-SSZ-13 supercell structures containing extremely heterogeneous Al distributions predicted by the machine learning model and DFT. Each of the structures are numbered 1-10, the plot shows the Al distributions contained within each of the numbered structures. It is evident that the structures are grouped together due to similarities in Al distribution.*

The supercell extension was then tested on 10 unseen H-SSZ-13 2x2x2 supercells containing extremely heterogeneous Al distributions. Figure 7.3 shows a correlation plot for the energies of these unseen structures according to the ML model and DFT. Whilst the correlation between the two levels of theory could be improved, the machine learning model is able to group together supercell structures, in terms of their relative energies, based on patterns in their framework Al distributions. For example, structures 3, 6 and 7 contain Al pairs as NNNN, and structures 5 and 1 contain Al pairs as NNN, these structures have similar energies which are predicted by the ML model. Furthermore, the machine learning model was able to calculate the energies for the 10 structures, each of which contained 880 atoms, in a matter of seconds.

This preliminary data demonstrates that not only can machine learning can be used as a tool for calculating the formation energies of zeolites, but it can be used as a high-throughput screening method which can provide insight into the most stable Al distribution in zeolite frameworks with DFT-level accuracy whilst being far less computationally expensive than DFT. As discussed, the transferability of this model means that in the future it can be used to calculate the energies of large numbers of different framework types with a range of Si/Al ratios. Furthermore, the supercell extension shows that this method is appropriate for predicting the energies of large

structures containing disordered Al, allowing more realistic Al distributions to be considered. Following further development, this tool can be used to provide a more comprehensive understanding of the most thermodynamically stable Al distributions in zeolites.

Finally, it should be noted that the work contained within this thesis only evaluates the most thermodynamically favoured and thermally accessible Al distributions in fully-formed zeolite frameworks. Whilst the Al distributions reported are the most thermodynamically favoured, discrepancies between the predictions made in these chapters and experiment are to be expected due to kinetic factors operative during zeolite synthesis that are not accounted for in these simulations. Such factors include the assemblage of aluminosilicate units during the pre-nucleating and nucleating stages of synthesis. Previous computational studies concerned with the stability of aluminosilicate cluster-species have determined non-Löwensteinian clusters to be less stable than Löwensteinian clusters, furthermore, these clusters have also been shown to follow Dempsey's rule.[23]

The aim of this study was to better understand the factors that influence Al distribution in zeolites, this aim has been addressed through the systematic examination of the most thermodynamically favourable Al distributions in a range of zeolites using DFT. The work contained within this thesis demonstrates the influence of extra-framework species on Al distribution, and *vice versa*. Furthermore, this work provides new insight into Löwenstein's and Dempsey's rules, demonstrating that adherence to these rules can be either encouraged or discouraged through an adept choice of counter-cation or templating species, or through the post-synthesis treatment of the zeolite crystal. The culmination of this work is the development of a machine learning model which provides insight into Al distributions in zeolite with DFT-level accuracy. I hope the work contained within this thesis contributes to understanding reaction mechanisms and deactivation mechanisms that occur in real catalysts, which was the main motivation of this work, and that it incites new experimental study into Al distribution in protonated zeolites.

References

1. Loewenstein, W. *Am. Mineral.* **39,** 92–96 (1954).
2. Dempsey, E. *J. Catal.* 115–119 (1977).
3. Fletcher, R.E., Ling, S., Slater, B. *Chem. Sci.* **8,** 7483–7491 (2017).
4. Zhao, Z., Xing, Y., Li, S., Meng, X., Xiao, F-S., McGuire, R., Parvulescu, A-N., Müller, U., Zhang, W. *J. Phys. Chem. C* **122,** 9973–9979 (2018).
5. Rey, J., Raybaud, P., Chizallet, C. *ChemCatChem* **9,** 2176–2185 (2017).
6. Holzinger, J., Beato, P., Lundegaard, L.F., Skibsted, J. *J. Phys. Chem. C* **122,** 15595–15613 (2018).
7. Perea, D. E., Arslan, I., Liu, J., Ristanović, Z., Kovarik, L., Arey, B.W., Lercher, J.A., Bare, S.R., Weckhuysen, B.M.*Nat. Commun.* **6,** 7589 (2015).
8. Zones, S. I. & Van Nordstrand, R. A. *Zeolites* **8,** 166–174 (1988).
9. Zones, S. I. *US 4544538: Zeolite SSZ-13 and its method of preparation* (1985).
10. International Zeolite Association. *Zeolite Synthesis Directory* (2001).
11. Pinar, A.B., Márquez-Álvarez, C., Grande-Casas, M., Pérez-Pariente, J. *J. Catal.* **263,** 258–265 (2009).
12. Márquez-Alvarez, C., Pinar, A.B., García, R., Grande-Casas, M., Pérez-Pariente, J. *Top. Catal.* **52,** 1281–1291 (2009).
13. Van Der Gaag, F.J., Jansen, J.C., Van Bekkum, H. *Appl. Catal.* **17,** 261–271 (1985).
14. Biligetu, T., Wang, Y., Nishitoba, T., Otomo, R., Park, S., Mochizuki, H., Kondo, J.N., Tatsumi, T., Yokoi, T. *Journal of Catalysis* **353**, 1-10 (2017).
15. Lok, B.M., Cannan, T.R., Messina, C.A. *Zeolites* **3,** 282–291 (1983).
16. Yokoi, T., Mochizuki, H., Biligetu, T., Wang, Y., Tatsumi, T. *Chem. Lett.* **46,** 798–800 (2017).
17. Althoff, R., Schulz-Dobrick, B., Schüth, F., Unger, K. *Microporous Mater.* **1,** 207–218 (1993).
18. Debras, G., Gourgue, A., Nagy, J.B., Clippeleir, G. De. *Zeolites* **5,** 369–376 (1985).
19. Ruiz-Salvador, A. R., Grau-Crespo, R., Gray, A. E., Lewis, D.W. *J. Solid State Chem.* **198,** 330–336 (2013).
20. Evans, J. D. & Coudert, F.-X. *Chem. Mater.* **29,** 7833–7839 (2017).
21. Pedregosa, F., Varoquaux, G., Gramfort, A., Michel, V., Thirion, B., Grisel, O., Blondel, M., Prettenhofer, P., Weiss, R., Dubourg, V., Vanderplas, J., Passos, A., Cournapeau, D., Brucher, M., Perrot, M., Duchesnay, É. *J. Mach. Learn. Res.* **12,** 2825–2830 (2011).

22. Lam Pham, T., Kino, H., Terakura, K., Miyake, T., Tsuda, K., Takigawa, I., Chi Dam, H. *Sci. Technol. Adv. Mater.* **18,** 756–765 (2017).

23. Yang, C.-S., Mora-Fonz, J. M., Catlow, C. R. A. *J. Phys. Chem. C* **115,** 24102–24114 (2011).

Appendix

Appendix A

SS MAS ^{29}Si NMR Data (Chapter 3)

Solid-state NMR calculations were performed for the L and NL 2 Al per unit cell global minimum structures using CASTEP (version 8.0) with the CP2K optimised geometry because of the high computational cost associated with geometry optimisations of large systems. Calculations were performed using the PBE functional, on-the-fly pseudopotentials and planewave basis sets with a cutoff of 60 Ry, and a Monkhorst-Pack *k*-points grids of (3x3x3) were used to sample the Brillouin zone. The ^{29}Si chemical shifts, referenced to tetramethylsilane (TMS), are shown below.

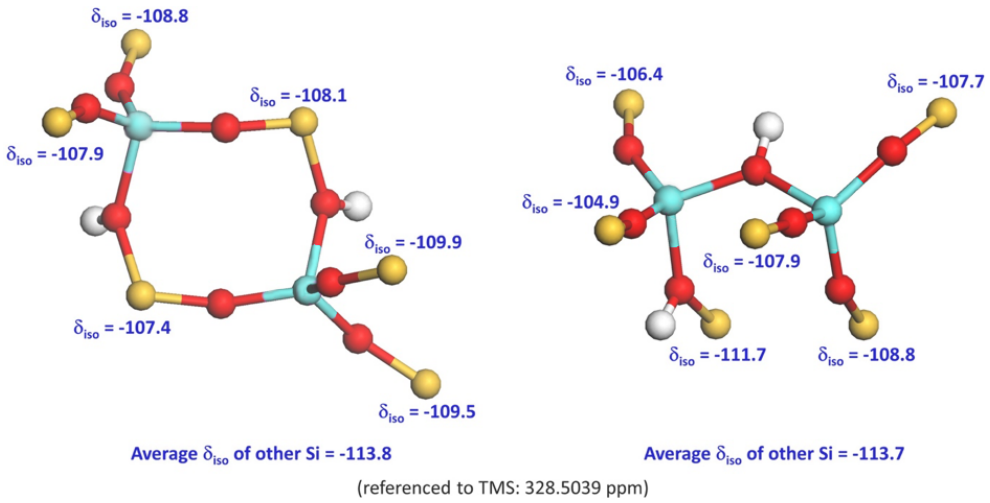

The anticipated chemical shifts (ppm) for different silica environments are as follows:[9]

4Si (0Al)	3Si (1Al)	2Si (2Al)	1Si (3Al)	0Si (4Al)
-100 to -115	-96 to -107	-91 to -100	-85 to -95	-80 to -91

Increasing the amount of aluminium bonded to the silica tetrahedra significantly decreases the negativity of the chemical shift (shifted downfield). This phenomenon is observed in our DFT predictions. The average chemical shift of 4Si in both frameworks is approximately -114 ppm, this increases to a maximum shift of -104·9 ppm for SiO_4 bonded to a single aluminium in the NL structure. This method could not be used to

characterize Al-O-Al at such a high Si/Al ratio as chemical shifts for all silica environments are far too similar, also any peaks that could be considered ‘characteristic’ of a nearby Al-O(H)-Al would be lost in background noise in the NMR spectrum.

Appendix B

Vibrational frequencies (Chapter 3)

Using CP2K, the vibrational frequencies of the L and NL 2 Al per unit cell H-SSZ-13 global minimum structures were predicted. The vibrational frequencies are shown below, the stretches are indicative of a free hydroxyl bonded at -Si-O-Al- and -Al-O-Al- (3500 - 3700 cm^{-1}) are highlighted in grey. These stretches overlap with other broad stretches and would not be uniquely discernible.

Vibrational Frequencies / cm^{-1}

NL H-SSZ-13				L H-SSZ-13			
41.086	280.913	459.911	775.480	34.079	276.316	451.709	773.324
60.700	284.215	464.448	776.906	55.845	279.429	453.624	774.907
62.841	285.040	466.106	780.052	58.215	281.211	457.809	778.264
66.204	286.070	467.836	780.401	67.772	282.933	462.642	779.523
71.213	288.480	470.124	794.045	69.986	285.094	464.906	793.011
79.036	291.250	470.484	796.538	73.962	286.222	467.940	794.640
83.716	293.592	472.992	800.852	77.216	288.777	469.025	798.655
91.913	295.027	476.505	974.877	79.369	289.208	470.884	993.773
93.805	296.247	477.041	977.147	84.305	290.988	473.611	1002.309
97.372	297.325	479.247	998.464	91.581	293.718	476.569	1003.629
101.567	298.764	480.501	1001.794	95.905	296.944	478.007	1008.455
103.036	301.419	480.755	1005.069	99.897	297.771	480.059	1009.491
109.587	302.791	482.842	1008.935	104.715	299.632	481.547	1012.134
112.457	303.172	484.444	1013.073	107.956	302.274	483.072	1014.181
115.894	305.490	487.453	1015.120	109.689	303.286	486.479	1015.945
122.126	308.469	490.901	1017.229	114.726	306.703	487.946	1017.846
123.307	310.304	491.421	1019.178	117.631	306.916	490.320	1018.454
127.511	314.905	493.762	1020.337	120.582	309.430	493.185	1019.376
134.077	317.646	495.863	1021.235	128.715	310.100	497.700	1022.931
134.407	319.222	499.681	1022.248	131.484	314.976	501.279	1024.867
137.322	320.221	506.260	1024.148	134.693	316.073	505.999	1027.613
142.557	324.034	509.776	1024.340	137.829	318.730	507.753	1028.312
145.870	326.486	511.175	1027.749	138.905	319.934	509.569	1029.497
147.035	330.468	515.541	1029.806	142.454	326.546	511.889	1031.092
147.733	331.858	536.236	1030.197	144.373	328.034	528.920	1032.354
151.114	333.907	544.018	1031.939	144.928	329.369	531.849	1033.877
152.361	337.729	551.341	1032.664	150.270	331.673	546.898	1034.714
156.749	338.623	563.546	1035.630	154.458	332.887	553.237	1036.601
158.904	340.575	568.779	1036.356	156.840	334.536	568.751	1039.284
160.488	341.975	583.620	1037.189	158.086	337.647	586.200	1039.398
161.486	342.371	591.713	1038.148	161.620	338.406	588.652	1040.573
165.783	344.140	593.259	1038.653	164.384	339.932	592.987	1041.621
166.708	347.491	596.488	1042.923	166.364	342.812	594.907	1044.496
170.959	350.620	598.476	1043.823	168.419	347.192	598.416	1045.304
172.948	352.842	601.131	1044.487	169.194	347.824	598.575	1047.497
174.223	354.989	601.522	1047.496	173.004	350.606	600.278	1047.930
177.640	358.478	608.647	1049.074	176.228	352.831	601.513	1051.638
178.923	360.613	612.718	1050.657	176.860	353.919	607.803	1053.262
182.899	361.603	614.399	1052.260	179.789	361.705	608.873	1054.064
183.027	363.761	616.432	1055.648	184.165	363.032	617.486	1055.753
184.783	367.420	620.433	1059.292	185.135	364.830	619.851	1056.985
185.955	371.459	624.156	1066.223	185.732	367.279	620.922	1073.847
188.620	373.127	627.769	1073.359	187.387	368.186	623.672	1082.761

190.671	374.184	637.823	1083.783	188.126	371.972	642.725	1087.536
192.691	376.490	652.838	1103.831	190.826	372.989	652.676	1099.736
193.738	377.708	666.989	1111.319	191.002	373.270	656.263	1110.110
194.571	379.022	677.882	1121.494	193.120	374.284	672.431	1116.757
195.994	380.609	680.600	1122.121	194.137	377.214	676.902	1117.905
196.682	382.328	685.354	1123.747	194.497	378.374	678.813	1121.236
198.895	383.619	686.535	1125.932	197.730	380.332	682.719	1126.825
200.963	385.723	693.316	1128.760	198.988	381.666	693.006	1128.819
202.850	386.332	697.145	1131.447	202.576	382.311	708.745	1129.863
203.654	387.263	713.096	1135.988	203.254	385.485	722.359	1134.511
204.135	388.917	730.237	1137.010	206.637	385.882	728.002	1135.050
207.644	391.012	734.399	1138.314	208.239	387.447	733.763	1140.596
209.803	391.441	738.851	1142.604	208.841	387.864	734.614	1142.541
213.123	394.794	742.477	1143.669	214.696	389.946	740.692	1146.420
216.380	395.470	746.615	1145.350	219.292	392.472	743.545	1147.640
221.024	397.282	748.056	1148.473	219.734	393.165	748.788	1148.864
224.110	399.088	750.353	1150.856	220.819	393.821	749.008	1152.122
226.453	401.381	751.393	1151.481	221.968	398.271	749.974	1152.560
228.693	402.226	752.215	1155.128	226.289	399.384	751.049	1156.436
230.187	403.995	752.989	1156.439	229.192	401.921	752.203	1158.169
232.893	405.128	754.186	1158.231	232.483	403.626	752.689	1159.746
235.102	407.200	754.979	1158.909	238.339	405.894	753.368	1163.000
245.470	413.514	756.073	1161.212	239.145	413.223	754.148	1164.140
247.639	413.935	756.288	1163.527	244.171	414.555	756.003	1165.520
250.655	416.097	757.296	1164.708	248.343	417.860	757.088	1165.981
252.351	418.391	759.423	1167.186	251.621	419.769	757.548	1167.974
258.163	421.317	760.947	1169.325	253.637	423.265	757.887	1170.740
261.616	422.868	763.969	1171.032	254.586	423.590	760.133	1172.795
263.343	425.553	765.144	1172.328	256.397	427.084	761.962	1174.619
264.785	428.809	766.028	1175.551	260.969	431.194	763.313	1176.196
266.483	432.927	766.922	1181.557	261.894	434.051	765.538	1177.260
268.482	436.148	767.268	1184.349	263.797	435.187	766.050	1179.158
270.691	437.957	767.892	1187.353	266.189	438.149	767.873	1181.042
272.142	438.603	769.125	1191.960	267.723	438.283	768.272	1185.312
273.041	438.751	769.933	1203.460	269.031	439.838	768.527	1190.400
275.187	442.348	770.510	1205.895	270.299	441.582	770.129	1201.193
276.693	445.236	772.746	3665.621	272.041	443.347	770.755	3696.139
276.938	448.423	773.513	3698.982	273.308	448.831	771.415	3699.446
277.645	454.582	774.920		275.201	449.963	772.230	

Appendix C

Vibrational frequencies for NL and L H-SSZ-13 structures (Si/Al = 17, 11 and 8) containing a single acetonitrile probe (Chapter 3)

Structure	O-H Vibrational Frequencies / cm^{-1}			
	Probe		No Probe	
	Al-O(H)-Al	Si-O(H)-Al	Al-O(H)-Al	Si-O(H)-Al
Ac1_2Al_NL	3714	2353	3713	2800
Ac1_4Al_NL	3703		3701	
	3690		3688	
	3420		3525	
	3351		3491	
Ac4_2Al_L		3713		3712
		3710		3711
Ac1_3AL_L		3713		3714
		3405		3508
		3244		3402

Appendix D

IR Spectra for 2 Al per unit cell NL and L H-SSZ-13 GM structures (Si/Al 17) containing a single acetonitrile probe (Chapter 3)

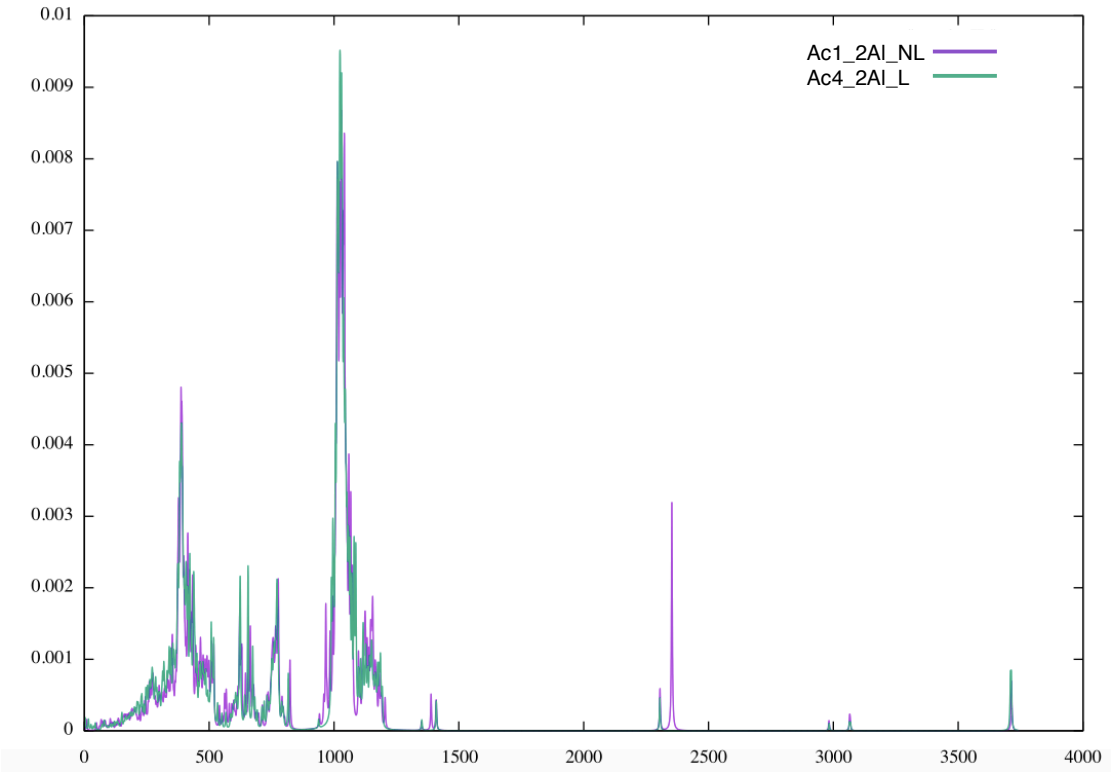

Whilst the stretch at 2353 cm^{-1} looks promising for characterising Al-O(H)-Al in NL frameworks the probe molecule is not coordinated to the Brønsted acidic protons in the L structure, hence a direct comparison cannot be made. Furthermore, in the NL structure the probe molecule is bound to an Si-O(H)-Al proton rather than an Al-O(H)-Al proton, demonstrating that there is no preference for acetonitrile to bind to the Al-O(H)-Al proton and further confirming that IR is not a suitable method to characterise NL ordered frameworks.

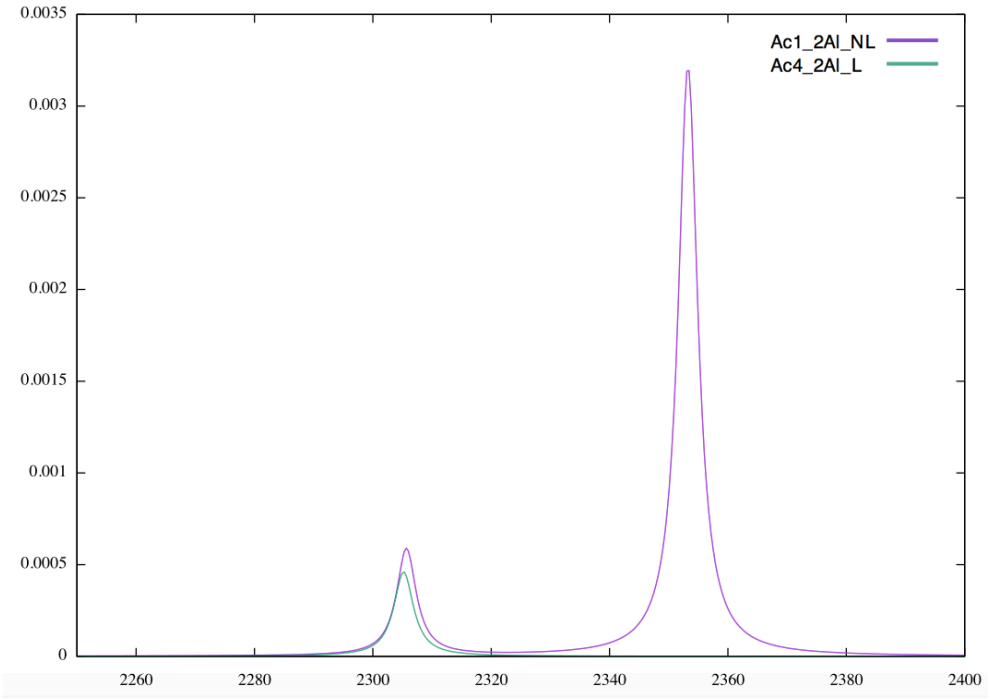
Ac1_2Al_NL
Ac4_2Al_L
0.0035
0.003
0.0025
0.002
0.0015
0.001
0.0005
0
2260
2280
2300
2320
2340
2360
2380
2400

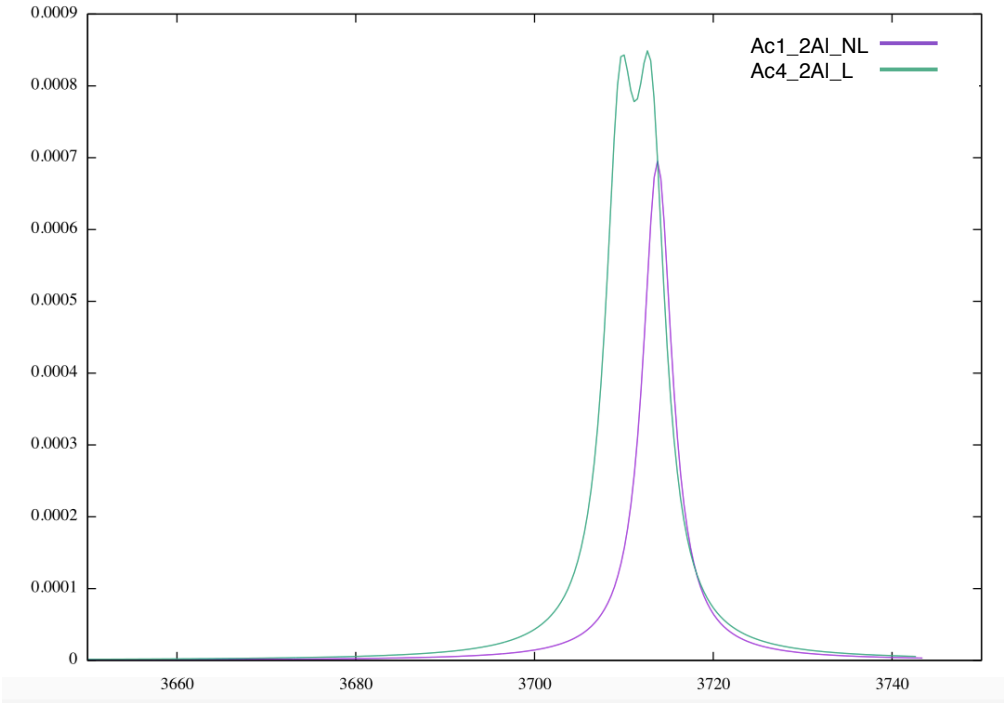
Ac1_2Al_NL
Ac4_2Al_L
0.0009
0.0008
0.0007
0.0006
0.0005
0.0004
0.0003
0.0002
0.0001
0
3660
3680
3700
3720
3740

Appendix E

BLYP-D3 data for 2 Al per (001) terminating slab structures (Chapter 4)

The BLYP-D3 vdW-corrected functional was used to reoptimise a subset of 2 Al per (001) terminating slab structures to determine whether the observed stabilisation energy on forming water at the surface of the zeolite, *via* the migration of an acidic proton to terminating hydroxyl, was a product of the functional used (as PBE is known to overbind hydrogen bonding and underestimate the barrier to proton transfer between O-H----O). However, whilst the values for PBE are higher (as expected) there is no significant change in $\Delta E(E_{Q3} - E_{Q4})$ or $\Delta E(E_{Q3Al\text{-}H_2O} - E_{Q3Al\text{-}OH})$ following reoptimisation with BLYP-D3.

	BLYP-D3 / kJ mol^{-1}	**PBE / kJ mol^{-1}**
$\Delta E(E_{Q3} - E_{Q4})$	33·4	44·9
$\Delta E(E_{Q3Al\text{-}H_2O} - E_{Q3Al\text{-}OH})$	60·4	69·6

Appendix F

AIMD data for the 2 Al per (001) terminating slab global minimum structure (Chapter 4)

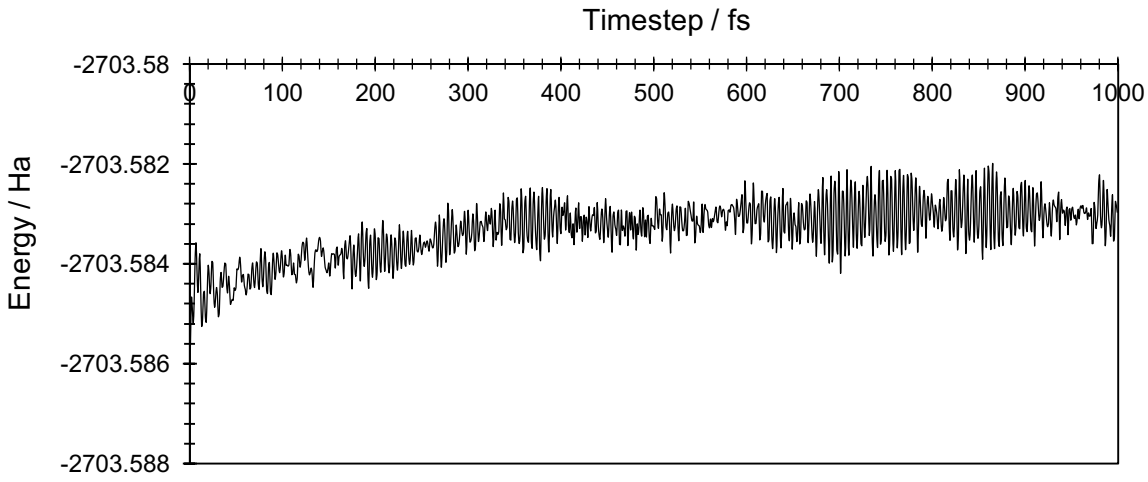

AIMD was used to further confirm that there is no proton transfer between O-H----O in the global minimum 2 Al per (001) terminating slab structure. AIMD simulations were performed using CP2K at the PBE level of theory, with a 1 fs timestep in the NVT ensemble at a temperature of 433 K.